

A Thesis Submitted for the Degree of PhD at the University of Warwick

Permanent WRAP URL:

<http://wrap.warwick.ac.uk/130972>

Copyright and reuse:

This thesis is made available online and is protected by original copyright.

Please scroll down to view the document itself.

Please refer to the repository record for this item for information to help you to cite it.

Our policy information is available from the repository home page.

For more information, please contact the WRAP Team at: wrap@warwick.ac.uk

279

D 67694/P6

TAM C.H.

279

WARWICK.

DESIGN AND DEVELOPMENT OF
AXIAL-FIELD AIR-CORED BRUSHLESS DC MOTORS

by
C H Tam B Sc (Hons)

A thesis submitted for the
degree of Doctor of Philosophy

to
The Department of Engineering
University of Warwick

May 1985

To Mary

TABLE OF CONTENTS

Table of Contents	i
List of Figures	vi
List of Tables	xiv
Acknowledgements	xv
Summary	xvi
List of Principle Symbols	xvii
CHAPTER 1 INTRODUCTION	1
1.0 Axial-Field Brushless DC Motor - An Overview	1
1.1 Motor Construction	4
1.1.1 The rotor	4
1.1.2 The armature	6
1.2 Motor Design Parameters	6
1.2.1 Active conductor dimensions	6
1.2.2 Air-gap flux density	10
1.2.3 Number of poles	12
1.2.4 Pole-arc/pole-pitch ratio	12
CHAPTER 2 PRINCIPLE OF ROTATING MAGNET AXIAL-FIELD MACHINES	14
2.0 Introduction	14
2.1 Types of Permanent Magnet Axial-field Machines	16
2.1.1 Stationary-field axial machines	16
2.1.2 Rotating-field axial machines	17
2.2 The Magnetic Circuit	20
2.2.1 The properties of magnetic materials	22
2.2.2 Magnet circuit principle	26
2.2.3 Air-gap flux distribution	29
2.2.3.1 EMF waveform and power inverter	29
2.2.3.2 Pole-arc/pole-pitch ratio	30
2.2.3.3 Number of poles	33
2.2.3.4 Field system arrangement	33
2.2.3.5 Choosing the value of α	34
2.3 The Electric Circuit	34
2.3.1 Design and assumptions	38
2.3.2 Approximation of the flux density function	38
2.3.3 The EMF equation	44
2.3.4 Distribution factor and the EMF equation	45

CHAPTER 3	BRUSHLESS DC MOTORS	48
3.0	Introduction	48
3.1	Induction Machine Fed by Variable Frequency Inverter	49
3.2	Inverter-fed Synchronous Machine with Rotor Positions Feedback	51
3.3	Derivation of Brushless DC Motor from Commutator DC Motor	52
3.4	Brushless DC Motor Configurations	54
3.4.1	The one-phase uni-polar brushless dc motor	57
3.4.2	The one-phase bi-polar brushless dc motor	57
3.4.3	The two-phase uni-polar brushless dc motor	57
3.4.4	The two-phase bi-polar brushless dc motor	61
3.4.5	The three-phase uni-polar brushless dc motor	61
3.4.6	The four-phase uni-polar brushless dc motor	61
3.4.7	The three-phase bi-polar brushless dc motor	61
3.4.8	Number of windings and excitation current pulses	62
3.5	Brushless DC Motor Constructions and Operations	62
3.5.1	High power thyristor-switched brushless dc motors	62
3.5.2	Medium power transistor-switched brushless dc motors	68
3.5.3	Small brushless dc motors	69
3.6	Rotor Position Detectors	70
3.6.1	Reluctance switches	72
3.6.2	Optical sensors	72
3.6.3	Hall-effect ICs	74
CHAPTER 4	MOTOR PERFORMANCE ASSESSMENT	75
4.0	Introduction	75
4.1	The Motor Scheme	75
4.2	Motor Parameter Modelling	78
4.2.1	Power device modelling	78
4.2.2	Machine equivalent circuit	79
4.3	Current Equation	83
4.4	Output Equations	91
4.5	Digital computation of the Performance Characteristics	93
CHAPTER 5	UNDERCOMMUTATION AND COMMUTATION ADVANCING	98
5.0	Overview	98
5.1	Effects of Undercommutation	98
5.2	Commutation Advancing	100
5.3	Optimum Commutation Advancing	101
CHAPTER 6	BRUSHLESS DC DISC-MOTOR PROTOTYPES	107
6.0	Introduction	107

6.1	Design Specifications of Prototypes	108
6.1.1	Motor 1	108
6.1.2	Motor 2	109
6.1.3	Motor 3	109
6.2	Magnetic Circuit Design	110
6.2.1	Properties of magnet materials	110
6.2.2	Selecting a permanent magnet material for Motors 2 and 3	112
6.2.3	The magnetic circuits	113
6.3	Electric Circuit Design	116
6.4	Mechanical Design	122
6.5	Motor Parameters	128
6.6	Rotor Position Detector	132
6.7	Operation of the Prototype Motors	134
6.7.1	Motor 1	134
6.7.2	Motor 2	136
6.7.2.1	Uni-polar mode	136
6.7.2.2	Bi-polar mode	138
6.7.3	Motor 3	146
CHAPTER 7	THE ELECTRONIC POWER REGULATOR	158
7.0	Introduction	158
7.1	Pulse-width Modulation	158
7.1.1	Sine-wave modulation	159
7.1.2	Harmonic elimination	161
7.2	Electronic Power Regulator Configuration	162
7.2.1	Establishing a modulation strategy	162
7.2.2	PWM pulse-train generation	166
7.3	The Power Circuit	169
7.3.1	Power transistor switching characteristics	169
7.3.2	Selecting the PWM power devices	170
7.3.3	The power MOSFET	173
7.3.3.1	Construction and properties	173
7.3.3.2	Driving the power MOSFET	174
7.3.4	The power circuit	175
7.3.5	Power circuit switching efficiency	177
7.4	Current Transfer Characteristics of The EPR	183
7.4.1	Assumptions	183
7.4.2	Motoring mode	184
7.4.2.1	The on-period equations	184
7.4.2.2	The off-period (free wheeling) equations	187
7.4.2.3	Continuous and discontinuous conductions	187
7.4.2.4	Average armature current	190

7.4.2.5	Average dc-line current	191
7.4.2.6	Computed results	192
7.4.3	Regenerative braking mode	192
7.4.3.1	The on-period equations	192
7.4.3.2	The regen-period equations	197
7.4.3.3	Average braking current	200
7.4.3.4	Average regenerative current	201
7.4.3.5	Computed results	201
CHAPTER 8 MOTOR DRIVE CONTROL SUB-SYSTEM		203
8.0	Introduction	203
8.1	Functional Requirements and Design Solution	204
8.1.1	Commutation control	204
8.1.2	PWM torque-control	205
8.2	Hardware Sub-system Design and Implementation	207
8.2.1	Overview	207
8.2.2	The MCU Module	208
8.2.3	Position Detection Module	212
8.2.4	Speed Detector Module	216
8.2.5	PWM Generation Module	218
8.2.6	Over-current Protection Logic	221
8.3	Software Sub-system Design and Implementation	221
8.3.1	Overview	221
8.3.2	Software design	222
8.3.3	Power Down	224
8.3.4	Position Decoding	224
8.3.5	PWM Control	226
8.3.6	Power-up Initialisation and Demand Input	229
8.3.7	Data Base	229
8.4	System Performance	231
8.5	Discussion of Drive Characteristics	234
8.5.1	Motoring mode	234
8.5.2	Regeneration mode	239
CHAPTER 9 CONCLUSIONS AND SUGGESTIONS FOR FURTHER WORK		240
9.0	Introduction	240
9.1	The Brushless DC Disc-motors	240
9.2	The Electronic Power Regulator	241
9.3	The Motor Controller Sub-system	242
9.4	Suggestions for further work	244
Appendix A Delta Function		246

Appendix B	Discrete Fourier Transform	247
Appendix C	Design Data and Performance of the Wheelchair Motor	249
Appendix D	Measurement of Armature Self-inductance	251
Appendix E	MPU Memory Map and Port Assignments	252
REFERENCES	254

LIST OF FIGURES

Figure 1.1	Functional block diagram of drive system	2
Figure 1.2	An exploded view of the machine	3
Figure 1.3	Double-sided field system	5
Figure 1.4	Single-sided field system	5
Figure 1.5	A preformed wire-wound coil	7
Figure 1.6	Dimensions of active conductors	8
Figure 1.7	An extreme case of very small inner diameter	11
Figure 1.8	Pole-arc/pole-pitch ratio	11
Figure 2.1	Axial-field principle	15
Figure 2.2	A practical axial-field design	15
Figure 2.3	DC disc-motor	18
Figure 2.4	Performance of the lawn-mower motor	18
Figure 2.5	Stationary-field ac disc-motor	19
Figure 2.6	Rotating-field ac disc-motor	19
Figure 2.7	Brushless dc disc-motor	21
Figure 2.8	Air-gap clearance	21
Figure 2.9	B-H hysteresis-loop	23
Figure 2.10	Normal and intrinsic magnetisation curves	23
Figure 2.11	Demagnetisation curve with contour of constant BH-product, and BH-product curve	25
Figure 2.12	Recoil lines	25
Figure 2.13	Cross-section of the flux path	27
Figure 2.14	Centres of pole-faces	27
Figure 2.15	Comparison of power output between sinewave and squarewave inverters	31
Figure 2.16	Position of point Q related to magnet face	31
Figure 2.17	Double-sided field-system flux distribution	35
Figure 2.18	Single-sided field-system flux distribution	35
Figure 2.19	Flux distribution for $\alpha=0.95$	36

Figure 2.20	Flux distribution for $\alpha=0.90$	36
Figure 2.21	Flux distribution for $\alpha=0.85$	36
Figure 2.22	Flux distribution for $\alpha=0.80$	37
Figure 2.23	Flux distribution for $\alpha=0.75$	37
Figure 2.24	An example of disc-motor winding arrangement	37
Figure 2.25	Position of the active conductor in the air-gap of a double-layer armature	39
Figure 2.26	Conductors are treated as with zero thickness	39
Figure 2.27	Position of the area dA related to the field-system and an armature coil	40
Figure 2.28	Measured radial flux distribution along three radial lines	40
Figure 2.29	Rectangular image co-ordinates of the polar co-ordinates of Figure 2.27	43
Figure 2.30	Distribution of the conductors around r_1	43
Figure 3.1	Functional diagram of an induction-type brushless dc motor	50
Figure 3.2	Torque-speed characteristic of a typical inverter-fed squirrel cage induction motor	50
Figure 3.3	Mechanical and electrical arrangement of a dc motor (coils 1-5, 5-1 about to enter commutation zone)	53
Figure 3.4	Coils 1-5, 5-1 in commutation zone	53
Figure 3.5	Coils 2-6, 6-2 about to enter commutation zone	53
Figure 3.6	Synthesis of a 3-phase brushless dc motor from a conventional dc motor	55
Figure 3.7	The 3-phase brushless dc motor with rotor position detector	56
Figure 3.8	One-phase uni-polar motor	58
Figure 3.9	One-phase bi-polar motor	58
Figure 3.10	Two-phase uni-polar motor	58
Figure 3.11	Two-phase bi-polar motor	59
Figure 3.12	Three-phase uni-polar motor	59
Figure 3.13	Four-phase uni-polar motor	59
Figure 3.14	Three-phase bi-polar motor	60
Figure 3.15	Voltage-fed thyristor-switched brushless dc motor	64
Figure 3.16	A controlled rectifier	65

Figure 3.17	A chopper regulator	65
Figure 3.18	Pulse-width modulation	65
Figure 3.19	Principle circuit of current-fed brushless machine	66
Figure 3.20	Inverter waveforms of current-fed brushless machine	66
Figure 3.21	A brushless dc motor commutated by transistors and steered by Hall-effect sensors	71
Figure 3.22	A skew-pole lamination	71
Figure 3.23	Effect of auxillary torque	71
Figure 3.24	Reluctance switch	73
Figure 3.25	Transmissive optical detector	73
Figure 3.26	Reflective optical detector	73
Figure 3.27	An arrangement of trigger magnets and Hall-effect ICs	73
Figure 4.1	Scheme of the brushless dc disc-motor	76
Figure 4.2	Phasor diagram of the nth harmonics	76
Figure 4.3	Connections of Darlington transistors	80
Figure 4.4	Circuit to measure the forward characteristics of a Darlington	80
Figure 4.5	Forward characteristics of MJ11015 and MJ11016	80
Figure 4.6	Equivalent circuit circuit of a switching Darlington	80
Figure 4.7	Relationship in time between the motor voltages and the switching sequence	81
Figure 4.8	Conduction-state diagram of the star-connected bi-polar motor	82
Figure 4.9	Transistor replaced by their circuit equivalents	84
Figure 4.10	Voltage sources of the transistors removed from the main loop	84
Figure 4.11	Equivalent circuit of the star-connected bi-polar motor	84
Figure 4.12	The brushless motor being represented by coupled circuits	85
Figure 4.13	Simple equivalent circuit of the motor	85
Figure 4.14	Simulated current waveforms of the brushless motor	90
Figure 4.15	Discrete-time approximation of a continuous-time function	90
Figure 4.16	Flow-chart of the output performance calculation process	94
Figure 4.17	Calculated output characteristics of the 600W brushless dc disc-motor	96

Figure 5.1	Linear commutation -- a linear change of current with time in the commutated coil 99
Figure 5.2	Commutation sequence, and the relationship in time between the voltage and current of a coil of the bi-polar motor 99
Figure 5.3	Effect of shifting the rotor position sensor by an angle 102
Figure 5.4	Effect on the coil current as a result of overcommutation 102
Figure 5.5	Trapezoidal approximation of the coil emf $e(t)$ 103
Figure 5.6	Relationship in time between v , e and i withing the rising edge of v as the zero reference 103
Figure 5.7	Calculated values of optimum angle of advancing for the 600W 3-phase bi-polar motor 106
Figure 6.1	Demagnetisation curves 111
Figure 6.2	Demagnetisation characteristics of Ferroba III and Supermagloy B2 115
Figure 6.3	Properties of Supermagloies 115
Figure 6.4	A preformed wire-wound coil 117
Figure 6.5	Arrangement of the armature coils 117
Figure 6.6	Winding diagram of the 3-phase disc-windings 119
Figure 6.7	Calculated voltage waveforms of Motors 1, 2 and 3 120
Figure 6.8	General assembly of Motors 1 and 2 123
Figure 6.9	Rotor assemblies of Motors 1, 2 and 3 126
Figure 6.10	Armatures of Motors 1, 2 and 3 126
Figure 6.11	Casings of Motors 1, 2 and 3 127
Figure 6.12	Phase emf waveforms of Motors 1, 2 and 3 129
Figure 6.13	Open circuit characteristics 130
Figure 6.14	Measurements of winding resistances 130
Figure 6.15	Measured phase inductance at different rotor orientations 131
Figure 6.16	Dvnamic loss characteristics 131
Figure 6.17	Principle of the rotor position detector 133
Figure 6.18	Physical arrangements of the rotor position detector 133
Figure 6.19	Segment of the rotor position coded disc 135
Figure 6.20	Effects of a 120°elec voltage pulse on the armature current of Motor 1 135
Figure 6.21	Drive configuration of Motor 2 in uni-polar mode 137

Figure 6.22	Relationship in time between the induced emfs, the phase currents, the applied voltages and the base drive signals of Motor 2 in uni-polar mode137
Figure 6.23	Output characteristics of Motor 2 in uni-polar mode139
Figure 6.24	Current and terminal voltage waveforms of Motor 2 in uni-polar mode141
Figure 6.25	Output torque ripple of Motor 2 in uni-polar mode142
Figure 6.26	Drive configuration of Motor 2 in bi-polar mode142
Figure 6.27	Relationship in time between the induced emfs, the applied voltages and the base drive signals of Motor 2 in bi-polar mode143
Figure 6.28	Output characteristics of Motor 2 in bi-polar mode144
Figure 6.29	Phase current waveform of Motor 2 in bi-polar mode145
Figure 6.30	Arrangements of separate power circuit for each winding147
Figure 6.31	Arrangements of Motor 2 in bi-polar mode with triacs inserted in series to interrupt the delta loop147
Figure 6.32	Schematic of the triac triggering circuit148
Figure 6.33	Relationship in time between the phase emfs, the base drive signals, and the triac triggering signals148
Figure 6.34	Current and terminal voltage waveforms of Motor 2 in bi-polar mode with triacs inserted149
Figure 6.35	Output characteristic of Motor 2 in bi-polar mode with triacs inserted150
Figure 6.36	Arrangement of Motor 3 in star-connected bi-polar mode153
Figure 6.37	Relationship in time between the phase emfs, the phase currents, the line emfs, and the base drive signals of Motor 3 in star-connected bi-polar mode154
Figure 6.38	Current and terminal phase voltage waveform of Motor 3 in star-connected bi-polar mode155
Figure 6.39	Output characteristics of Motor 3 in star-connected bi-polar mode156
Figure 7.1	A pulse-width modulated waveform160
Figure 7.2	Asynchronous and synchronous sine-wave modulation160
Figure 7.3	Harmonic elimination PWM ($m = 3$)163
Figure 7.4	Equivalent conduction loop of the conduction-states163

Figure 7.5	Allowable ripple current of the power devices MJ11015 and MJ11016	...165
Figure 7.6	Sub-harmonic modulation with a square modulation-wave	...165
Figure 7.7	The PWM scheme used by the EPR	...165
Figure 7.8	Relationship in time between the induced emfs, the driving signals and the PWMed armature current	...167
Figure 7.9	Functional block diagram of the PWM generator	...167
Figure 7.10	The timing of the PWM carrier signal	...168
Figure 7.11	Switching times of transistors	...168
Figure 7.12	Relative performance of switching power devices	...171
Figure 7.13	Double-diffused structure of a MOSFET cell	...171
Figure 7.14	Power MOSFET driven by a CMOS gate	...176
Figure 7.15	Power MOSFET driven by an emitter-follower buffer	...176
Figure 7.16	Power MOSFET driven by a 74 TTL gate	...176
Figure 7.17	Power MOSFET driven by a high-speed capacitive driver	...176
Figure 7.18	The basic power circuit of the EPR	...176
Figure 7.19	The collector-emitter saturation characteristics of the Darlington	...178
Figure 7.20	Forward characteristic of the Schottky diode	...178
Figure 7.21	Schematic circuit diagram of the power regulator	...179
Figure 7.22	Static equivalent circuit of the power circuit output-states	...180
Figure 7.23	Block diagram of the test circuit for assessing the EPR's switching efficiency	...181
Figure 7.24	Efficiency characteristic of the drive system under PWM control	...181
Figure 7.25	Switching efficiency of the power circuit	...182
Figure 7.26	PWM terminal voltage and current waveforms	...182
Figure 7.27	Motoring mode current flow paths	...185
Figure 7.28	Motoring mode equivalent circuits	...186
Figure 7.29	Motoring mode steady-state armature currents	...188
Figure 7.30	Motoring mode steady-state armature current transfer characteristics (carrier frequency = 20KHZ)	...193
Figure 7.31	Motoring mode steady-state armature current transfer characteristics (carrier frequency = 10KHZ)	...193

Figure 7.32	Motoring mode steady-state dc-link armature current transfer characteristics (carrier frequency = 20KHz)194
Figure 7.33	Relationship in time between the induced emfs, the driving signals, and the PWMed armature current for regenerating mode194
Figure 7.34	Regen. mode current flow paths195
Figure 7.35	Regen. mode equivalent circuits196
Figure 7.36	Regen. mode steady-state armature currents198
Figure 7.37	Regen. mode steady-state armature current transfer characteristics202
Figure 7.38	Regen. mode steady-state regen. current transfer characteristics202
Figure 8.1	Block diagram of the commutation control logic206
Figure 8.2	Two-dimensional array of PWM on-times206
Figure 8.3	Block diagram of the PWM torque-control logic206
Figure 8.4	Equivalent system diagram of the controller209
Figure 8.5	Outline of the controller's hardware sub-system209
Figure 8.6	Picture of the hardware sub-system210
Figure 8.7	Functional block diagram of the MPU Module210
Figure 8.8	Schematic of the MCU logic211
Figure 8.9	Functional block diagram of the Position Detector Module213
Figure 8.10	Schematic of the Position Detector logic214
Figure 8.11	Timing relationship of the signal processing logic215
Figure 8.12	Schematic and signal timings of the Speed Detector logic217
Figure 8.13	Schematic diagram of the PWM Generation Logic219
Figure 8.14	Signal timings of the PWM Generation Logic220
Figure 8.15	Schematic diagram of the Over-current Protection Logic220
Figure 8.16	Transfer characteristics of the Over-current Protection Logic220
Figure 8.17	Functional diagram of the software sub-system223
Figure 8.18	Flow-chart of the Power Down Module225
Figure 8.19	Flow-chart of the Position Dector Module225
Figure 8.20	Flow-chart of the PWM Control Module227
Figure 8.21	Flow-chart of subroutine SUB1227

Figure 8.22	Flow-chart of subrouting SUB2228
Figure 8.23	Flow-chart of Power-up Initialisation & Demand Input Module230
Figure 8.24	Position decoding look-up tables230
Figure 8.25	Circuit diagram of the Ward-Leonard test system232
Figure 8.26	Picture of the test rig233
Figure 8.27	Motoring mode output characteristics235
Figure 8.28	Regenerative mode output characteristics237
Figure 8.29	Calculated motoring mode torque variations against rotor speed238
Figure 8.30	Braking energy flow diagram238
Figure 9.1	Suggested configuration for higher power regulator243
Figure A1	Graphical representation of the impulse function246
Figure B1	Impulse approximation of function248
Figure D1	Circuit to measure armature self-inductance251
Figure D2	Coil current oscillogram251

LIST OF TABLES

Table 6.1	Properties of magnets111
Table 6.2	List of parts for Motors 1 and 2124
Table 6.3	Electrical characteristics of MJ11015 and MJ11016124

ACKNOWLEDGEMENTS

I would like to acknowledge the help of those who have encouraged and assisted me during the period of my research. First of all, I would like to extend my sincere gratitude to my supervisor, Mr. A.E. Corbett, for his helpful advice, suggestions and comments.

I also wish to thank all the members of staff in the Engineering Department, without whose help much of the work described here would not have been possible. In particular, I would like to express my gratitude to Peter Hunt for letting me use the Machines Lab. and for charging the batteries. To Dave Thomson and Graham Robinson for building the prototype motors and grinding the magnets. To Dave Roberts and Phil Cope for getting me those impossible-to-get components. To Bruce Cosh and Selami Soylemez for doing the mechanical design and drawings of the motors. To John Corbett for making the armatures. And to Alan Hume for his patience and instruction in the use of the Prime computer.

Specially, I would like to thank my wife, Mary, for her patience, understanding and support, and for her lessons in 'how to write in English'; my parents for their moral and financial support; and Sunny for lending me his wordprocessor.

Finally I record my gratitude to Cableform Ltd. for their financial support of this project.

SUMMARY

This thesis is concerned with the principle and operation of axial-field brushless dc motors. It also describes the development of a brushless dc drive system which consists of three system elements: a disc-motor, an electronic power regulator, and a microprocessor-based controller.

The principle of axial-field machines is discussed, and attention is given to the effect of the air-gap flux distribution on the emf waveform. By controlling the flux distribution, the induced emf is optimised for inverter-fed operation. The aim of the optimisation is to increase the motor's power density, and to simplify the interfacing between the control electronics and the motor. The designs and operations of three prototype motors are described, and certain problems relating to brushless dc motors, and to disc-motors in particular, are discussed. These problems include undercommutation, and the effect of the drive configuration on the armature current.

The design of the electronic power regulator and the selection of a suitable pulse-width modulation (PWM) strategy for current control are presented. The features of the 3-phase 4-quadrant regulator, which capitalised on the special characteristics of the disc-motor, include the use of power MOSFETs as the PWM devices, and the use of an inverter bridge of which only the bottom-half is PWMed. A model of the switching regulator is also presented.

The microprocessor-based controller sub-system controls the commutation sequence and the switching pulse-width of the power regulator to provide a constant torque output from the drive system. Both the commutation and the pulse-width controls are implemented by using the look-up table technique. The commutation signals are derived from a specially developed rotor position detector which can be used to provide automatic commutation advancing.

LIST OF PRINCIPLE SYMBOLS

ac	alternating current
\bar{A}_C	specific electric loading
α	pole-arc to pole-pitch ratio
A_{pn}	area of pole face
A_{pp}	area of pole area
B	specific magnetic loading
B_g	air-gap flux density
B_m	flux density of magnet
B_{ms}	maximum flux density allowable in mild steel
B_θ	circumferential flux distribution in the air-gap
C_r	reduction factor
d_1, d_2	inner, and outer active diameters of disc-motor
dc	direct current
e_a, e_b, e_c, e	induced phase voltages
emf	electro motive force
f	frequency
g	number of turns per coil
H_g	magnetising force of the air-gap
H_m	magnetising force of magnet
i_a, i_b, i_c, i	armature currents
K_{en}	chord factor for the nth harmonic
K_{sn}	skew factor for the nth harmonic
K_w	winding factor
l_g	length of air-gap
l_m	total thickness of magnet
$L_{aa}, L_{bb}, L_{cc}, L$	winding self-inductances
L_{ab}, L_{ba}, \dots, M	mutal inductances
LF	loss factor

mmf	magnetomotive force
p	number of poles
ϕ_m	total flux per pole
r_1, r_2	inner, and outer active radii of disc-motor
R_a, R_b, R_c, R	winding resistances
S	number of slots
SF	space factor
t_f	thickness of flux return ring
v_a, v_b, v_c, v	applied voltages
ω	angular frequency

CHAPTER 1 INTRODUCTION

1.0 Axial-Field Brushless DC Motor - An Overview

Axial-field machines, which have disc-shaped armatures and short axial lengths, have long been an active research subject at the University of Warwick. The development of such machines at Warwick began in 1967 with an industrial contract for research into 'in wheel' traction-drive applications (1). Developments since then have produced a number of motors for both domestic and industrial applications (2,3,4). These were mostly of the dc commutator type.

A major break from the established mode of dc axial-field motor research was made when the university received a new contract for the development of a brushless dc drive system in 1979. This system was to consist of a commutatorless axial-field motor, a rotor position-sensor, and a microprocessor-based power regulator. Figure 1.1 gives the functional block diagram of the drive system.

The most interesting component of this system is the motor. The motor has a topological lay-out which is similar to that of a typical dc disc motor; but its construction differs from the conventional dc disc machine in such a way that, instead of having a moving armature, its armature is stationary, and it is the permanent magnet field system which rotates instead. Figure 1.2 shows an exploded view of the machine; and its salient features are listed below:

- (1) The topology of the motor gives rise to a short axial-length, and hence a compact machine.
- (2) The armature is completely free of iron.
- (3) There is no discrete slot in the armature.
- (4) Field excitation is provided by permanent magnets.
- (5) Machine operation is completely brushless.

These features give rise to various useful characteristics, which are as

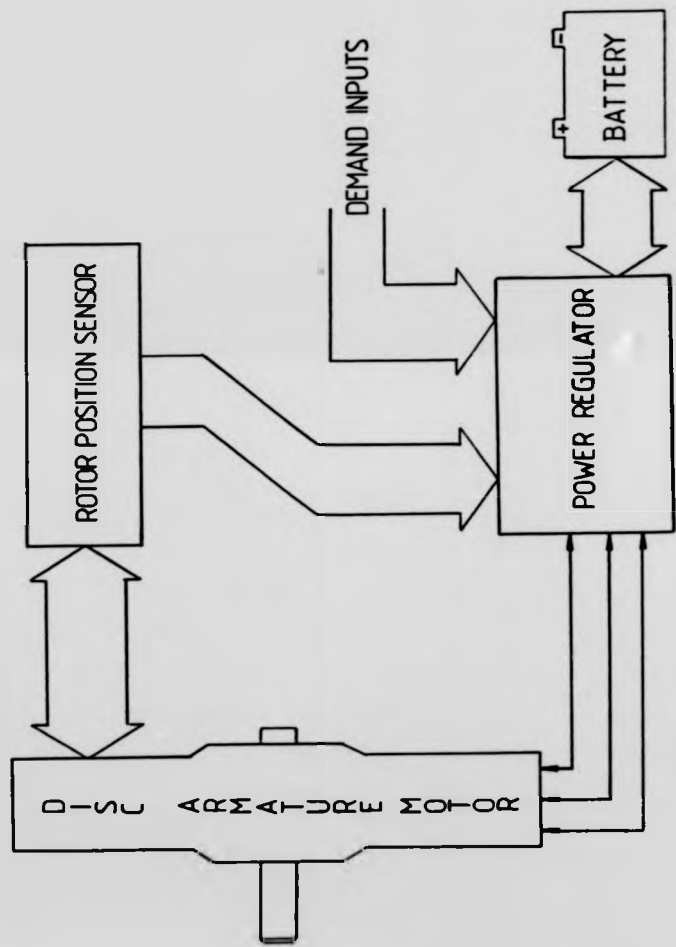


Figure 1.1 Functional block diagram of drive system

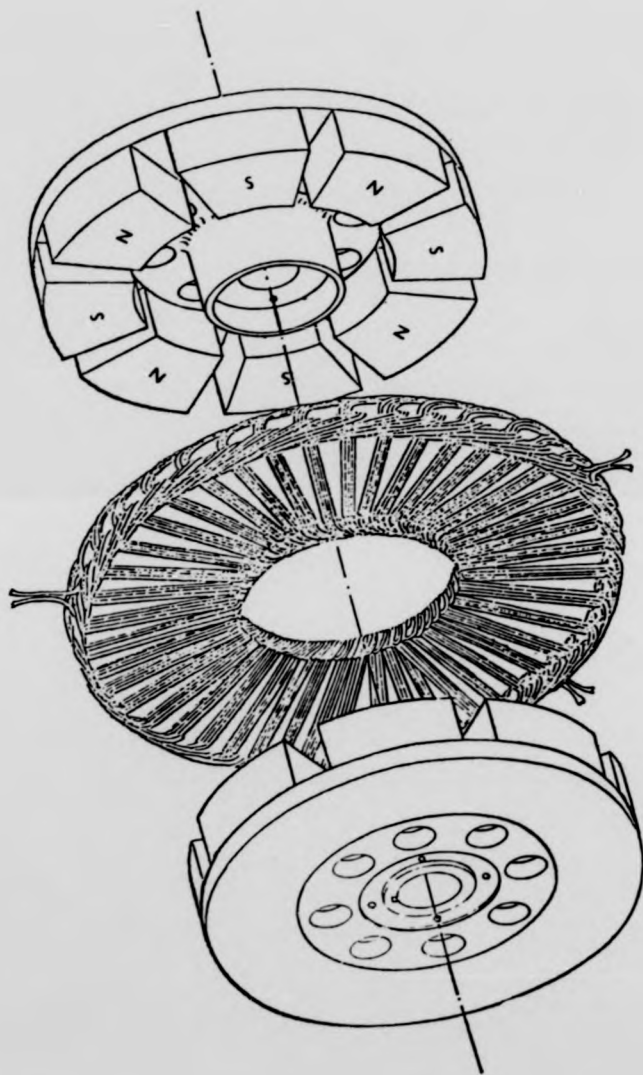


Figure 1 2 An exploded view of the machine

follows:

- (1) The compactness of the motor gives rise to high power-to-weight, and power-to-volume, ratios.
- (2) Because of the ironless armature, under normal operating conditions, the armature reaction flux is extremely small, so that it is practically impossible, either to saturate the magnetic circuit, or to de-magnetise the permanent magnets.
- (3) As there is no iron, iron-losses (eddy currents and hysteresis) are almost completely eliminated.
- (4) Since there are no discrete slots in the armature, breakaway friction normally caused by hysteresis, and cogging, which usually results from the interaction between the discrete magnetic poles and the armature slots, are eliminated.
- (5) The machine's efficiency is inherently greater, because no field excitation is required.
- (6) The maintenance problems associated with the brushes and the commutator are removed.
- (7) As there is no wearing of essential components, the machine has a longer life-span and improved reliability.
- (8) Brushless operation produces low electrical and acoustic noise.
- (9) Being brushless, these machines are explosion-proof and can operate in hostile and explosive environments; they are operative even in hard vacuum.
- (10) These machines are capable of very high speed operations, again due to their brushlessness.

1.1 Motor Construction

1.1.1 The Rotor

The field excitation of the motor is provided by a multi-polar system of rotating magnets with sector-shaped pole-faces. The length of the magnets

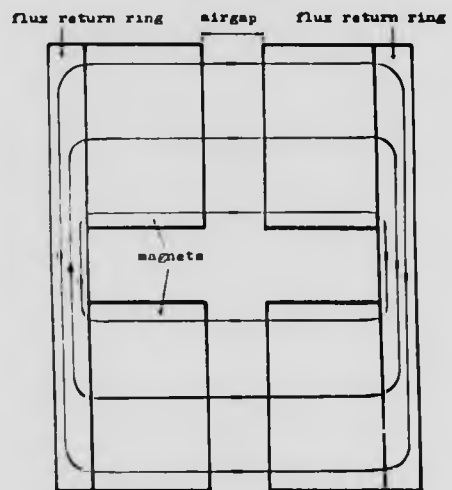


Figure 1.3 Double-sided field system

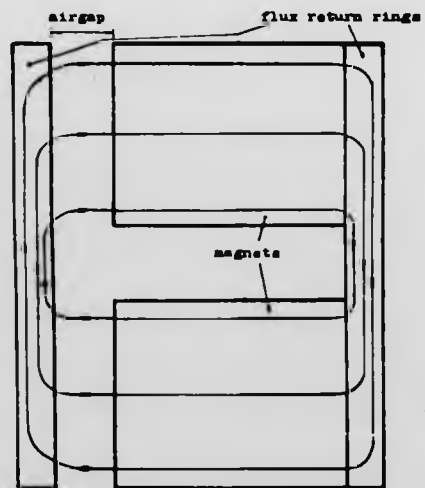


Figure 1.4 Single-sided field system

depends on the type of permanent magnet material used, the length of the airgap, and the required flux-density. The poles are magnetised in alternating sequence, and are bonded to a thin annular mild steel plate which nevertheless has sufficient thickness to provide a magnetic path to adjacent magnets without being saturated. The magnetic return path on the remote side of the air-gap is completed by an identical magnet assembly, as shown in Figure 1.3; or alternatively, the magnetic return path can be completed by a single steel plate, but the same total magnet volume is required to maintain the air-gap flux density, as shown in Figure 1.4.

1.1.2 The Armature

Situated in the air-gap is a disc-shaped armature. This armature is constructed by nesting the individually formed wire-wound coils (Figure 1.5) in a winding jig, and the ends of the coils are connected together to form a three-phase winding in the normal way. The whole armature is either encapsulated in epoxy resin or taped with heat-curing, impregnated glass tape, to provide rigidity and strength.

1.2 Motor Design Parameters

1.2.1 Active Conductor Dimensions

Among the design parameters of an axial-field brushless motor, there are four parameters that are of particular importance in determining the motor's characteristics. The first parameter is the radial dimension of the active armature conductors. This dimension is defined by the inner diameter, d_1 , and the outer diameter, d_2 , of the magnet pieces, as shown in Figure 1.6.

From Figure 1.6, it is clear that the total number of conductors is dictated by the inner diameter for a given armature thickness. In designing the armature it is necessary to maximize the use of the inner diameter to accommodate the largest amount of copper that is possible. However, to completely fill the inner

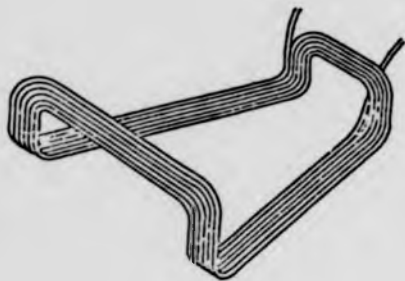


Figure 1.5 A preformed wire-wound coil

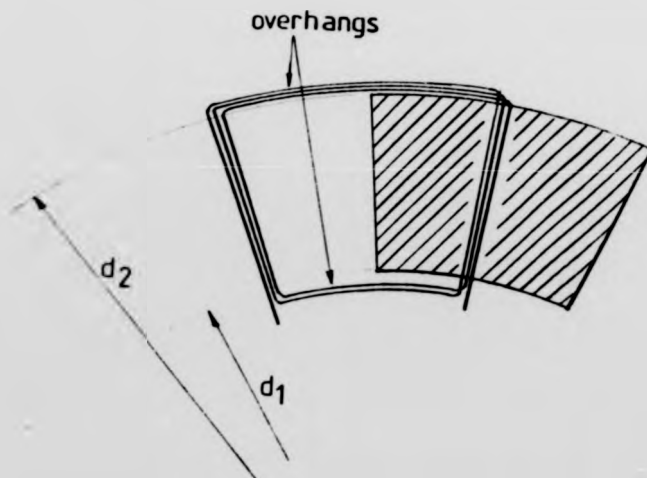


Figure 1.6 Dimensions of active conductors

diameter d_1 would leave no room for the end-windings, which must exit at diameters less than d_1 . A space factor is therefore defined to account for the end-winding space requirement:

$$SF = \frac{nTG}{4r_1L} \quad \dots (1.1)$$

where n = no. of phases

T = turns/phase

L = no of layers

G = wire gauge

In designing an armature, one should ensure that the space factor is not too close to unity, so that the inner end windings can be stacked together comfortably. The exact value of the space factor is dependent on the particular armature construction. But as a general rule, the location of the end windings must be as close to d_1 as possible, whilst allowing a suitable clearance (normally of about 1mm) between the end windings and the magnet edges.

If d_1 is fixed by the number of armature conductors, then the output power can be increased by the lengthening of the active conductors. This is done by enlarging the outer diameter d_2 . In doing so, a short-coming of the disc armature winding arrangement -- the usage of the available armature space decreases with an increased d_2 -- is revealed. An extreme case is shown in Figure 1.7. Undoubtedly, this is wasteful in the sense that it is not filled with current-carrying conductors to take advantage of the available magnetic field to produce torque.

On the other hand, if the rotor inertia is to be kept low, d_2 should be reduced. But if d_2 is allowed to decrease the power output would be decreased due to the diminished active conductors. Of course the lost power output can be restored by increasing the copper content in the armature thickness. But then the air-gap must be enlarged to accommodate the expanded armature, and either a longer

magnet, or a totally different magnet material, is required to maintain the air-gap flux density.

There are also other aspects of machine performance, such as efficiency, power-to-weight ratio and power-to-volume ratio, which are affected by the choice of d_2 . It is therefore necessary to establish a relationship between d_1 and d_2 , in which the optimum performance is obtained. However, it is impossible to find a single relationship that relates all the performance characteristics. From the point of view of the potential application of the motor, one feels that the relationship between d_1 and d_2 should be optimised against the output power. This is confirmed by the finding of the Electrical Reviews (5) that it is important to reduce the size and weight of the motors designed for traction applications as much as possible.

It has been shown by Campell (18) that the output power can be expressed in terms of the two diameters, using expressions for the specific magnetic, and electric loadings of the machine:

$$P = 0.1387 k_w \bar{B} \bar{A}_c n (d_2^2 - d_1^2) d_1 \cdot 10^{-3} \text{ (kW)} \quad \dots (1.2)$$

where k_w = winding factor
 \bar{B} = specific magnetic loading
 \bar{A}_c = specific electric loading
 n = number of poles

In this equation, if we assume that \bar{B} , \bar{A}_c are fixed and k_w is an estimated value, then the power output is proportional to $(d_2^2 - d_1^2) d_1$. The maximum power for a given d_2 can be found by equating the differential dP/dd_1 to zero:

$$\frac{dP}{dd_1} = (0.1387 k_w k_f \bar{B} \bar{A}_c n \cdot 10^{-3}) (d_2^2 - 3d_1^2) = 0 \quad \dots (1.3)$$

Thus $d_2 = \sqrt{3}d_1 \quad \dots (1.4)$

By substituting (1.4) into (1.2), we have

$$P = 0.1387 k_f k_w \bar{B} \bar{A}_c n \frac{2}{3\sqrt{3}} d_2^3 \times 10^{-3} \text{ (kw)} \quad \dots (1.5)$$

Consequently, one can conclude that the power output of an axial-field machine is a function of the outer diameter as well as the values of \bar{B} and \bar{A}_c . In designing an axial-field machine, therefore, these values must be chosen carefully, so that the armature thickness is minimised in order to maintain a short air-gap, while at the same time allowing the armature to handle the rated current.

1.2.2 Air-gap Flux Density

The second important design parameter is the air-gap flux density. This parameter directly affects the choice of the type of magnet material used and the air-gap length; and ultimately, the motor's operating efficiency. For a specified output power, a disc motor's electric loading is reduced by means of increasing the air-gap flux density (proportional to the magnetic loading). This would lead to a reduction in the copper loss, and hence to increased efficiency. However, raising the air-gap flux density would involve the changing of the magnet material, or increasing the magnetic volume, or both. But the exact course will depend on the nature of the motor's application.

The meaning of 'air-gap' in the axial-field brushless machine does not comply with that of the air-gap of the conventional machine, where it simply means the gap between the stator and rotor cores. In the ironless axial-field machine, it actually includes the armature thickness and the running clearance on both sides of the armature. Supposing that this air-gap has a length l_g , and the reluctance of the flux return path is negligible, then all of the mmfs of the magnet must drop across the air-gap, thus,

$$H_m l_m = H_g l_g \quad \dots (1.6)$$

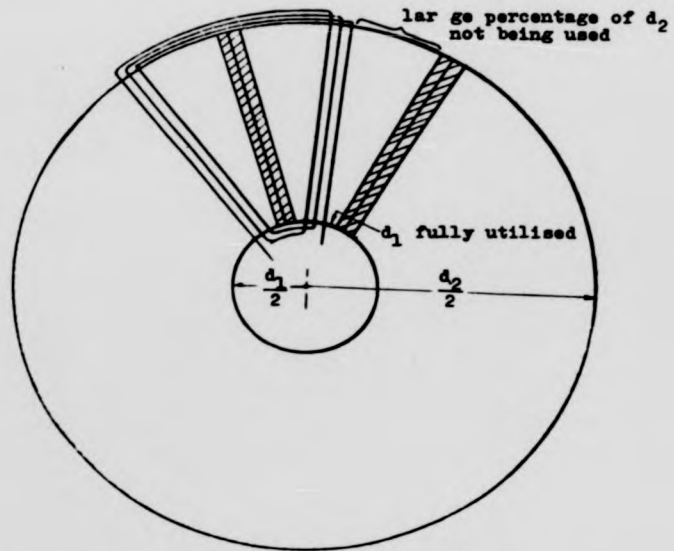


Figure 1.7 An extreme case of very small inner diameter

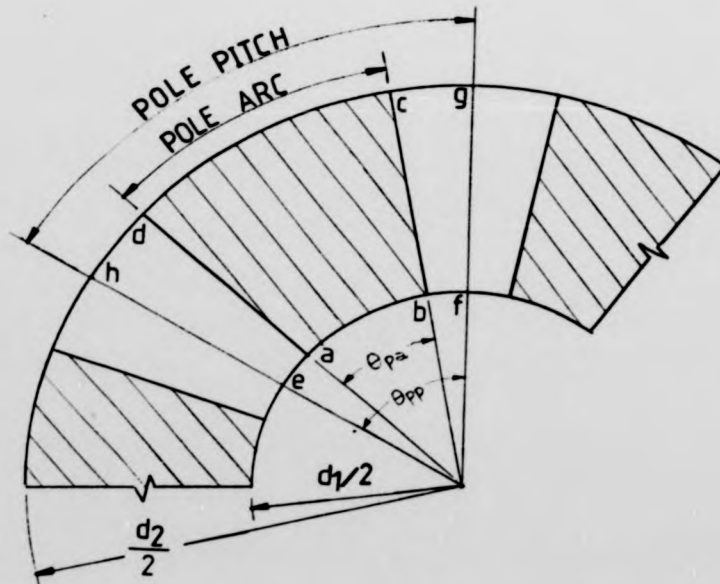


Figure 1.8 Pole-arc/pole-pitch ratio

where H_m = magnetising force of the magnet
 l_m = total length of the magnet
 H_g = magnetising force of the air-gap

This equation shows the dependence of both the magnet length, and the magnetising force, on the air-gap length. One of these quantities must therefore increase to accommodate a larger l_g , while maintaining a specified flux density within the air-gap. Nowadays, it is taken for granted that permanent magnets with high coercivities should be chosen to provide the field. Invariably, this choice is influenced by the general availability of modern magnet materials with high coercivities and high energy contents. However, a higher premium has to be paid for this 'obvious' choice, and one should bear in mind the fact that the type of magnet material eventually chosen is still determined by the specific application of the motor. Chapter 2 will deal with this subject in more detail.

1.2.3 Number of poles

The third design parameter is the choice of the pole number. Specifying too few poles leads to excessively long end-windings thereby increasing the associated I^2R loss. On the other hand, a large number of poles can result in an excessive number of coils, and consequently makes the design impracticable. Also, magnetic leakage increases with pole number. Therefore, when designing with axial-field motors, the pole number must be chosen carefully.

1.2.4 Pole-arc/pole-pitch Ratio

The fourth important parameter of the motor is the pole-arc/pole-pitch ratio, α , of the magnet pole pieces. Referring to Figure 1.8, this ratio is defined as,

$$\alpha = \frac{\text{pole-arc}}{\text{pole-pitch}} \quad \text{or} \quad = \frac{\theta_{pa}}{\theta_{pp}}$$

$$= \frac{\theta_{pa} (r_2 - r_1) / 2}{\theta_{pp} (r_2 - r_1) / 2} \quad \dots (1.7)$$

$$\text{or,} \quad \alpha = \frac{A_{pa}}{A_{pp}} \quad \dots (1.8)$$

where A_{pa} = area of pole face (area of abcd)

A_{pp} = effective pole area (area of efgh)

From equation (1.8), it can be seen that for a given operating flux density, B_m , the total air-gap flux, $B_m A_{pa}$, will become greater as α increases. However, the percentage of the useful flux (which is the flux cutting the armature conductors in perpendicular to their direction of travel) will also be reduced, due to a greater leakage of flux between adjacent poles. This means that the capacity of the magnet material is not utilised to its fullness. For the brushless axial-field motor, it also means an adverse increase in the rotating mass of the field system. Hence, there is clearly a need to optimize the pole-arc/pole-pitch ratio. This subject will also be dealt with in greater detail in Chapter 2.

CHAPTER 2

PRINCIPLE OF ROTATING MAGNET AXIAL-FIELD MACHINES

2.0 Introduction

The essential difference between an axial-field machine and its conventional counterpart lies in the dispositions of the active conductors and the working magnetic flux. In an axial-field machine, the magnetic flux flows in parallel with, while the active conductors run perpendicular to, the shaft of the machine. This construction lends itself to a motor design which is slimmer and lighter than the conventional type, although it has a slightly larger diameter. Despite the differences in their field and winding arrangements, the operating principle of the axial field machines is exactly the same as that of all conventional electrical machines. In other words, in order to produce optimum energy conversion, the direction of the magnetic field and the active conductors must be perpendicular. The axial-field principle is best illustrated by the single conductor machine, which is shown in Figure 2.1. Figure 2.2 shows a practical axial-field design which is based on the same principle. However, in order for this machine to produce rotary motion, the direction of the coil current must be reversed as the polarity of the flux influencing the coils is changed -- this is done by rotating either the field system, or the coil winding, through one pole-pitch. The process of current reversal is called commutation. Commutation can be achieved by various means; the method will depend on the arrangement of the field-system and of the windings. The various methods will be discussed in section 2.1. An overview of the different types of permanent magnet axial-field machines is also given in that section.

Section 2.2 of this chapter explains the principle of the magnetic circuit of brushless axial-field machines. Firstly, the properties of permanent magnets will be described; this is then followed by an explanation of the design principle. The effect of the pole-arc/pole-pitch ratio on the flux distribution will also be discussed.

The last section is devoted to the electric circuit principle of the machine.

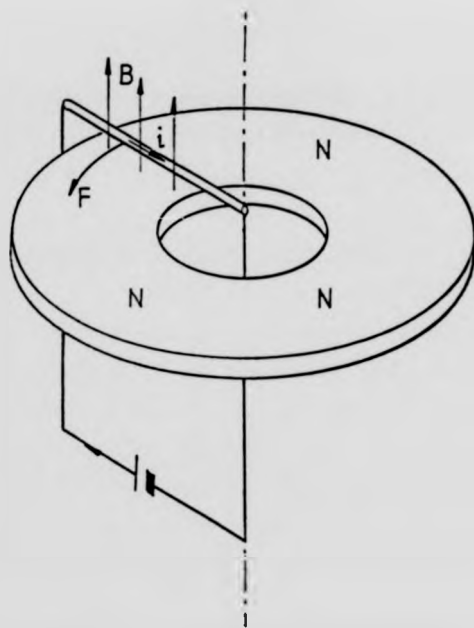


Figure 2.1 Axial-field principle

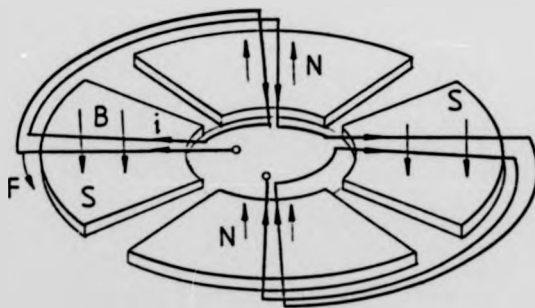


Figure 2.2 A practical axial-field design

Firstly, the construction of the armature winding is described; and this is followed by the derivation of the emf equation.

2.1 Types of Permanent Magnet Axial-field Machines

There are two types of axial-field machines. These are: stationary-field machines, and rotating-field machines. In a stationary-field machine, mechanical energy is transformed into electrical energy, and vice versa, by the rotation of the windings. In a rotating-field machine, the transformation of energy is achieved by the rotation of the field system. Almost without exception, all of the commutator dc axial-field motors belong to the first type, and most of the synchronous axial-field machines belong to the second type.

The machine which is to be described in detail in this thesis is in fact a rotating-field machine.

2.1.1 Stationary-field axial machines

A stationary-field axial machine has a rotating armature-winding into which current is fed, and as a result, electro-mechanical energy conversion takes place. The armature of such a machine is built in the shape of a flat disc, and can be of either the printed-circuit type (6) or the wire-wound type (7). The armature can be of either the dc or ac design.

In a dc armature, commutation is achieved firstly by connecting the winding terminations to copper segments (the commutator), and secondly by applying the current to the commutator through a set of stationary carbon brushes. The fixed relationship between the position of the brushes and the field system invariably causes the current to reverse at the right moment, and this guarantees a uni-directional torque output.

Machines of this type are generally known as dc disc-motors, and Figure 2.3

shows the arrangements of such a machine: it has 2 coils, 4 poles and 4 commutator copper segments. But in order to reduce torque ripples, and to obtain better commutation characteristics, motors of this type usually have more than two coils and many more commutator segments. The work on axial-field machines at Warwick University since 1967 has mainly concentrated on this type. The first prototype to be built at Warwick was a motor for an electric lawn-mower (8); its performance curves are shown in Figure 2.4. When delivering a rated output of 1.25 HP, the machine's efficiency of 76% is extremely good, bearing in mind that the supply voltage is only 12V (the battery voltage). Encouraged by the performance of the lawn-mower motor, further developments were pursued. Subsequent research into practical applications include a radiator fan motor for automotive application (9), several 'wheel-chair' motors (10,11), and a 10 kW traction motor (12).

By making a slight modification to the connections of the dc armature, and by replacing the commutator segments with a pair of slip rings, the motor can also be driven by an ac current, as shown in Figure 2.5. Commutation is now achieved by the ac supply itself. But to produce uni-directional torque output, the frequency of the ac supply and that of the armature rotation must be synchronised, i.e. there is no relative motion between the stator and rotor mmfs; and the resulting ac machine is a synchronous disc-motor. Prior to the project described here no work on this kind of machine had been done at Warwick.

2.1.2 Rotating-field axial machines

The armature of a rotating-field axial machine is stationary. It is also built in the shape of a flat disc such as that of the dc disc-motor. The basic difference between a stationary-armature machine and a stationary-field machine is that the former does not require the commutator and slip rings used in the latter.

When an ac current is applied to the armature, as shown in Figure 2.6, the machine will behave like a synchronous motor. An example of such a motor-type is

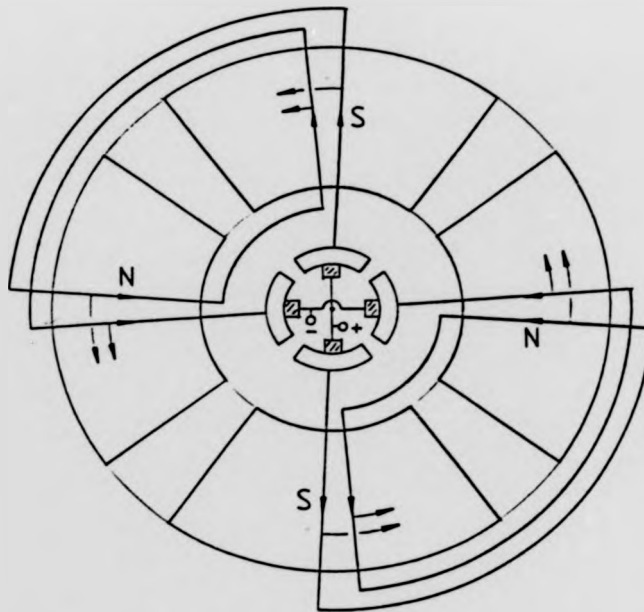


Figure 2.3 DC disc-motor

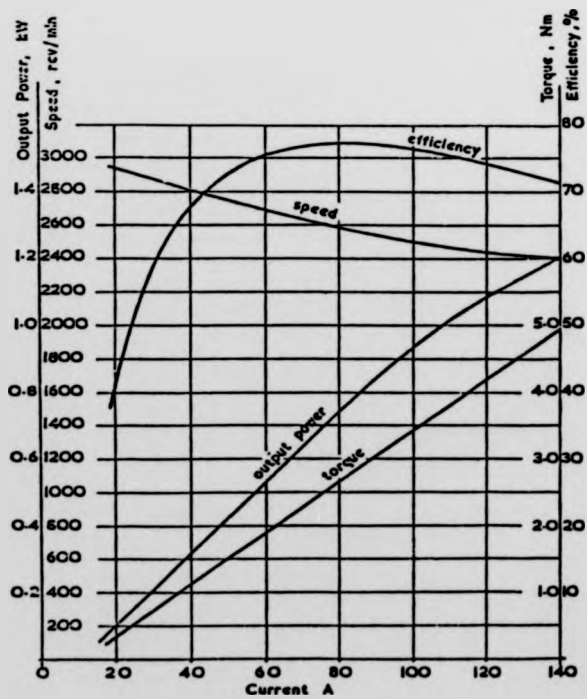


Figure 2.4 Performance characteristics of the lawn-mower motor
supply voltage = 12V

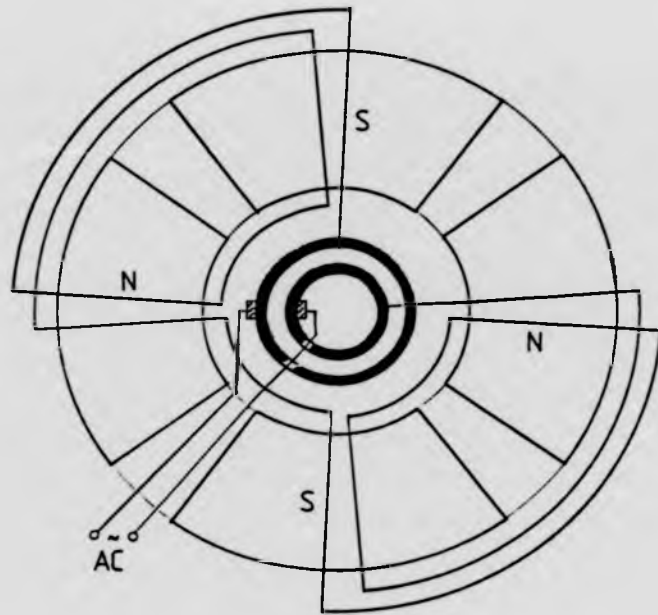


Figure 2.5 Stationary-field ac disc-motor

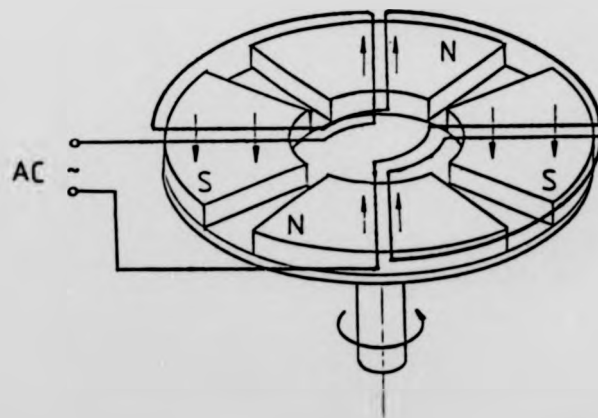


Figure 2.6 Rotating-field ac disc-motor

given by Leung and Chan (13). (Note: in their motor, electro magnets were used instead of permanent magnets.) When the machine is driven by a prime mover, it becomes an alternator. An example of this can be found in Soylemez's thesis (14), where an axial alternator was developed for welding applications.

But, by employing a pair of electronic switches and a rotor position detector, as shown in Figure 2.7, dc supply can also be used. The armature current of the motor is now commutated by the electronic switches, which are in turn controlled by the rotor position. This kind of electronically commutated axial-field machine has output characteristics similar to those of a commutator dc disc-motor and is often referred to as a brushless dc disc-motor. The brushless dc disc-motor forms the main subject of this thesis, and its basic principles will be discussed.

2.2 The Magnetic Circuit

As mentioned in Chapter 1, there are two possible means of completing the magnetic circuit of a permanent magnet disc-motor. One is by using the single-sided arrangement (Figure 1.4), and the other is by using the double-sided arrangement (Figure 1.3). In both of these arrangements, the air-gap is large enough to accommodate the total armature thickness and to allow sufficient running clearance on either side of the armature, as shown in Figure 2.8.

In a closed magnetic circuit, the integral $\oint Hdl$ is equal to zero. Based on this premise, and assuming infinite permeability in the remainder of the magnetic circuit, the mmf in the air-gap H_g can be related to that of the magnet H_m by

$$H_g l_g = H_m l_m \quad \dots(2.1)$$

where l_g is the air-gap width, and l_m the total magnet length. Thus it can be

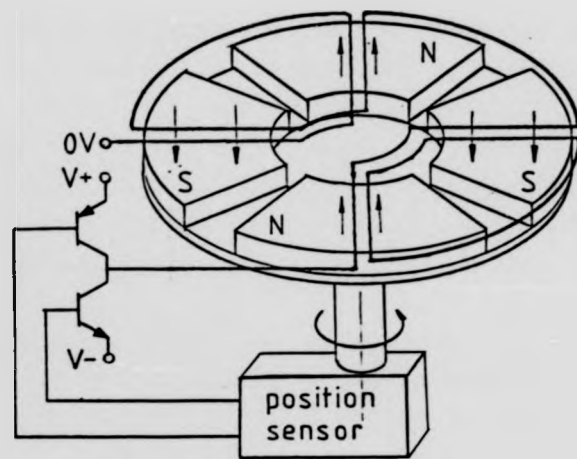


Figure 2.7 Brushless dc disc-motor

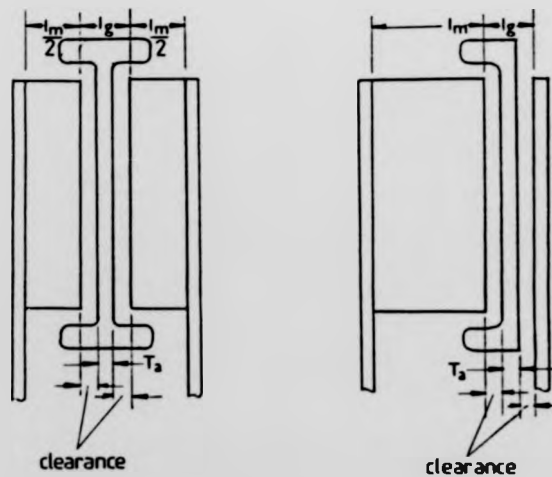


Figure 2.8 Air-gap clearance

seen that in order to accommodate the large air-gap whilst maintaining a given flux density in it, requires a long magnet or one with a high coercive force. In normal circumstances, the latter course is always followed in order to avoid excessive machine weight. Suitable magnet materials include the inexpensive ferrites, the very expensive rare-earth cobalts, and the less expensive polymer-bonded rare-earth cobalts. But the choice of material used will always depend on the particular application in question.

Before proceeding any further with the discussion of the design of the magnetic circuit, it is useful at this stage to consider some of the basic properties of magnetic materials.

2.2.1 The properties of magnetic materials

The reaction of a specimen of magnetic material to a magnetic field depends on the nature and the history of the specimen, and the magnitude and direction of the field. The material's behaviour can be described in terms of the applied field H and the resulting flux-density B , and is summed up in Figure 2.9. The B-H hysteresis-loop represents the complete cycle of the magnetisation and demagnetisation of the material. This B-H loop, known as the normal magnetisation curve, is the sum of the magnetic polarisation J and the flux-density B resulting from the applied field, i.e.

$$B = J + B_0 = J + \mu_0 H \quad \dots(2.2)$$

In this equation, J is also known as the intrinsic flux-density. If J is plotted against H , the effect of B is excluded, and the resultant loop, which represents the intrinsic magnetisation curve, is shown in Figure 2.10 (the heavy lines). The point H_{cJ} represents the polarisation coercivity and is greater than the normal coercivity H_c .

When designing with permanent magnets, which normally operate in a demagnetisation field, the second quadrant of the loop is of greatest interest;

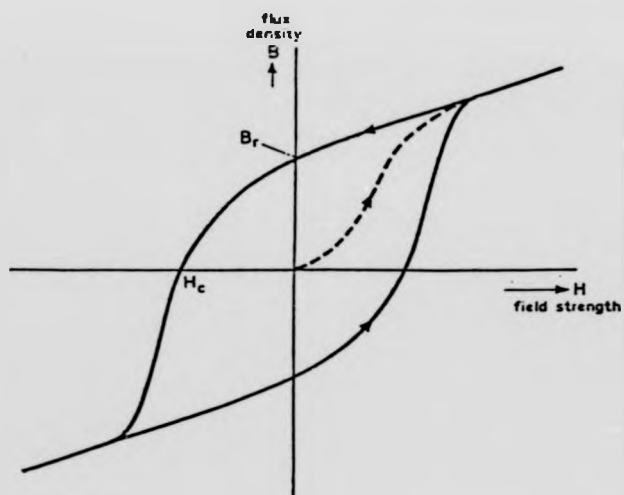


Figure 2.9 B-H hysteresis-loop

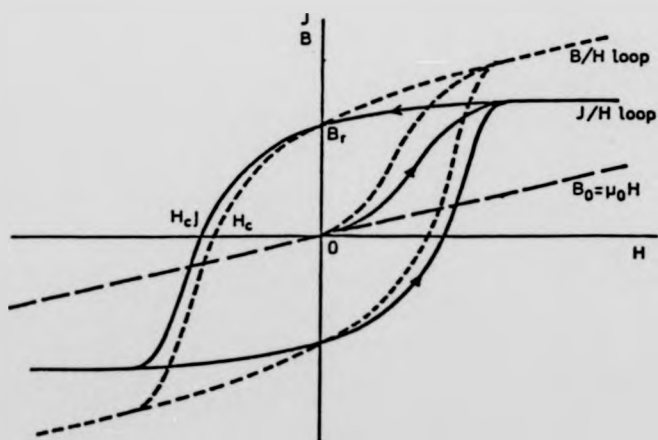


Figure 2.10 Normal and intrinsic magnetisation curves

however, for the purpose of machine design, it is only necessary to consider the normal curve within that quadrant. This part of the normal curve is often referred to as the demagnetisation curve.

Figure 2.11 shows a typical demagnetisation curve of a permanent magnet material. The circle marked on the curve represents the ideal working point BH_{\max} of the material. This BH_{\max} point corresponds to the maximum energy available from the material and thus to optimum utilisation. H_c is the coercive force of the material and it is an indication of the material's resistance to demagnetisation. B_r is the remanence and it is the flux-density of a magnet in a closed magnetic circuit after saturation. If the point (B_m, H_m) is the working point of the magnet, then the line intersecting the demagnetisation curve of the material at the working point is known as the load line. The slope of this line B_m/H_m (or $\cot\theta$) is the permeance of the magnetic circuit.

The demagnetisation curve shown in Figure 2.11 represents the steady decrease in flux-density with increasing demagnetisation of the material. If a magnet is saturated, and then subjected to a certain demagnetising field less powerful than the coercivity, then the flux-density in the magnet will be given by the demagnetisation curve. Under normal conditions, however, the demagnetisation field applied to the magnet is rarely constant; and the working point will not necessarily follow the normal demagnetisation curve. This is most apparent when a magnet is subjected to a given value of demagnetising field which is subsequently reduced. This situation is shown in Figure 2.12.

A saturated magnet is subjected to a demagnetising field H_1 . When this field is reduced, the working point of the material does not follow the demagnetisation curve back towards the remanence, but moves along the curve C. If the demagnetising field is reduced to zero, the working point follows the curve C to B_0 ; restoring the original value of demagnetising field thus causing the working point to fall back to A_1 . In doing this the working point follows the curve D, thus tracing out a small loop in the process. If instead of reducing to zero,

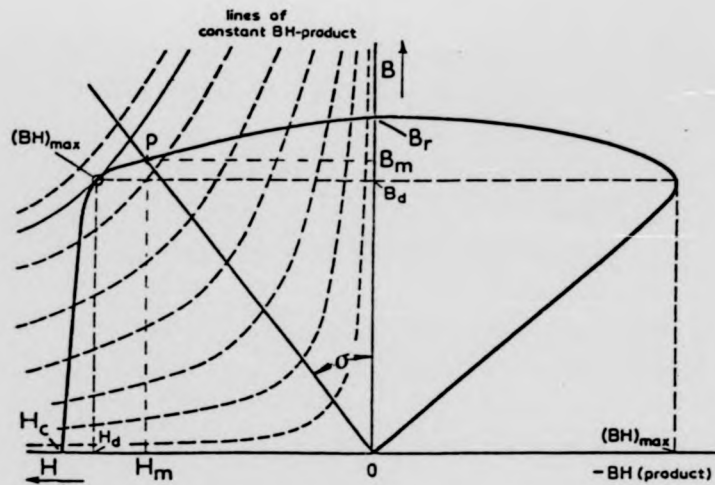


Figure 2.11 Demagnetisation curve with contours of constant BH-product, and BH-product curve

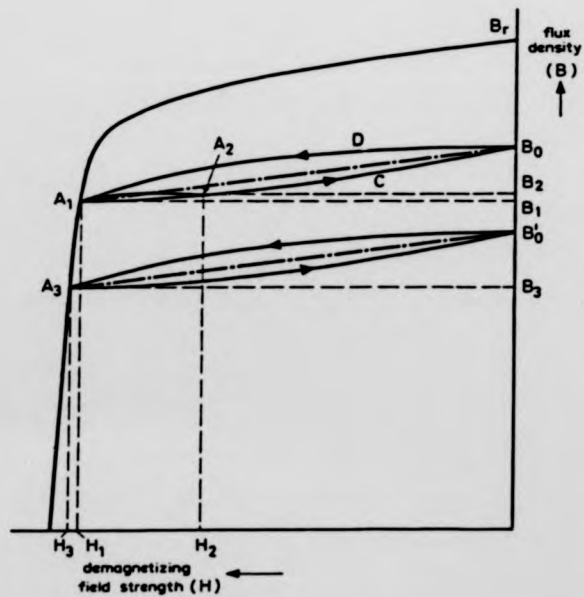


Figure 2.12 Recoil lines

the demagnetising field falls only to H_2 , than the working point moves to A_2 . When restoring the original demagnetising field, a smaller loop is traced. For permanent magnet materials, these loops are usually of very small area, and can be represented as straight lines known as recoil lines. The slope of these recoil lines represents the recoil permeability. Normally the recoil permeability is equal to the slope of the normal curve at B_r .

If after tracing out the loop $A_1CB_0DA_1$, the demagnetising field is further increased to H_3 , the working point will move down the normal demagnetisation curve to A_3 . Reducing the field to zero and then restoring it will cause the working point to follow the loop A_3B_0 , which corresponds to another recoil line parallel to the first.

Care should be taken, to avoid irreversible demagnetisation, when designing magnetic circuit where recoil conditions (such as demagnetising effect of armature reaction in motors) are likely to exist. But in certain types of magnets such as ferrites and rare-earths, recoil conditions do not present any real problems. This is because these magnets possess straight line demagnetisation characteristics which ensure recoil occurs along the original B-H curve and therefore it is possible for them to work under a high demagnetising field without the working point being pushed into a minor loop.

2.2.2 Magnet circuit principle

Since the copper wires and the materials which provide rigidity and strength for the armature all have permeabilities that are only slightly greater than that of air, as far as the magnetic circuit is concerned, the permeability of the armature is taken to be that of air. Figure 2.13 shows a cross-sectional view of the magnetic circuit of an axial-field machine.

Assuming that a magnet material has been chosen, to estimate the thickness of the magnet l_m and the thickness of flux return ring t_r ; the following assumptions are also made:

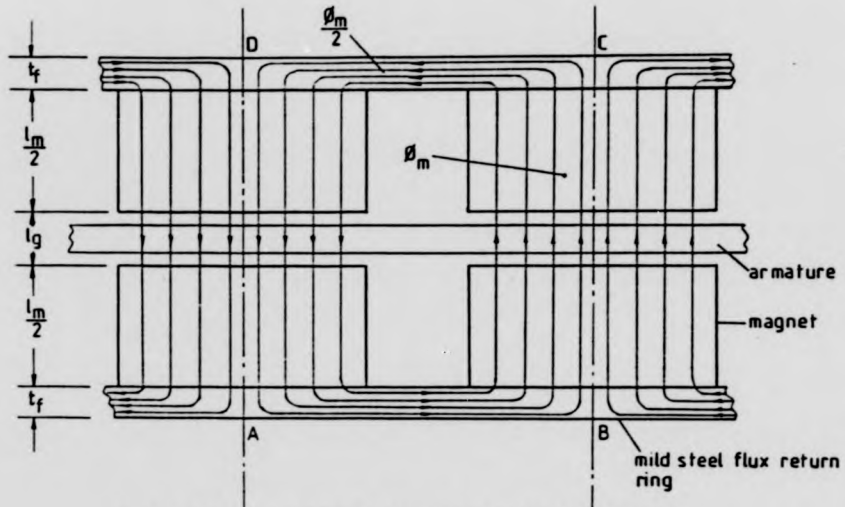


Figure 2.13 Cross-section of the flux path

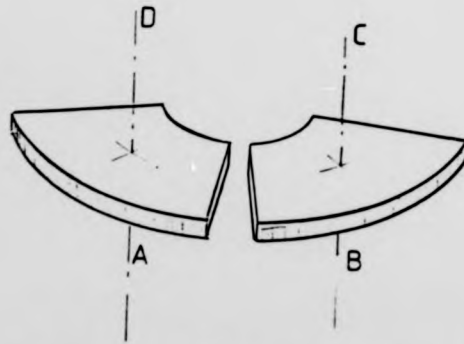


Figure 2.14 Centres of pole-faces

- (1) That the magnetic circuit has a static working condition, because (a) armature reaction is negligible, and (b) the air-gap has constant permeability.
- (2) That the flux pattern is symmetrical along the centre line of the magnet, i.e. symmetrical along AD of Figure 2.13.
- (3) That the flux return ring carries one-half of the flux of the magnet.
- (4) That the calculation is based on the loop ABCD, which passes through the centres of the pole-faces of two adjacent magnets.

Referring to equation 2.1, the magnet mmf was equated only to the air-gap mmf. In practice however, because of the various reluctances which exist in series with the circuit (such as at the joints), not all the magnet mmfs will reach the air-gap. A loss factor LF is introduced. Equation 2.2 thus becomes

$$H_m l_m = LF H_g l_g \quad \dots(2.3)$$

Since $B_g = \mu_0 H_g \quad \dots(2.4)$

hence (2.3) becomes

$$l_m = \frac{LF B_g l_g}{\mu_0 H_m} \quad \dots(2.5)$$

Since the leakage at the centre of the magnet pole-faces is very small indeed, it is therefore ignored. Hence

$$B_g = B_m \quad \dots(2.6)$$

(Note that both B_g and B_m are both measured along the line which passes through the centres of the pole-faces.)

Substituting (2.6) to (2.5), we have

$$l_m = \frac{LF l_g}{\mu_0} \cdot \frac{B_m}{H_m} \quad \dots(2.7)$$

$$\text{or } l_m = LF l_g \cdot \frac{\mu_m}{\mu_0} \quad \dots(2.8)$$

The total flux per pole ϕ_m , generated by the magnet is

$$\phi_m = B_m A_{pa} \quad \dots(2.9)$$

By substituting (1.8) to (2.9), the following is obtained

$$\begin{aligned} \phi_m &= B_m \alpha A_{pp} \\ &= B_m (d_2^2 - d_1^2) \frac{\pi \alpha}{4p} \quad \dots(2.10) \end{aligned}$$

The flux return rings must be of sufficient thickness to take a flux of $\phi_m/2$ (assumptions 3 & 4) without being saturated. Letting B_{ms} be the maximum flux density allowable in the mild steel and t_f its thickness, t_f is given by

$$B_{ms} \left(\frac{d_2 - d_1}{2} \right) t_f = \frac{\phi_m}{2} \quad \dots(2.11)$$

From (2.10)

$$\begin{aligned} B_{ms} (d_2 - d_1) t_f &= B_m (d_2^2 - d_1^2) \frac{\pi \alpha}{4p} \\ \therefore t_f &= \frac{B_m}{B_{ms}} (d_2 + d_1) \frac{\pi \alpha}{4p} \quad \dots(2.12) \end{aligned}$$

2.2.3 Air-gap flux distribution

Having determined the magnet length, the pole-arc/pole-pitch ratio α has to be chosen. This ratio will affect the air-gap flux distribution and the inter-polar flux leakage. For Warwick commutator dc disc-motors, this ratio is typically 0.75. But for brushless dc motors, a trapezoidal induced voltage is required, and a larger ratio is more appropriate. This is described in the following sections.

2.2.3.1 EMF waveform and power inverter

In traction applications, the peak supply voltage is often dictated by the

practical number of batteries that can be installed in a particular vehicle, and the peak supply current from the power inverter is dictated by the current rating of its power switches. But it can be seen from Figure 2.15 that, when given the same supply conditions, an inverter with rectangular voltage and current can produce up to twice the power output of an inverter with sine voltage and current. It is, therefore, more cost effective to use square wave inverters than sine wave inverters in traction applications.

However, although a square voltage is the easiest voltage waveform for an inverter to generate -- as it is only necessary to switch the power devices at a rate equal to the fundamental frequency of the motor -- it is ironically sine voltages which are instead required to drive ac motors. This is because almost all ac motors are designed for mains operation, and therefore have sinusoidal emfs. When these motors are driven by inverters, they require matching sinusoidal drive voltages, and failure to provide these results in undue current harmonics, which at best reduce the operating efficiency, and at worst overload the power devices.

But producing sine voltage from an inverter is a complicated business, as one has to use either the pulse-width modulation (PWM) method, which requires the power devices to be switched at a much higher frequency than the fundamental, or the very inefficient class B linear-amplifier method.

It is, therefore, one of the objectives of this project to design a motor which has a trapezoidal emf that is as close to rectangular as possible. This will simplify the inverter circuitry and increase the power density of the inverter.

2.2.3.2 Pole-arc/pole-pitch ratio

The shape of the emf waveform of the brushless disc-motor is dependent on two factors: 1) the arrangement of the electric circuit and 2) the air-gap flux distribution. The electric circuit will be covered in the next section, and the flux distribution will be discussed here.

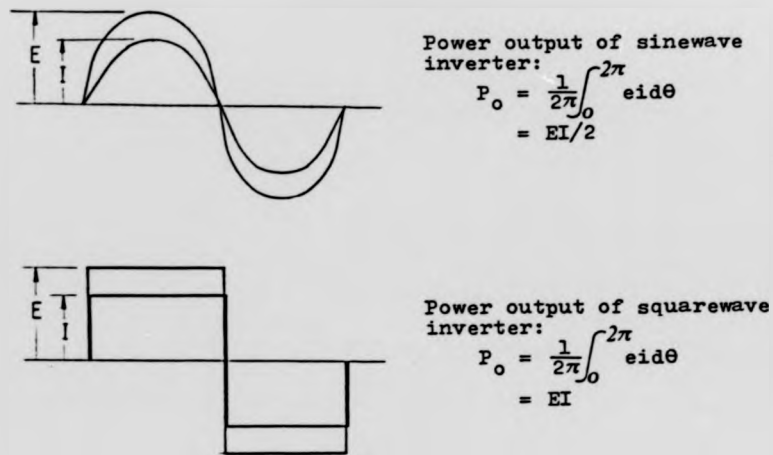


Figure 2.15 Comparison of power output between sinewave and squarewave inverters

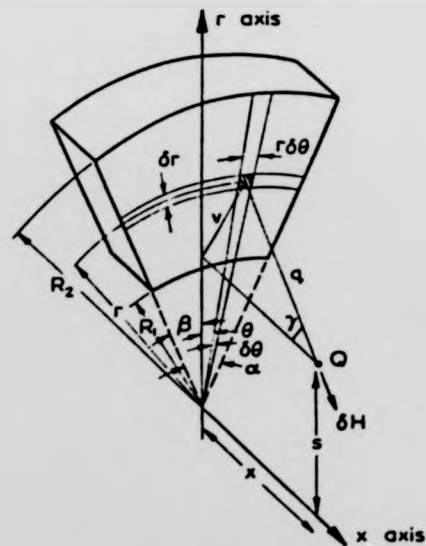


Figure 2.16 Position of point Q related to magnet face (taken from reference (15))

In order for the motor to generate a trapezoidal emf, a rectangular air-gap flux distribution is required. The shape of the flux distribution is effectively controlled by the pole-arc/pole-pitch ratio α of the magnet pieces. By increasing the value of α , the flux distribution usually becomes more rectangular. But as the ratio increases, the flux leakage between the adjacent pole edges also increases. This increase in flux leakage imposes an upper limit to the value of α , which means that any further increase in its value would produce no significant changes in the flux distribution.

To establish the ideal value of α for a particular motor design, the air-gap flux distribution must be studied. This is done either by theoretical evaluation or by actual experiment.

Much theoretical analysis has been carried out in predicting the flux distribution for an array of magnetic poles. Sommerfield [15] showed that the magnetic potential ψ at any point Q (Figure 2.16) from some permanent magnet material, is given by

$$\Delta\psi = \int \frac{\text{div}\mathbf{M}}{q} dV + \int \frac{M_s}{q} dA \quad \dots(2.13)$$

where \mathbf{M} is the intrinsic magnetisation, M_s the pole strength on the magnet pole-face, q the distance from the point of interest to the area element dA , and dV is an element of magnet volume. Campbell [16] also suggested that for the high-coercivity anisotropic magnets used in the majority of disc-motors, it is a good approximation to assume that \mathbf{M} is constant in magnitude and direction, and so equation (2.13) simplifies to

$$\Delta\psi = \int \frac{M_s}{q} dA \quad \dots(2.14)$$

By assuming that M_s is constant on the magnet pole-face and is zero on its sides, and by taking the gradient of equation (2.14), Campbell [17] showed that

if the radial and angular positions are denoted by subscripts r and θ , then the flux density function $B_{r\theta}$ in the axial direction is given by

$$B_{r\theta} = \frac{\mu_0 M_s}{4\pi} \int \frac{\cos\gamma}{q^3} dA \quad \dots(2.15)$$

Where γ is the angle between the normal at dA and a line drawn from dA to (r,θ) . It has also been reported by Campbell (17) that the calculated results showed close agreement with the measured values of the flux produced by a set of segmented ferrite magnets.

However, as the value of α increases, the leakage effect and the interactions between adjacent poles also increase. It is found by measurements that the surface pole strength M_s dropped significantly around the edges of adjacent poles, when α is sufficiently large (about 0.9). This means that the assumptions that M_s is constant and $\text{div } \underline{M} = 0$ have become invalidated. Faced by this problem, the solution of equation (2.13) is beset with difficulties. For practical design purposes, it is more convenient to measure the flux distribution in the air-gap directly.

2.2.3.3 Number of poles

Before a suitable α can be found, a suitable number of poles p has to be chosen. Too few poles will result in the overhangs being too long; whereas too many poles will mean a large number of coils are required and higher leakage.

Based on repeated experiments, at Warwick University, using motors with an external diameter of around 200mm. It was found that the pole number of 8 allows the best compromise between the flux leakage and the amount of overhangs. Thus this pole number is chosen for the prototype brushless disc-motors.

2.2.3.4 Field system arrangement

It has been suggested that the double-sided field system would produce more

useful flux than its single-sided counterpart because of lesser leakage (18). What has not been suggested is that the first arrangement would also produce a flux distribution that is more rectangular than the latter.

The fact is that most modern magnets are anisotropic, and the flux leaving a pole-face has a strong tendency to flow along the direction of magnetisation. In a double-sided field system, such tendency will be re-inforced by the magnet on the other side of the air-gap. The result is therefore a concentrated flux pattern under the pole-face, as shown in Figure 2.17. On the other hand, single-sided systems would produce a spread out flux pattern as shown in Figure 2.18. Hence, the double-sided system is used.

2.2.3.5 Choosing the value of α

To obtain a suitable α , the flux distributions of a series of α values are measured. The measurements are taken from a full-pitched, non-skewed search coil. The coil is placed in the middle of the air-gap which is 6mm wide. 4mm thick polymer-bonded samarium cobalt magnets are used in a double-sided arrangement to give a total magnet thickness of 8mm. To avoid skewing effect, the magnets are cut in such a way so that edges of adjacent poles run parallel to radial lines. The flux distributions are logged by a minicomputer, and the results are given in Figure 2.19 to Fig 2.23. To give a clearer picture of the flux distributions the flux spectras are also plotted.

It can be seen from the figures that as α increases, the flux pattern becomes more rectangular. But as α is increased from 0.9 (Figure 2.20) to 0.95 (Figure 2.19) there is only a slight change in the flux pattern. A closer look at the flux spectras reveals that the 3rd harmonic flux only increases by 4%, and is insignificant. Therefore, the pole-arc/pole-pitch ratio of the prototype brushless disc-motors is chosen to be 0.9.

2.3 The Electric Circuit

2.3.1 Design and assumptions

The armature of a brushless axial-field machine is constructed by nesting

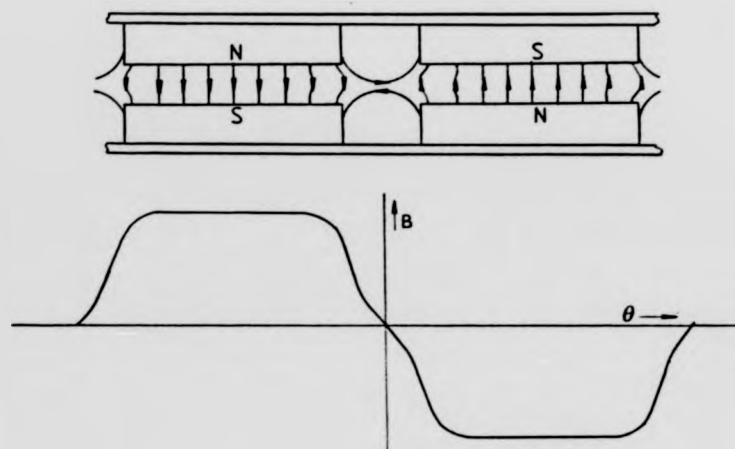


Figure 2.17 Double-sided field-system flux distribution

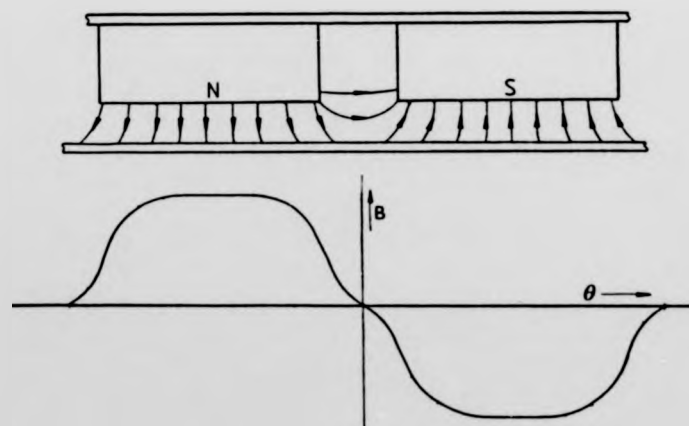


Figure 2.18 Single-sided field-system flux distribution

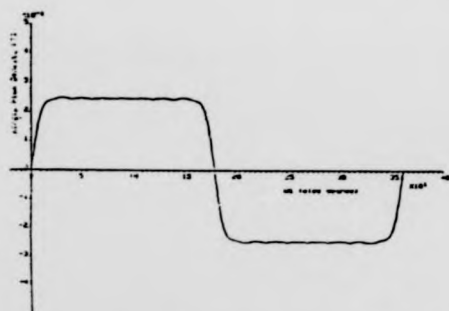
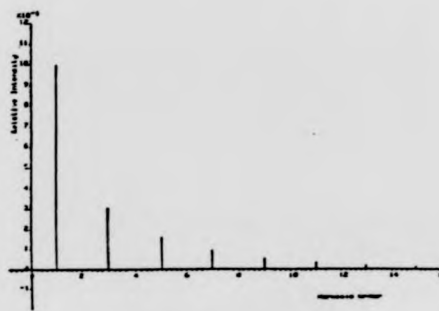


Figure 2.19 a) Flux distribution for $\alpha=0.95$



b) flux spectrum

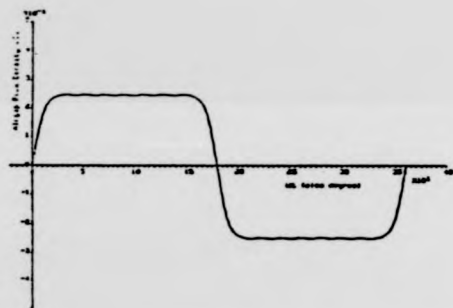
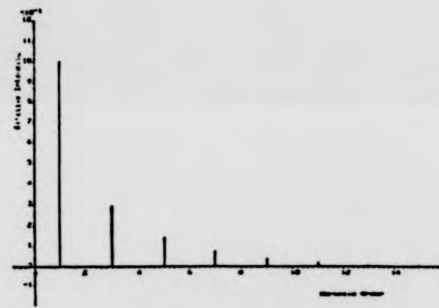


Figure 2.20 a) Flux distribution for $\alpha=0.90$



b) flux spectrum

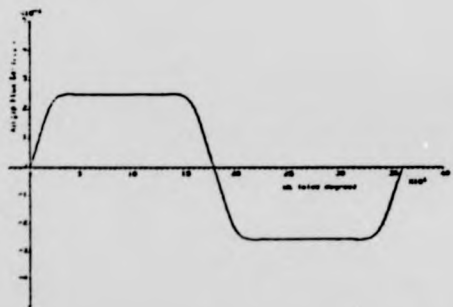
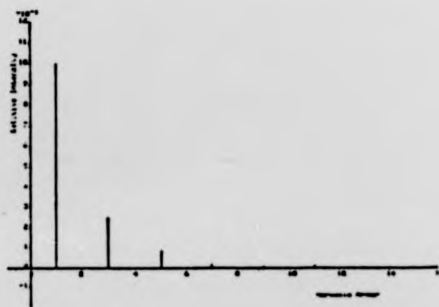


Figure 2.21 a) Flux distribution for $\alpha=0.85$



b) flux spectrum

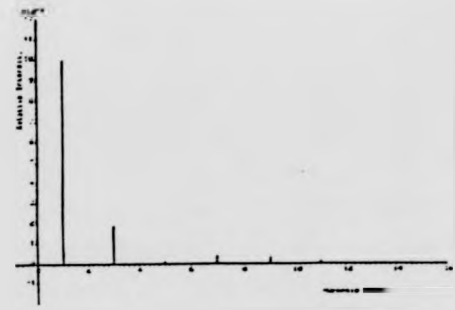
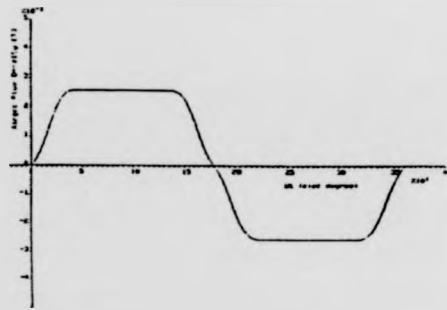


Figure 2.22 a) Flux distribution for $\alpha = 0.80$

b) flux spectrum

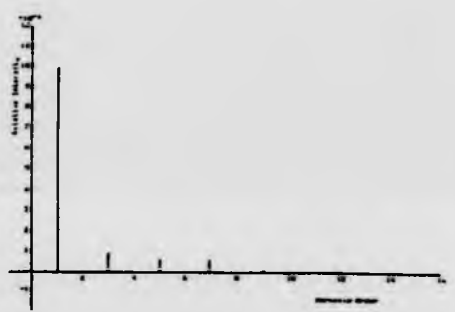
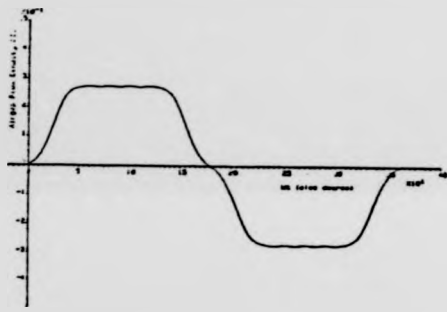


Figure 2.23 a) Flux distribution for $\alpha = 0.75$

b) flux spectrum

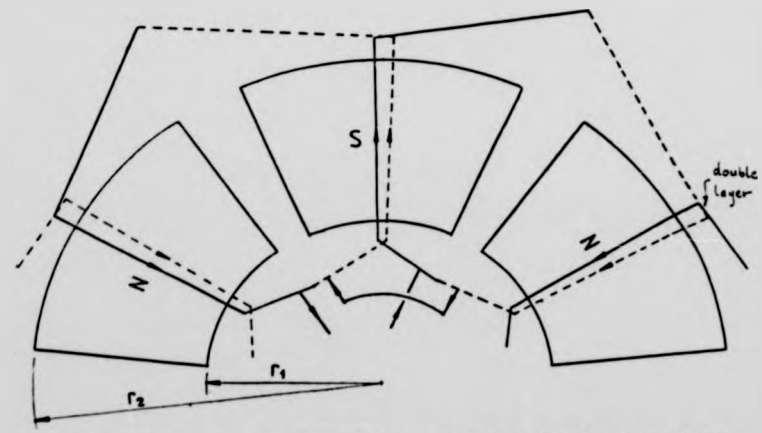


Figure 2.24 An example of disc-motor winding arrangement

together preformed coils. The number of coils and the number of layers is dependent on the design requirements. The number of phases is usually three; the number of 'slots' is dependent on the numbers of poles and phases, and the dimension of the inner active diameter, so that the space factor is not too close to unity. The active lengths of the coils lie approximately in the radial direction of the machine. The coils are connected in groups to form the individual phase-windings in the usual manner. Figure 2.24 shows an example of a two-layer winding arrangement.

The armature flatness, and the uniformity of its thickness are ensured by either encapsulating the armature with epoxy resin by moulding, or baking the armature when placed inside a mild steel mould after it has been taped with glass tape and dipped with polyurethane varnish. It is therefore assumed that the coil-layers are flat, and lie together in the middle of the air-gap.

Further it is assumed that the coil-layers are in perfect stacking order and hence the coils in each 'slot' are in space-phase with each other. Figure 2.25 shows how the active conductors of a double-layer armature are positioned in the air-gap of the machine.

For the purpose of determining the conductor emf, the finite conductor diameter is ignored. The coil-layers are assumed to be lying on flat planes which pass through the centres of the active conductors, which are assumed to have zero thickness, as shown in Figure 2.26. It is further assumed that the flux across the air-gap is uniform.

2.3.2 Approximation of the flux density function

Referring to Figure 2.27, the flux linkage $d\phi$ in the area dA is

$$\begin{aligned} d\phi_{r\theta} &= B_{r\theta} dA \\ &= B_{r\theta} r dr d\theta \end{aligned} \quad \dots(2.16)$$

where $\phi_{r\theta}$ and $B_{r\theta}$ are the flux linkage and the flux density functions,

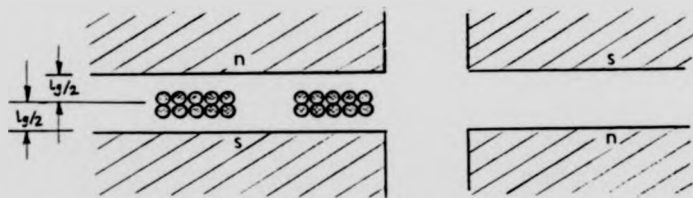


Figure 2.25 Position of the active conductors in the air-gap of a double-layer armature

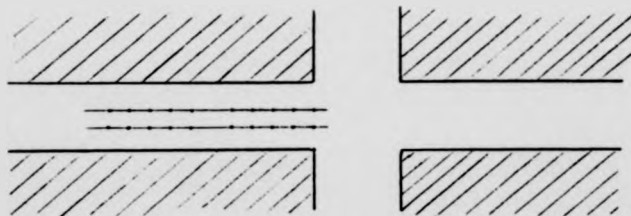


Figure 2.26 Conductors are treated as with zero thickness

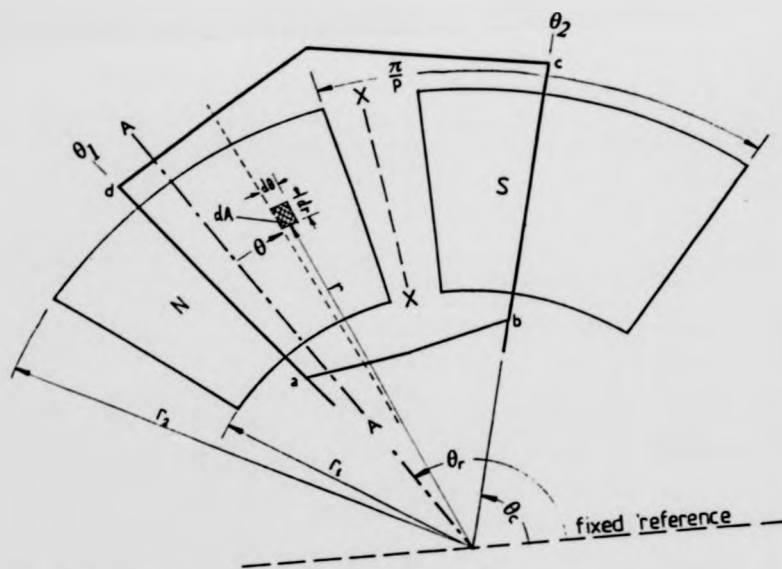


Figure 2.27 Position of the area dA related to the field-system and an armature coil

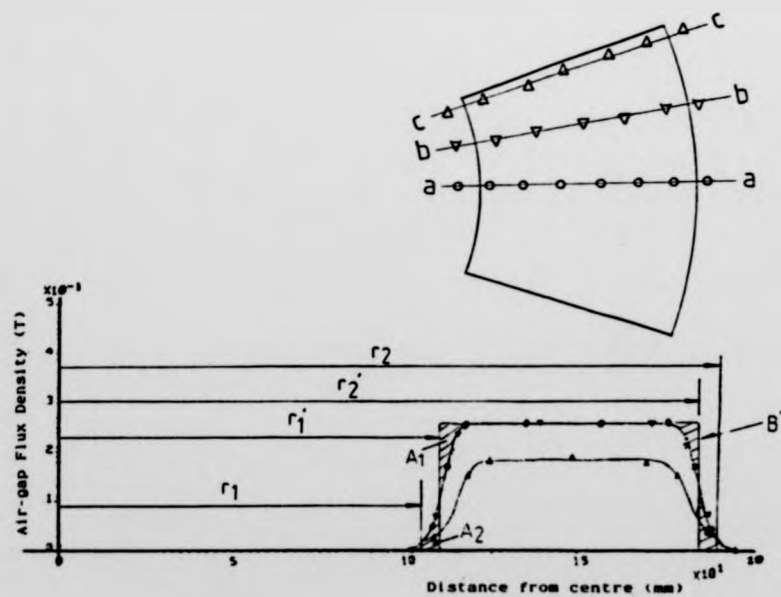


Figure 2.28 Measured radial flux distribution along three radial lines

respectively, expressed in polar form. The total flux linkage ϕ of the closed circuit abcd is

$$\phi = \iint_R d\phi_{r\theta} = \iint_R B_{r\theta} r dr d\theta \quad \dots(2.17)$$

Where R = area of abcd

As the two-dimensional flux density function is quite complex, it would be much easier to solve (2.17) if the two variables r and θ can be separated, so that the integrations can be carried out independently. To investigate if this is possible, the radial flux distribution B_r is measured. Figure 2.28 shows the measured flux distribution along three radial lines in the middle of the air-gap. It can be seen that B_r is almost constant within a large portion of the active radii. A zeroth order approximation of B_r is therefore made. The approximation is made by equalising the areas A_1 and A_2 of the flux distribution along the line a-a, such that the total flux remains the same, and $B_{r\theta}$ is now defined as

$$\left. \begin{aligned} B_{r\theta} &= B_\theta & r_1' < r < r_2' \\ &= 0 & r_1' > r > r_2' \end{aligned} \right\} \quad \dots(2.18)$$

as shown in Figure 2.8. Where r_1' and r_2' are the effective inner and outer active radii, respectively. It should be pointed out that the approximation is valid only when the magnet pieces are non-skewed. (The reason for only considering the flux distribution along the line a-a in the approximation is that it gives the most representative radial flux distribution.)

This approximation leads to a reduction in the active length of the conductor, and a reduction factor C_r is introduced:

$$C_r = \frac{r_2' - r_1'}{r_2 - r_1} \quad \dots(2.19)$$

For the prototype brushless disc-motors, this factor has a value of 0.88. The

effective active radii are given as

$$r_1' = r_1 + (r_2 - r_1)(1 - C_r)/2 \quad \dots (2.20)$$

$$r_2' = r_2 - (r_2 - r_1)(1 - C_r)/2 \quad \dots (2.21)$$

Based on the above approximation, the dependence of the flux density function in the radial direction is removed. And from equation (2.17), the flux linkage of the closed circuit abcd (Figure 2.27) becomes

$$\begin{aligned} \phi &= \int_{\theta} \int_{r_1'}^{r_2'} B_{\theta} r \, dr \, d\theta \\ &= \int B_{\theta} \, d\theta \int_{r_1'}^{r_2'} r \, dr \\ &= \frac{1}{2}(r_2'^2 - r_1'^2) \int B_{\theta} \, d\theta \end{aligned} \quad \dots (2.22)$$

As the circumferential flux distribution B_{θ} is periodic and is symmetrical about the pole axis A-A (see Figure 2.27), it can be expressed as the sum of a series of odd harmonics, i.e.

$$B_{\theta} = \sum_{n=1}^{\infty} B_n \cos(np(\theta_r - \theta)) \quad \dots (2.23)$$

where B_n = peak value of the nth order harmonic flux

θ_r = mechanical angle of the pole axis A-A from a stationary reference

To further simplify the integration, the polar co-ordinates in Figure 2.27 are mapped into rectangular ones by the complex transformation $w = \ln z$ (19). The transformed image co-ordinates are shown in Figure 2.29. Now if we consider a single turn in the circuit, which is short chorded by an angle $2\theta_s$ and skewed by an angle $2\theta_k$, the nth harmonic flux linkage with the turn is

$$\begin{aligned} \phi_n &= \frac{1}{2}(r_2'^2 - r_1'^2) \int_{\theta_1}^{\theta_2} B_n \cos(np(\theta_r - \theta)) \, d\theta \\ &= \frac{(r_2'^2 - r_1'^2) B_n}{2np} \cos(np\theta_s) \frac{\sin(np\theta_k)}{np\theta_k} \sin(np(\theta_r - \theta_c)) \end{aligned}$$

(θ_c = mechanical angle of the coil from a stationary reference)

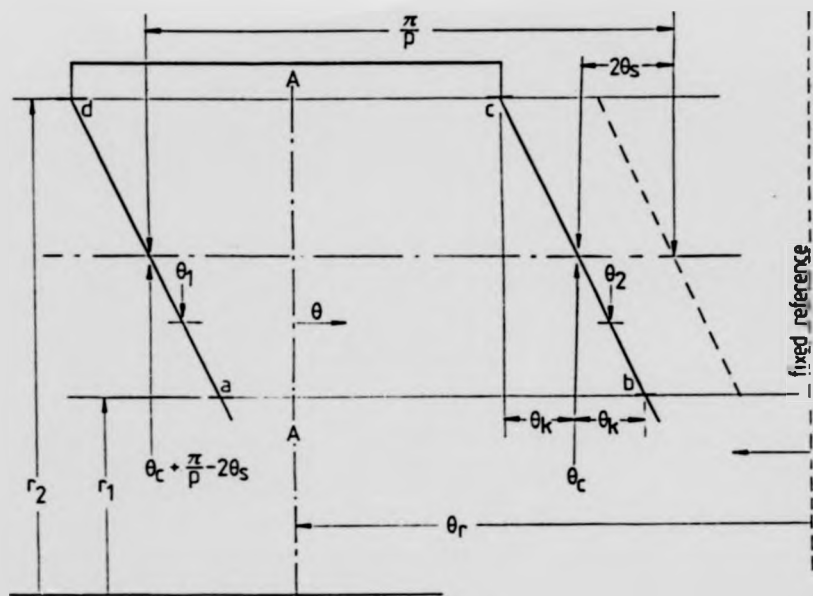


Figure 2.29 Rectangular image co-ordinates of the polar co-ordinates of Figure 2.27

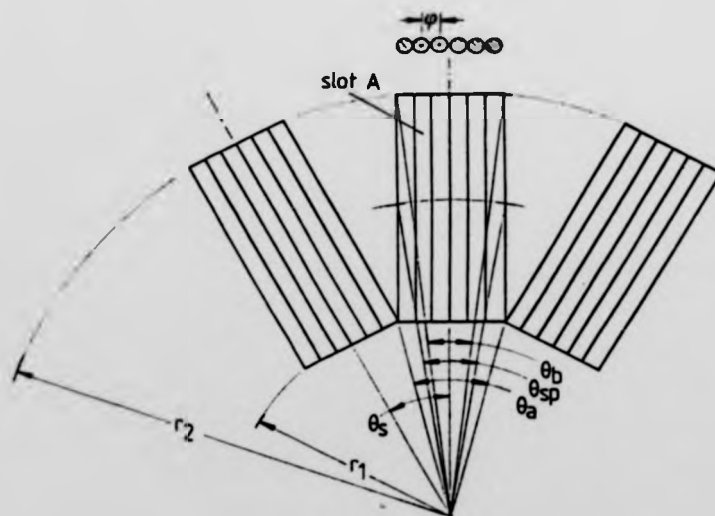


Figure 2.30 Distribution of conductors around r_1

$$\phi_n = \frac{(r_2^2 - r_1^2) B_n}{2np} K_{en} K_{sn} \sin(np(\theta_r - \theta_c)) \quad \dots(2.24)$$

where $K_{en} = \cos(np\theta_s)$
 = chord factor (or pitch factor) for the nth harmonic
 $K_{sn} = \sin(np\theta_k) / np\theta_k$
 = skew factor for the nth harmonic

Both the chord factor and the skew factor have a maximum value of unity. These factors are invaluable to the motor designers because they can improve the performance of electrical machines by the reduction of parasitic effects. For example, short-chording is used in some commutator machines as a method of improving commutation or in synchronous machines to reduce harmonic in the generated emf; whilst skewing the conductor by approximately one slot reduces the slot harmonics, and hence the inherent noise, and improves the low speed performance.

2.3.3 The EMF equation

Faraday's Law of Electromagnetic Induction states that the emf e induced in a closed circuit is equal to the rate of change of the flux linkage ϕ of the circuit, i.e.

$$e = - \frac{d\phi}{dt} \quad \dots(2.25)$$

If the flux linkage is both time and space dependent, and if the coil rotates, then the application of Faraday's Law shows that there are three possible means by which the nth order emf may be induced in a turn by the time function of the flux linkage:

$$e_n = - \left(\frac{\partial \phi_n}{\partial t} + \frac{\partial \phi_n}{\partial \theta_r} \frac{d\theta_r}{dt} + \frac{\partial \phi_n}{\partial \theta_c} \frac{d\theta_c}{dt} \right) \quad \dots(2.26)$$

The first term of the above equation represents transformer action due to the

time variation of the flux. The second term represents rotational emf due the movement of the field. The last term represents rotational emf due to the movement of the conductors.

For the brushless disc-motor, the first and the last terms of equation (2.26) are all equal to zero. The nth harmonic emf e_{nt} induced in a single turn by the effect of the nth harmonic flux is

$$\begin{aligned} e_{nt} &= - \frac{\partial \phi_n}{\partial \theta_r} \frac{d\theta_r}{dt} \\ &= - w_r \frac{\partial \phi_n}{\partial \theta_r} \end{aligned} \quad \dots (2.27)$$

Also, the brushless disc-motor, which is required to generate a trapezoidal emf, has both the skew and chord factors equal to unity. By substituting (2.24) to (2.27), the following expression is obtained:

$$\begin{aligned} e_{nt} &= - w_r \frac{\partial}{\partial \theta_r} \left(\frac{(r_2^{2n} - r_1^{2n})}{2np} B_n \sin(np(\theta_r - \theta_c)) \right) \\ &= - \frac{1}{2}(r_2^{2n} - r_1^{2n}) w_r B_n \cos(np(\theta_r - \theta_c)) \end{aligned} \quad \dots (2.28)$$

2.3.4 Distribution factor and the EMF equation

Since the brushless machine has its armature windings spread evenly around the inner circumference, the spreading effect must be accounted for in the emf equation. Supposing that the conductors are uniformly distributed around r_1 as given in Figure 2.30, the angle contained by the inner arc of slot A is θ_a , and is given as

$$\theta_a = \frac{2\pi}{S} \quad \dots (2.29)$$

where S = number of 'slots'. And the angle contained by the outer arc of slot A is θ_b , and is given as

$$\theta_b = \theta_a \frac{r_1}{r_2} = \frac{2\pi}{S} \cdot \frac{r_1}{r_2} \quad \dots (2.30)$$

The average angular spread θ_{sp} of that slot is

$$\begin{aligned} \theta_{sp} &= \frac{1}{2}(\theta_a + \theta_b) \\ &= (1 + r_1/r_2) \frac{\pi}{S} \end{aligned} \quad \dots(2.31)$$

Hence, the average wire-pitch (the angle contained by the centres of adjacent wires) ϕ is

$$\begin{aligned} \phi &= \theta_{sp} / g \\ &= (1 + r_1/r_2) \frac{\pi}{Sg} \end{aligned} \quad \dots(2.32)$$

(g = no. of turns/coil)

Based on the conventional theory of coil spread, the spread factor K_{dn} of the nth order emf for one slot is given as

$$\begin{aligned} K_{dn} &= \frac{\sin(gnp\phi/2)}{g \sin(np\phi/2)} \\ &= \frac{\sin(np(1 + r_1/r_2) \frac{\pi}{S})}{g \sin(np(1 + r_1/r_2) \frac{\pi}{Sg})} \end{aligned} \quad \dots(2.33)$$

By multiplying this factor with equation (2.28), the emf equation for the nth harmonic for one coil is

$$e_{nc} = - \frac{1}{2}(r_2'^2 - r_1'^2) \omega_r g K_{dn} B_n \cos(np(\theta_r - \theta_c)) \quad \dots(2.34)$$

For the adjacent slot, the induced voltage will be phased-shifted by an amount equal to the angular displacement between two slots (θ_s) and is given as

$$e'_{nc} = - \frac{1}{2}(r_2'^2 - r_1'^2) \omega_r g K_{dn} B_n \cos(np(\theta_r - \theta_c + \theta_s)) \quad \dots(2.35)$$

Supposing that the armature has q coils/pole/phase and p pole-pairs, then the phase voltage for the nth harmonic is

$$e_n(t) = -\frac{1}{2}(r_2^{p+1} - r_1^{p+1}) \omega_r p \sum_{k=0}^q K_{dn} B_n \cos(np(\omega_r t - \theta_c - k\theta_s)) \quad \dots (2.36)$$

$(\theta_r = \omega_r t)$

By combining the individual harmonic components, the final form of the emf equation (per phase) is given as

$$e(t) = -\frac{1}{2}(r_2^{p+1} - r_1^{p+1}) \omega_r p \sum_{n=0}^{\infty} \sum_{k=0}^q K_{dn} B_n \cos(np(\omega_r t - \theta_c - k\theta_s)) \quad \dots (2.37)$$

CHAPTER 3

BRUSHLESS DC MOTORS

3.0 Introduction

The concept of the brushless (or commutatorless) dc motor was first proposed by Alexanderson and Mittag (20) in 1938, when thyratrons were the switching elements. Owing to the limited device technology available at the time, the motor acquired only a passing interest. But since the introduction of fast switching semiconductor devices, such as the thyristors, in the late 1950s there has been a great upsurge in the development, production and application of brushless dc motors. As the brushless concept evolves, the motor design diversifies. The term 'brushless dc' is now being used, although sometimes inappropriately, to refer to most kinds of poly-phase machines which are inverter-fed and which do not require sliding contacts in passing electrical energies to (or from) the armatures (21,22).

The brushless dc motor, with its excellent performance specifications, e.g. long life, low maintenance and high speed, has already penetrated in many application areas -- ranging from aerospace, computer peripherals, robotics and NC machines, to general industrial drives and, to a lesser extent, traction applications. To satisfy the diverse market, numerous brushless dc motor designs have been made available. The characteristics of these motor therefore vary widely, and consequently it is very difficult to give a generalised description of their properties. However, having said this, the majority of the designs fall into two categories (21). They are: 1) induction machines fed by variable frequency inverters, and 2) inverter-fed synchronous machines with rotor-position feedback.

The axial-field brushless dc motor, which is the subject of this thesis, falls into the latter category. And after giving a brief overview of the induction-type brushless dc motor in Section 3.1, for the sake of comparison,

the remainder of the chapter concentrates on describing the operating principle of the synchronous-type brushless dc motor, starting with a general introduction in Section 3.2.

In Section 3.3, the principle of exactly how the commutator of a dc motor is replaced to become a brushless motor are described. Section 3.4 discusses the different types of synchronous brushless dc motors by grouping them according to the arrangement of their armature windings and to their conduction modes.

Section 3.5 describes the constructions and the operating principle of different classes of brushless dc motors according to their power ratings; and application examples of each class of machine are given.

Section 3.6 completes this chapter by describing some of the position detectors most commonly used in brushless dc motors.

3.1 Induction Machine Fed by Variable Frequency Inverter

Over the last fifteen years, comprehensive studies have been carried out on the inverter-fed induction motor, producing a mass of literature (22 to 29). The functional block diagram and the torque-speed characteristic of a typical inverter-fed squirrel cage induction motor are given in Figure 3.1, and Figure 3.2, respectively. The motor is essentially an open-loop system, and its speed is dictated by the output frequency of the inverter. Normally, the rotor resistance of the motor is low relative to its reactance for most conditions of applied frequency, and is ignored. When varying the frequency, the voltage/frequency (v/f) ratio of the inverter is kept constant so that a constant air-gap flux is maintained. This is to achieve a constant torque output. At low operating frequency, however, the phase resistance becomes a significant component of the phase impedance, and as a result there will be a decrease in the air-gap flux. To maintain the required level of flux density, it

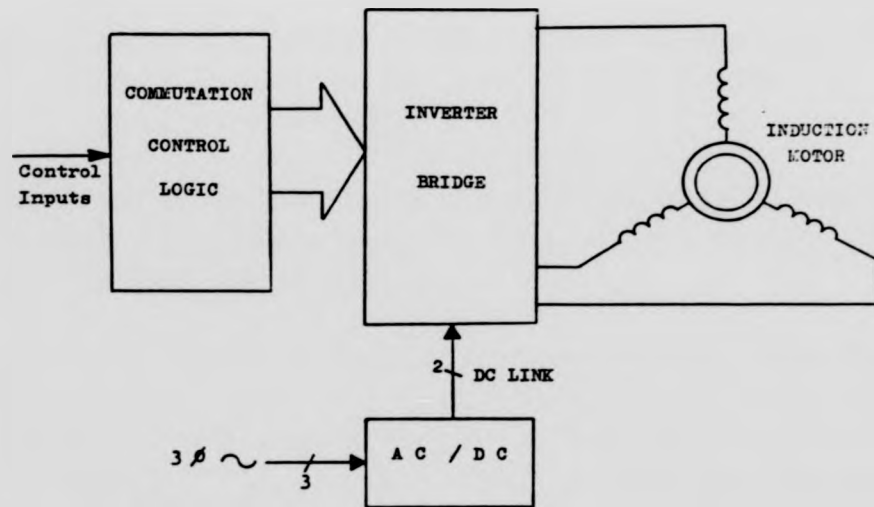


Figure 3.1 Functional diagram of an induction-type brushless dc motor

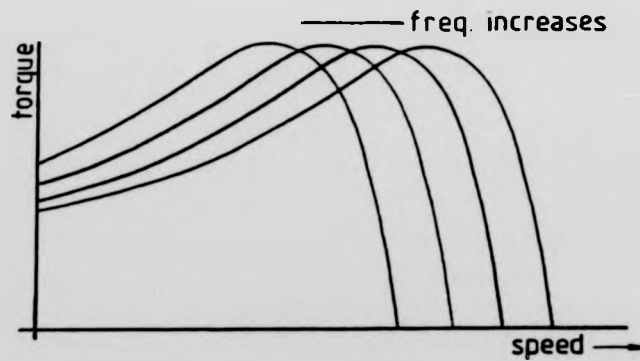


Figure 3.2 Torque-speed characteristic of a typical inverter-fed squirrel cage induction motor

is therefore necessary to arrange the inverter electronics in such a way so as to give an increased v/f ratio at low frequency. Such function can be implemented by using microprocessors (28).

The main advantages of an inverter-fed induction motor system are that the operation of the motor is completely brushless, and that the rotor is very robust, simple to construct and cheap to make.

The disadvantages of this motor system are that they usually have a low power factor and it is therefore necessary to specify a higher inverter rating than normal, in order to handle the reactive current. Also because the induction motor is singly-excited, i.e. energised through the stator only with torque reaction produced by induced rotor current, this results in a lower efficiency than that of doubly-excited motors such as the permanent magnet dc motor.

But strictly speaking, inverter-fed induction machines should not be called as brushless dc motors, as they have characteristics that are entirely different from proper dc machines; and, therefore, they will not be discussed further.

3.2 Inverter-fed Synchronous Machine with Rotor Position Feedback

In a synchronous brushless dc drive, the motor is usually of the polyphase rotating-magnet type. In order to enable the motor to produce a continuous torque output, the armature windings must be energised in such a way that a certain space angle is always maintained between the armature mmf and the rotor mmf. To achieve this, a rotor position detector is used. The detector is located in space-phase with the armature, and its output is in time-phase with the rotor field. As the rotor rotates, the detector controls the inverter electronics to switch the armature windings in an appropriate sequence, such that the armature mmf and the rotor mmf always run in synchronism, thus maintaining the desired level of developed torque.

This switching procedure is, in essence, identical to the operation of the commutator/brushes of a conventional dc motor. In fact, it is precisely because they exhibit similar torque-speed characteristics to dc commutator motors that synchronous brushless dc motors are most suitable for precision control applications.

However, the more complicated rotor structures and the rotor position detectors leads to a higher cost machine than the induction motor.

3.3 Evolution of Brushless DC Motor from Commutator DC Motor

The commutator of a conventional dc machine can be regarded as a system of controlled switches which reverse the voltage across the armature coils at certain positions of the rotor. Figure 3.3 illustrates how the slots, windings, magnetic poles, brushes and commutator are positioned in such a way that the direction of the induced torque is dictated by the polarity of the dc supply. As the coils rotate, the current flowing in each coil is reversed as the active sides of the coil pass from the influence of one magnetic pole, through zero flux, to the opposite polarity, so that uni-directional torque is developed. This is accomplished with the use of a mechanical commutator and brushes. Figure 3.4 and Figure 3.5 show the commutation sequence at the point where the rotor has moved by $1/2$, and 1 commutator bar, respectively. It can be seen that the commutator/brush assemblies enable the axis of the armature magnet field to be kept stationary in space, and displaced by 90° elec from the axis of the main field poles at all times.

To replace the mechanical commutator by electronic switches, it is required to have the switching elements stationary. The armature winding is mounted on the stator and the field poles are set to rotate. The result is a brushless machine which has an equal number of phases as the number of commutator segments per pole.

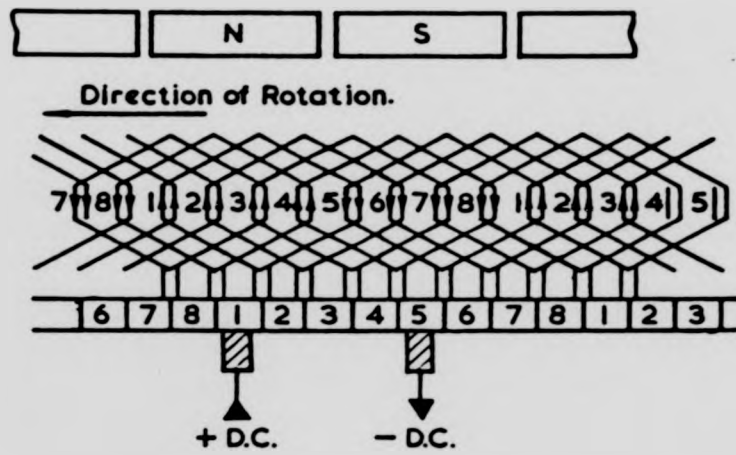


Figure 3.3 Mechanical and electrical arrangement of a dc motor (coils 1-5, 5-1 about to enter commutation zone)

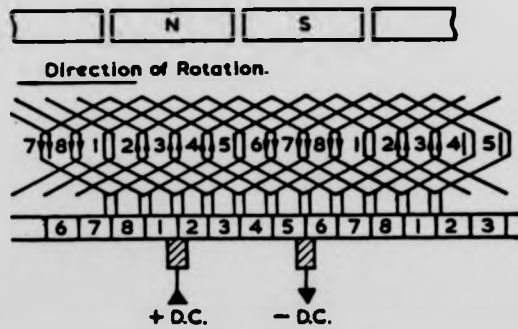


Figure 3.4 Coils 1-5, 5-1 in commutation zone

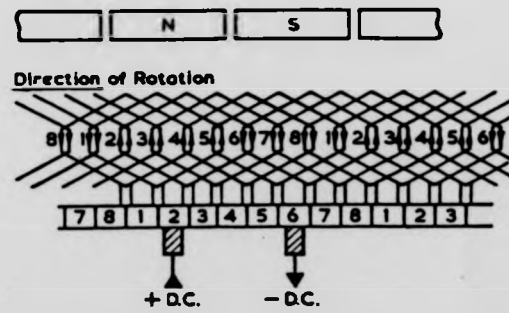


Figure 3.5 Coils 2-6, 6-2 about to enter commutation zone

For example, Figure 3.6(a) to 3.6(d) illustrate how a 3-phase brushless dc motor is synthesised from a conventional dc machine. It should be noted that machines with different numbers of coils can be synthesised in the same way.

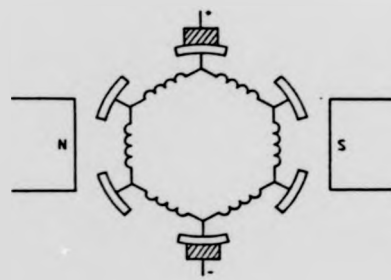
In order to maintain a constant production of positive torque, it is essential to ensure that the phases are energised correctly to keep pace with the rotating field poles. To this end, a rotor position detector is used to control the power switches in such a way that the windings of the 3-phase brushless motor receive the same voltage excitations as in the 3-bar motor (Figure 3.6(e)). Figure 3.7 shows the final form of the motor. (It should be noted that the motor and the electronics have now become an integral system, and the function of the electronics is identical to that of a dc/ac inverter.)

3.4 Brushless DC Motor Configurations

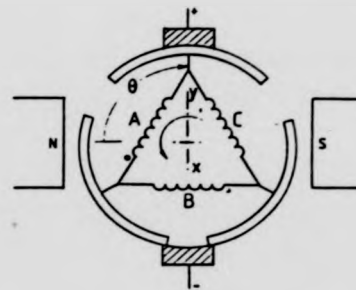
In a conventional dc motor, the conduction of the armature windings is controlled by a mechanical commutator, so that the mode of operation is always bi-polar, i.e. the current in a coil flows in both directions. On the other hand, the windings of a brushless dc motor are controlled electronically by semiconductor switches, and can readily be configured to operate in either the bi-polar mode or the uni-polar mode where the coil current only flows in one direction.

In the uni-polar mode, a winding is controlled by a single transistor (or any semiconductor devices) which conducts in only one direction. Consequently, the conduction period of the winding over an electrical cycle is limited to 180° elec, and the winding utilisation is limited to 50%.

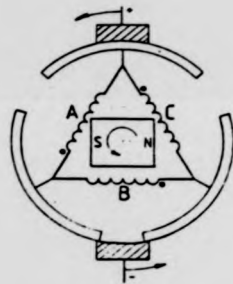
In the bi-polar mode, a winding is controlled by two transistors, each of which carries current in a direction opposite to the other. Therefore, the total period



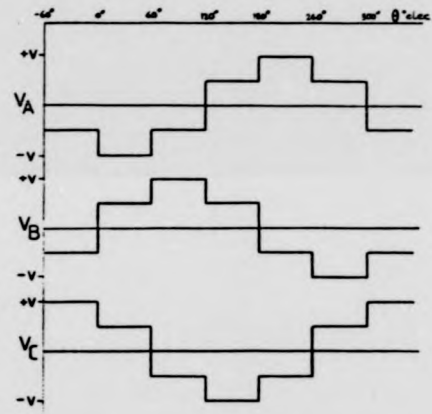
a) Conventional 6-Bar dc motor



b) 3-Bar dc motor



c) Inverted dc motor



e) Winding voltages of 3-Bar dc motor



d) Commutator replaced by electronic switches

Figure 3.6 Synthesis of a 3-phase brushless dc motor from a conventional dc motor

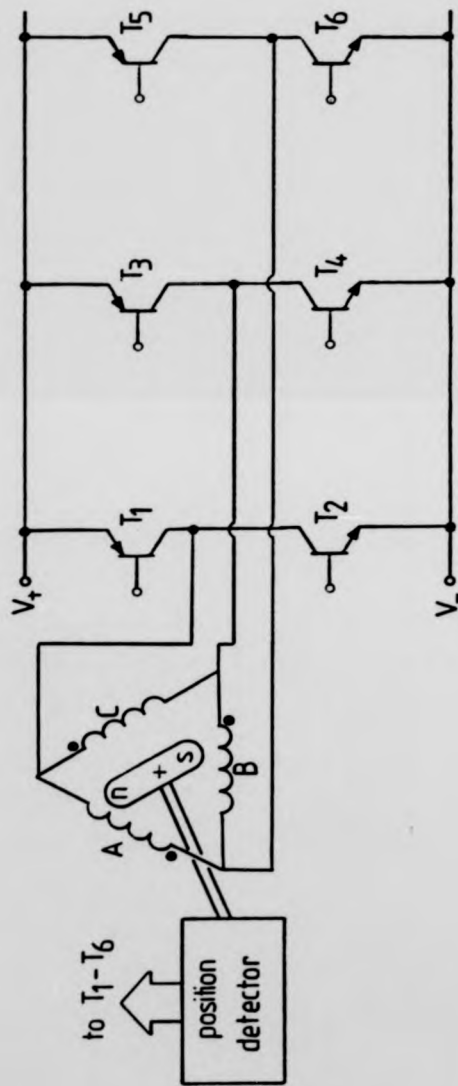


Figure 3.7 The 3-phase brushless dc motor with rotor position detector

of conduction over one cycle can be as much as 360° elec. and a much higher winding utilisation can be achieved. As a result, a bi-polar brushless motor can output up to twice the power of a similar size uni-polar motor.

A uni-polar motor has very simple control electronics as only one transistor is required per winding. It is usually used in low power (less than 10W), and cost-sensitive application where the cost of the electronics represents a major slice of the cost of the motor system, and where the size of the motor is only a secondary consideration. For high power application bi-polar motors are generally used.

Apart from the mode of conduction, the cost and the characteristics of a brushless dc motor are also determined by the number of independent phase windings. Before actually selecting a particular motor configuration, it is therefore imperative to understand the characteristics of the different configurations.

3.4.1 The one-phase uni-polar brushless dc motor

The stator of this motor has only a single winding (Figure 3.8(a)) which is energised once per electrical revolution. The electro-magnetic torque output is shown in Figure 3.8(b). It is obvious that this motor can only generate torque for 180° elec. and the remaining angular rotation has to be overcome by inertia of the rotor or by means of auxiliary torques.

3.4.2 The one-phase bi-polar brushless dc motor

The stator of this motor also has only a single winding, but it is energised twice per electrical revolution by two current pulses of opposite directions. The resulting torque distribution (Figure 3.9(b)) is more favourable than with the uni-polar counterpart. However, a continuous torque output is still not achieved. There are small regions without torque which have to be bridged by suitable auxiliary torque. This motor has a 100% winding utilisation; and its configuration is shown in Figure 3.9(a).

3.4.3 The two-phase uni-polar brushless dc motor

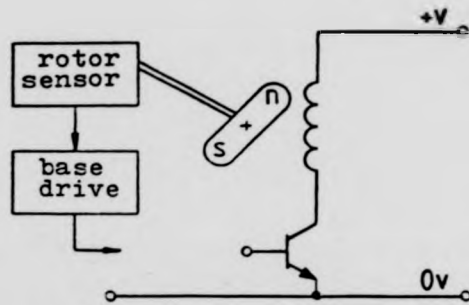
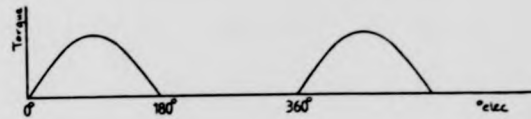


Figure 3.8 a) one-phase uni-polar motor



b) torque output vs. rotor rotation

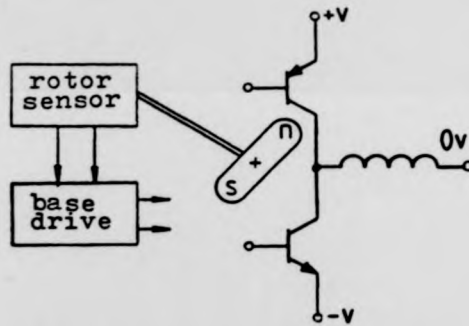
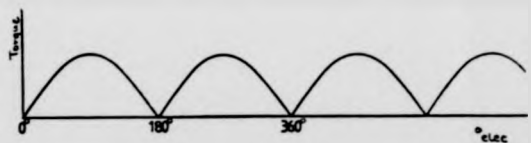


Figure 3.9 a) one-phase bi-polar motor



b) torque output vs. rotor rotation

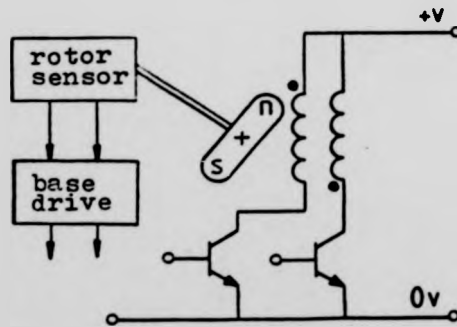
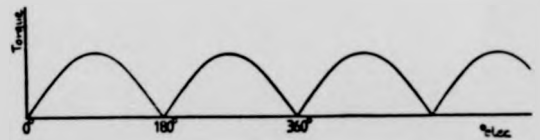


Figure 3.10 a) two-phase uni-polar motor



b) torque output vs. rotor rotation

The stator of this motor has a set of bifilar windings which are energised alternatively by two current pulses (Figure 3.10). Although the motor's characteristics are basically the same as those of a one-phase bi-polar motor, the winding usage is only a half of that of the bi-polar motor. The advantages of this motor are that the control electronics are simple, and that it only requires a single power supply.

3.4.4 The two-phase bi-polar brushless dc motor

This motor has two windings, with one being displaced by 90° elec in space from the other. Each winding is energised by two alternate current pulses, thus four current pulses are fed to the stator per electrical cycle. This results in an uninterrupted torque output. The configuration and the torque profile of this motor are shown in Figure 3.11.

3.4.5 The three-phase uni-polar brushless dc motor

This motor has a stator with three windings, each one being displaced from others by 120° elec. The windings are energised in cyclical sequence with each winding receives one current pulse for every electrical cycle. The configuration and the output torque are shown in Figure 3.12. It can be seen from Figure 3.12(b) that this motor has a more favourable torque profile than the two-phase uni-polar motor. Its disadvantage is the low winding usage (between 33% & 50%).

3.4.6 The four-phase uni-polar brushless dc motor

The stator of this motor is wound with four windings (Figure 3.13(a)). Each winding receives a single current pulse in each electrical cycle. The torque profile (Figure 3.13(b)) is slightly better than that of the three-phase uni-polar motor.

3.4.7 The three-phase bi-polar brushless dc motor

This machine has three windings which can be connected in delta or in star. The windings are energised by six current pulses from six transistors (Figure 3.14(a)). This motor not only delivers a very even torque output (Figure

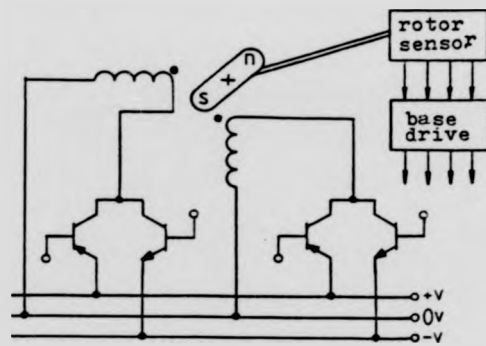
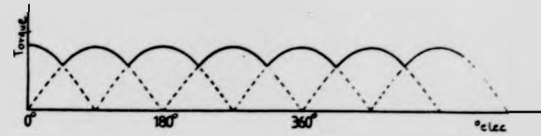


Figure 3.11 a) two-phase bi-polar motor



b) torque output vs. rotor rotation

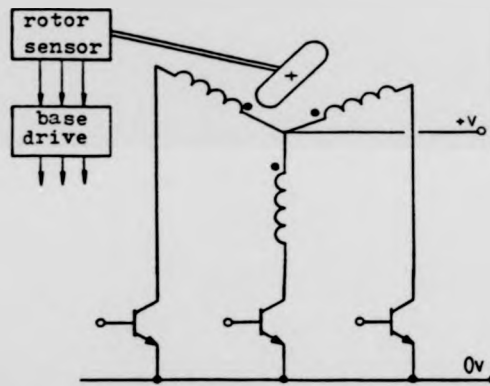
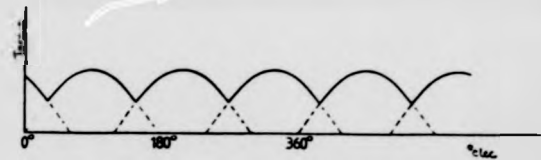


Figure 3.12 a) three-phase uni-polar motor



b) torque output vs. rotor rotation

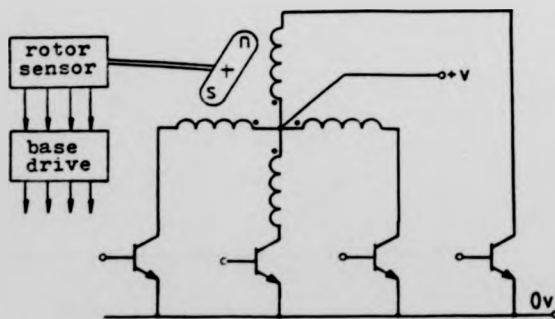
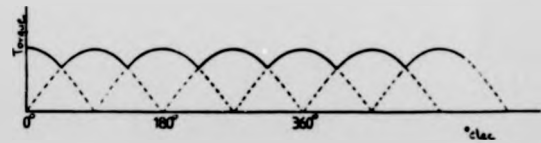


Figure 3.13 a) four-phase uni-polar motor



b) torque output vs. rotor rotation

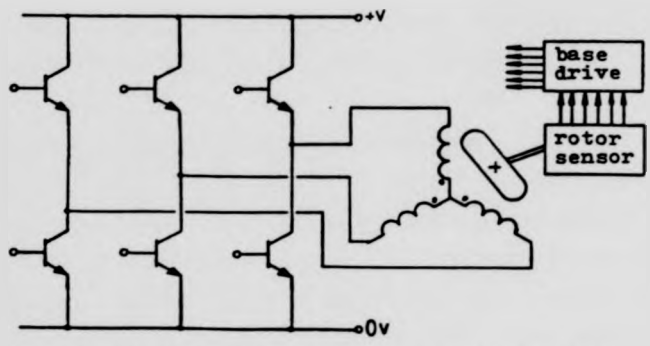


Figure 3.14 a) three-phase bi-polar motor

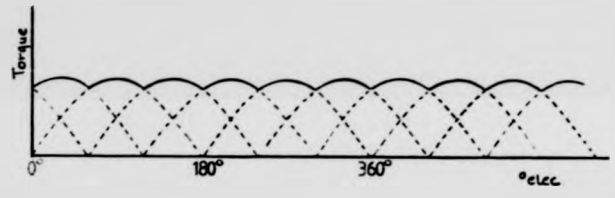


Figure 3.14 b) torque output vs. rotor rotation

3.14(b)), but also gives a very high winding usage (between 67% and 100%). However, it does require more complex control electronics.

3.4.8 Number of windings and excitation current pulses

It has become evident that, in order to obtain a smooth torque output, a brushless dc motor is required to have a large number of windings and a high number of excitation current pulses. However, the improvement in the smoothness of the torque output does not correspond linearly to the increase in the number of windings and of excitation current pulses. In fact, brushless dc motors with more than four windings and six current pulses do not offer any technical advantages; and the exact number of windings and of current pulses is still dictated by the nature of the application.

3.5 Brushless DC Motor Constructions and Operations

In a brushless dc motor system, the output performance is largely determined by the characteristics of the switching device. That is, the device's peak current rating determines the motor's starting and stalling torques; and the device's switching speed, controllability (the ease with which it is switched on or off) and forward voltage drop all affect the motor system's efficiency. Usually, the choice of the type of switching device is dictated by the motor's power rating. That is, a high power motor requires thyristor switches, and medium and low power motors will use power transistors.

The following sub-sections describe the constructions and the operating principles of practical brushless dc motor systems, according to their power ratings.

3.5.1 High power thyristor-switched brushless dc motors

High power brushless dc motors are constructed from conventional 3-phase synchronous motors. And although very high power transistors are available

today, most high power brushless systems still use thyristors as their switching elements. This is because thyristors are much more rugged than transistors -- a thyristor can withstand a high surge current well over 10 times rated value (30), and also thyristors have a very high off-state blocking voltage.

The ratings of thyristor-switched brushless dc motors range from 5kW (31) to 1500kW (32). These machines are operated in either the voltage-fed mode or the current-fed mode. Application examples include: paper mills, textile mills, large water pump and steel mills.

Voltage-fed systems

The basic configuration of a voltage-fed brushless dc motor is shown in Figure 3.15. In this system, the instantaneous applied voltage of the motor (the instantaneous line voltage) is at all time directly dependent upon that of the dc supply V_{dc} , which is of low impedance at all frequencies of interest. The motor's output torque is controlled by varying the average line voltage, and the firing angles of the thyristors in relation to the rotor's position.

The line voltage can be controlled by varying the dc link voltage V_{dc} using a controlled rectifier (Figure 3.16), or a dc chopper (Figure 3.17). Alternatively pulse-width modulation (PWM) within the inverter can be used, whereby the conduction of the thyristors are interrupted several times per cycle to produced a chopped line voltage (Figure 3.18), such that the average line voltage is proportional to the pulse-width.

Both methods of line voltage control are now commonly used, but with the availability of fast turn-off thyristors the PWM method seems to have an edge over the other method in that it provides an economically advantageous arrangement. This is due to the fact that both voltage- and frequency- control are obtained from the same thyristors within the inverter, thus eliminating the need for extra controllable devices.

The firing angles of the thyristors are controlled by rotating the rotor

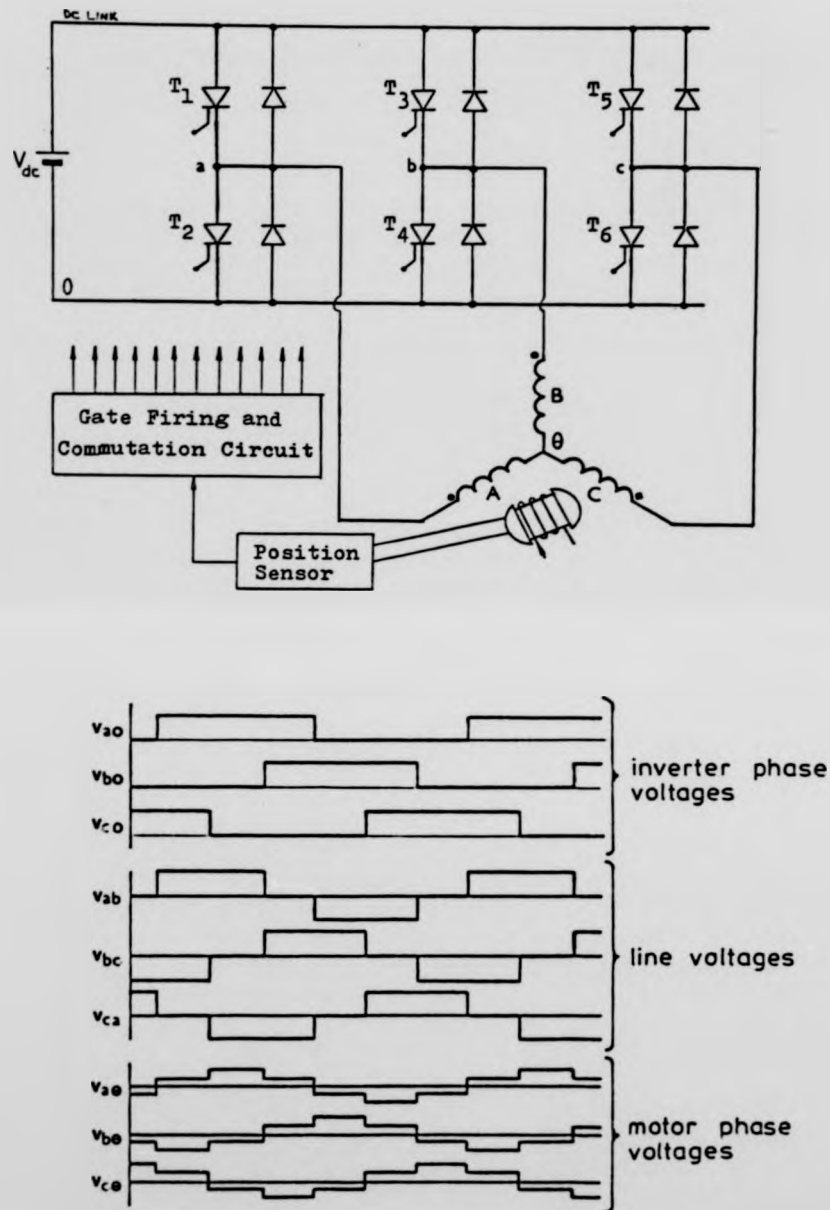


Figure 3.15 voltage-fed thyristor-switched brushless dc motor

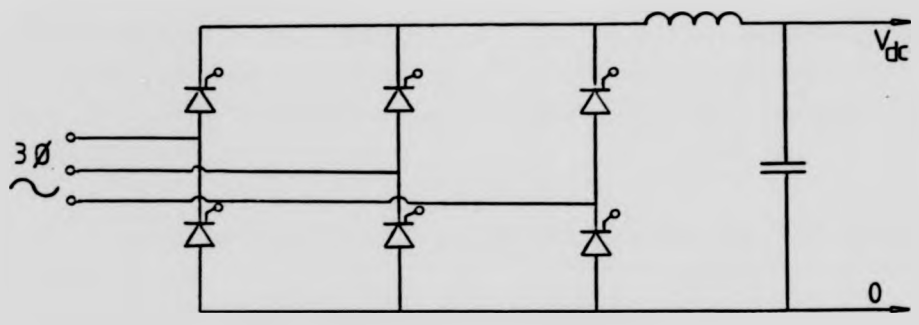


Figure 3.16 A controlled rectifier

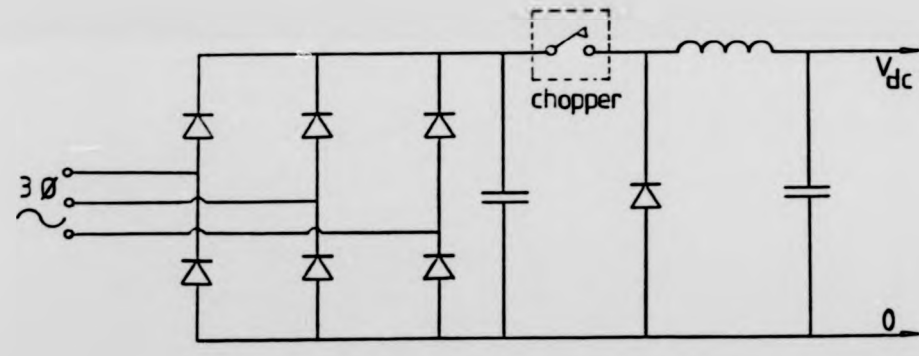


Figure 3.17 A chopper regulator

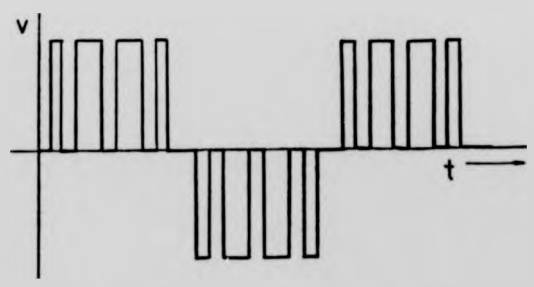


Figure 3.18 Pulse-width modulation

position detector with respect to the stator. This controls the relative angle between the armature mmf and the rotor mmf, and consequently the torque output. To obtain the maximum torque for a specific armature current, this angle must be at 90° elec.

Since the thyristors used in the voltage-fed inverter have no inherent ability to interrupt an established current, auxiliary commutation circuits are therefore needed to force-commutate the thyristors. As the power rating of the inverter increases, the power losses incurred by the force commutation also increase. When the commutation losses become excessive, a force-commutated voltage-fed system will be impractical, and the load-commutated current-fed system is considered.

Current-fed system

In a current-fed system, the inverter's dc link is of high impedance, by virtue of a series inductor, such that the link current is held constant by the inductance. The armature current waveform is determined by the operation of the inverter, while the line voltage depends upon the motor load.

Unlike the voltage-fed system, which, neglecting thyristor commutating intervals, has three thyristors conducting at any given instant, the current-fed system has only two thyristors conducting at any given time. Commutation is effected by firing the proper thyristor in such a way that the polarity of the induced voltage is directed to turn off the last thyristor. Figure 3.19 shows the principle circuit of a current-fed brushless machine.

Assuming that the dc current flowing through the inductor L is smooth, its magnitude is I_d , and thyristors T_1 and T_6 are conducting, so that $i_a = I_d$, $i_b = 0$ and $i_c = -I_d$. At a rotor angle θ_o , device T_3 is triggered, effectively connecting together terminals a and b, and initiating the commutation. If θ_o is well chosen and the machine excitation level sufficient, a current i will circulate between phases A and B, such that $i_a = I_d - i$ and $i_b = i$, and in an

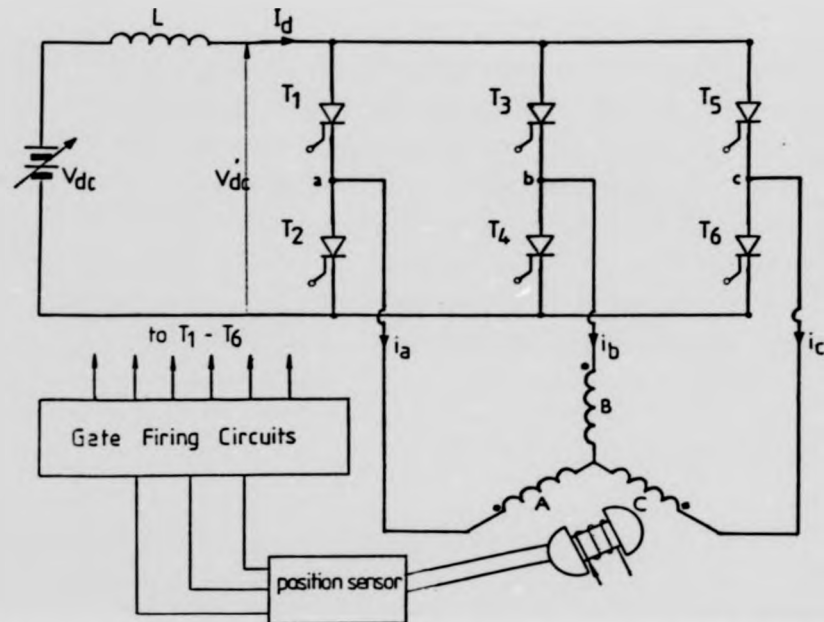


Figure 3.19 Principle circuit of current-fed brushless machine

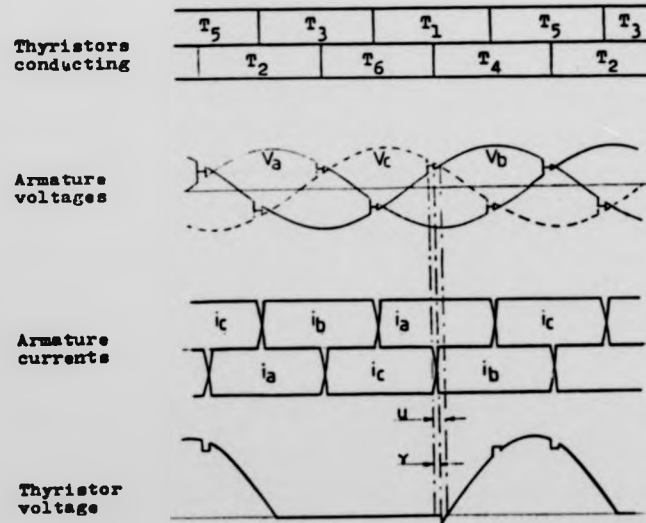


Figure 3.20 Inverter waveforms of current-fed brushless machine

angle u will block T_1 , when $i = I_d$. There follows an interlude period, in which $i_a = 0$, $i_b = I_d$ and $i_c = -I_d$, which ends at $\theta_o + \pi/3$ when T_2 is triggered to commutate T_0 . This sequence repeats itself at the rate of six per electrical cycle. Figure 3.20 shows the inverter waveforms, angle u represents the overlapping angle, the angle γ is the no-load angle of advance of converter firing angle, and the angle $(\gamma - u)$ affords the reverse bias for the commutated thyristor. Commutation in such systems is therefore achieved by the armature induced voltage, and commutation devices such as capacitors, inductors and auxiliary thyristors are not required.

3.5.2 Medium power transistor-switched brushless dc motors

The trend for medium power brushless dc motors is towards using power transistors and permanent magnet synchronous motors (33,34,35). These motors have ratings ranging from 100W to 100kW; and they are truly brushless because the rotor fields are provided by permanent magnets.

Medium power brushless dc motors come in different shapes. But most of them are built conventionally with cylindrical rotors, and their armature are wound on slotted laminated steel stators. A typical motor of this kind is given by Demerdash and Nehl (36). The rotor of their motor is an 8-pole samarium cobalt structure consisting of 48 blocks of 18 MGO samarium cobalt material mounted on an octagonal motor shaft. The armature is housed in a 24-slot 7mil vanadium-permendur laminated stator, and is fed by a 3-phase transistor inverter which operates the machine in both directions and in three different modes: motoring, plugging and regenerative braking. This 17hp motor is rated at 270V and 9000rpm.

A completely different motor construction is given by Weh, Wahlen, Grumbrecht and Brauckmann (34). Their motor consists of two main components: a disc-shaped rotor composed of 20 high coercivity ferrite magnets, which are embedded in a

light weight fibreglass-reinforced plastic disc; and a gramme type ringwinding wound on a laminated steel ring with 60 radial slots. The power circuit is a 100kVA 3-phase transistor inverter rated at 250V. The output stage consists of six darlington circuits, each circuit having two parallel Thomson CSF ESM738 drive transistors feeding six further transistors of the same type. The maximum output current of a darlington circuit is 280A, which is capable of driving the motor to give a peak output torque of 400Nm.

Applications of medium power brushless dc motors include high-power servo-control, traction drives and machine tool drives.

3.5.3 Small brushless dc motors

Small brushless dc motor were first developed by NASA (37) in the early sixties for space-flight application, a situation where cost was a secondary consideration in an effort to achieve highest performance. But as the cost of semiconductor components gradually fell during the past decade, brushless dc motors have become more and more competitive against standard dc motors in servo applications (38,39,40).

An early example of the small brushless dc motor available commercially was that manufactured by Siemens America Inc. (41), and this is shown in Figure 3.21. The small motor has a cylindrical two-pole permanent magnet; the stator has a two-phase winding with one coil per pole per phase, and four coils in all. The coils are commutated by four transistors which are controlled by two Hall-effect sensors, and speed control is achieved by controlling the bias current to the bases of the transistors. This particular motor gave an output of only 1W at 3000rpm.

One very interesting recent application of small brushless dc motor is in the field of low-cost, fast mass data storage, and in particular, in small Winchester hard-disc memories (42). The latest generation of this kind of disc memories, which operate with discs of 5 $\frac{1}{2}$ " diameter, are all fitted with

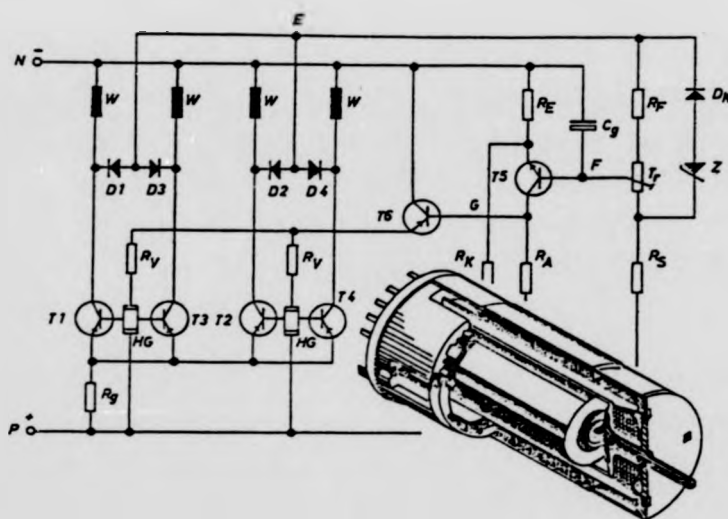


Figure 3.21 A brushless dc motor commutated by transistors and steered by Hall-effect sensors. (Siemens America, Inc.)



Figure 3.22 A skewed-pole lamination

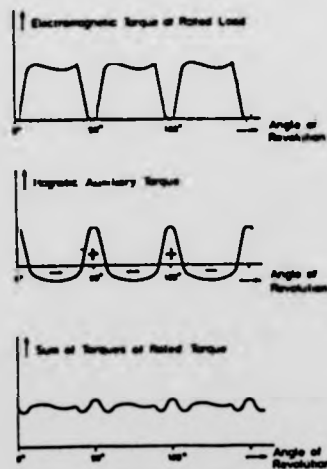


Figure 3.23 Effect of auxiliary torque

direct-driven spindles, and the motors are, without exception, of the brushless dc type. Only the extremely smooth performance of the motor, the high mechanical precision of the bearing system and of the hub of the spindle can guarantee an error-free operation of the drive, as slight vibrations of the machine may cause errors in the read/write electronics because of the extremely low flying read/write heads.

Apart from the hard-disc drives, the floppy-disc drives also make extensive use of brushless direct-drive dc motors (43). The reason for this preference over ac motors is to reduce the size and to improve the reliability of the drives by eliminating the belts, pulleys and bearings used in ac motors.

Another popular usage for small brushless dc motors is the driving of cooling fans in electronic instruments. In such applications, it is essential to keep the component cost of the motor as low as possible. To achieve this goal, the number of position sensors and transistors must be kept to a minimum, and a two-phase uni-polar design (Figure 3.10) is generally adopted. However, it has been shown that the torque output of such motors is discontinuous and fluctuating. But these problems are overcome by generating an auxiliary reluctance torque between the permanent magnets of the rotor and the magnetic resistance of the stator. This auxiliary torque is produced by changing the stator from its cylindrical shape to a skewed pole shape as shown in Figure 3.22. The combined effects of the electromagnetic torque and the auxiliary reluctance torque are shown in Figure 3.23, whereby the resultant torque becomes continuous and much less fluctuating. By optimising the auxiliary torque to a specific loading point, these motors can produce a very smooth torque output, making them also suitable for propelling tape recorders and turntables.

3.6 Rotor Position Detectors

Having described the different types of brushless dc motors, it is appropriate

at this stage to review briefly the various position detectors which are available today. They include the synchro resolver, inductive pick-up coil, optical sensor, reluctance switch and Hall-effect sensor. However, the most commonly used devices are: 1) reluctance switches, 2) optical sensors, and 3) Hall-effect ICs.

3.6.1 Reluctance switches

A functional sketch of a reluctance switch is given in Figure 3.24. The revolving, slotted iron disc couples and decouples the primary and secondary of a fixed transformer. The primary is fed by a high frequency supply; and the change of reluctance due to the varying orientation of the slotted disc modulates the amplitude of the induced voltage in the secondary. A demodulator is used to convert the signal to a suitable form to drive the power switches.

Although the reluctance switch is very robust and is unaffected by dirt and grit, it is nevertheless prone to be affected by stray magnetic fields which affect demodulation; and the bulk and weight of the assemblies make the system unsuitable for small motors.

3.6.2 Optical sensors

There are two types of optical sensors, they are the transmissive- and the reflective- sensor. In the first type, a revolving, slotted disc is used to interrupt a beam of light between a fixed source and the detector, as shown in Figure 3.25. In the second type, the light-emitter and the photo-detector are arranged in such a way that the photo-detector responds to radiation from the source when a reflective object is placed within the field of view (Figure 3.26).

The advantages of optical sensors are that the photo-detectors have a very fast response time, i.e. they can be used in very high speed motors, and unlike the reluctance switch, they are not affected by stray magnetic fields. Also, they are unaffected by temperature variations. However, they are less robust, and can

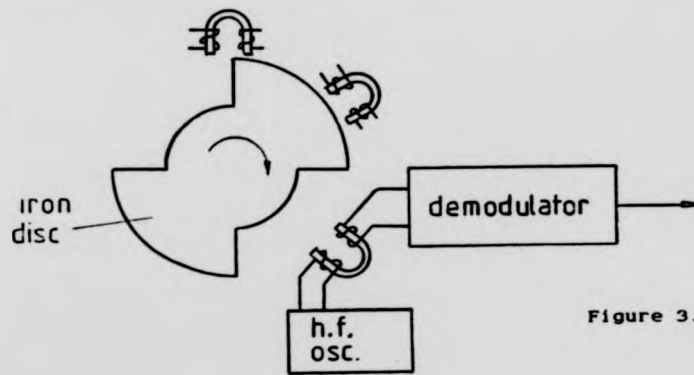


Figure 3.24 Reluctance switch

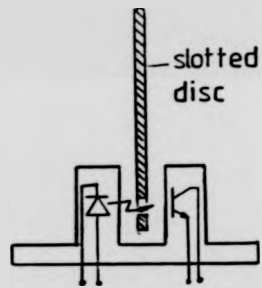


Figure 3.25 Transmissive optical detector

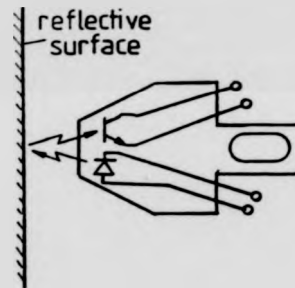


Figure 3.26 Reflective optical detector



Figure 3.27 An arrangement of trigger magnets and Hall-effect ICs

be affected by dirt and grit.

3.6.3 Hall-effect ICs

Hall-effect ICs are miniature integrated-circuit proximity switches that give bounce-free switching when influenced by a magnetic field. They are the most common position detectors found in small brushless dc motors. The triggering magnetic field in these motors is usually provided by a separate small magnet system as shown in Figure 3.27. The signal conditioning circuit is included within the device package, thus the output of the IC can be used to drive the switching transistors directly. Because of the popularity of the small Hall brushless motors, Hitachi has produced a Hall-effect power IC (44) specially for these motors. The built-in power transistor of the IC is capable of driving the armature winding directly, resulting in a minimal component count and a major reduction of overall motor size.

Advantages of Hall-effect ICs are that they are very robust, small in size, inexpensive and that they are unaffected by dirt and grit. Their disadvantages are temperature sensitivity and susceptibility to stray magnetic fields.

CHAPTER 4

MOTOR PERFORMANCE ASSESSMENT

4.0 Introduction

Before building the prototype brushless dc disc-motors, it is necessary to develop equations modelling the operation of the motor. This enables machine performance to be computed under the operating constraints so as to provide a preliminary assessment of the suitability of a design in fulfilling a certain role.

In this chapter a discrete-time approach is used to predict the performance of a 3-phase star-connected bi-polar machine. Such an approach is not only straight forward and accurate, but it also has the ability to cope with non-sinusoidal waveforms. The analysis can also be easily applied to other machine configurations.

Section 4.1 of this chapter describes the basic scheme of the brushless dc disc-motor system to be investigated. Section 4.2 presents a model of the motor system, which takes into account the characteristics of the switching devices.

Section 4.3 lays down the current equation of the motor; and section 4.4 describes the output equations. The computed performance of a 600W motor design is given in Section 4.5.

4.1 The Motor Scheme

The basic scheme to be investigated is illustrated schematically in Figure 4.1. The motor receives its supply from an inverter, which in turn gets its supply from a variable dc voltage source of negligible impedance. The switching

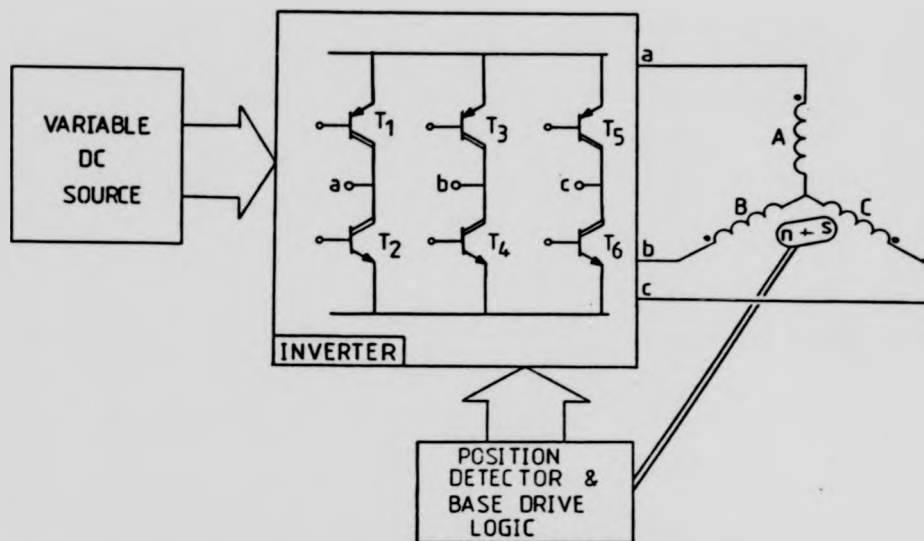


Figure 4.1 Scheme of the brushless dc disc-motor

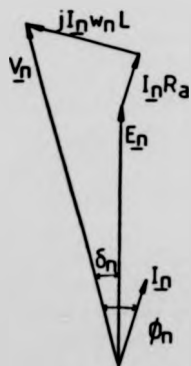


Figure 4.2 Phasor diagram of the n th harmonics

sequence of the inverter is governed by a position detector attached to the rotor. The electrical angle δ between the line-voltage and the motor's back emf (the load angle) is controlled by adjusting the relative angular position between the rotor position detector and the stator. The scheme of the motor system is therefore similar to that of a synchronous motor with a constant load angle.

If, as is frequently the case, the armature resistance is negligible, the power output P_{out} delivered by a conventional synchronous machine operating from 3-phase mains can be estimated by the well known equation (4.5),

$$P_{out} = 3 \left(\frac{E_1 V_1}{X_{d1}} \sin \delta_1 + V_1^2 \frac{X_{d1} - X_{q1}}{2X_{d1} X_{q1}} \sin 2\delta_1 \right) \quad \dots (4.0)$$

where E_1 = RMS value of the fundamental component of the armature phase emf
 V_1 = RMS value of the fundamental phase voltage
 X_{d1} = the fundamental direct-axis synchronous reactance
 X_{q1} = the fundamental quadrature-axis synchronous reactance
 δ_1 = the phase angle between the phasors E_1 and V_1

Although the above equation represents the power generated of the machine by the fundamental components only, the low harmonic contents of conventional machines means that Equation (4.1) will give a very close estimate to the true output. On the other hand, the generated emf of a brushless dc disc-motor is trapezoidal and is rich in harmonics. Therefore, as it stands, Equation (4.1) will not give a close estimate of the disc-motor's output as it does not take into account the harmonic components.

To model the brushless disc-motor accurately, the harmonic components of the same order are analysed separately. The continuous-time function relating the nth harmonic components is first formulated according to the phasor diagram given in Figure 4.2. And, because of the time-invariance of the system, the overall continuous-time function is therefore obtained by combining together

linearly all the harmonic functions. The performance characteristics of the motor are then calculated by using a discrete-time approach.

In a brushless motor, the switching devices are as much a part of the motor as the commutator and brushes of a conventional dc machine. It is therefore impossible to obtain an accurate modelling of the brushless motor without taking into account the characteristics of the switching devices. Before formulating the output equations, the parameters of the motor system will first be studied.

4.2 Motor Parameter Modelling

Due to the low operating voltage of the motor system, the forward conduction voltage drop of the switching devices must be included in the machine modelling. However, semiconductors have very complex characteristics, and a full device modelling is outside the scope of this thesis. Fortunately, the power devices of a brushless motor are only used in the switching mode, i.e. either off or fully on, at frequencies several orders of magnitude lower than their cut-off frequencies (i.e. a typical power transistor such as the MJ11016 has a cut-off frequency of 4MHz), and it is therefore possible to use a simplified dc model of the devices.

The first step towards establishing a device model is an accurate measurement of its dc forward characteristics. This will lead, firstly, to an indication of the device's properties under operating conditions, and, secondly, to a direct approximation of the device characteristics.

4.2.1 Power device modelling

The switching devices chosen for this project were power darlingtontons of type MJ11015 (pnp) and MJ11016 (npn) manufactured by Motorola. Their electrical characteristics are given in Table 6.3. A power darlington has a very high dc current gain, which is typically greater than 1000, and this makes it very easy

to drive. Each device is constructed by fabricating two or more transistors on the same substrate and connecting them together as in Figure 4.3. An anti-parallel protection diode is usually provided in the same package, as this adds little or no extra cost to the fabrication process. Darlingtons can of course be constructed from discrete transistors using similar connections.

The forward characteristics of the darlingtons were measured using the circuit given in Figure 4.4. The mounting-base temperature was maintained at approximately 65 C to simulate the operating environment. The results are shown in Figure 4.5 where the base current was 200mA. The forward characteristics were also obtained using $I_B = 300\text{mA}$, but the results were very close to that at $I_B = 200\text{mA}$, and are not shown in the figure for the sake of clarity.

It can be seen from Figure 4.5 that at currents higher than 1A, the forward characteristics are more or less linear. In normal operations the armature current seldom actually drops below 1A, and therefore a first order approximation would be adequate to represent the characteristics of the darlingtons. The equivalent circuit of a saturated (fully on) darlington is thus equal to a resistance in series with a voltage source, as shown in Figure 4.6(a). When it is switched off, the device is equivalent to a diode connected in anti-parallel with the collector and the emitter (Figure 4.6(b)).

4.2.2 Machine equivalent circuit

The relationship in time between the various motor voltages and the switching sequence of the transistors are shown in Figure 4.7. Also, the conduction diagrams of the six conduction-states are shown in Figure 4.8. It can be seen that at any of the conduction-states, there are always two transistors being switched on and conducting in series with two armature windings. Considering State I for example, T_1 and T_6 are conducting in series with windings A and C. This property of the brushless motor can be used to derive an equivalent circuit of the motor.

Considering State I and replacing the transistors by their equivalent

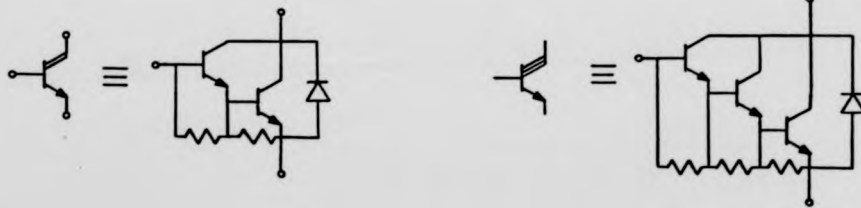


Figure 4.3 a) Darlington pair

b) Triple darlington

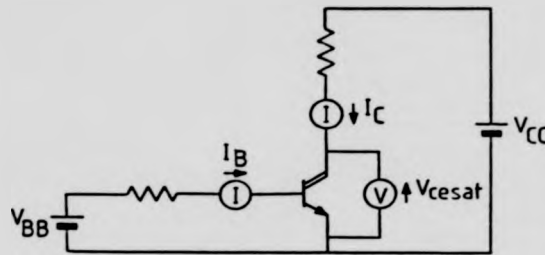


Figure 4.4 Circuit to measure the forward characteristics of a darlington

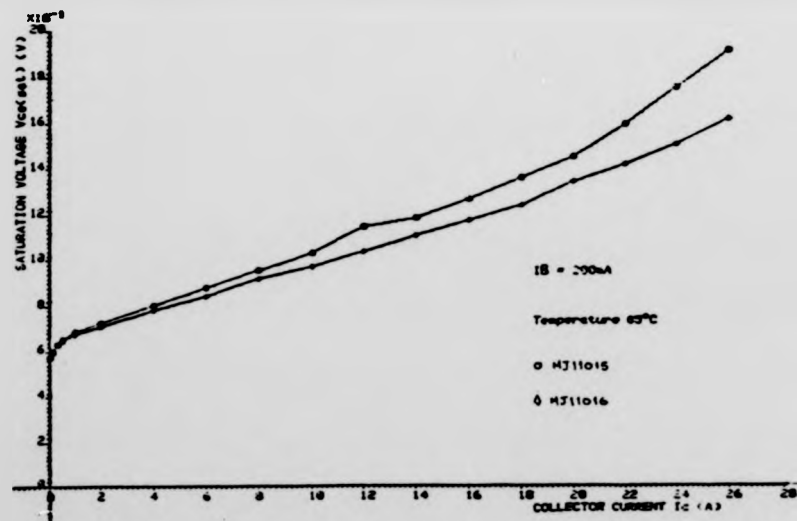


Figure 4.5 Forward characteristics of MJ11015 and MJ11016



Figure 4.6 Equivalent circuit of a switching darlington

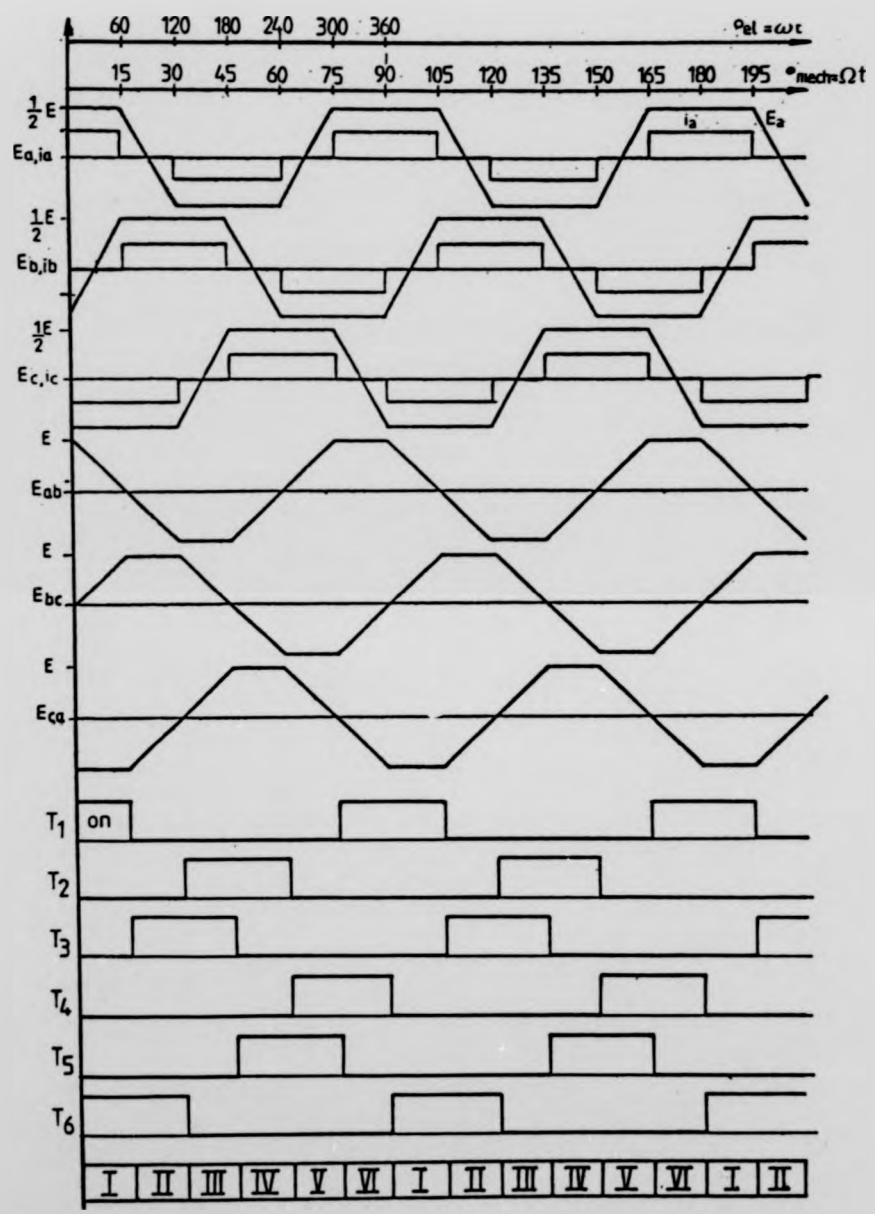


Figure 4.7 Relationship in time between the motor voltages and the switching sequence

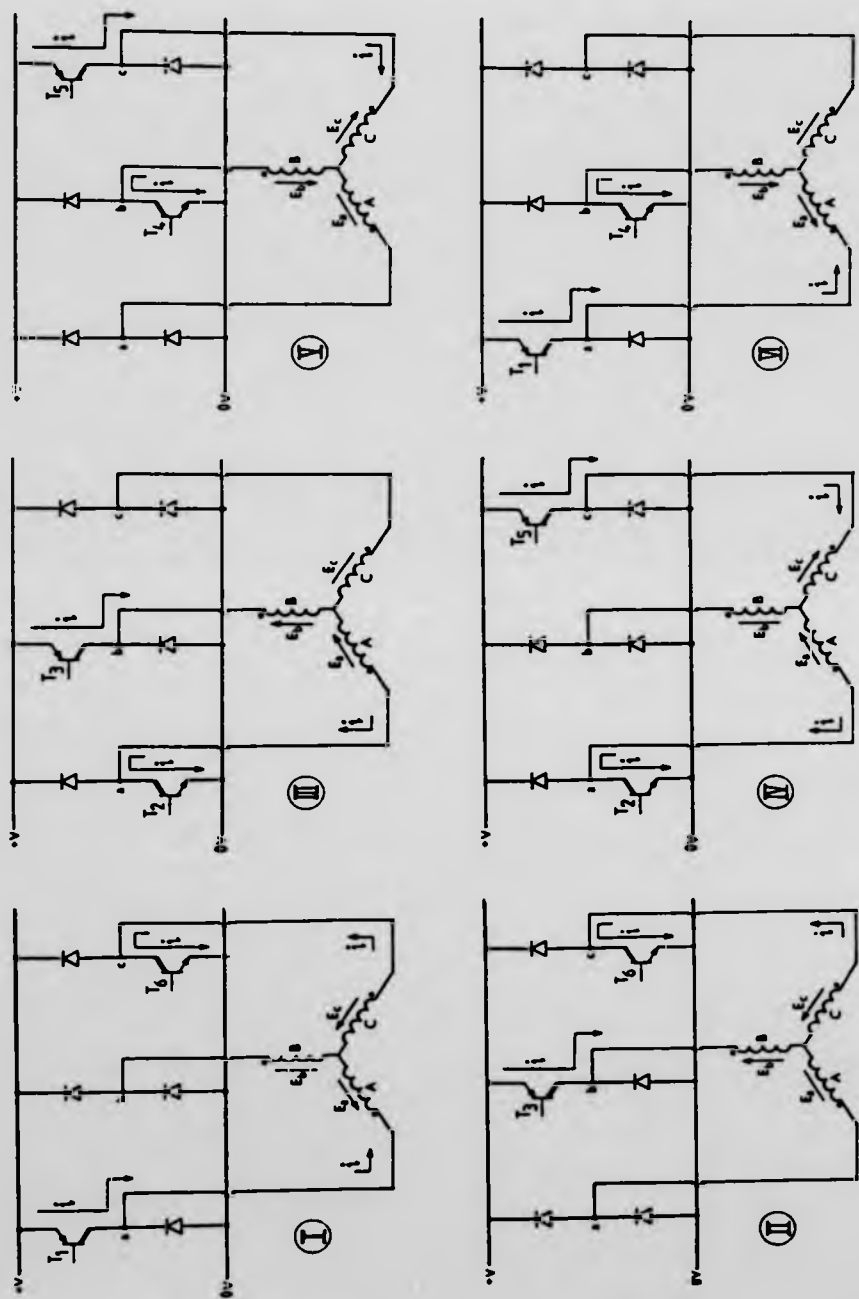


Figure 4.8 Conduction-state diagram of the star-connected BLPM motor

circuits, Figure 4.9 is obtained. Assuming that the two conducting transistors have similar on-state slope resistance, Figure 4.9 can be redrawn to give the circuit in Figure 4.10 where the voltage sources of the transistors are removed from the main loop, and the collector-emitter slope resistances are merged with the armature resistances. The armature resistance per phase now becomes R_a' , and $R_a' = R_a + R_T$, where $R_T =$ the average slope resistance of the devices $= (R_{T1} + R_{T6})/2$. As all other conduction-states can be represented in the same way, the equivalent circuit of the brushless motor can therefore be represented by the circuit given in Figure 4.11. The effective supply voltage now becomes V_{dc}' , where $V_{dc}' = V_{dc} - V_{pnp} - V_{npn}$, and S_1 to S_6 are perfect switches.

4.3 Current Equation

Before laying down the current equation, the following assumptions are made:

- 1) That the armature reaction is negligible, and is ignored.
- 2) That because of the poor electrical conductivity of polymer bonded SmCo_5 magnets and the low level of eddy currents induced in the mild steel flux return rings, rotor damping effects are ignored.
- 3) That the machine is non-salient-pole because the permeability of SmCo_5 is similar to that of air.
- 4) That the machine operates in a balanced condition.
- 5) That switching transients are ignored.

Accordingly, the machine is represented by four coupled circuits -- three represent the 3-phase armature windings and the remaining one represents the field winding (the permanent magnets), as shown in Figure 4.12. The voltages and currents of the machine are therefore governed by a coupled circuit equation as expressed in matrix form as follows:

$$\begin{bmatrix} v_a \\ v_b \\ v_c \\ v_f \end{bmatrix} = \begin{bmatrix} R_a & 0 & 0 & 0 \\ 0 & R_b & 0 & 0 \\ 0 & 0 & R_c & 0 \\ 0 & 0 & 0 & R_f \end{bmatrix} \begin{bmatrix} i_a \\ i_b \\ i_c \\ i_f \end{bmatrix} + \frac{d}{dt} \begin{bmatrix} L_{aa} & L_{ab} & L_{ac} & L_{af} \\ L_{ba} & L_{bb} & L_{bc} & L_{bf} \\ L_{ca} & L_{cb} & L_{cc} & L_{cf} \\ L_{fa} & L_{fb} & L_{fc} & L_{ff} \end{bmatrix} \begin{bmatrix} i_a \\ i_b \\ i_c \\ i_f \end{bmatrix} \quad \dots (4.1)$$

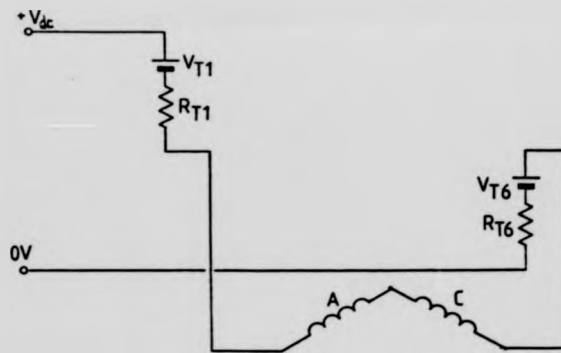


Figure 4.9 Transistors replaced by their circuit equivalents

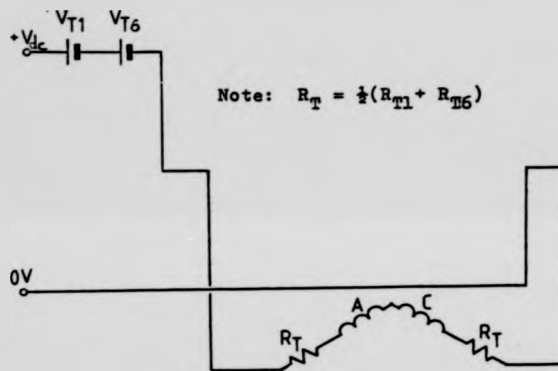


Figure 4.10 Voltage sources of the transistors removed from the main loop

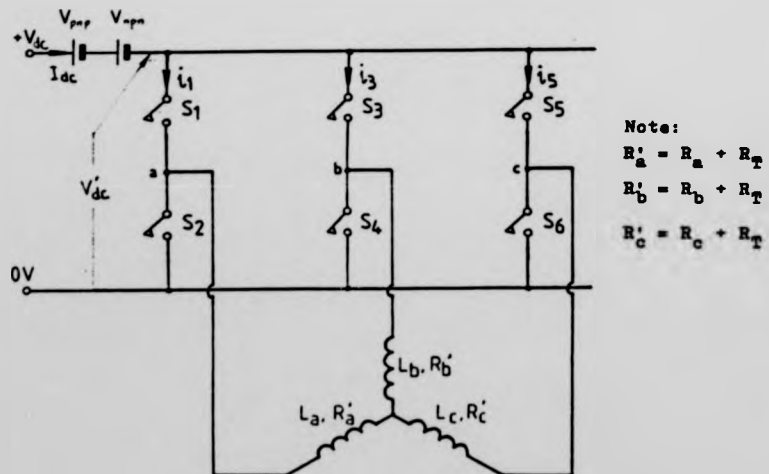


Figure 4.11 Equivalent circuit of the star-connected bi-polar motor

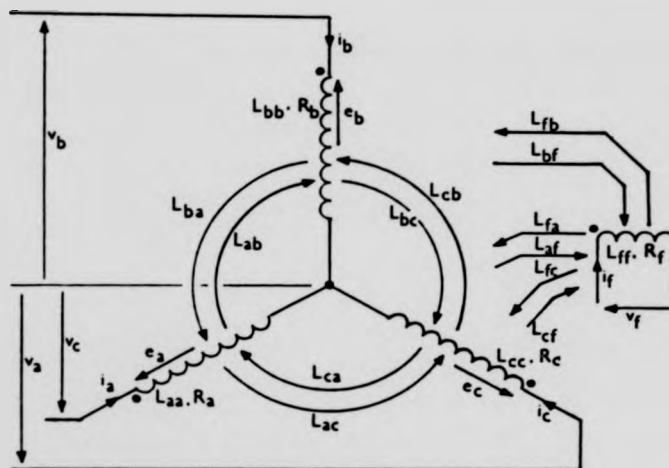


Figure 4.12 The brushless motor being represented by coupled circuits

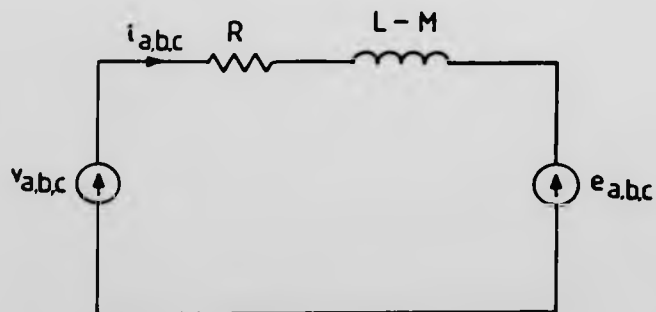


Figure 4.13 Simple equivalent circuit of the motor

where R_a, R_b, R_c = phase winding resistances (including the transistor slope resistances)
 R_f = field winding resistance
 L_{aa}, L_{bb}, L_{cc} = phase winding self-inductances
 L_{ff} = field winding self-inductance
 L_{ab}, \dots, L_{fc} = mutual inductances

The permanent magnet field-system is in actual fact equivalent to a field winding with a constant current, and the ampere-turn is proportional to the coercivity of the magnet material and the length of the magnet. Also, as the armature reaction mmf is relatively small, it produces no significant demagnetisation effects on the magnet poles. Hence, as long as the armature current is not excessively higher than the rated value, the mutual inductances L_{fa}, L_{fb} and L_{fc} can be discarded from Equation (4.1) without significantly affecting the accuracy of the model. Thus Equation (4.1) is rewritten as

$$\begin{bmatrix} v_a \\ v_b \\ v_c \end{bmatrix} = \begin{bmatrix} R_a & 0 & 0 \\ 0 & R_b & 0 \\ 0 & 0 & R_c \end{bmatrix} \cdot \begin{bmatrix} i_a \\ i_b \\ i_c \end{bmatrix} + \frac{d}{dt} \begin{bmatrix} L_{aa} & L_{ab} & L_{ac} \\ L_{ba} & L_{bb} & L_{bc} \\ L_{ca} & L_{cb} & L_{cc} \end{bmatrix} \cdot \begin{bmatrix} i_a \\ i_b \\ i_c \end{bmatrix} + \frac{d}{dt} \begin{bmatrix} L_{af} & i_f \\ L_{bf} & i_f \\ L_{cf} & i_f \end{bmatrix} \quad (4.2)$$

As the disc-motor is basically a non-salient-pole machine, the inductances $L_{aa}, L_{ab}, \dots, L_{cc}$ are independent of the rotor position. Accordingly, the resistances and the inductances for a balanced machine can be written as

$$R_a = R_b = R_c = R \quad \dots (4.3)$$

$$L_{aa} = L_{bb} = L_{cc} = L \quad \dots (4.4)$$

$$L_{ab} = L_{ba} = L_{ac} = L_{ca} = L_{bc} = L_{cb} = M \quad \dots (4.5)$$

Letting $i_f = \text{constant} = I_f$, and substituting (4.3), (4.4) and (4.5) into (4.2), we have

$$\begin{bmatrix} v_a \\ v_b \\ v_c \end{bmatrix} = \begin{bmatrix} R & 0 & 0 \\ 0 & R & 0 \\ 0 & 0 & R \end{bmatrix} \cdot \begin{bmatrix} i_a \\ i_b \\ i_c \end{bmatrix} + \begin{bmatrix} L & M & M \\ M & L & M \\ M & M & L \end{bmatrix} \cdot \frac{d}{dt} \begin{bmatrix} i_a \\ i_b \\ i_c \end{bmatrix} + I_f \frac{d}{dt} \begin{bmatrix} L_{af} \\ L_{bf} \\ L_{cf} \end{bmatrix} \quad \dots (4.6)$$

The last term in the above equation is the phase induced voltages e_a, e_b and e_c .

in the windings A, B and C, respectively, i.e.

$$I_f \frac{d}{dt} \begin{bmatrix} L_{af} \\ L_{bf} \\ L_{cf} \end{bmatrix} = \begin{bmatrix} e_a \\ e_b \\ e_c \end{bmatrix} \quad \dots(4.7)$$

Also, for a star connected 3-phase armature with floating neutral, the following conditions exist

$$i_a + i_b + i_c = 0 \quad \dots(4.8)$$

and

$$\frac{di_a}{dt} + \frac{di_b}{dt} + \frac{di_c}{dt} = 0 \quad \dots(4.9)$$

By substituting Equations (4.7) and (4.9) into Equation (4.6), the following is obtained

$$\begin{bmatrix} v_a \\ v_b \\ v_c \end{bmatrix} = \begin{bmatrix} R & 0 & 0 \\ 0 & R & 0 \\ 0 & 0 & R \end{bmatrix} \begin{bmatrix} i_a \\ i_b \\ i_c \end{bmatrix} + \begin{bmatrix} (L-M) & 0 & 0 \\ 0 & (L-M) & 0 \\ 0 & 0 & (L-M) \end{bmatrix} \frac{d}{dt} \begin{bmatrix} i_a \\ i_b \\ i_c \end{bmatrix} + \begin{bmatrix} e_a \\ e_b \\ e_c \end{bmatrix} \quad \dots(4.10)$$

This is a decoupled system of equations from which a simple equivalent circuit is derived (Figure 4.13). The equations that govern the system now becomes

$$v_{a,b,c} = i_{a,b,c} R + (L-M) \frac{di_{a,b,c}}{dt} + e_{a,b,c} \quad \dots(4.11)$$

Taking the fundamental supply voltage of phase A as the reference phasor, and considering a balanced system, the following relationships exist

$$v_a(\omega t) = \sum_{n=1}^{\infty} v_n \sin(n\omega t + \theta_n) \quad \dots(4.12)$$

$$v_b(\omega t) = \sum_{n=1}^{\infty} v_n \sin(n(\omega t + 2\pi/3) + \theta_n) \quad \dots(4.13)$$

$$v_c(\omega t) = \sum_{n=1}^{\infty} v_n \sin(n(\omega t - 2\pi/3) + \theta_n) \quad \dots(4.14)$$

where $\theta_1 = 0$

θ_n = phase angle of the nth harmonic supply voltage in relation to θ_1

v_n = peak value of the nth harmonic supply voltage

ω = angular frequency of the motor

Similarly, the back emfs induced in the armature windings can be expressed as

$$e_a(\omega t) = \sum_{n=1}^{\infty} E_n \sin(n\omega t + \delta_n) \quad \dots(4.15)$$

$$e_b(\omega t) = \sum_{n=1}^{\infty} E_n \sin(n(\omega t + 2\pi/3) + \delta_n) \quad \dots(4.16)$$

$$e_c(\omega t) = \sum_{n=1}^{\infty} E_n \sin(n(\omega t - 2\pi/3) + \delta_n) \quad \dots(4.17)$$

where δ_n = phase angle of the nth harmonic emf in relation to θ_1

E_n = peak value of the nth harmonic emf

Also, for the armature currents, the following relationships exist

$$i_a(\omega t) = \sum_{n=1}^{\infty} I_n \sin(n\omega t + \theta_n) \quad \dots(4.18)$$

$$i_b(\omega t) = \sum_{n=1}^{\infty} I_n \sin(n(\omega t + 2\pi/3) + \theta_n) \quad \dots(4.19)$$

$$i_c(\omega t) = \sum_{n=1}^{\infty} I_n \sin(n(\omega t - 2\pi/3) + \theta_n) \quad \dots(4.20)$$

where θ_n = phase angle of the nth harmonic phase current in relation to θ_1

I_n = peak value of the nth harmonic phase current

As the system is decoupled, it is only necessary to consider one of the three phases. Now, consider phase A, and by substituting (4.12), (4.15) and (4.18) into (4.11), we get

$$\sum_n V_n \sin(n\omega t + \theta_n) = R \sum_n I_n \sin(n\omega t + \theta_n) + (L - M) \frac{d}{dt} (\sum_n I_n \sin(n\omega t + \theta_n)) + \sum_n E_n \sin(n\omega t + \delta_n) \quad \dots(4.21)$$

Correspondingly, the equation for the nth harmonic is

$$\begin{aligned} V_n \sin(n\omega t + \theta_n) &= R I_n \sin(n\omega t + \theta_n) + (L - M) \frac{d}{dt} (I_n \sin(n\omega t + \theta_n)) \\ &\quad + E_n \sin(n\omega t + \delta_n) \\ &= R I_n \sin(n\omega t + \theta_n) + (L - M) I_n n\omega \cos(n\omega t + \theta_n) \\ &\quad + E_n \sin(n\omega t + \delta_n) \quad \dots(4.22) \end{aligned}$$

By rewriting (4.22) in polar form, we get

$$V_n \angle \theta_n = R I_n \angle \phi_n + j n \omega (L - M) I_n \angle \phi_n + E_n \angle \delta_n$$

$$\therefore I_n \angle \phi_n = \frac{V_n \angle \theta_n - E_n \angle \delta_n}{R + j n \omega (L - M)} \quad \dots (4.23)$$

(note: I_n , V_n and E_n are the peak values, not the rms values)

By equating the in phase and the quadrature components, the following expressions are obtained

$$I_n = \left[\frac{V_n^2 + E_n^2 - 2 V_n E_n \cos(\delta_n - \theta_n)}{R^2 + n^2 \omega^2 (L - M)^2} \right]^{\frac{1}{2}} \quad \dots (4.24)$$

and

$$\phi_n = \tan^{-1} \frac{V_n \sin \theta_n - E_n \sin \delta_n}{V_n \cos \theta_n - E_n \cos \delta_n} - \tan^{-1} \frac{n \omega (L - M)}{R} \quad \dots (4.25)$$

Substituting (4.24) and (4.25) into (4.18), the total armature current in phase A is given as

$$i_a(\omega t) = \sum_n \left[\frac{V_n^2 + E_n^2 - 2 V_n E_n \cos(\delta_n - \theta_n)}{R^2 + n^2 \omega^2 (L - M)^2} \right]^{\frac{1}{2}} \sin[n \omega t + \tan^{-1} \frac{V_n \sin \theta_n - E_n \sin \delta_n}{V_n \cos \theta_n - E_n \cos \delta_n} - \tan^{-1} \frac{n \omega (L - M)}{R}] \quad \dots (4.26)$$

Since the waveform of $v_a(\omega t)$ is determined by the dc link voltage and the conduction angle of the power devices (Figure 4.14), by taking the fundamental component of v_a as the reference phasor, the coefficients V_n and θ_n can be obtained by using Discrete Fourier Transform (see Appendix B) on $v_a(\omega t)$. The waveform of $e_a(\omega t)$ is calculated by the voltage equation developed in Chapter 2. If the orientation of the rotor position detector is known, then the relationship in time between e_a and v_a are determined. The coefficients e_n and δ_n can be calculated by Discrete Fourier Transform. Also, the motor parameters R , L and M can be measured experimentally. Hence, the waveform of $i_a(\omega t)$ can therefore be calculated if the operating conditions are specified, and Figure 4.14 gives the example of two simulated current waveforms, calculated using Equation (4.26).

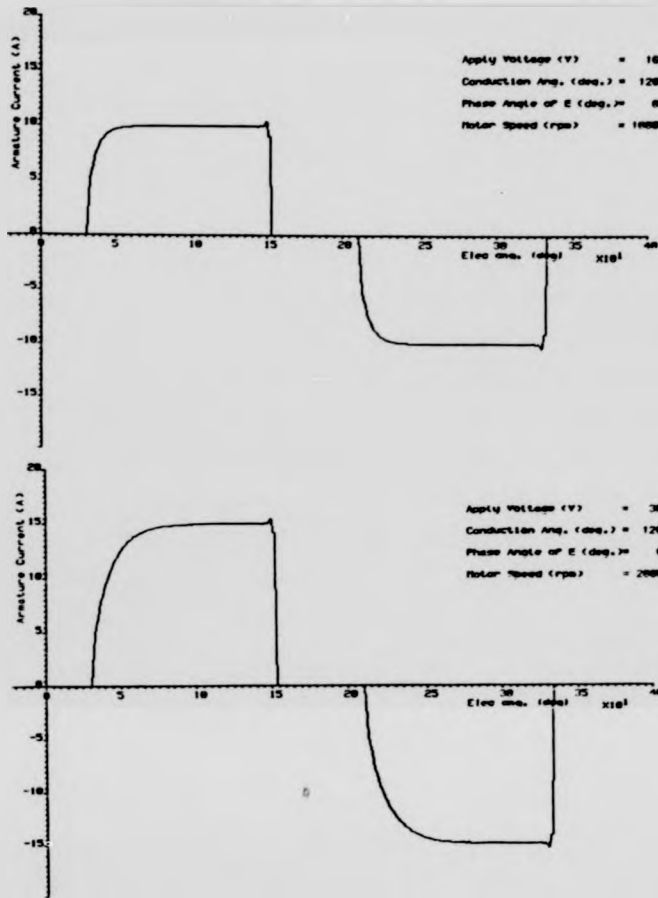


Figure 4.14 Simulated current waveforms of the brushless motor

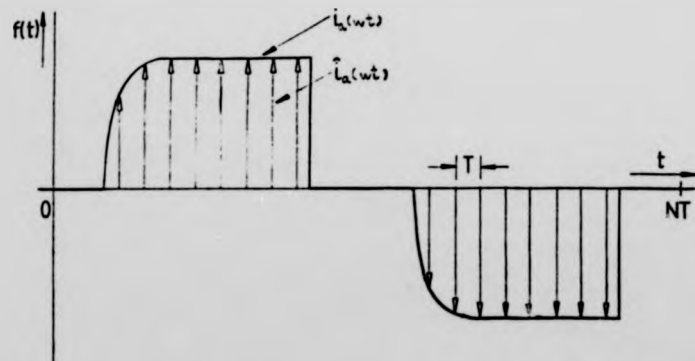


Figure 4.15 Discrete-time approximation of a continuous-time function

4.4 Output Equations

A discrete-time approach is used here to assess the output characteristics of the disc-motor. First of all, consider a continuous-time function $i_a(wt)$, that exists over the time interval $0 \leq t \leq NT$. The function can be represented by a sequence of N equally spaced impulses, where the strength of the impulse at $t = nT$ is the area under the function $i_a(wt)$ in the interval $(n-1/2)T \leq t \leq (n+1/2)T$. Such a representation is shown in Figure 4.15. If the sampling interval T is small enough, so that the function does not change appreciably over an interval, then the strength of the impulse at $t=nT$ can be taken as $Ti_a(nwT)$. And the continuous-time function can be approximated by a discrete-time function (see Appendix A) as

$$\begin{aligned} i_a(wt) &\approx \hat{i}_a(wt) = T \sum_{n=0}^{N-1} i_a(nwT) \delta(wt - nwT) \\ &= T \sum_{n=0}^{N-1} i_a(nwT) \delta(wt - nwT) \end{aligned} \quad \dots(4.27)$$

where $\hat{i}_a(wt)$ stands for an approximation of $i_a(wt)$. And, similarly the supply voltage $v_a(wt)$ and the induced voltage $e_a(wt)$ can also be written in discrete form as

$$v_a(wt) \approx \hat{v}_a(wt) = T \sum_{n=0}^{N-1} v_a(nwT) \delta(wt - nwT) \quad \dots(4.28)$$

$$e_a(wt) \approx \hat{e}_a(wt) = T \sum_{n=0}^{N-1} e_a(nwT) \delta(wt - nwT) \quad \dots(4.29)$$

Now, the average total power input to the shaft, P_{shaft} is given as

$$P_{shaft} = \frac{3}{NT} \int_0^{NT} i_a(wt) e_a(wt) dt \quad \dots(4.30)$$

Substituting (4.27) and (4.29) into the above, the following is obtained

$$P_{shaft} = \frac{3}{NT} \int_0^{NT} \left(T \sum_{n=0}^{N-1} i_a(nwT) \delta(wt - nwT) \right) \left(T \sum_{m=0}^{N-1} v_a(mwT) \delta(wt - mwT) \right) dt \quad \dots(4.31)$$

$$\text{Since } \left. \begin{aligned} \delta(\omega t - n\omega T) \delta(\omega t - m\omega T) &= 0 & n \neq m \\ &= \delta^2(\omega t - n\omega T) & n = m \end{aligned} \right\} \dots (4.32)$$

$$\begin{aligned} \text{Thus } P_{\text{shaft}} &= \frac{3I}{N} \int_0^{NT} \sum_{n=0}^{N-1} i_a(n\omega T) e_a(n\omega T) \delta^2(\omega t - n\omega T) dt \\ &= \frac{3I}{N} \sum_{n=0}^{N-1} i_a(n\omega T) e_a(n\omega T) \int_0^{NT} \delta^2(\omega t - n\omega T) dt \\ &= \frac{3I}{N} \sum_{n=0}^{N-1} i_a(n\omega T) e_a(n\omega T) \dots (4.33) \end{aligned}$$

Also, the total power input to the motor system P_{in} is

$$P_{in} = V_{dc} I_{dc} \dots (4.34)$$

where V_{dc} = dc link voltage
 I_{dc} = dc link current

$$\text{And } \begin{aligned} I_{dc} &= \bar{i}_1 + \bar{i}_3 + \bar{i}_5 \\ &= 3 \bar{i}_1 \dots (4.35) \end{aligned}$$

where i_1, i_3, i_5 = device currents in the upper legs of the inverter
 $(\bar{i}$ = average value of i , and for a balanced system $\bar{i}_1 = \bar{i}_3 = \bar{i}_5$)

Referring to the conduction sequence diagram in Figure 4.17, \bar{i}_1 can be calculated as

$$\begin{aligned} \bar{i}_1 &= \frac{1}{2NT} \int_0^{NT} |i_a(\omega t)| dt \\ &= \frac{1}{2NT} \int_0^{NT} \frac{1}{T} \sum_{n=0}^{N-1} |i_a(n\omega T)| \delta(\omega t - n\omega T) dt \\ &= \frac{1}{2N} \sum_{n=0}^{N-1} |i_a(n\omega T)| \int_0^{NT} \delta(\omega t - n\omega T) dt \\ &= \frac{1}{2N} \sum_{n=0}^{N-1} |i_a(n\omega T)| \dots (4.36) \end{aligned}$$

Substituting (4.35) and (4.36) into (4.34), we get

$$P_{in} = 3 V_{dc} \frac{1}{2N} \sum_{n=0}^{N-1} |i_a(n\omega T)| \dots (4.37)$$

If the total mechanical loss is denoted by P_{loss} , then the net power output P_{out} is

$$P_{out} = P_{shaft} - P_{loss} \quad \dots (4.38)$$

and the efficiency is

$$\eta = \frac{P_{out}}{P_{in}} \times 100\% \quad \dots (4.40)$$

And the output torque T_{out} is

$$T_{out} = \frac{P_{out}}{\omega} \quad \dots (4.41)$$

4.5 Digital Computation of the Performance Characteristics

The equations developed in the last section can be used to compute the performance characteristics of the disc-motor. Several programs have been written to do this, and the flow chart of the calculation process is given in Figure 4.16.

The armature current i_a (wt) at a specified operating condition, i.e. when the dc link voltage, the motor speed and the orientation of the rotor position detector are known, is firstly estimated by Equation (4.26). Secondly, the waveforms of e_a , v_a and i_a are approximated by their respective discrete-time functions. The number of samples N is taken to be 360 and the samples are taken over one complete electrical cycle. If the angular frequency is ω , then the sampling interval T is

$$T = \frac{2\pi}{\omega N} \quad \dots (4.42)$$

The dc link current, power output and efficiency values at the specified

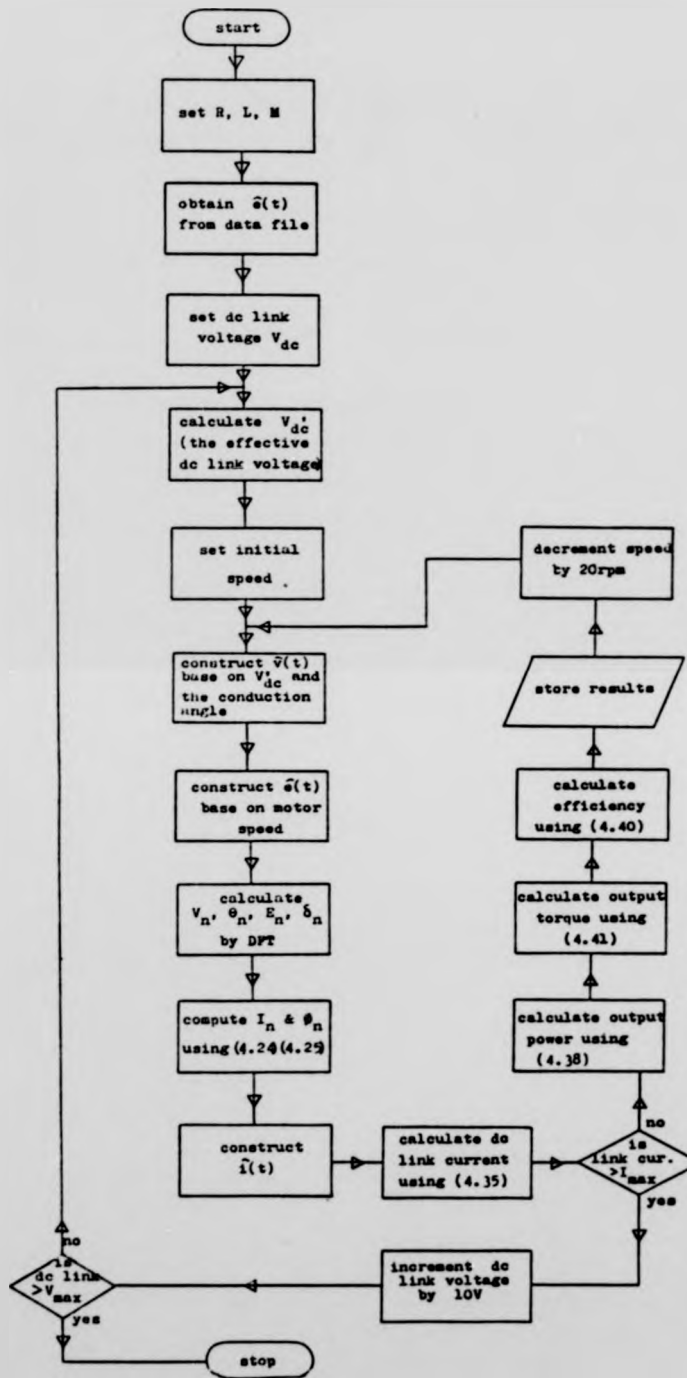


Figure 4.16 Flow chart of the output performance calculation process

operating point can be calculated by Equations (4.36), (4.38) and (4.40) respectively. The complete picture of the motor's output characteristics is obtained by repeating the calculations at different operating points. Figure 4.17 gives the computed characteristics of the 600W 3-phase bi-polar brushless dc disc-motor which will be described in Chapter 6.

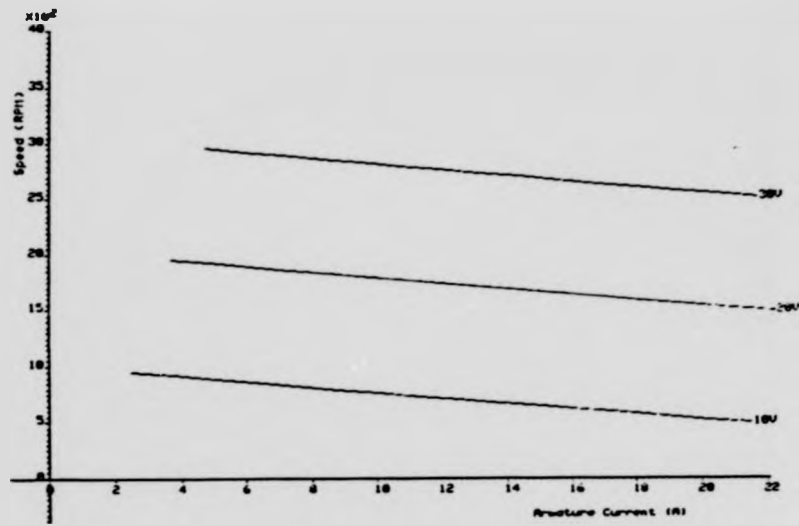


Figure 4.17 a) Calculated speed characteristics of the 600W brushless dc disc-motor

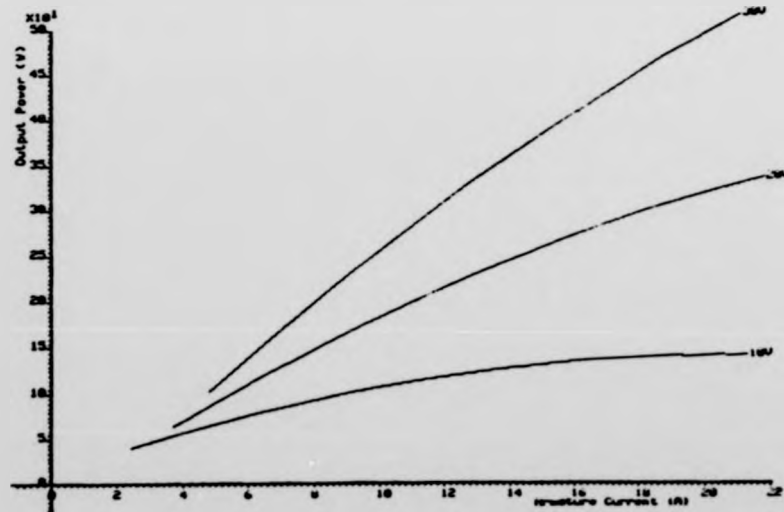


Figure 4.17 b) Calculated output characteristics of the 600W brushless dc disc-motor

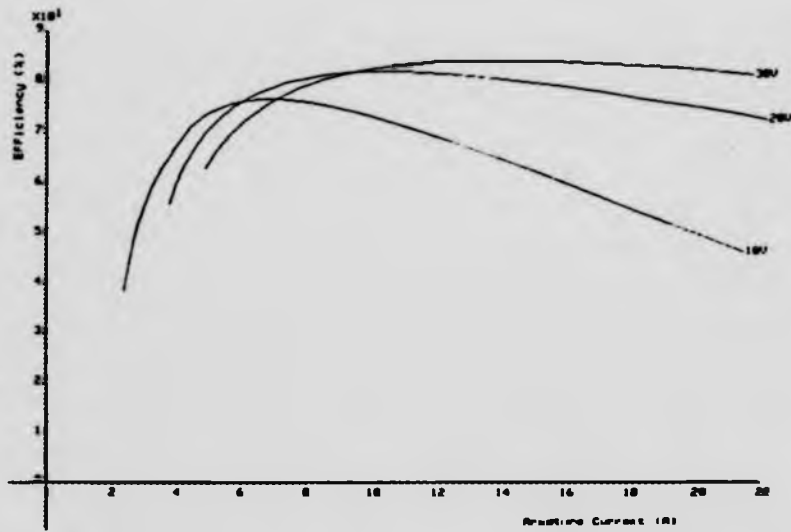


Figure A.17 c) Calculated efficiency characteristics of the 600W brushless dc disc motor

CHAPTER 5UNDERCOMMUTATION AND COMMUTATION ADVANCING5.0 Overview

A property of the Warwick dc disc-motors is the very low inductances of the armature windings. This property is a direct result of the ironless construction of the armature, and it is understood to have led to the motors' excellent commutation characteristics which help to raise the limit of their operating speed (18).

Section 5.1 of this chapter describes the effects of armature winding inductance on the commutation characteristics of dc motors; Section 5.2 describes exactly how the already excellent high speed characteristics of the brushless dc disc-motors can be improved by means of commutation advancing; and Section 5.3 describes the conditions for optimum commutation advancing.

5.1 Effects of Undercommutation

In a conventional dc motor, it is essential to avoid excessive current density at any point in the commutator-brush contact in order to prevent sparks during commutation (45). This indicates that optimum conditions are obtained when the current density is uniform over the entire commutation period. A linear change of current with time in the commutated coil, corresponding to linear commutation as shown in Figure 5.1 (refer to Figures 3.4 and 3.5 for the commutation sequence), brings about this condition and is accordingly the optimum.

However, linear commutation is hindered by the coil inductance. Both the voltage of self-induction in the commutated coil, and the voltage of mutual induction from other coils undergoing commutation at the same time, oppose changes in

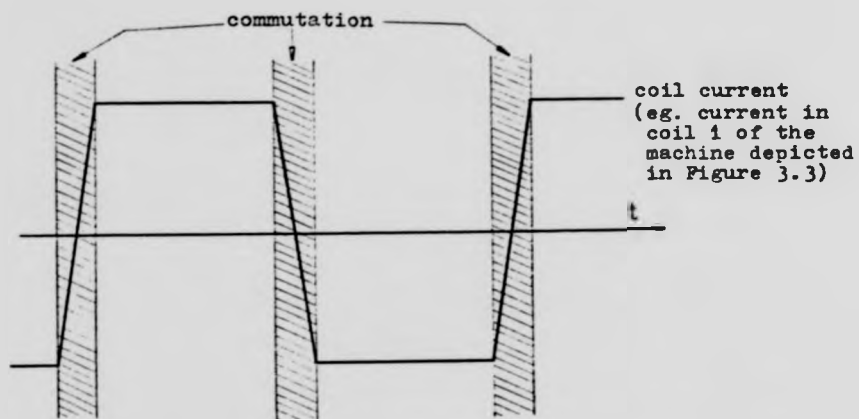


Figure 5.1 Linear commutation -- a linear change of current with time in the commutated coil

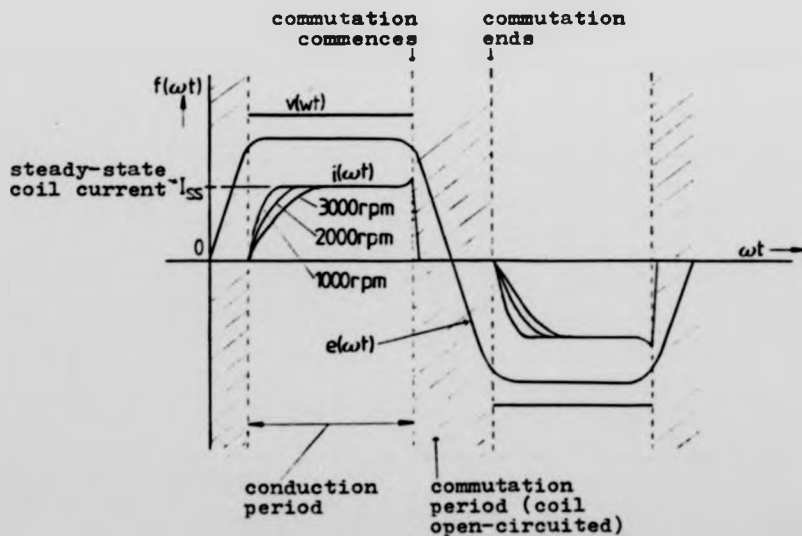


Figure 5.2 Commutation sequence, and the relationship in time between the voltage and current of a coil of the bi-polar motor

current in the commutated coil. The sum of these two voltages is often referred to as the reactance voltage. The result is that current values in the short-circuit coil lag in time behind the values dictated by linear commutation. This condition is known as undercommutation, or delayed commutation.

Armature inductance thus tends to produce high losses and sparking at the trailing brush tip. The normal practice to overcome undercommutation is to inject an opposite emf into the coil under commutation to cancel out the reactance voltage. This is achieved by placing auxiliary interpoles between the main poles (46). Another method of reducing undercommutation is to shift the brushes forward until the short-circuited coil comes under the fringe of the next pole, thereby inducing the required emf (46). This is called commutation advancing.

Unlike the dc motors, the coil of a bi-polar brushless dc motor undergoing commutation is open-circuited at the beginning of the commutation period. This leads to rapid drop of the coil current. Voltage of the opposite polarity is then reapplied to the coil at the end of the period. The coil current then starts to flow in the opposite direction. The sequence of commutation is shown in Figure 5.2.

Like the dc motor, however, the reactance voltage of the coil limits the rate of rise in current in the commutated coil. The rising of the coil current lags more and more in phase as the motor speed increases. This condition of undercommutation is also depicted in Figure 5.2. The effect of undercommutation thus limits the effective coil current, and, consequently, the motor's operating speed.

5.2 Commutation Advancing

Undercommutation in a brushless dc disc-motor is reduced by injecting an emf into

the coil undergoing commutation to cancel out the reactance voltage. This is achieved by reapplying the voltage to the commutated coil in a slightly earlier time by shifting the rotor position detector by an angle β , as shown in Figure 5.3. This method is similar to the brush shifting in a dc motor. The net effect of this is the forcing of the coil current to rise quickly by the large instantaneous potential difference between the apply voltage and the coil's back emf. An optimum condition occurs when the coil current rises quickly to its desired steady-state value as the trapezoidal coil emf begins to level. This condition results in an optimum power transfer during the machine's conduction period.

When the angle β is greater than the optimum value, the condition of overcommutation will occur. Overcommutation in a brushless dc disc-motor leads to an overshoot of the coil current in the leading edge of the current-pulse, as depicted in Figure 5.4, and to an increase of the power input to the motor. However, the power output from the motor does not necessarily increase proportionally. This is because the level of power transfer to the shaft within the period of advance is rather low due to the low instantaneous value of E , despite a higher coil current. Also, the higher coil current within the period of advance induces a higher ohmic loss. In most case, this will give rise to a drop in the output efficiency.

5.3 Optimum Commutation Advancing

The exact angle of optimum advancing depends on the steady-state coil current and on the motor speed. To calculate the optimum value of β , the assumption that the coil's back emf $e(t)$ can be approximated by a trapezoidal wave is made (Figure 5.5). Now consider the first quarter wave of $e(t)$, its equation is given as

$$e(t) = \begin{cases} \frac{6E\omega t}{\pi} & 0 \leq t < \frac{\pi}{6\omega} \\ E & \frac{\pi}{6\omega} \leq t < \frac{\pi}{2\omega} \end{cases} \quad \dots (5.1)$$

where E is the peak value of $e(t)$ at angular frequency ω .

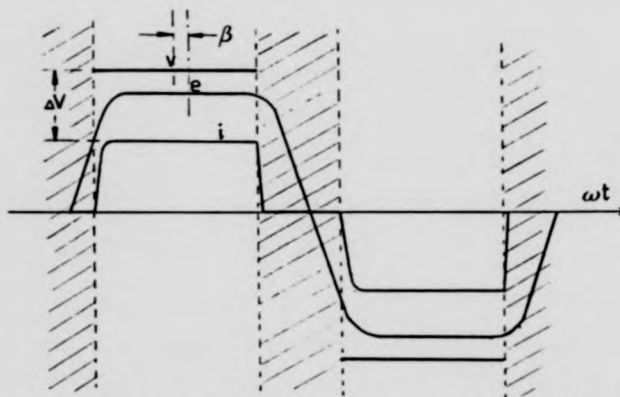


Figure 5.3 Effect of shifting the rotor position sensor by an angle β

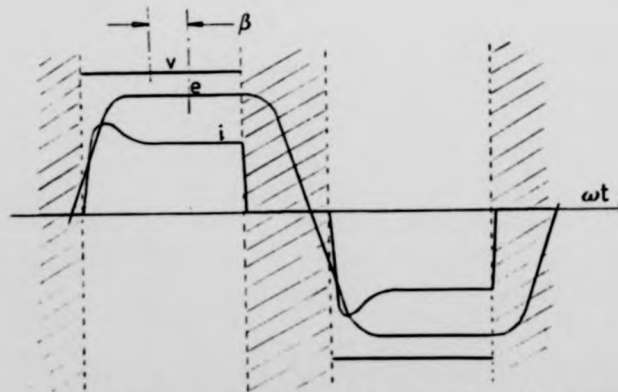


Figure 5.4 Effect on the coil current as a result of overcommutation

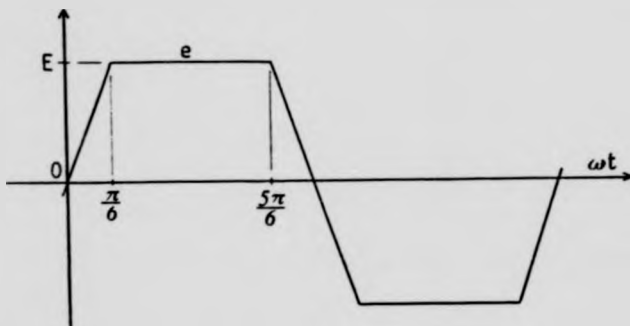


Figure 5.5 Trapezoidal approximation of the coil emf $e(t)$

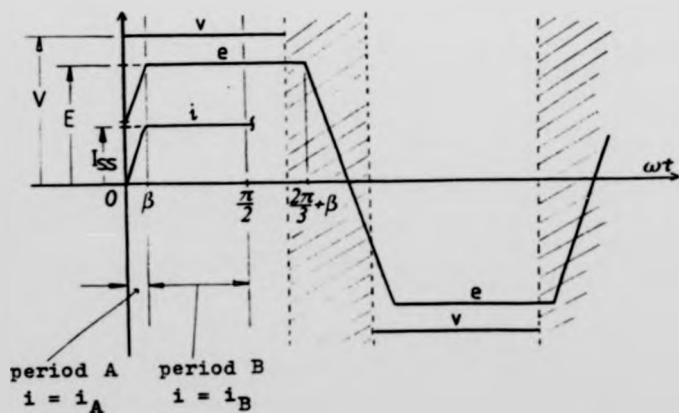


Figure 5.6 Relationship in time between v , e and i with the rising edge of v as the zero reference

Referring to the situation depicted in Figure 5.6, where the end of the commutation period is being taken as the zero reference. The equations of voltages during the conduction period are expressed as follows:

$$e(t) = \frac{6E}{\pi} (wt + \frac{\pi}{6} - \beta) \quad 0 \leq t < \frac{\beta}{\omega} \quad \left. \begin{array}{l} \\ \\ \end{array} \right\} \dots(5.2)$$

$$= E \quad \frac{\beta}{\omega} \leq t < \frac{\pi}{2\omega}$$

and $v(t) = V \quad 0 \leq t < \frac{\pi}{2\omega} \dots(5.3)$

From the equivalent circuit of the bi-polar brushless dc motor (Figure 4.13), the voltage equation is

$$v = IR + (L - M) \frac{di}{dt} + e \dots(5.4)$$

Period A $(0 \leq t < \frac{\beta}{\omega})$

Letting $i = i_A(t)$, $L_a = L - M$, and substituting (5.2) and (5.3) into (5.4), we get

$$V = i_A(t) \cdot L_a \frac{di_A(t)}{dt} + \frac{E}{\pi} (6\omega t + \pi - 6\beta) \dots(5.5)$$

Laplace Transform both sides of (5.5), and assuming $i_A(0) = 0$, it gives

$$\frac{V}{s} = I_A(s) R + s L_a I_A(s) + \frac{E}{\pi} (\frac{6\omega}{s^2} + \frac{\pi - 6\beta}{s}) \dots(5.6)$$

Rearranging the above expression, we get

$$I_A(s) = \frac{1}{R + s L_a} (\frac{V}{s} - \frac{E}{\pi} (\frac{6\omega}{s^2} + \frac{\pi - 6\beta}{s})) \dots(5.7)$$

Taking inverse transform on (5.7), the following is obtained

$$i_A(t) = (\frac{6\omega E L_a}{\pi R^2} + \frac{V - E}{R} + \frac{6\beta E}{\pi R}) (1 - \exp(-\frac{R}{L_a}t)) - \frac{6\omega E t}{\pi R} \dots(5.8)$$

Period B $(\frac{\theta}{w} < t < \frac{\pi}{2w})$

Letting $i = i_B(t - \theta/w)$, $L_a = L - M$, and substituting (5.2) and (5.3) into (5.4), we get

$$V = i_B(t - \theta/w) + L_a \frac{d}{dt} i_B(t - \theta/w) + E \quad \dots (5.9)$$

Letting $i_B(0) = i_A(\theta/w)$, and solving (5.9) in the same way as previously, the coil current becomes

$$i_B(t - \theta/w) = \frac{V - E}{R} + (i_A(\theta/w) - \frac{V - E}{R}) \exp(-\frac{R}{L_a}(t - \theta/w)) \quad \dots (5.10)$$

If the steady-state coil current is denoted by i_{ss} , then

$$i_{ss} = \frac{V - E}{R} \quad \dots (5.11)$$

The optimum advance occurs when

$$i_A(\theta/w) = i_B(0) = \frac{V - E}{R} = i_{ss} \quad \dots (5.12)$$

i.e. when $\frac{V - E}{R} = i_A(\theta/w)$

$$= (\frac{6EwL_a}{R^2\pi} + \frac{V - E}{R} + \frac{6\theta E}{R\pi})(1 - \exp(-\frac{\theta R}{wL_a})) - \frac{6\theta E}{R\pi} \quad \dots (5.13)$$

Substituting (5.11) into (5.13), the following is obtained

$$i_{ss} = (\frac{6EwL_a}{R^2\pi} + i_{ss} + \frac{6\theta E}{R\pi})(1 - \exp(-\frac{\theta R}{wL_a})) - \frac{6\theta E}{R\pi} \quad \dots (5.14)$$

As a general solution for Equation (5.14) is very difficult to obtain, numerical methods were used to calculate the solution of (5.14); and Figure 5.7 gives the calculated values of θ for the 600W 3-phase bi-polar motor. It can be seen that the maximum value of θ is about 6°elec. The small value of θ required by the brushless dc disc-motor confirms that the ironless construction of the armature lends to the motor some very favourable commutation characteristics.

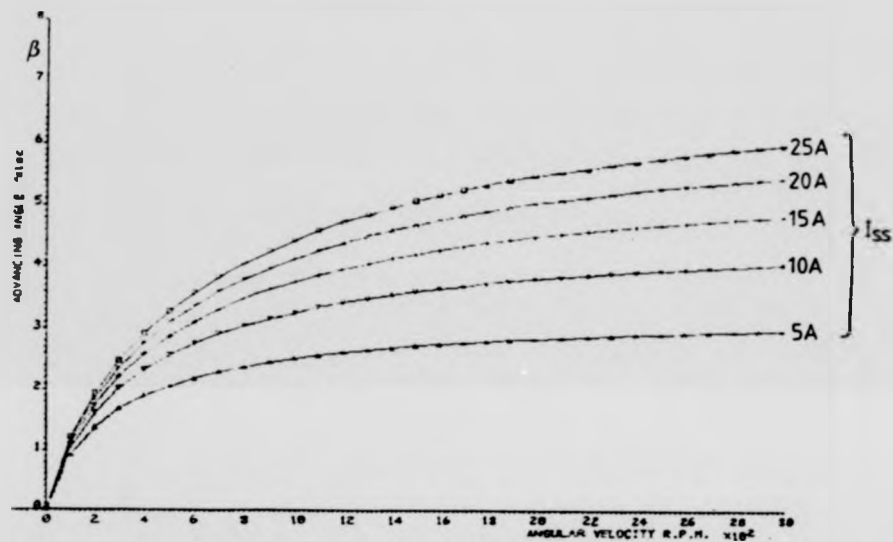


Figure 5.7 Calculated values of optimum angle of advancing for the 600W 3-phase bi-polar motor (see Chapter 6)

CHAPTER 6

BRUSHLESS DC DISC-MOTOR PROTOTYPES

6.0 Introduction

Air-cored brushless dc disc-motors have characteristics which are very different from those of conventional brushless dc motors. The major differences are: 1) the disc-motor has a trapezoidal emf waveform, 2) it has an extremely low armature inductance, and 3) it has a negligible armature reaction. In order to investigate, and to explore these unique characteristics, three prototype motors were built, and they were designed with the following aims in mind:

- 1) To select and to evaluate a new permanent magnet material as an alternative to ferrite, which has been used extensively on previous Warwick disc-motors.
- 2) To develop a rotor position detector.
- 3) To investigate the properties of the different motor configurations.
- 4) To confirm that the motor performance characteristics are as predicted.
- 5) To compare the brushless dc disc-motors with the brush-type disc-motors in terms of power output and efficiency.

Section 6.1 of this chapter gives the design specifications of the prototypes. Section 6.2 describes the magnetic circuit designs, and the properties of some modern magnet materials are also described in order to aid the selection of a new material for Motors 2 and 3. Section 6.3 will give the electric circuit designs. While Section 6.4 presents the mechanical designs of the prototype motors.

Section 6.5 gives the measured motor parameters. Section 6.6 describes an optical rotor position detector developed specially for the brushless dc disc-motors. Finally, the operation and the test results of the motors are described in Section 6.7.

6.1 Design Specifications of the Prototypes

The three prototypes will be referred to as Motor 1, 2 and 3 by the chronological order in which they were built.

6.1.1 Motor 1

This motor was initially designed with the intention of comparing its performance characteristics with those of an existing dc disc-motor (aim 5). But due to the difficulties in obtaining the ferrite magnets with a pole-arc to pole-pitch ratio α of 0.9, magnets with a smaller α were used. As a result, the motor cannot induce the required emf waveform, making Motor 1 unsuited to being used as a brushless dc motor. This motor was later dropped from the project. But in order to illustrate the effect of a smaller α on the induced emf waveform, and to give an idea of how the magnet material's properties affect a motor design, the complete design description of Motor 1 is given here.

Because of the original intention to compare the performance of a brushless dc disc-motor with a brush-type counterpart, Motor 1 was specified according to an existing dc disc-motor. The existing motor was designed for electric wheelchair propulsions (11); its specifications, design data and performance curves are given in Appendix C. As the brushless motor had a different intended application, its speed and voltage ratings were both increased. But to keep the comparison comparable, the values of d_1 and d_2 , the number of poles, and the magnet material were kept the same. The design specifications of this first prototype are given below:

Motor 1 Design Specifications

output	:	180W (uni-polar) / 360W (bi-polar)
supply voltage	:	30V
speed	:	3000rpm
d_2	:	190mm
d_1	:	105mm
number of poles	:	8

magnet material : Ferroba III
motor arrangement : 3-phase uni-polar / 3-phase bi-polar

6.1.2 Motor 2

Since the first prototype was unsuitable as a brushless motor, a second prototype was designed using a different magnet material. The new material chosen was polymer-bonded rare-earth cobalt, and the specifications of Motor 2 are given below:

Motor 2 Design Specifications

output : 180W (uni-polar) / 360W (bi-polar)
supply voltage : 30V
speed : 3000rpm
 d_2 : 190mm
 d_1 : 105mm
number of poles : 8
magnet material : polymer-bonded SmCo_5
motor arrangement : 3-phase uni-polar / 3-phase bi-polar

6.1.3 Motor 3

Having gained some experience in designing brushless dc disc-motors, and having tested the first two prototypes, a third motor, with a higher rating, was then designed. This motor was designed to operate in the 3-phase star-connected bi-polar mode, and was intended to power an experimental electric truck for automated warehouse application. The specifications of Motor 3 are as follows:

Motor 3 Design Specifications

output : 600W
supply voltage : 30V
speed : 3000rpm
 d_2 : 190mm
 d_1 : 105mm
number of poles : 8
magnet material : polymer-bonded SmCo_5
motor arrangement : 3-phase bi-polar (star-connected)

6.2 Magnetic Circuit Designs

In order to carry out the magnetic circuit designs for the prototypes, it was first necessary to select a magnet material for each motor. Ferroba III was chosen for Motor 1 for reasons stated earlier. For Motor 2 and 3, polymer-bonded rare-earth SmCo_5 was provisionally selected. To finalise on this decision, the properties of different magnet materials must be studied and compared.

6.2.1 Properties of magnet materials

Although a variety of permanent magnet materials are currently available, the type eventually selected would depend heavily on a motor's application. In order to get a simplified picture of the properties of the materials, and to help the process of selection, it is necessary to group together materials with similar properties, and then examine in detail some of the materials which represent their respective groups. From the motor designer's point of view there are three main groups of magnets which are of commercial importance. These are:

- 1) Alnico alloys: these are aluminium/nickel/cobalt alloys.
- 2) Ferrite materials: these include barium, strontium or lead ferrite and their composites, they are also known as 'ceramic' because their physical properties are similar to those of porcelain.
- 3) Rare-earth cobalt alloys: these are rare-earth transition metal/cobalt composites which included samarium-cobalt and platinum-cobalt. Also included in this group are polymer-bonded cobalt materials which have been processed into a synthetic bonding material to enable them to be formed for specialised applications.

Four materials representative of the three groups are examined here, they are Columax (Alnico group), Ferroba III (Ferrite group), and Samarium Cobalt and Polymer-bonded Samarium Cobalt (Rare-earth group). The properties of these magnets are summarised in Table 6.1; and Figure 6.1 shows their demagnetisation characteristics.

It can be seen that from Figure 6.1 that the Alnico magnet has a very high

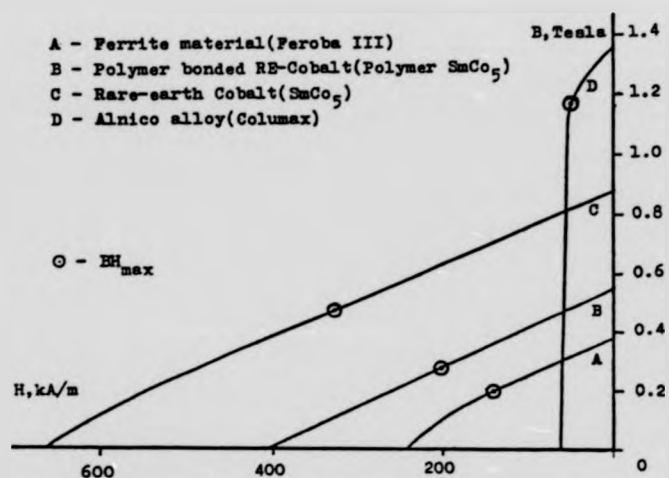


Figure 6.1 Demagnetisation curves

Material	Barium Ferrite (Feroba III)	Polymer RE (polymer SmCo ₅)	Rare-earth (SmCo ₅)	Alnico alloy (Columax)
(BH) _{max} (KJ/m ³)	26	55	152	60
Remance B _r (Tesla)	0.37	0.55	0.87	1.35
Coercive Force H _c (KA/m)	239	400	660	59
Curie Temp. (°C)	450	--	740	--
Max. operating temp. (°C)	180	100	250	200
Min. Magnetising force (KA/m)	870	2400	2400	250
Density Kg/m ³	4700	5200	8200	7300
Comments:	Anisotropic. Hard & brittle-grinding only.	Anisotropic. Excellent resistance to demagnetisation. Relatively high power. Easily machined & drilled.	Anisotropic. Outstanding resistance to demagnetisation coupled with high power. Very brittle-grinding only.	Anisotropic. High power, relative low resistance to demagnetisation forces. Hard & brittle-grinding only.

Table 6.1 Properties of magnets

remenance; it is able to produce a very high flux which makes it highly suitable for applications requiring a high output torque. However, the Alnico has a low coercivity, such that excessive armature current can cause demagnetisation. Also, magnetisation before assembly is not feasible for this material, and it must be magnetised 'in situ'. Alnico magnets are very hard and brittle, and are supplied cast to shape.

The ferrite magnet has a much higher coercivity than the Alnico alloy; it is very cheap, and is easily available. However, its energy product is the lowest, although a relatively high performance can be achieved for short duty cycles since it does not demagnetise easily. Physical properties of ferrite materials are just like porcelain -- very hard and brittle, and are very difficult to machine.

The new rare-earth magnets, such as samarium cobalt, have energy products which are considerably higher than the best of the Alnicos. The increase in the energy product is achieved by the improvement in the coercive force rather than the flux density. Although these magnets are considerably more expensive than Alnico alloys for the same volume, a much higher performance is achieved from the motor in return. Alternatively, one can achieve the same performance from a smaller volume of material and the cost is more directly comparable. Samarium cobalt magnets cannot be machined easily; they are normally supplied in the magnetised condition which raises a problem in handling. Also belonging to the same rare-earth group are the polymer-bonded derivatives. The material given in Figure 6.1 is the polymer-bonded samarium cobalt; it has a very high coercive force, and has an energy product more than twice that of the Feroba III, yet, it is extremely easy to machine.

6.2.2 Selecting a permanent magnet material for Motor 2 and 3

In view of the traction application of the motors, it is necessary to maximise both the output efficiencies and their power-to-weight ratios. As already mentioned in Section 2.2, the air-gap of a disc motor is much longer than that

of a conventional motor, and therefore the air-gap reluctance is considerably higher. To overcome the high air-gap reluctance, and at the same time not allowing the machine's weight to become excessive, magnets with a high coercivity should be used to provide the field.

The Alnico alloys, which require long magnet lengths to compensate for their low coercivity, were ruled out on grounds of their weight. Rare-earth cobalt was initially chosen for the prototypes because of its extremely high coercivity and higher-than average flux density. But due to the difficulties in getting these magnets in the required dimensions, it was finally decided to select polymer-bonded SmCo_5 magnets for the two motors. This material can be machined very easily, and is cheaper than the sintered rare-earth materials.

6.2.3 The magnetic circuits

Having chosen a material for a particular design, the next step in the magnetic circuit design is to calculate the required thickness of the magnet pieces. Before this can be done two parameters must be specified, these are the operating point of the chosen material, and the air-gap length.

To specify the first parameter, one must first determine the operating condition of the magnetic circuit, i.e. static or dynamic. As already described in Section 2.2, if there is no reluctance change within, and no external flux influence to the magnetic circuit, then the magnet is operating at a specific point on the demagnetisation curve; this is known as the static operating condition. Otherwise the magnet is operating in a dynamic condition. Because of the non-salient nature of the armature, and the low level of the armature reaction flux, a static working condition is assumed, and, an operating point can be specified.

The operating point determines the air-gap flux density, which is, in turn, used by Equation (6.1) to determine the total number of turns of the armature winding. The number of turns is used together with the conductor gauge, which

is selected according to the rated current density, to determine the armature thickness. Finally, the thickness and the running clearance on both sides of the armature will determine the air-gap length.

Having specified the two parameters, the magnet thickness is then calculated by using Equation (2.8). It can be seen that, by specifying a low operating point, shorter magnets can be used, and thus a lower rotor mass is obtained. On the other hand, the electric loading must increase to make up for the lower flux density. This would mean that either the efficiency will suffer or a large amount of copper is required. To balance the electric and magnetic loadings, it is normal practice to specify the operating point at the $(BH)_{\max}$. But in the case of low flux materials, such as the ferrites, it is beneficial in terms of output efficiency to specify a higher operating point.

The magnet chosen for the first prototype was Feroba III; its demagnetisation characteristics are given in Figure 6.2 (line Fe). Its operating point (point 'a') was chosen to be slightly higher than that at $(BH)_{\max}$ to provide a higher flux density at the expense of longer magnets. The magnet chosen for Motors 2 and 3 was Supermagloy B2, a polymer-bonded rare-earth cobalt material manufactured by Preformations Ltd. Its demagnetisation characteristics and physical properties are given in Figure 6.2 and Figure 6.3 respectively. (Note that the properties of other rare-earth materials are also included in the figures for comparison.) Both Motors 2 and 3 use the same magnetic circuit design, and the operating point (point 'b') is specified at $(BH)_{\max}$. The details of the magnetic circuits are given below:

Motor 1 Magnetic Circuit Data

rotor type	: double-sided
material	: Feroba III (ferrite)
flux density B_m	: 0.21 T
magnetising force H_m	: 95 kAm^{-1}
magnet thickness $l_m/2$: 7 mm

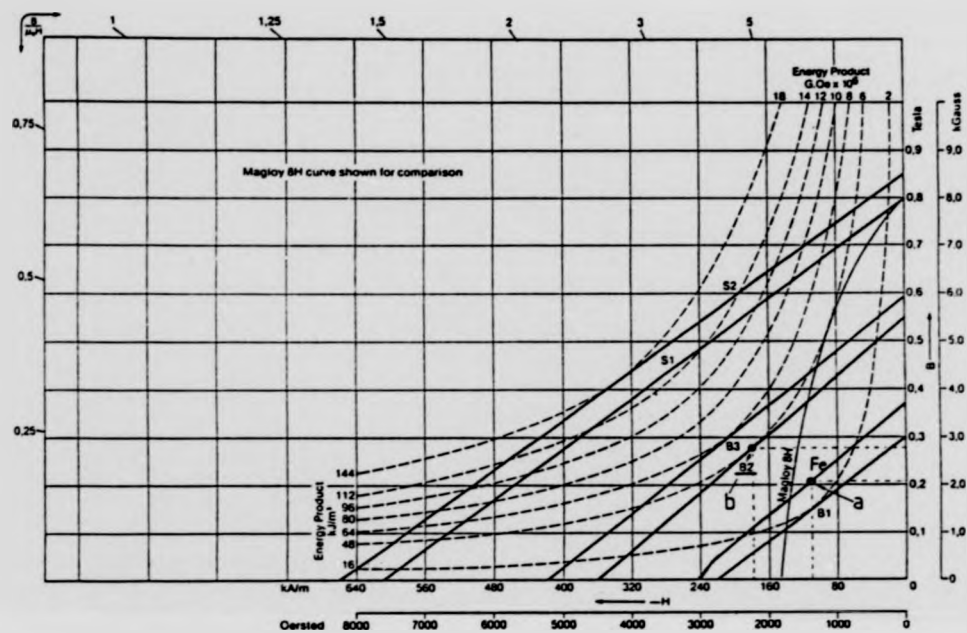


Figure 6.2 Demagnetisation characteristics of Peroba III and Supermagloy B2

MINIMUM MAGNETIC PERFORMANCE DATA

MATERIAL	ENERGY PRODUCT		REMANENCE		COERCIVE FORCE		INTRINSIC COERCIVE FORCE		A - Austenitic F - Ferritic
	BH _{max}		B _r		H _c		J _{Hc}		
	kJ/m ³	G.Oe x 10 ⁶	Tesla	Gauss	kA/m	Oersted	kA/m	Oersted	
Supermagloy B1	16	2	0.30	3000	220	2750	480	6000	F
Supermagloy B2	48	6	0.55	5500	380	4500	720	9000	A
Supermagloy B3	64	8	0.58	5900	420	5250	800	10000	A

Physical Properties

- Density 5.1 g/cm³
- Machinability: Good

MATERIAL	ENERGY PRODUCT		REMANENCE		COERCIVE FORCE		INTRINSIC COERCIVE FORCE	
	BH _{max}		B _r		H _c		J _{Hc}	
	kJ/m ³	G.Oe x 10 ⁶	Tesla	Gauss	kA/m	Oersted	kA/m	Oersted
Supermagloy S1	120	15	0.80	8000	610	7650	1200	15000
Supermagloy S2	145	18	0.85	8500	660	8250	1440	18000

Physical Properties

- Density 8.3 g/cm³
- Hardness: Rockwell C 50
- Machinability: Grinding only, Brittle

Figure 6.3 Properties of Supermagloies

air-gap length l_g	: 5.6 mm
loss factor LF	: 1.2
reduction factor C_r	: 0.88
thickness of flux return ring t_m	: 2.5 mm
pole-arc/pole-pitch ratio α	: 0.75

Motors 2 and 3 Magnetic Circuit Data

rotor type	: double-sided
material	: Supermagloy B2 (polymer SmCo_5)
flux density B_m	: 0.275 T
magnetising force H_m	: 180 kAm^{-1}
magnet thickness $l_m/2$: 4.1 mm
air-gap length l_g	: 5.6 mm
loss factor LF	: 1.2
reduction factor C_r	: 0.88
thickness of flux return ring t_m	: 2.5 mm
pole-arc/pole-pitch ratio α	: 0.9

6.3 Electric Circuit Design

A disc-armature winding is constructed by nesting together individually formed coils (Figure 6.4) to give equally spaced coil-strips, which are placed in such a way so that they lie approximately in the radial direction of the machine, as shown in Figure 6.5. These strips are the active lengths of the armature and are equivalent to the slotted conductors of a conventional machine. However, it should be noted that the term 'slot' has no significant meaning here. In order to minimise the harmonic elimination effects caused by the spacial distribution of the winding, the coils are fully-pitched and are non-skewed.

All the prototypes use the same armature design; they have the same number of coils, and the coils are connected in an identical manner. Forty-eight coils are

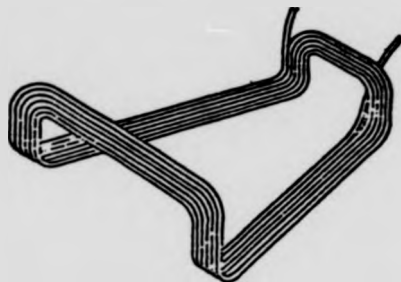
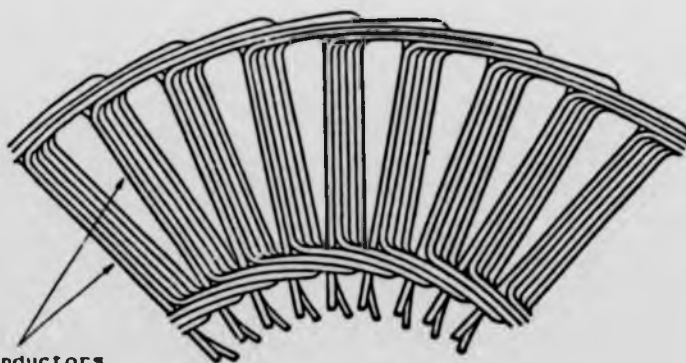


Figure 6.4 A preformed wire-wound coil



strips of active conductors

Figure 6.5 Arrangement of the armature coils (taken from reference (17))

used in each armature to construct a double-layered winding. Each pair of adjacent coils are connected in series to give 24 pairs of coils which are known as phase bands. A phase winding is completed by linking together in series phase bands that are separated by one pole-pitch, with adjacent poles connected in opposition. Figure 6.6 gives the winding diagram of the three-phase armatures.

Having laid down the arrangement for the coils, the next stage in the electric circuit design is to calculate the total number of turns required per phase T_{ph} , so that the number of turns per coil g can be determined. As the emf waveform of a brushless disc-motor is trapezoidal, it is the peak phase voltage which needs to be considered, and the peak phase voltage is induced by the influence of the peak flux distribution on its phase winding. Letting V_p , B_p and w be the peak phase voltage, the peak flux density and the angular frequency respectively. Then T_{ph} is given as

$$V_p = T_{ph} \frac{d\theta}{dt} = T_{ph} (\omega r_2^2 - r_1^2) B_p w \quad \dots (6.1)$$

$$T_{ph} = \frac{V_p}{(\omega r_2^2 - r_1^2) B_p w} \quad \dots (6.1)$$

And the number of turns per coil g is

$$g = \frac{T_{ph}}{p L q} \quad \dots (6.2)$$

where p = number of pole pairs, L = number of coil layers, and q = number of coils/pole/phase.

Having determined the winding data, the induced emf waveforms of the armatures are plotted by Equation (2.30) to confirm the design. The calculated waveforms are shown in Figure 6.7; and the design data of the armatures are given below:

Motor 1 Electric Circuit Data

method of drive

: uni-polar/bi-polar

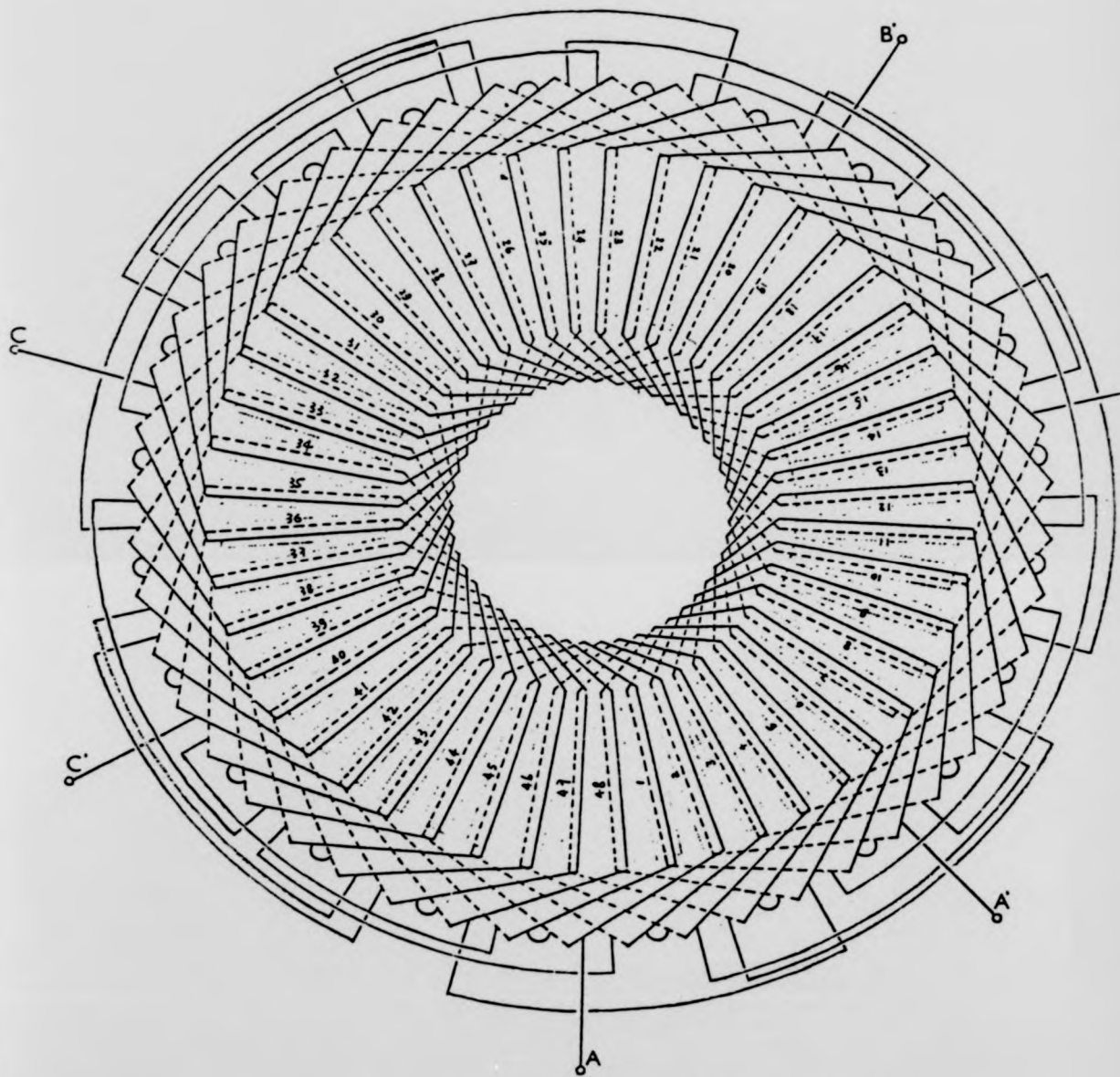
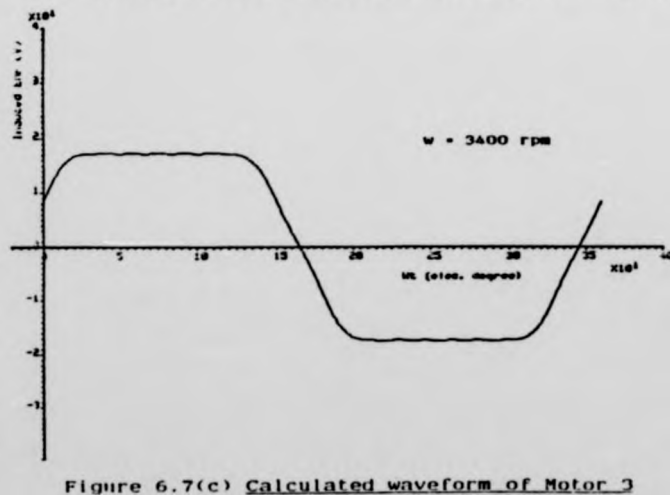
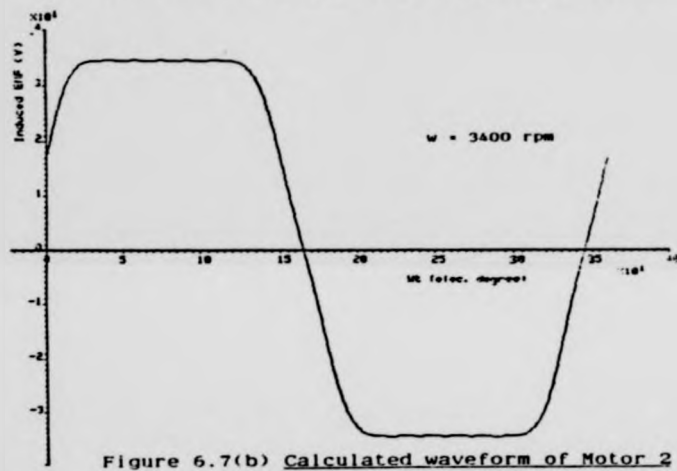
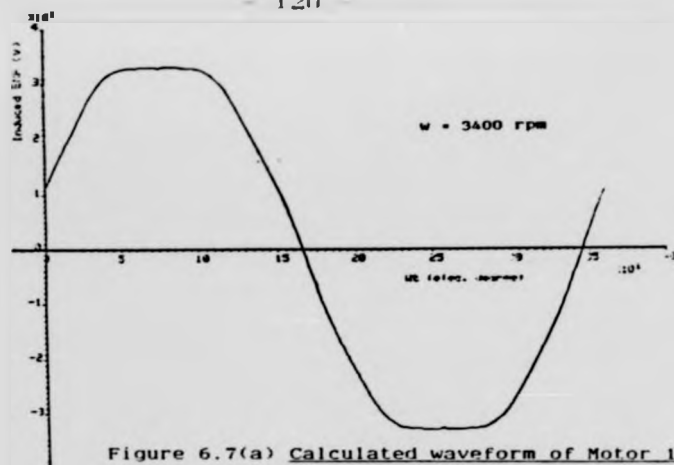


Figure 6.6 Winding diagram of the 3-phase disc windings



winding type : 3-phase distributed
 pitch factor K_{en} : 1
 skew factor K_{sn} : 1
 number of slots S : 48
 number of coils/pole/phase q : 2
 number of turns/coil g : 5
 number of layers L : 2
 number of turns/phase T_{ph} : 80
 voltage coefficient K_v : 0.0955 Vs/rad (per phase)
 current density : 7 A/mm²
 wire gauge d_c : 1.2 mm
 space factor SF : 0.72

Motor 2 Electric Circuit Data

method of drive : uni-polar/bi-polar
 winding type : 3-phase distributed
 pitch factor K_{en} : 1
 skew factor K_{sn} : 1
 number of slots S : 48
 number of coils/pole/phase q : 2
 number of turns/coil g : 4
 number of layers L : 2
 number of turns/phase T_{ph} : 64
 voltage coefficient K_v : 0.0955 Vs/rad (per phase)
 current density : 7 A/mm²
 wire gauge d_c : 1.2 mm
 space factor SF : 0.70

Motor 3 Electric Circuit Data

method of drive : star-connected bi-polar
 winding type : 3-phase distributed
 pitch factor K_{en} : 1

skew factor K_{sn}	:	1
number of slots S	:	48
number of coils/pole/phase q	:	2
number of turns/coil g	:	2
number of layers L	:	2
number of turns/phase T_{ph}	:	32
voltage coefficient K_v	:	0.0477 Vs/rad (per phase)
current density	:	7 A/mm ²
wire gauge d_c	:	1.8 mm
space factor SF	:	0.52

6.4 Mechanical Design

The prototype motors all have a similar mechanical design which consists of three main parts: a double-sided rotor, where the magnet segments on both sides are sited face to face; a disc-shaped armature, which is sandwiched between the two rotor halves; and a casing. The dimensions of Motors 1 and 2 are identical, while Motor 3 has a larger casing to accommodate the bigger armature. The mechanical drawings for Motors 1 and 2 are found in University of Warwick Drawing no. ES2/507. Drawings for Motor 3 are found in Drawing no. ES2/551. The general assembly and a list of parts for Motors 1 and 2 are given in Figure 6.7 and Table 6.2 respectively. Motor 3 has a similar general assembly, and is therefore not shown here.

The rotor assembly is designed in such a way that the air-gap length is adjustable (approximately by 6mm in 0.5 mm increments). This permits some fine adjustments of the air-gap flux density to take place. The magnets are bonded to the mild steel flux return ring by Loctite 317 Adhesive, catalysed by the Loctite NF Activator. Experiments showed that these fixing agents are able to provide on grease free bondings, a minimum tensile shearing strength of 1800kNm^{-2} at room temperature. The calculated centrifugal shearing stress

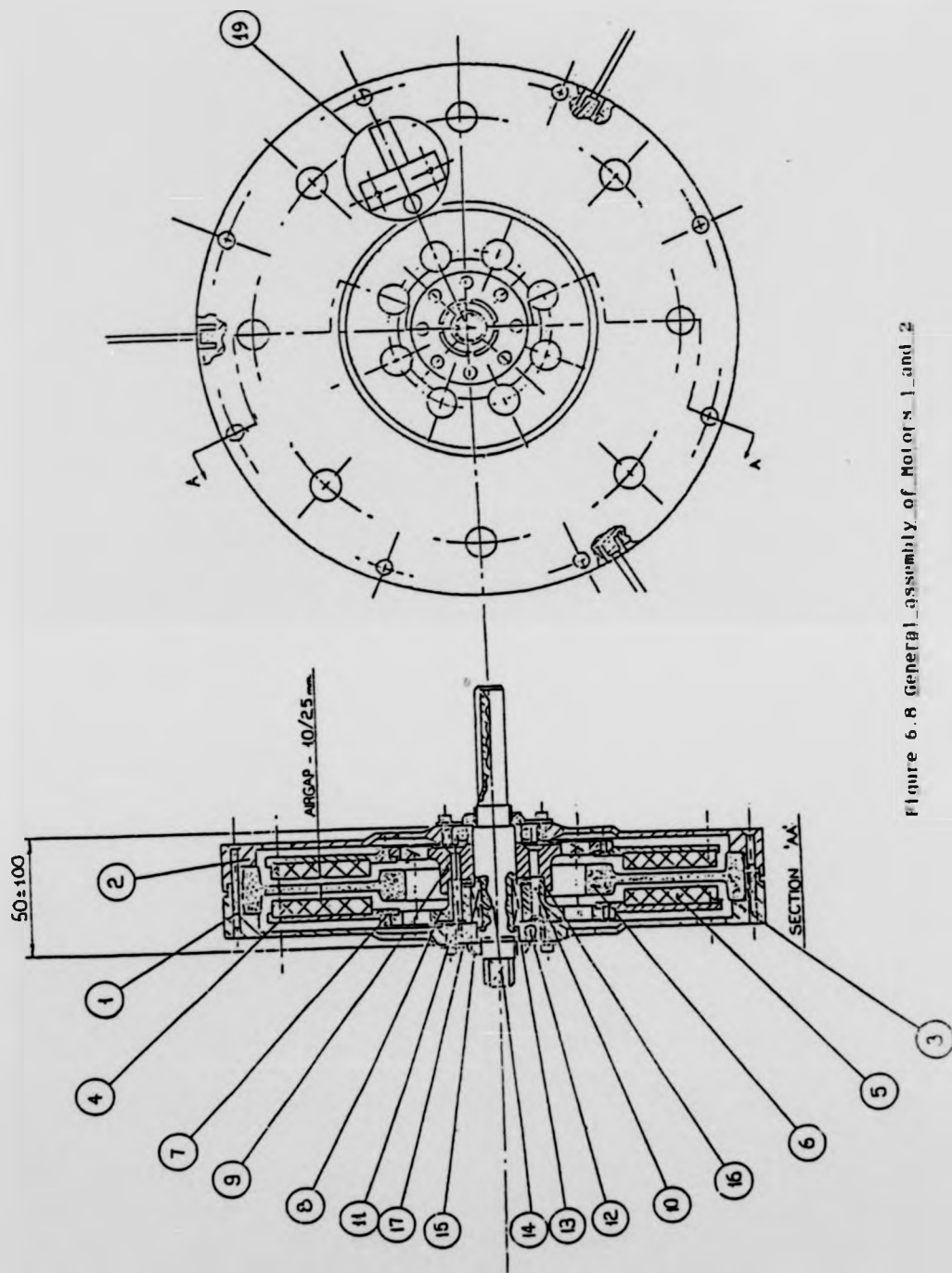



Figure 6.8 General assembly of Motors 1 and 2

	1	SENSOR UNIT, COMPRISING:		
	2	+1 MTG. BLOCK M2 NUTS & WASHERS	ALUM.	--
	2	M2x15mm LG. SET SCREWS	--	--
	1	5/16"-24 UNF LOCKNUT	M.S.	BOUGHT OUT
	5	S13223 SKANNERS	--	--
19	1	S3010-3 SKANNER	--	5/16"-24 UNF
17	2	DUST COVER	M.S.	(EN2)
16	AR	ROTOR COVER	SHIM STEEL	--
15	2	SPINDEL KEY	SHIM STEEL	--
14	1	MAIN SPINDLE	M.S.	--
13	2	BEARING LOCKNUT	SKP LOCKNUT KM2	
12	2	BEARING	SFK BEARING 16003	
11	16	CAP HD SOCKET SCREW	--	M3x8
10	4	CSK. HD SOCKET SCREW	--	M4x25
9	1	ROTOR CENTRE-RH	ALUM.	--
8	1	ROTOR CENTRE-LH	ALUM.	--
7	16	CSK. HD SOCKET SCREW	--	M3x6
6	1	ARMATURE	POLYURETHANE VARNISH	
5	16	MAGNET	POLYMER-BONDED SmCo5	
4	2	FLUX RETURN RING	M.S.	--
3	1	CASING-LH	ALUM.	--
2	1	CASING-RH	ALUM.	--
1	8	CSK. HD SOCKET SCREW	--	M3x25
ITEM	No.OFF	DESCRIPTION	MATERIAL	REMARKS



UNIVERSITY OF WARWICK

Table 6.2 List of parts for Motors 1 and 2

		MJ11015	MJ11016	
collector-base voltage (open emitter)	V_{CBO} max.	-120	120	V
collector-emitter voltage (open base)	V_{CEO} max.	-120	120	V
collector current (peak value)	I_{CM} max.	30	30	A
total power dissipation (up to $T_{mb} = 25^{\circ}C$)	P_{tot} max.		200	W
Junction temperature	T_j		150	$^{\circ}C$
dc current gain:				
$I_c = 2A; V_{CE} = 5V$	h_{FE} typ.		3000	
$I_c = 2A; V_{CE} = 5V$	h_{FE}		1000	
cut off frequency	f_{hfe} typ.		4	KHz

* mounting-base temperature

Table 6.3 Electrical characteristics of MJ11015 and MJ11016

exerting on the magnet/mild steel bondings of Motor 1, at 3000 rpm, is only 150kNm^{-2} . The shearing strength is therefore well over ten times the maximum shearing stress, and provides a very wide safety operating margin for Motor 1. Motors 2 and 3 both have lighter magnets, and therefore have a even wider safety operating margin. The picture of the rotor assemblies is given in Figure 6.9.

The armature winding is constructed from forty-eight individually formed coils. Each coil has one side longer than the other so that the coils can be nested neatly together to form a disc-shaped armature. The coils are then connected together electrically according to the wiring diagram shown in Figure 6.6. Mechanical strength and rigidity of the armature are provided by two alternative processes: by epoxy resin encapsulation, or by polyurethane varnish coating.

In the first process, the armature winding is first loaded into a mild steel injection mould. The mould is then preheated to 60°C followed by the injection of liquid epoxy resin. The mould is left in an oven at 100°C for 10hrs. Finally, the mould is removed from the oven and is allowed to cool in free air for an hour, and the armature is then lifted from the mould. Although this process requires specialised injection tools, it provides a high mechanical strength for the armature.

In the second process, the armature is first taped with heat-curing impregnated glass tape, and is then dipped into a polyurethane varnish bath for several minutes. The armature is put inside a mould, and the whole assembly is then put into an electric oven at 150°C for 8hrs. After the mould is allowed to cool down in free air, the armature is then removed. This process has the advantages of being very simple, and does not require specialised tools. However, it does not provide the same mechanical strength as the first process.

For the purpose of comparing the mechanical strength and rigidity provided by each process, it was decided to use the encapsulation process for Motor 1's armature and the coating process for Motor 2's. It was found from the

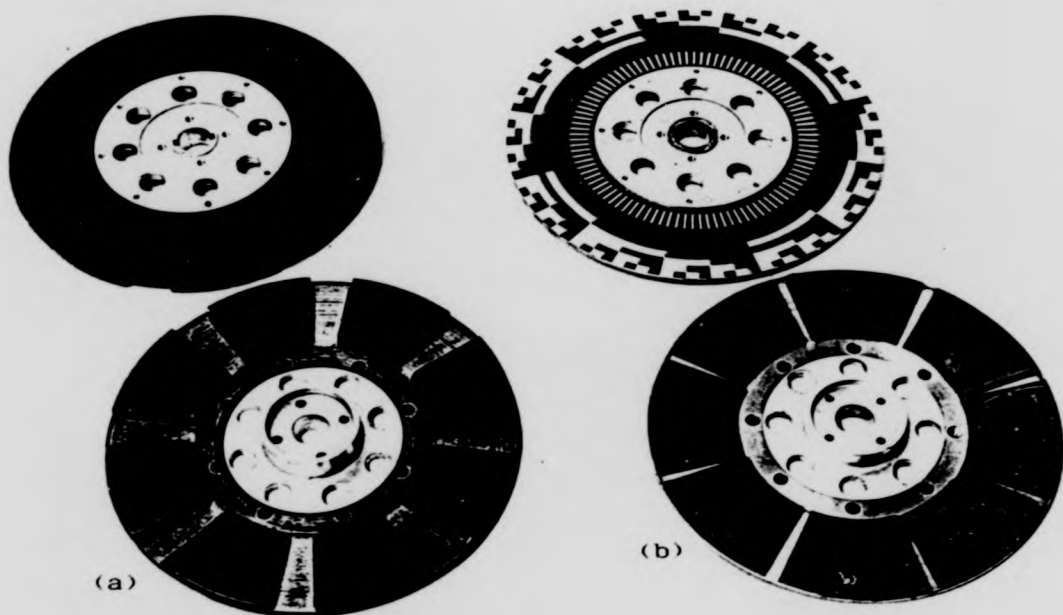


Figure 6.9 Rotor assemblies of (a) Motor 1, and (b) Motors 2 and 3

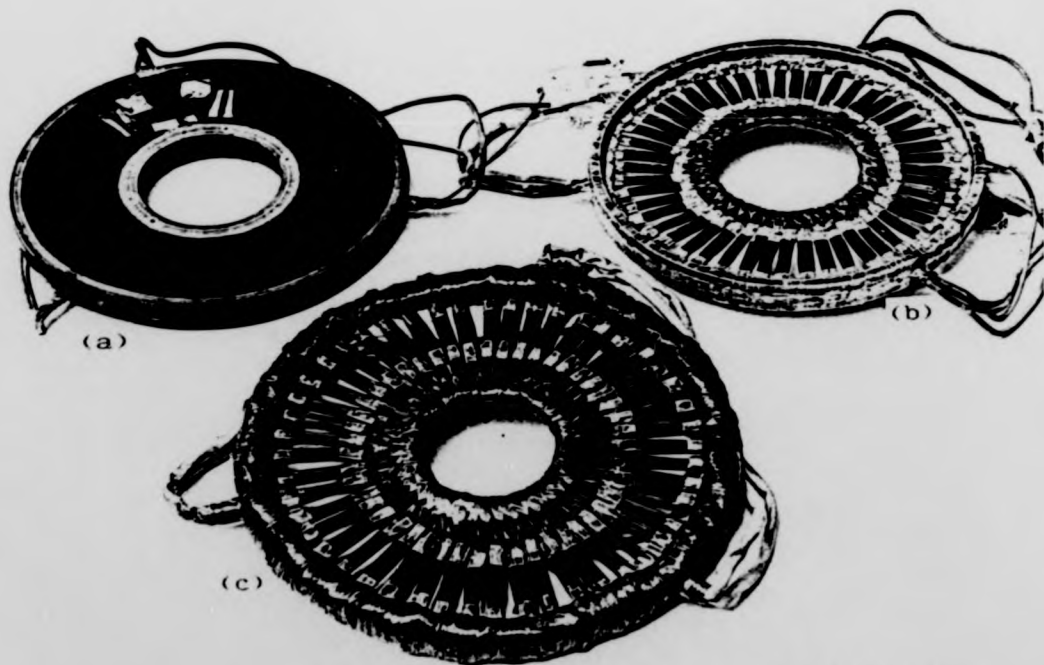


Figure 6.10 Armatures of (a) Motor 1, (b) Motor 2, and (c) Motor 3

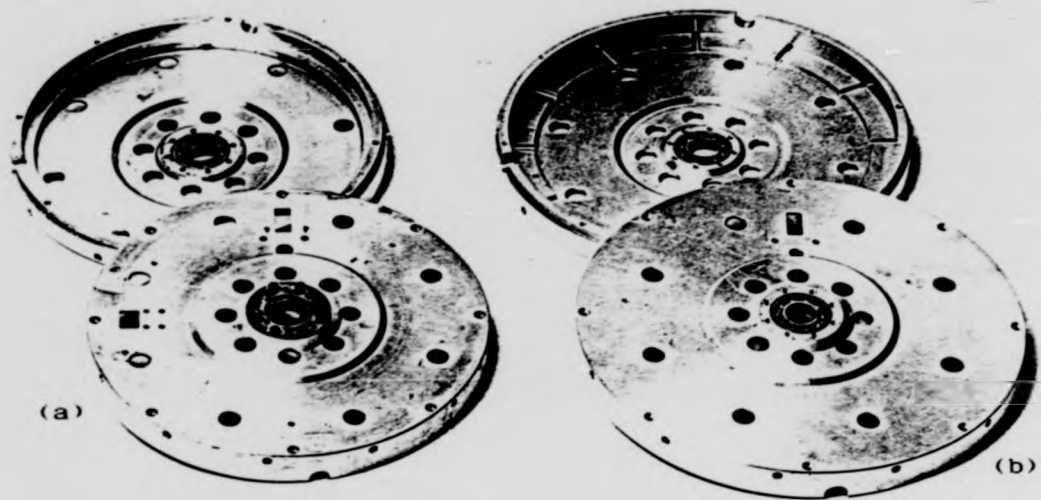


Figure 6.11 Casings of (a) Motors 1 and 2, and (b) Motor 3

encapsulation process that it is essential to match the thermal expansion coefficient of the copper with that of the epoxy resin; as otherwise, cracking and rumpling of the armature may have resulted. The coating process proved to be simple and straight forward, and the mechanical strength was more than adequate for a non-rotating armature. This same process was therefore used to make Motor 3's armature. Figure 6.10 shows the three armatures in their finished form.

Aluminum casings were made to hold the armatures firmly between the two rotor halves and to enclose the mechanical assembly; Figure 6.11 gives the picture of the casings.

6.5 Motor Parameters

Having designed and built the motors, the next stage was to measure the motors' parameters. From the induced voltage oscillograms of Figure 6.12, it can be seen that Motors 2 and 3, both having α equal to 0.9, produced a better trapezoidal waveform than Motor 1 whose α is 0.75. Also, the shapes of the measured waveforms were very close to those of the calculated waveforms shown in Figure 6.7. The open circuit peak phase voltage characteristics were also measured, and are shown in Figure 6.13. The open circuit characteristics were in general very close to the designed values. (The higher output voltage of Motor 1 is due to the fact that the magnets used were slightly longer than the designed length.)

The winding resistances of the armatures were obtained by applying a dc current to a winding, and by measuring the voltage drop across it. The results are shown in Figure 6.14. The winding self-inductances were measured by using the method given in Appendix D. The measurements were taken at different rotor orientations, and these results are shown in Figure 6.15.

It can be seen that the winding inductance of a motor is largely independent of its rotor orientation, which confirms the assumption that the poles have no

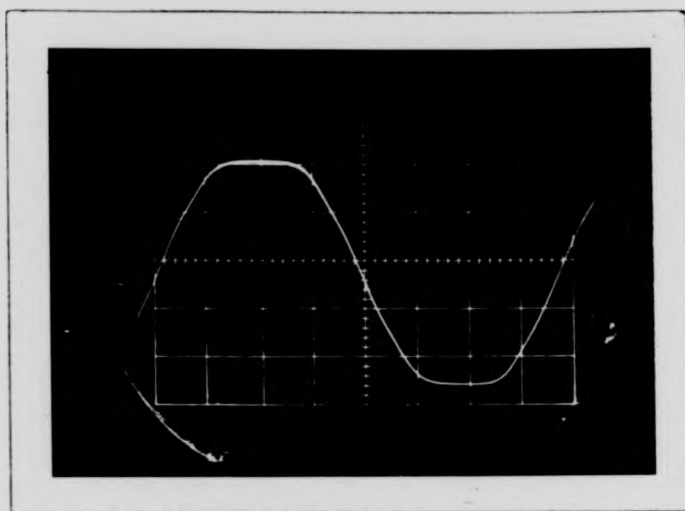


Figure 6.12(a) Phase emf waveform of Motor 1, speed = 3000rpm,
voltage = 66.7V peak to peak
horizontal scale = 0.66 ms/div

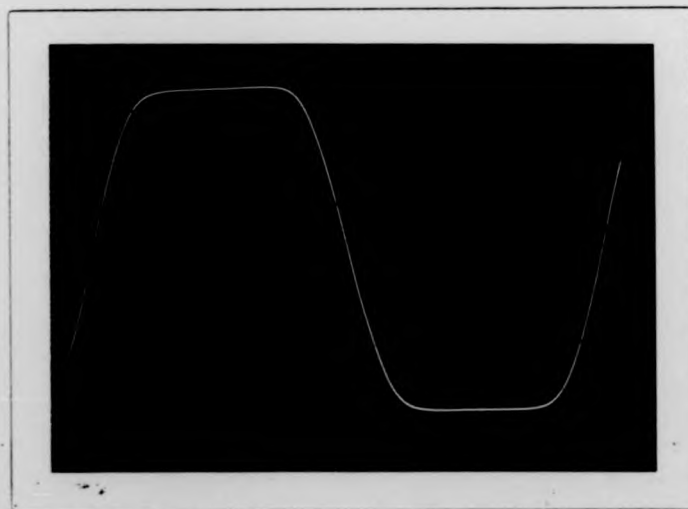


Figure 6.12(b) Phase emf waveform of:
Motor 2, speed = 3000rpm, voltage = 61.2V peak to peak
Motor 3, speed = 3000rpm, voltage = 30.4V peak to peak
horizontal scale = 0.66 ms/cm

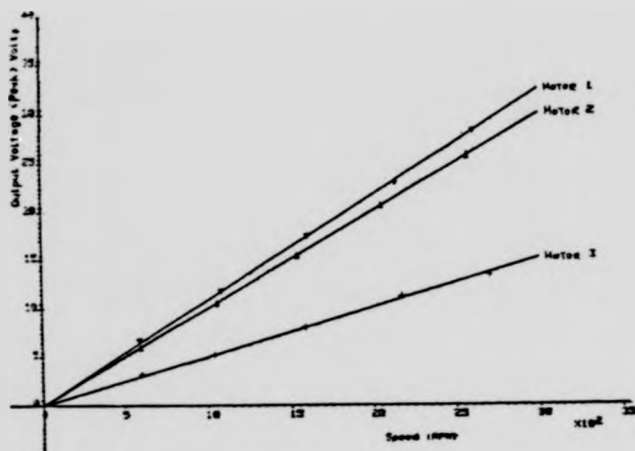


Figure 6.13 Open circuit characteristics

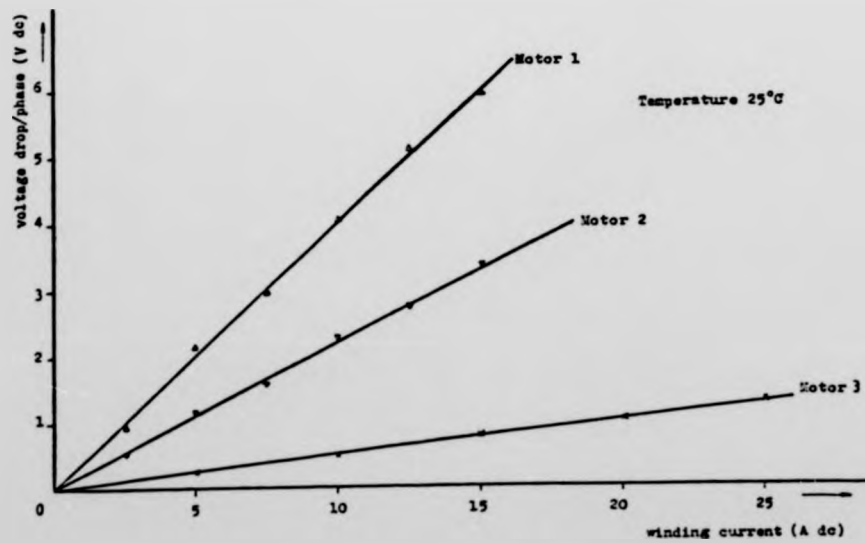


Figure 6.14 Measurements of winding resistances

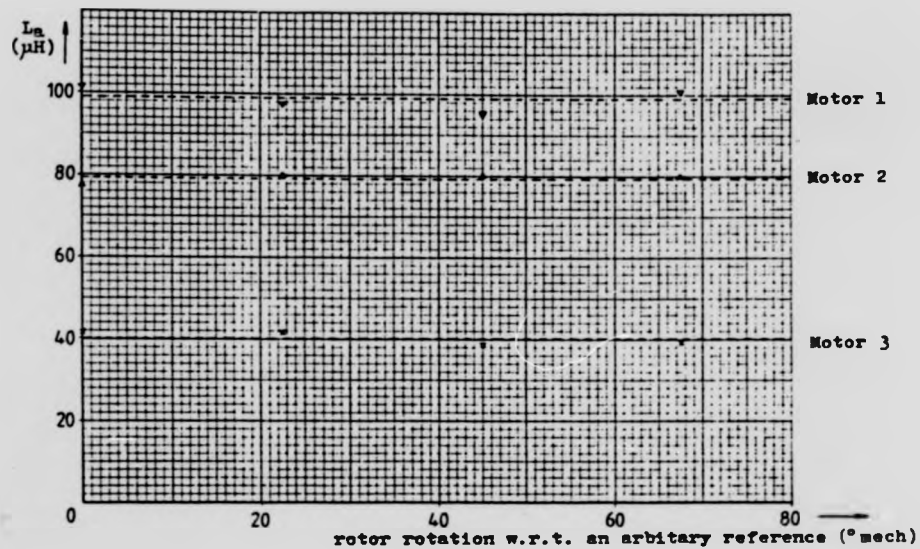


Figure 6.15 Measured phase inductance at different rotor orientations

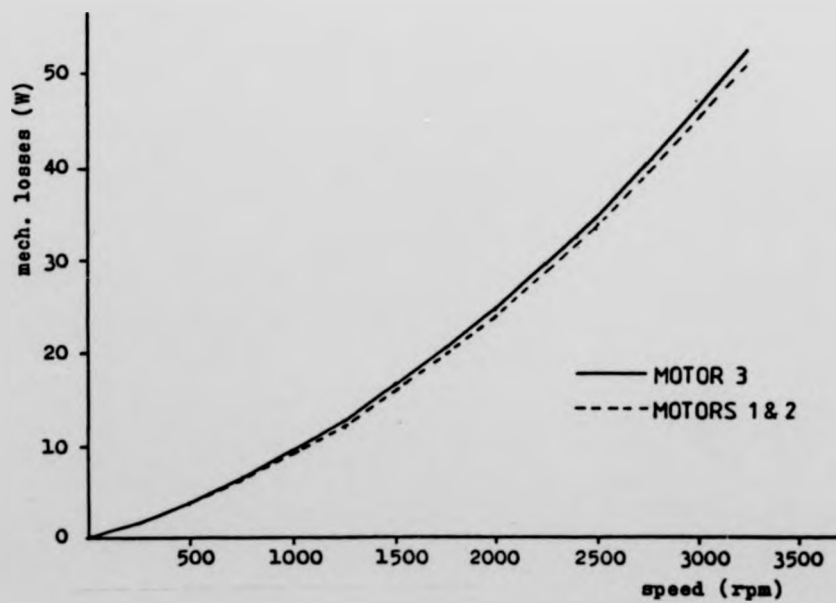


Figure 6.16 Dynamic loss characteristics

saliency and that it can be taken as a cylindrical pole machine. To obtain the mutual inductances, an ac current (at mains frequency) was applied to one of the phase windings of the motor, and the voltages induced in the adjacent windings were measured. As the machines are treated as cylindrical poles, it was only necessary to carry out the measurements at an arbitrary rotor orientation. A summary of the electrical parameters is given below:

	<u>Motor 1</u>	<u>Motor 2</u>	<u>Motor 3</u>
voltage coefficient K_v (Vs/rad)	0.1062	0.0974	0.0484
armature resistance R_a (ohms)	0.398	0.221	0.049
phase self-inductance L_a (uH)	98.5	79.5	40.1
mutual inductance M (uH)	42.7	24.3	12.0

Finally, the dynamic losses were measured. These losses are contributed by three sources, they are bearing friction, windage, and eddy currents. The measured results are shown in Figure 6.16. The losses of Motors 1 and 2 are the same. The slightly higher losses of Motor 3 are due to a higher eddy current loss as a result of thicker armature conductors.

6.6 Rotor Position Detector

An accurate rotor position detection is essential for the effective operation of a brushless dc motor. For the prototypes, this is achieved by using a set of reflective optical sensors to scan a coded disc which is positioned on the uncommitted side of one of the flux return rings. This is illustrated in Figure 6.17.

The sensor assembly comprises five medium resolution Skan-A-Matic S13224 infra-red scanners and a high speed, high resolution Skan-A-Matic S3010-3 optic fibre scanner. The scanners are stacked together and are attached to the casing as shown in Figure 6.18.

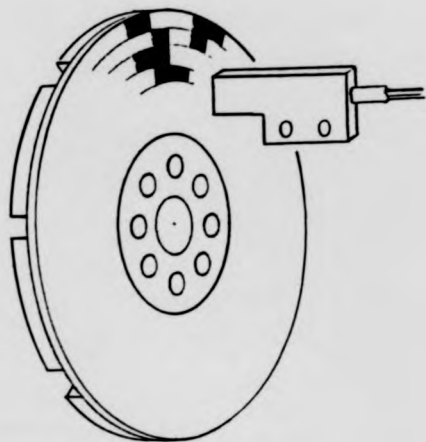


Figure 6.17 Principle of the rotor position detector

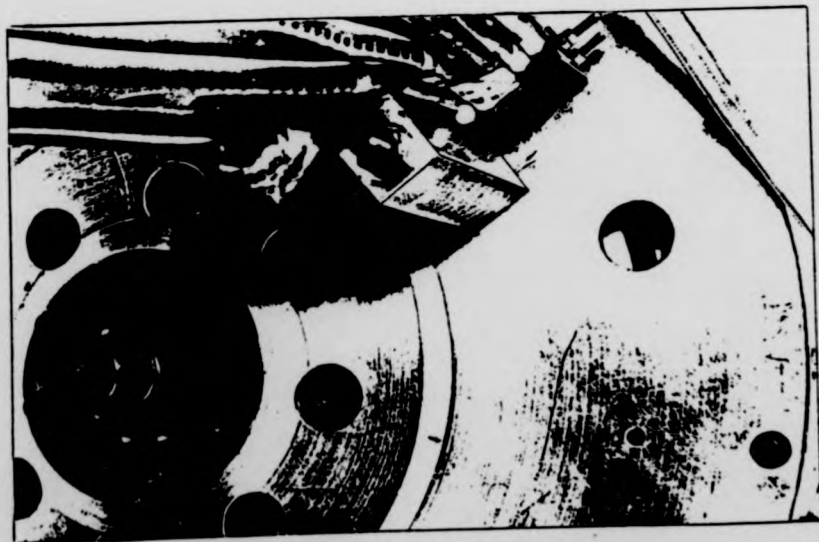


Figure 6.18 Physical arrangements of the rotor position detector

The coded disc is made of high contrast Kodak photographic paper and is encoded with five concentric tracks of black and white patterns. Each track is divided into four identical sectors, each of which represents 360° elec and is sub-divided into twenty-four rectangles. Each rectangle can be either black, or white, and represents logic level '0' or '1'. Five radially inline rectangles are combined to form a 5-bit binary number which is used to represent one of the possible 24 electrical rotor orientations. Thus, the 24 orientations divide the 360 electrical degrees equally, giving a resolution of 15° elec per orientation. The concentric tracks are scanned by the five infra-red scanners.

In order to implement an automatic commutation advancing scheme, a sixth track is added to the coded disc. This track has 96 equally spaced narrow white strips which are in line with the binary patterns in the radial directions as shown in Figure 6.19. As the rotor rotates, the optic fibre scanner scans over this track and a trigger signal is issued when a white strip is detected. This signal then triggers the microprocessor based controller to execute a software routine which reads in the 5-bit rotor position data, decodes it according to a look-up table and outputs the drive signals to the power switches. By changing the index pointer of the look-up table, the commutation sequence can be advanced. The trigger signal is also used to drive a timer module to provide the microprocessor with the rotor speed data. This data is, in turn, used by a software routine to set the value of the index pointer of the position look-up table for automatic commutation advancing. Details of the rotor position detector and the software routines are found in Chapter 8.

6.7 Operation of the Prototype Motors

6.7.1 Motor 1

Although Motor 1 was designed to be used as a brushless dc motor, its emf waveform makes it unsuited to being operated in such a brushless mode. The reason is that, taking the uni-polar mode as an example, in order for the

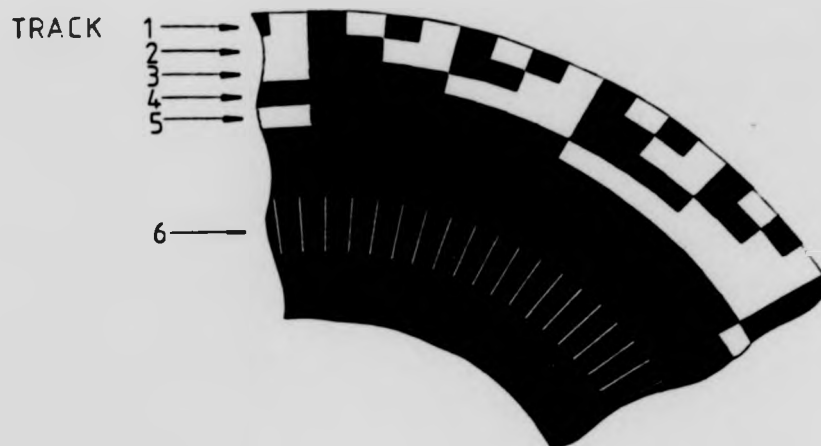


Figure 6.19 Segment of the rotor position coded disc

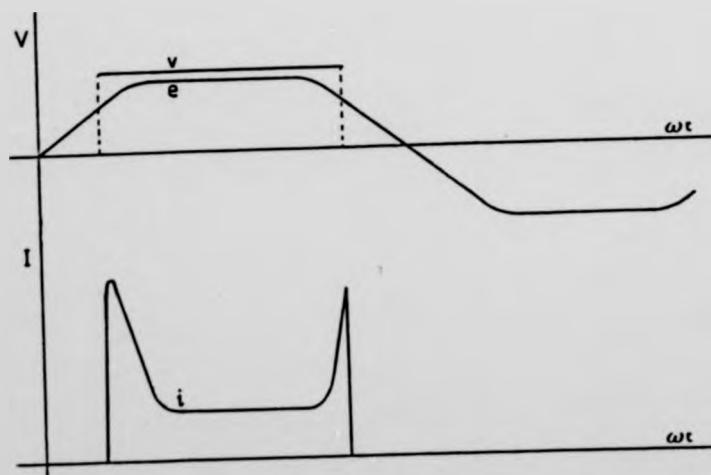


Figure 6.20 Effects of a 120° elec voltage pulse on the armature current of Motor 1

3-phase brushless motor to be self-started at any rotor orientations, the conduction angle of each phase winding must be at least 120°elec . But the constant voltage region of the phase emf is only 90°elec (per half-cycle). If an unmodulated dc voltage is applied to a phase winding for 120°elec , high current peaks will be produced, as is depicted in Figure 6.20. Furthermore, the low armature inductance of the disc motor does not provide any significant damping effect to the rising of the armature current, and at low rotor speed very high instantaneous current could be generated. The high current transients not only have a detrimental effect on the motor's efficiency, but also produce a severe overload to the power devices that could result in their destruction.

In the case of bi-polar mode, the minimum conduction angle can be reduced to 60°elec . But such conduction angle will give a very low winding utilisation, and it does not justify the expense of the extra power devices.

For these reasons Motor 1 will not be used as a brushless dc motor.

6.7.2 Motor 2

This motor has a constant voltage region close to 120°elec , which is ideal for brushless dc operation. The motor was tested in both the uni-polar mode and the bi-polar mode. The power devices used were Darlington transistors; the PNP Darlington were MJ11015s, and the NPN Darlington were MJ11016s. The transistors are manufactured by Motorola, and their specifications are given in Table 6.3.

6.7.2.1 Uni-polar mode

Uni-polar brushless dc motors have a poor winding utilisation, and this disc-armature version has a utilisation factor of only 0.33. But, on the other hand, the configuration of its power stage is very simple, and, consists of three NPN Darlington connected in the common emitter mode, as shown in Figure 6.21. The power device control signals are derived from the rotor position detector which was described in Section 6.6. The relationship in time between the induced phase

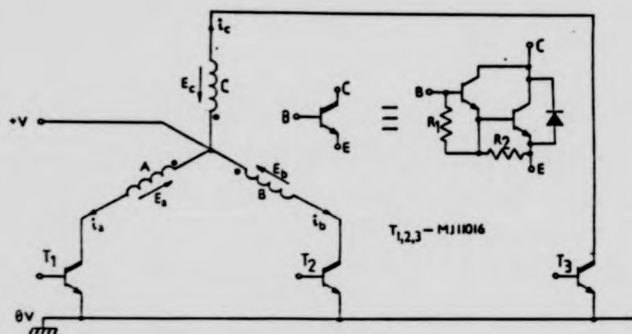


Figure 6.21 Drive configuration of Motor 2 in uni-polar mode

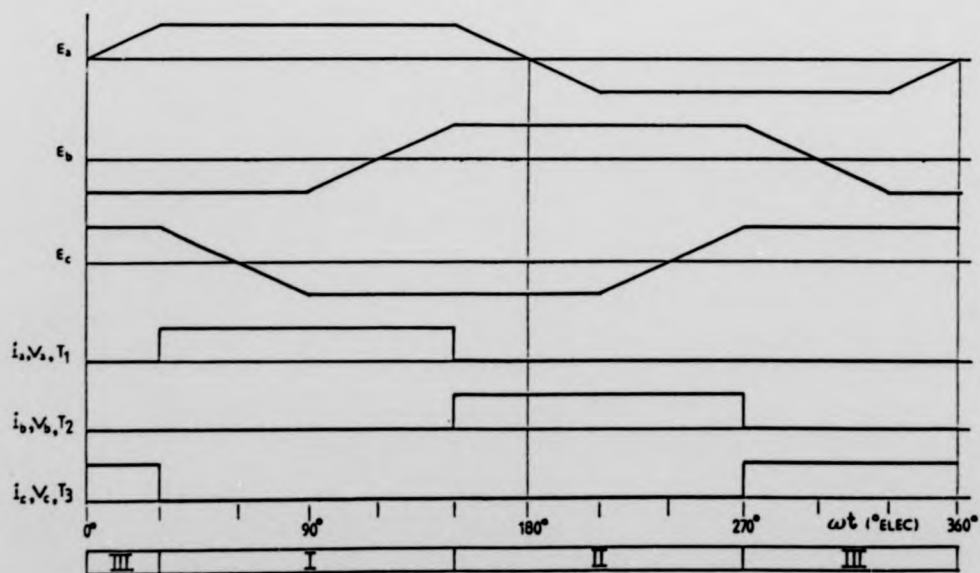


Figure 6.22 Relationship in time between the induced emfs, the phase currents, the applied voltages and the base drive signals of Motor 2 in uni-polar mode

emfs, the phase currents, the applied voltages and the base drive signals are illustrated in Figure 6.22.

The performance characteristics of this motor are shown in Figure 6.23, in which the curves marked x represent the motor's characteristics when commutation is advanced by 15° elec. Despite the low winding utilisation of this motor, its output efficiency of 74%, at rated output, compares very favourably to that of the existing dc disc-motor (Appendix C) of 65%. Figure 6.24 shows the oscillograms of the terminal phase voltage and the armature current. Because of the inertia of the rotating magnets, the output torque ripple is very low, as shown in Figure 6.25.

6.7.2.2 Bi-polar mode

In order to increase the winding utilisation of Motor 2, and thus its power density, bi-polar driving mode is used. In this configuration six power Darlington's are required; its circuit diagram is given in Figure 6.26. As the windings are connected in delta, the power devices must be rated to carry the current of two winding.

A combination of NPN and PNP Darlington's are used in the power circuit, this is to avoid the need for floating base drive signals, which would be required by T_1 , T_3 and T_5 if they were NPN transistors. The relationship in time between the base drive signals, the induced phase emfs and the applied voltages are given in Figure 6.27; the output characteristics of the motor are shown in Figure 6.28. It can be seen that the bi-polar motor's performance falls short of that of the uni-polar's in spite of the higher winding usage. A close examination of its phase current waveform (Figure 6.29) reveals that it contains a large percentage of negative torque-producing components. These current components circulate in the delta loop, and are generated by the mismatch between the waveform of the applied voltage and that of the induced emf. The circulating current reacts with the air-gap flux and produces torque which acts in an opposite direction to the rotation of the rotor, and reduces the output torque.

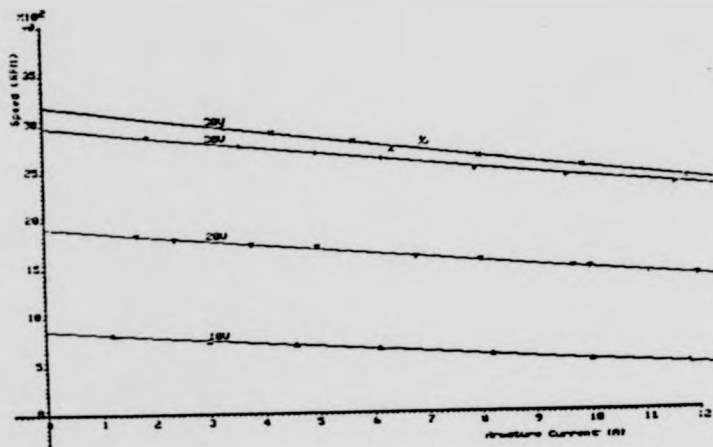


Figure 6.23(a) Speed characteristics of Motor 2 in uni-polar mode

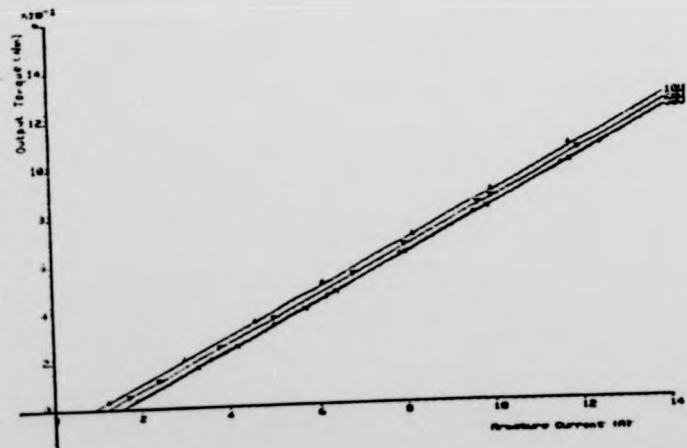


Figure 6.23(b) Output torque characteristics of Motor 2 in uni-polar mode

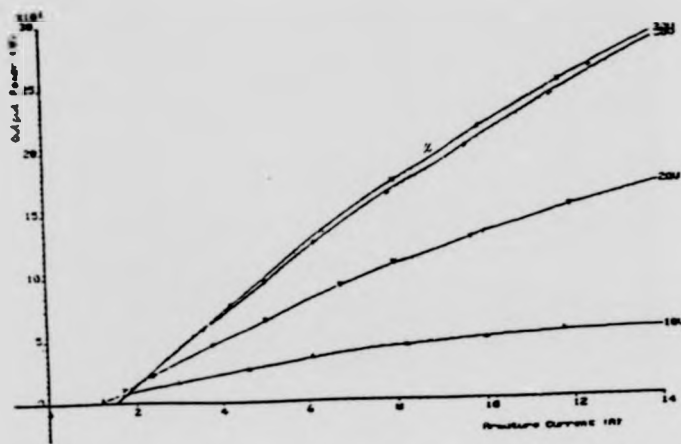


Figure 6.23(c) Output power characteristics of Motor 2 in uni-polar mode

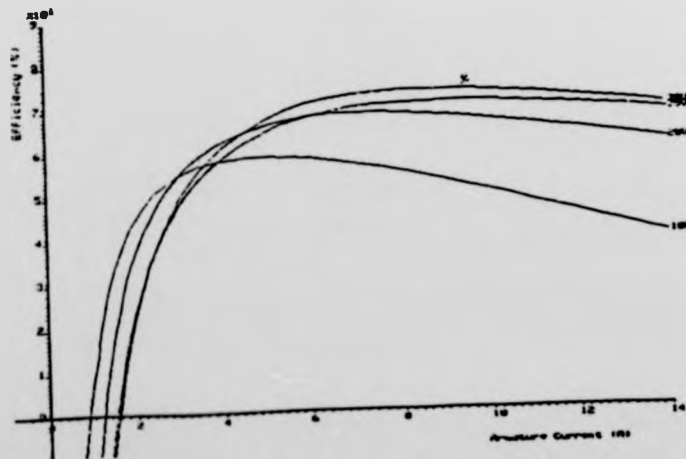


Figure 6.23(d) Efficiency characteristics of Motor 2 in uni-polar mode

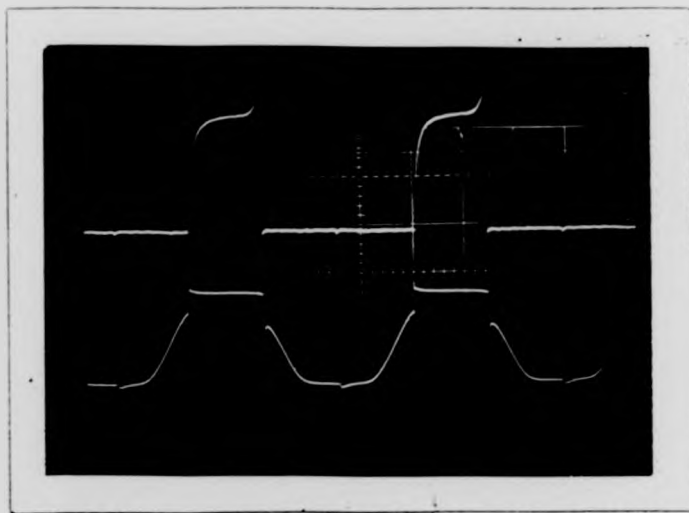


Figure 6.24(a) Current waveform (upper trace) and terminal phase voltage waveform (lower trace) of Motor 2 in uni-polar mode
Horizontal scale : 2msec/div
Vertical scale : upper trace 5.2A/div
lower trace 20V/div

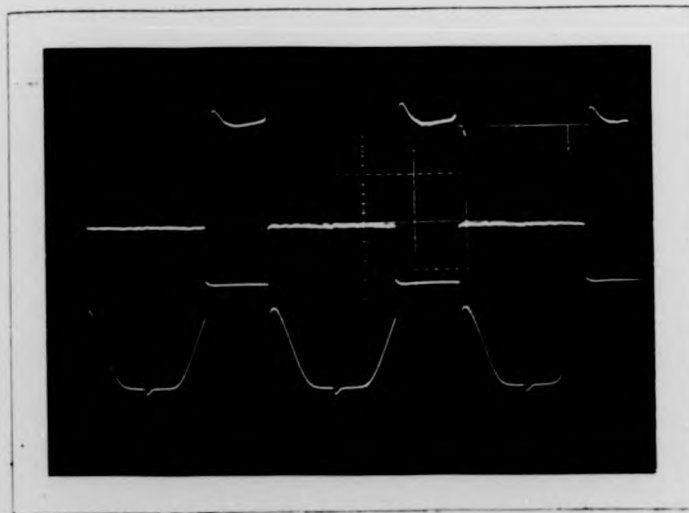


Figure 6.24(b) Current waveform (upper trace) and terminal phase voltage waveform (lower trace) of Motor 2 in uni-polar mode, with commutation advanced by 15°elec
Horizontal scale : 2msec/div
Vertical scale : upper trace 5.2A/div
lower trace 20V/div

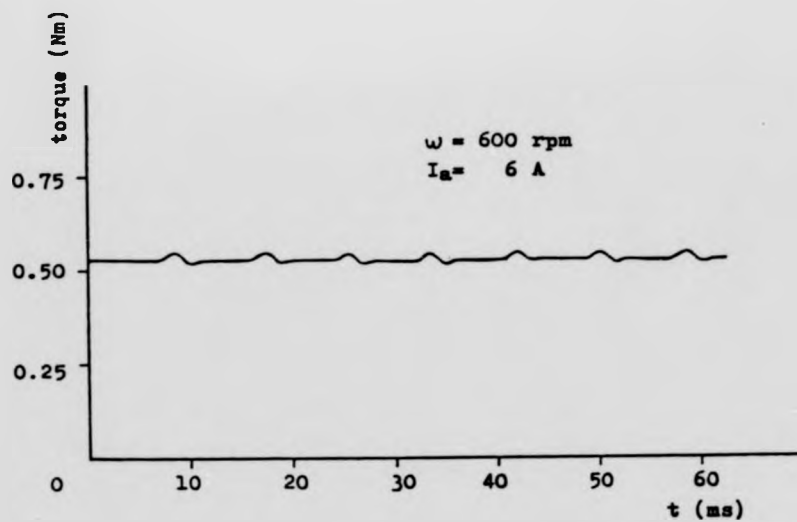


Figure 6.25 Output torque ripple of Motor 2 in uni-polar mode

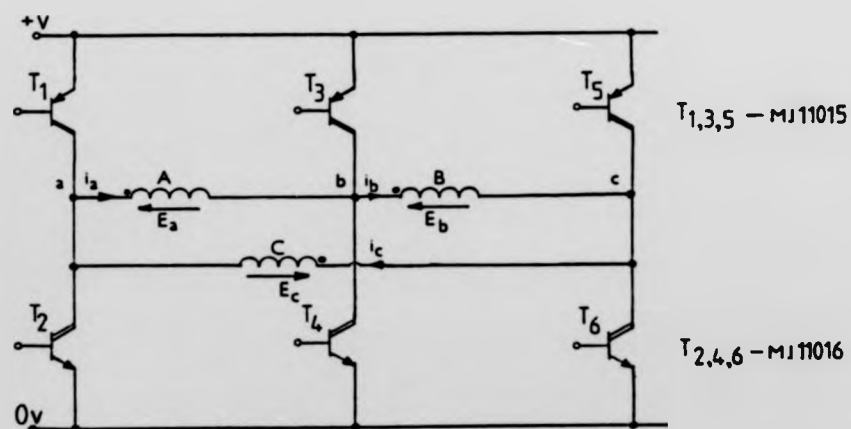


Figure 6.26 Drive configuration of Motor 2 in bi-polar mode

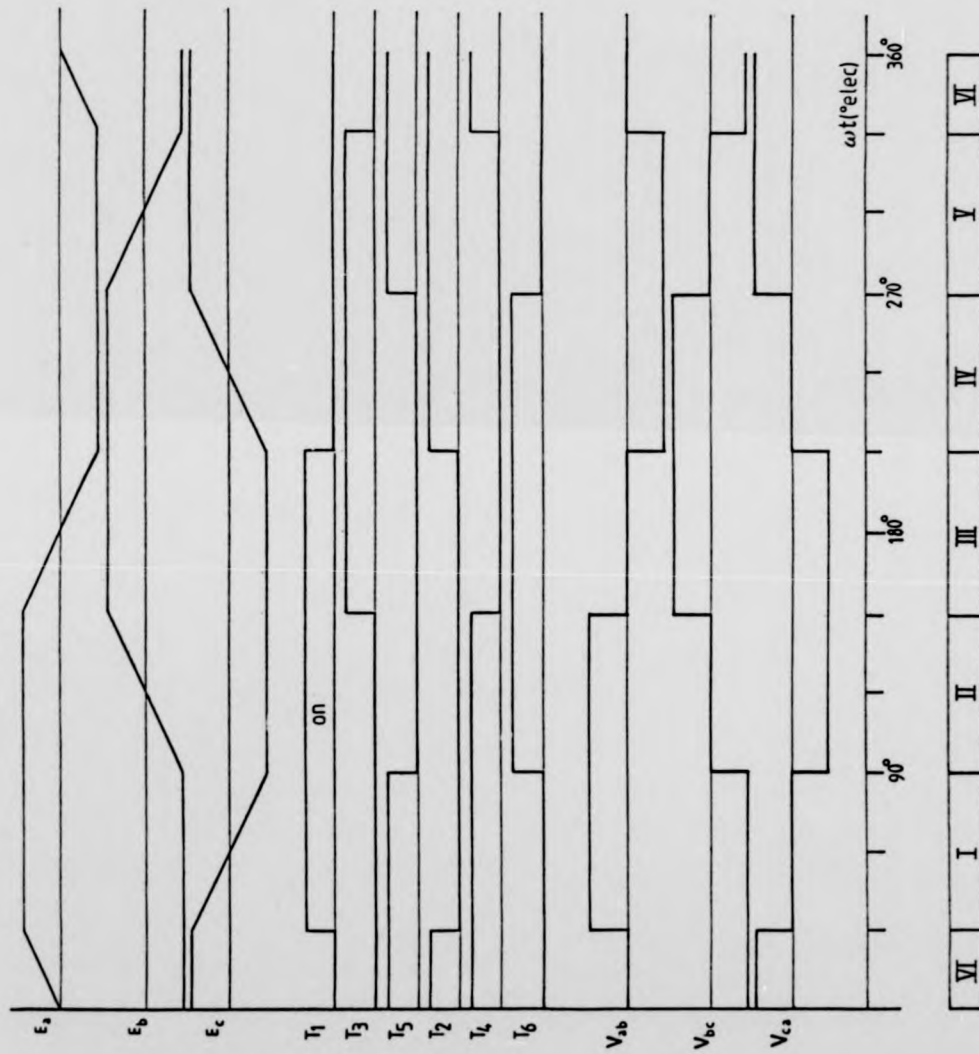


Figure 6.27 Relationship in time between the induced emfs, the applied voltages and the base drive signals of Motor 2 in bi polar mode

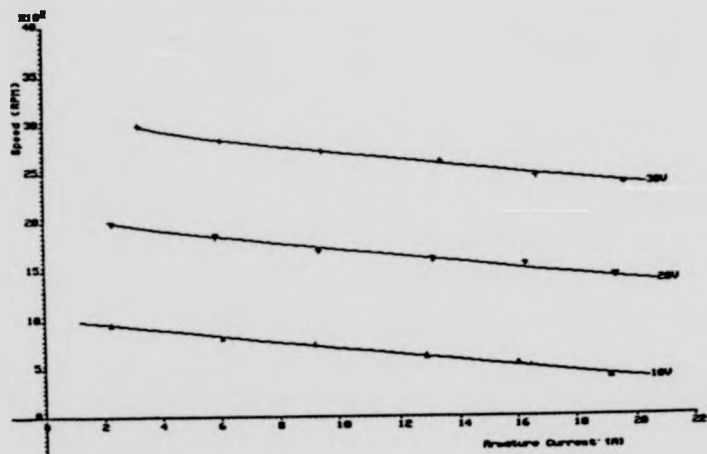


Figure 6.28(a) Speed characteristics of Motor 2 in bi-polar mode

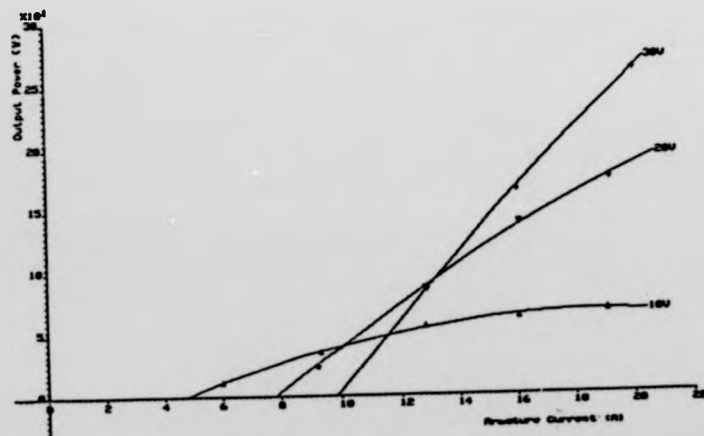


Figure 6.28(b) Output power characteristics of Motor 2 in bi-polar mode

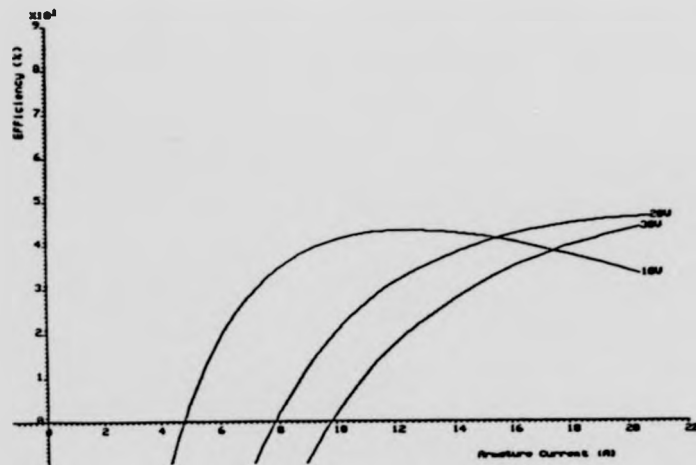


Figure 6.28(c) Efficiency characteristics of Motor 2 in bi-polar mode

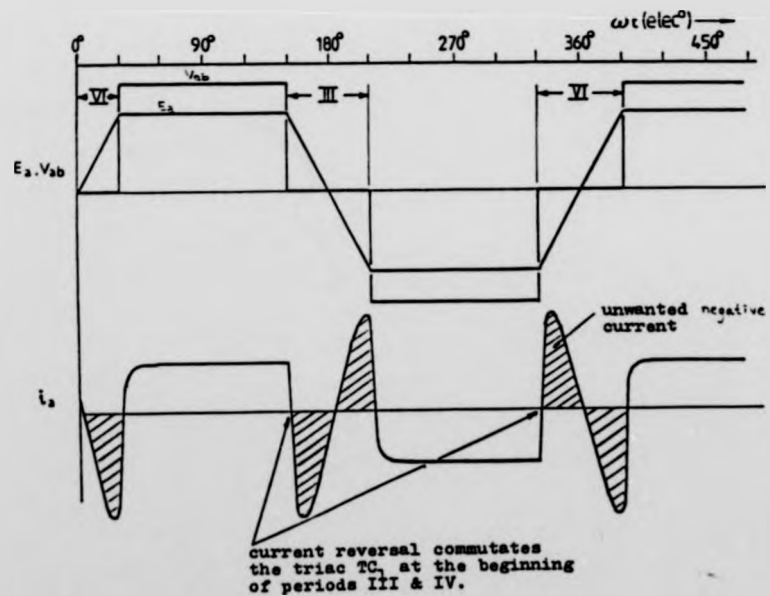


Figure 6.29 Phase current waveform of Motor 2 in bi-polar mode

To remove the unwanted circulating current, the delta loop must be interrupted. This can be done quite easily by separating the phase windings and by providing each winding with an independent power circuit, as shown in Figure 6.30. However, this arrangement requires twelve power transistors, and is therefore very expensive. An alternative arrangement is to insert three triacs in series with the delta loop, this is shown in Figure 6.31. The triacs are controlled by the firing circuit given in Figure 6.33. The gate firing signals are applied to the triacs during the constant voltage periods, and are removed during the commutation intervals when the phase voltages are changing from positive to negative, or vice versa. For example, TC_1 's gating signal is applied during periods I, II, IV and V, and is removed during periods III and VI. A triac is commutated by the reversal of phase current at the beginning of a commutation interval, as depicted in Figure 6.29. In order to ensure that the high commutating dv/dt , which is produced by the fast switching of the transistors, does not induce any commutation failure, high speed triacs and snubber circuit are employed.

The oscillograms of the terminal phase voltage and armature current are shown in Figure 6.34, and it can be seen that the negative torque-producing current components are completely eliminated. Figure 6.35 shows the output characteristics of the improved bi-polar arrangement.

6.7.3 Motor 3

Although the improved bi-polar delta configuration of Motor 2 gives a very good output characteristic, i.e. an efficiency of 82% at rated output, its power circuit is very complicated. In order to maintain a usage of the windings and at the same time avoiding the use of complicated power circuit, star bi-polar connection can be used. But, in doing so a new armature is needed.

The design of a star connected armature is different from that of a delta connected one in two respects. Firstly, the magnitude of the induced phase emf

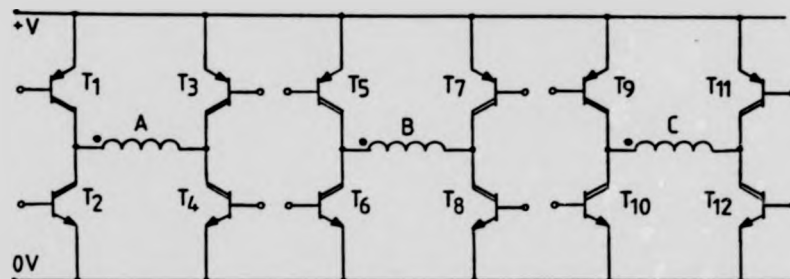


Figure 6.30 Arrangements of separate power circuit for each winding

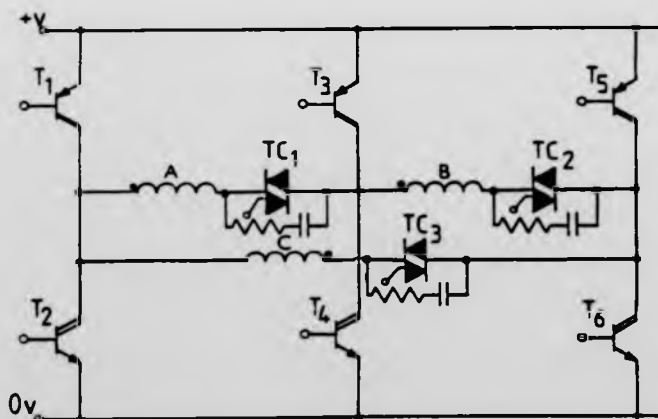


Figure 6.31 Arrangements of Motor 2 in bi-polar mode with triacs inserted in series to interrupt the delta loop

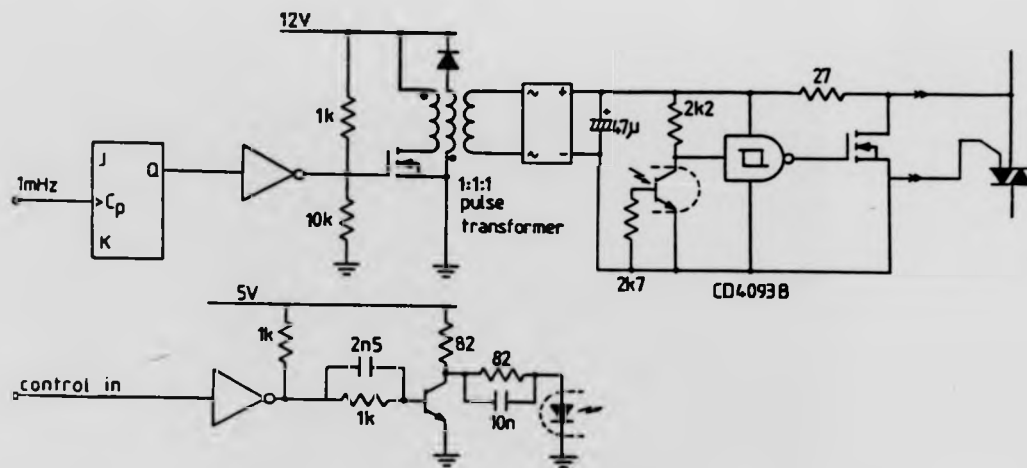


Figure 6.32 Schematic of the triac triggering circuit

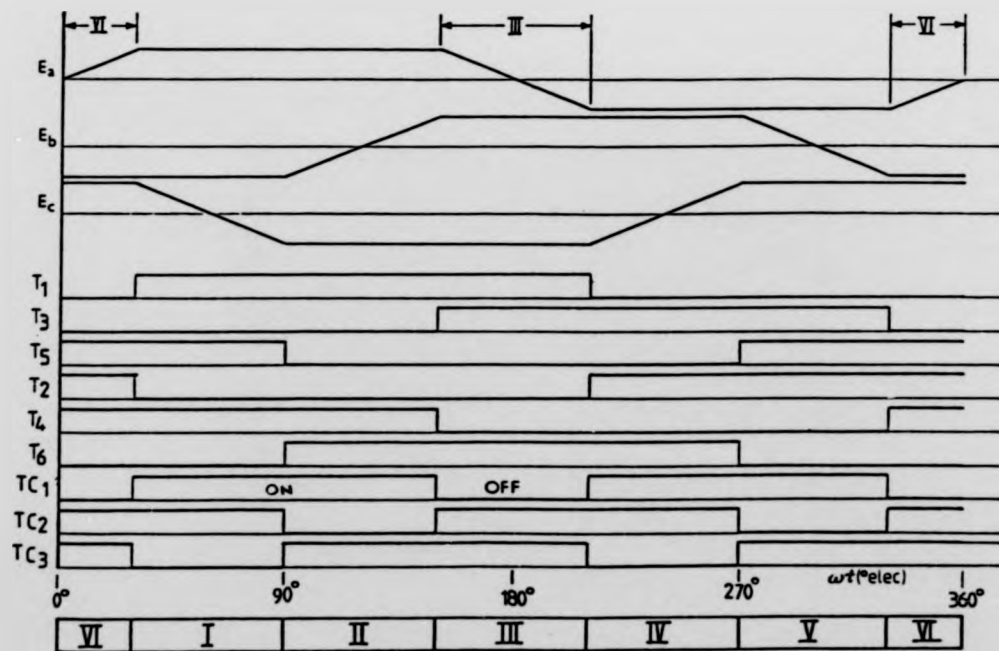


Figure 6.33 Relationship in time between the phase emfs, the base drive signals, and the triac triggering signals

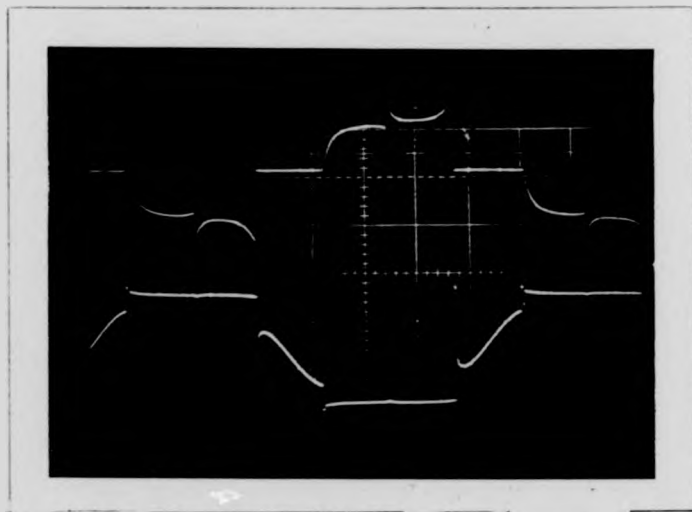


Figure 6.34(a) Current waveform (upper trace) and terminal phase voltage waveform (lower trace) of Motor 2 in bi-polar mode
Horizontal scale : 1msec/div
Vertical scale : upper trace 9.1A/div
lower trace 20V/div

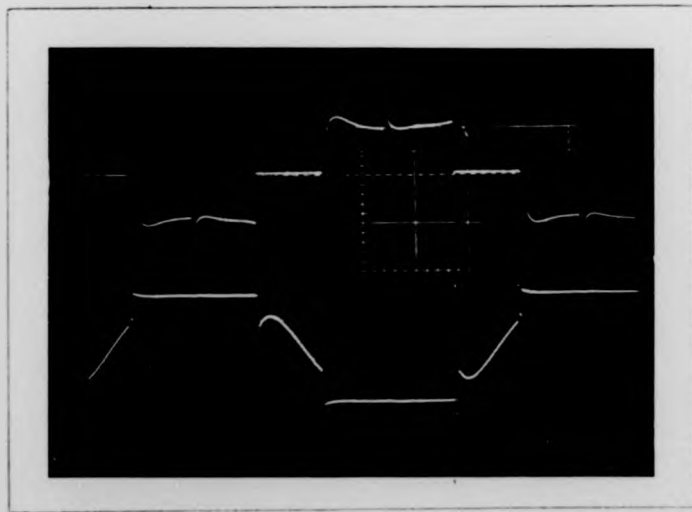


Figure 6.34(b) Current waveform (upper trace) and terminal phase voltage waveform (lower trace) of Motor 2 in bi-polar mode, with commutation advanced by 15°elec
Horizontal scale : 1msec/div
Vertical scale : upper trace 9.1A/div
lower trace 20V/div

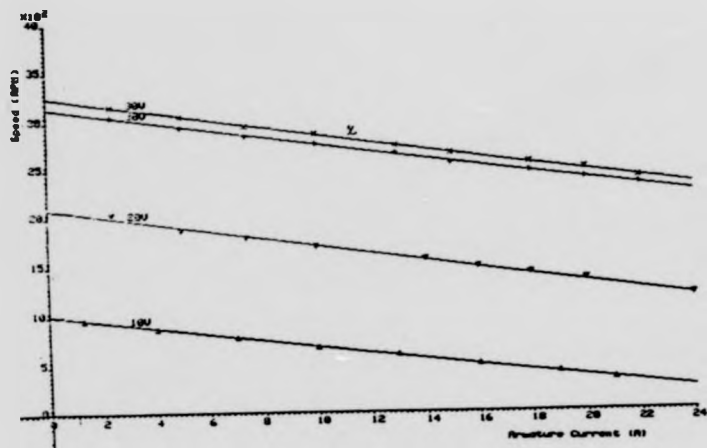


Figure 6.35(a) Speed characteristics of Motor 2 in bi-polar mode

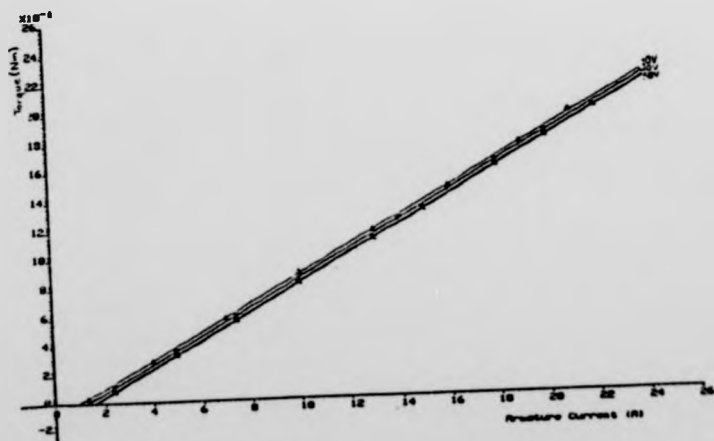


Figure 6.35(b) output torque characteristics of Motor 2 in bi-polar mode

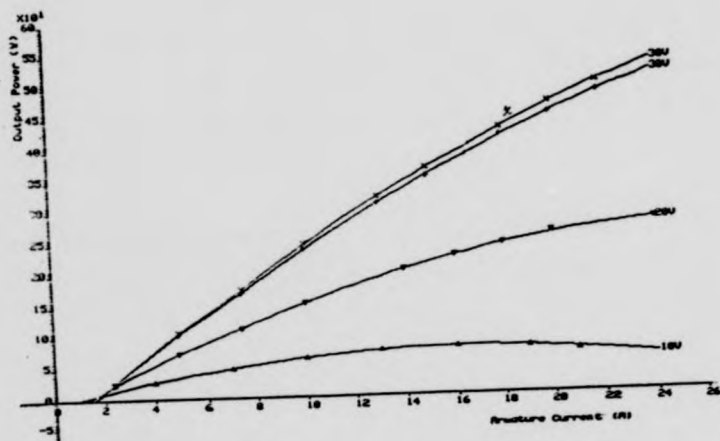


Figure 6.35(c) Output power characteristics of Motor 2 in bi-polar mode

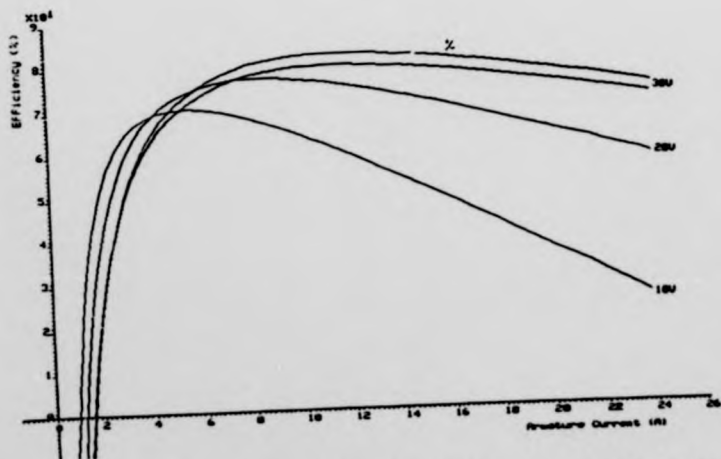


Figure 6.35(d) Efficiency characteristics of Motor 2 in bi-polar mode

are halved, as two phase windings are connected in series. Secondly, the wire gauge is increased, as the phase current is doubled. The armature of Motor 3 is designed specifically for star connection in that it has half the number of turns as in Motor 2, and the wire gauge is increased to 1.8mm which is 2.25 times the cross-section of that of Motor 2.

The configuration of the power circuit and the timing diagram of this motor are shown in Figures 6.36 and 6.37 respectively. The conduction-state diagram is already given in Figure 4.8; and the oscillograms of the line current and the terminal phase voltage are given in Figure 6.38. The dips in the middle of the current pulses are caused by the rapid inductive discharge of the current in the coil undergoing commutation via the free wheeling diodes. The test results of the motor's output characteristics are shown in Figure 6.39. It can be seen that the test results agree very well with the computed characteristics given in Figure 4.18.

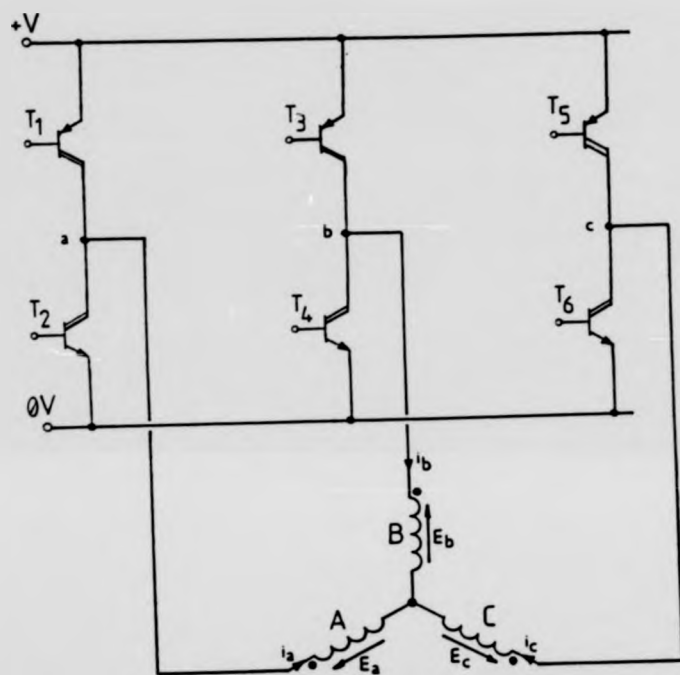


Figure 6.36 Arrangement of Motor 3 in star-connected bi-polar mode

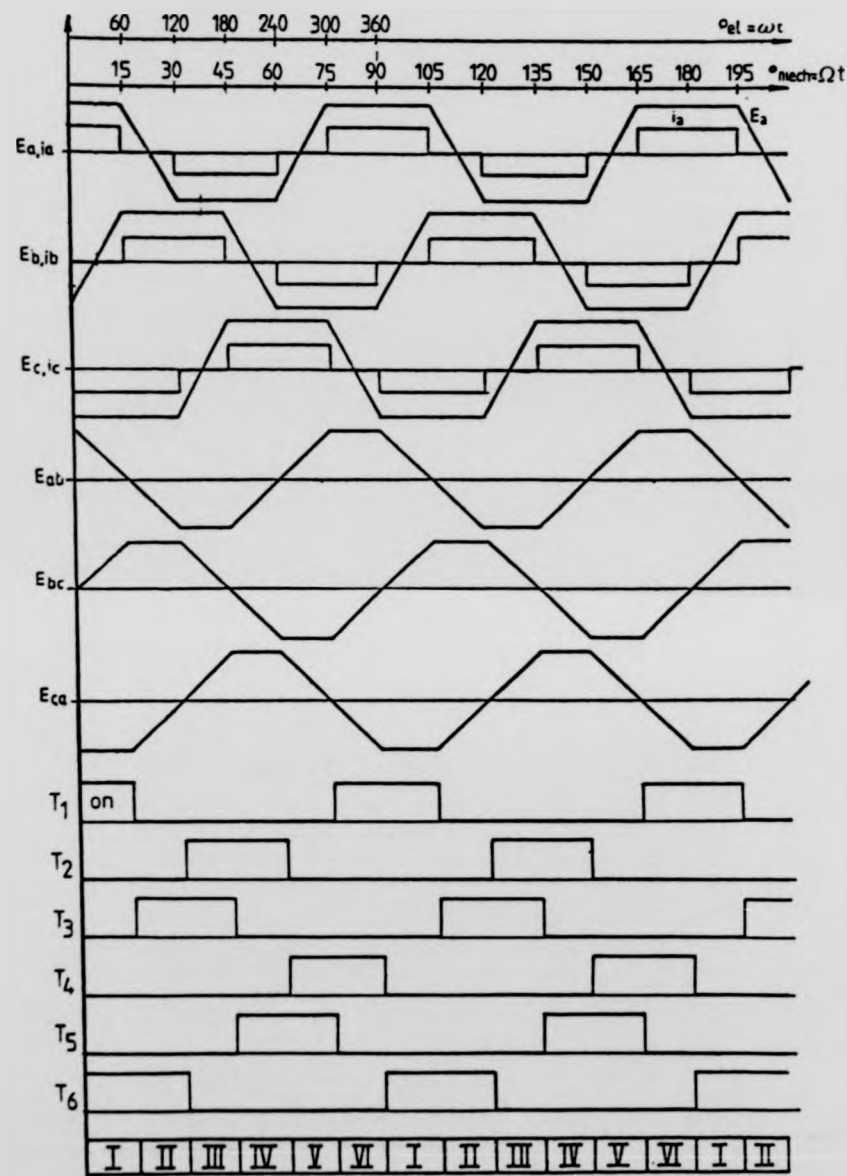


Figure 6.37 Relationship in time between the phase emfs, the phase current, the line emfs, and the base drive signals of Motor 3 in star-connected bi-polar mode

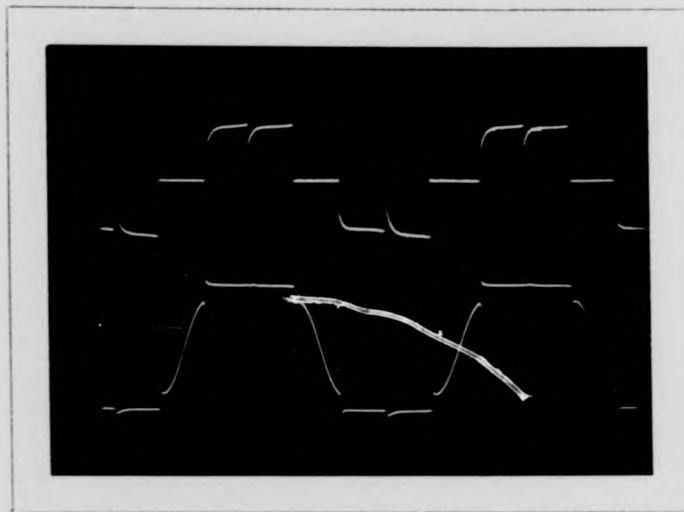


Figure 6.38(a) Current waveform (upper trace) and terminal phase voltage waveform (lower trace) of Motor 3 in star-connected bi-polar mode
Horizontal scale : 1.4msec/div
Vertical scale : upper trace 20A/div
lower trace 20V/div

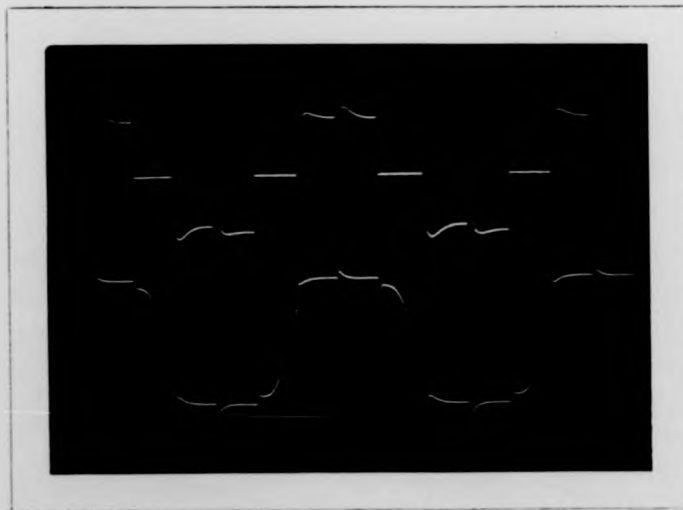


Figure 6.38(b) Current waveform (upper trace) and terminal phase voltage waveform (lower trace) of Motor 3 in star-connected bi-polar mode, with commutation advance by 15 elec
Horizontal scale : 1.4msec/div
Vertical scale : upper trace 20A/div
lower trace 20V/div

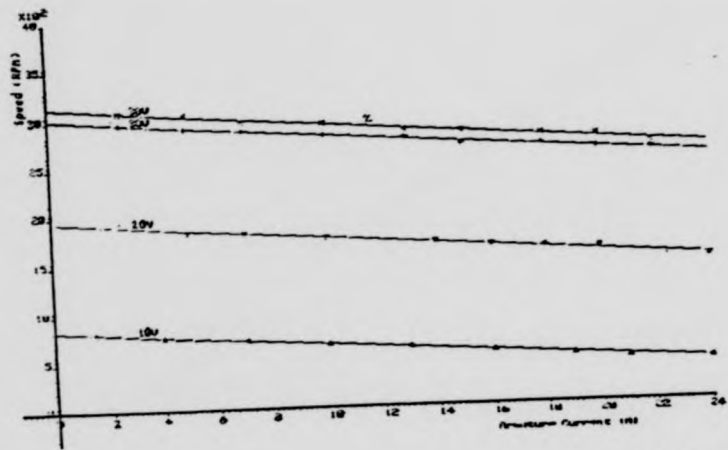


Figure 6.39(a) Speed characteristics of Motor 3 in star-connected bi-polar mode

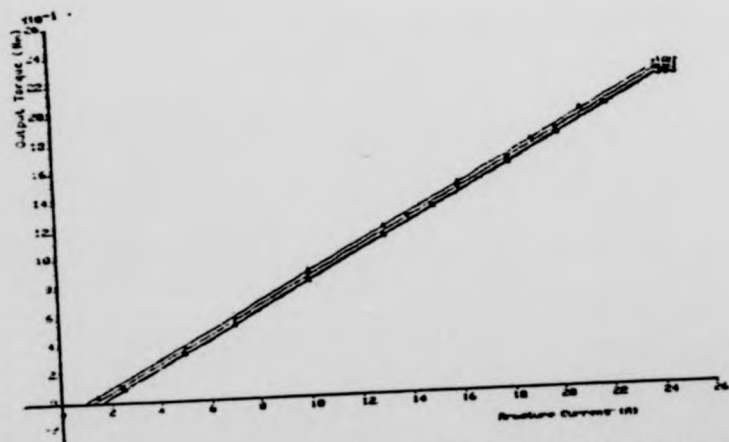


Figure 6.39(b) Output torque characteristics of Motor 3 in star-connected bi-polar mode

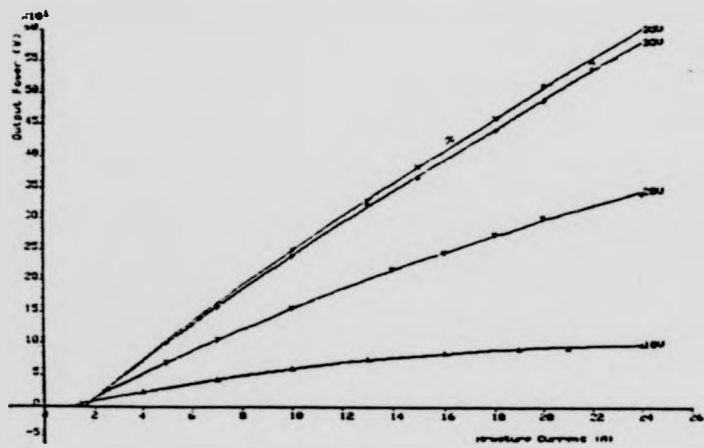


Figure 6.39(c) Output power characteristics of Motor 3 in star-connected bi-polar mode

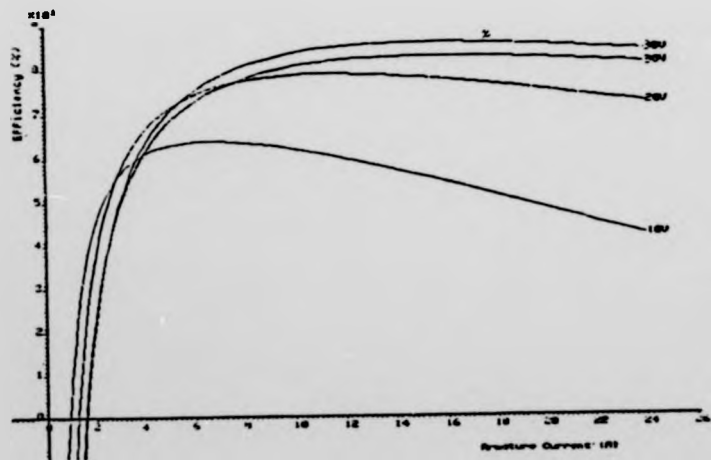


Figure 6.39(d) Efficiency characteristics of Motor 3 in star-connected bi-polar mode

CHAPTER 7 THE ELECTRONIC POWER REGULATOR

7.0 Introduction

Having designed, built and tested the prototype motors, the next phase of the project was to develop an Electronic Power Regulator (EPR) to regulate the power flow of the 600W brushless dc disc-motor (Motor 3). The functions of the EPR are: 1) to operate the motor in both the motoring and the regenerating modes, and 2) to control the motor's shaft torque.

The first function is achieved by controlling the conduction sequence of the power devices. The second function is achieved by modulating the conduction of the power devices at a rate higher than the commutating frequency. This technique is known as the Pulse-Width Modulation (PWM).

This chapter will begin with the description of the PWM power regulator: Section 7.1 will discuss two of the most commonly used PWM techniques, in order to aid the establishing of a modulation strategy for the EPR. Section 7.2 gives the configuration of the 4-quadrant EPR. Special emphasis is on the choosing of a modulation strategy, and the generation of the PWM signals. Section 7.3 describes the EPR in detail. Emphasis is given to the choosing of the power devices and the operation of the power circuit. Finally, Section 7.4 will study the transfer characteristics of the EPR.

7.1 Pulse-Width Modulation

The operational advantages of the pulse-width modulated inverter over other inverter techniques are now generally recognised (47,48,49). In a PWM inverter, both voltage and frequency control are achieved by rapidly switching the same

set of power semiconductors, such that each cycle of the output voltage consists of a number of pulses of equal amplitude (Figure 7.1). The periodicity of the pulse pattern determines the fundamental frequency, and the voltage of the fundamental is controlled by variation of the pulse-widths. The higher order harmonics are suppressed by a low pass filter.

PWM also offers a means to control the spectral power of the inverter whereby the filter cost can be minimised and good spectral performance can be maintained. This is achieved by suitably controlling the widths of the pulses to eliminate or suppress the lower order harmonics and utilizing harmonic filters to minimise the higher order harmonics (50). In motor drive applications, the load itself serves as the filter, and it is desirable to keep the pulse repetition rate as high as possible, so that the higher order harmonics are filtered out by the motor inductance alone without additional filter components.

Before implementing a modulation strategy for the EPR, it is useful to study some of the existing PWM techniques, and two of the most commonly used techniques are described here.

7.1.1 Sine-wave modulation (51,52,53)

The principle of sine-wave modulation, or sub-harmonic modulation is illustrated in Figure 7.2. Referring to Figure 7.2(a) a reference sine-wave ② of frequency f_m is compared to a triangular-wave ① (the carrier) of fixed amplitude and frequency (f_c) by the comparator ③. The output of the comparator is positive when the signal level of the reference exceeds that of the carrier, and negative when the reference level is below the carrier. The resulting output is the PWM signal, and this is known as the asynchronous modulation. In this simple technique the carrier frequency is fixed so that for practically all values of the reference frequency, the ratio f_c/f_m is non-integer and the PWM pattern is continually changing. And, for certain ranges of f_m , there will be an unwanted component with a frequency lower than that of the wanted component. At some specific values of f_c/f_m the unwanted component can be dc. Since the flux

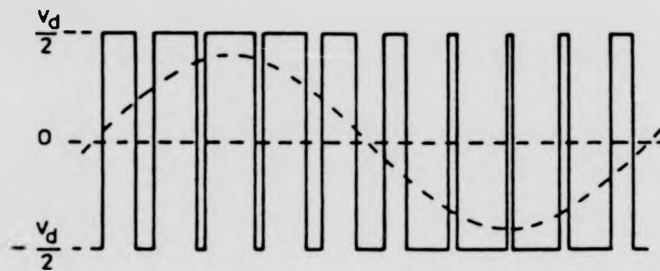


Figure 7.1 A pulse-width modulated waveform

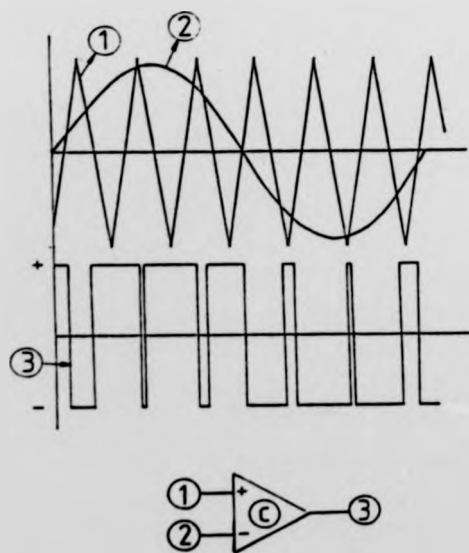


Figure 7.2(a) Asynchronous sine-wave modulation

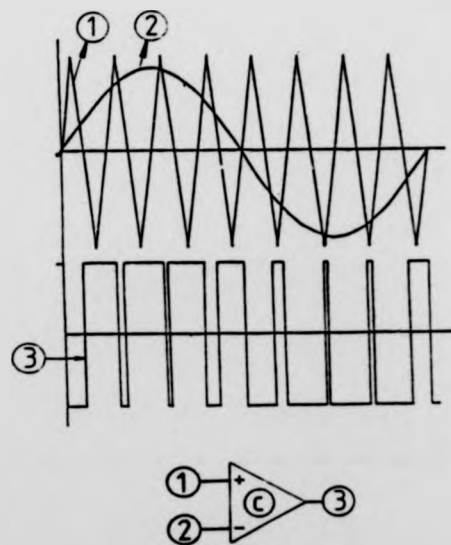


Figure 7.2(b) Synchronous sine-wave modulation

produced by a particular component is proportional to v/f , the flux produced by these sub-harmonic components can be large even if their amplitudes are small. But, the amplitudes of the sub-harmonics can be reduced by making f_c/f_m large. However, if f_c is increased switching losses are increased proportionally.

In order to suppress the sub-harmonics without increasing f_c substantially, the technique of synchronous modulation (Figure 7.2(b)) can be used. In this technique f_c is made to be an integer multiple of f_m , such that all the harmonic components are multiples of f_m . Thus the lowest unwanted component is at frequency $2f_m$. If f_c/f_m is odd, then only odd harmonics are generated. The 3rd harmonic can be suppressed by connecting the motor windings either in star, with the star point floating, or in delta. The other higher order harmonics (5th, 7th, etc.) are suppressed by the armature inductance of the machine. Clearly, synchronous modulation is far superior to the asynchronous technique. However, the synchronous scheme only operates over a narrow frequency range. This is because if f_c and f_m are locked, the range of f_c is the same as that of f_m which is typically required to be at least 20:1. This frequency locking is not usually possible since if f_c is too low, the motor inductance will become insufficient for adequate armature current smoothing, and if f_c is too high, switching losses will become excessive. To overcome this problem the method of 'ratio changing' (54) is used, whereby the ratio f_c/f_m is changed in accordance with the reference frequency so as to maintain f_c within certain limits.

7.1.2 Harmonic elimination (50)

Another often used PWM technique is the harmonic elimination method. In order to illustrate the principle of this method, the single-phase situation is considered. Consider a PWM waveform with quarter-wave and half-wave symmetry with m switching per quarter cycle, and with unity amplitude. The waveform can be represented by a Fourier series as follows:

$$v(\omega t) = \sum_{n=1}^{\infty} V_n \cos n\omega t \quad \dots(7.1)$$

where

$$V_n = \frac{4}{n\pi} \left[1 - 2 \sum_{k=1}^m (-1)^k \cos n\alpha_k \right] \quad \dots(7.2)$$

for $n = 1, 3, 5, \dots, (2m-1)$

Each switching angle in the first quarter cycle provides a degree of freedom in Equation (7.2). By selecting the appropriate switching angles, voltage control and harmonic elimination can be achieved. Thus, for example, with $m = 3$ (Figure 7.3), one may control the amplitude of the fundamental and have any two harmonics eliminated, by setting V_1 at some magnitude and two harmonics (e.g. 5th and 7th) to zero; and numerically solve for the values of α_1 , α_2 and α_3 , i.e.

$$V_1 = \frac{4}{\pi} (1 - 2\cos\alpha_1 + 2\cos\alpha_2 - 2\cos\alpha_3) \quad \dots(7.3)$$

$$V_5 = 0 = \frac{4}{5\pi} (1 - 2\cos 5\alpha_1 + 2\cos 5\alpha_2 + 2\cos 5\alpha_3) \quad \dots(7.4)$$

$$V_7 = 0 = \frac{4}{7\pi} (1 - 2\cos 7\alpha_1 + 2\cos 7\alpha_2 + 2\cos 7\alpha_3) \quad \dots(7.5)$$

This PWM technique allows precise selection of harmonics to be eliminated, and can be conveniently implemented by using microprocessors (55). A typical implementation is to generate a look-up table by solving Equations (7.3), (7.4) and (7.5) for a range of fundamental voltages (56). The wave patterns are then stored in the memory of a microcomputer. The required wave pattern for a specific output voltage is then generated by retrieving the data from the look-up table during run-time.

7.2 Electronic Power Regulator Configuration

7.2.1 Establishing a modulation strategy

In the preceding section two of the most commonly used PWM techniques were described; this section will establish a modulation strategy for the EPR. Referring to the conduction-states diagram of Motor 3 (Figure 4.8), it can be seen that the conduction loop of all the conduction-states are identical to each other, i.e. a conduction loop consists of the battery, two semiconductor switches and two coupled coils, as shown in Figure 7.4.

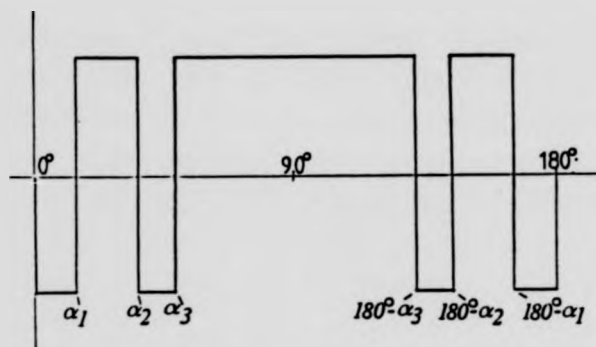
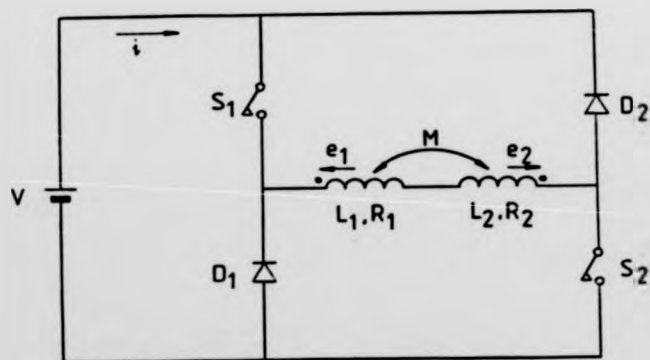


Figure 7.3 Harmonic elimination PWM (m = 3)



- S_1, S_2 = semiconductor switches
- e_1, e_2 = induced emfs
- R_1, R_2 = armature resistances
- L_1, L_2 = self-inductances
- M = mutual inductance

Figure 7.4 Equivalent conduction loop of the conduction-states

In order to achieve PWM control of the current i , either S_1 or S_2 , or both S_1 and S_2 , can be PWMed. The PWM switching frequency is determined by the equivalent series inductance of the circuit, and the allowable current ripple which is dependent on the current rating of S_1 and S_2 . The approximate relationship between the inductance and the current ripple for an LR load is given as (57):

$$f_c = \frac{V}{4 L_s \Delta I} \quad \dots (7.6)$$

where f_c = carrier frequency (switching frequency)

V = supply voltage

L_s = equivalent series inductance

ΔI = load current ripple

If the power devices being used are MJ11015 and MJ11016 (see previous chapter) which have a maximum continuous current rating of 30A and a pulsed current rating of 45A, and allowing for 30% derating at elevated junction temperature (which is usually 100°C) (58) the maximum continuous and peak ratings become 21A and 31.5A respectively. By taking the maximum average load current to 21A and allowing a ripple current of 9A (Figure 7.5) such that the peak value is not too close to the maximum rating, the minimum carrier frequency is calculated to be 20KHz. Although the determination of the carrier frequency is clearly not as straight forward as is indicated by Equation (7.6), (as other factor such as the PWM generator's frequency limitation, and the power device's switching speed, will also affect the choice,) it does nevertheless indicate the order of magnitude of the required carrier frequency.

It becomes obvious that with such a high carrier frequency, it would be impractical to apply the method of harmonic elimination as an extremely fast processor is required to implement it. On the other hand, the method of sub-harmonic modulation is more appropriate for the brushless motor; although squarewave armature current is now required. Such waveform can be obtained,

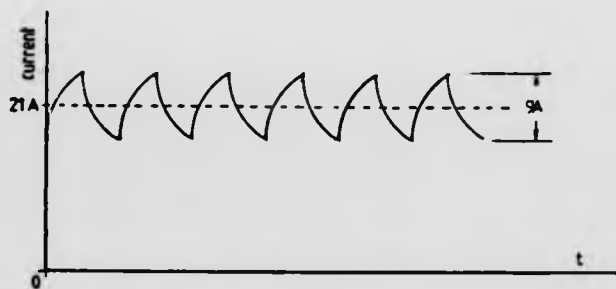


Figure 7.5 Allowable ripple current of the power devices MJ11015 & MJ11016

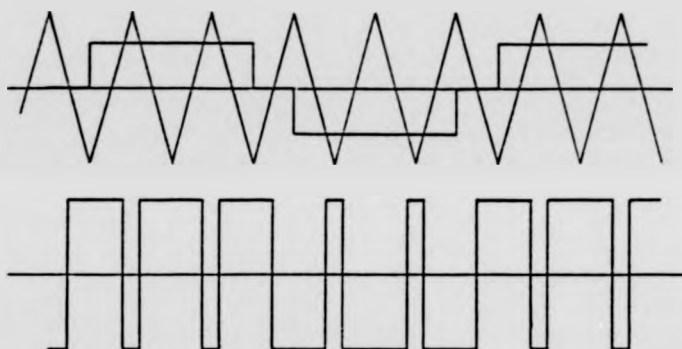


Figure 7.6 Sub-harmonic modulation with a square modulation-wave

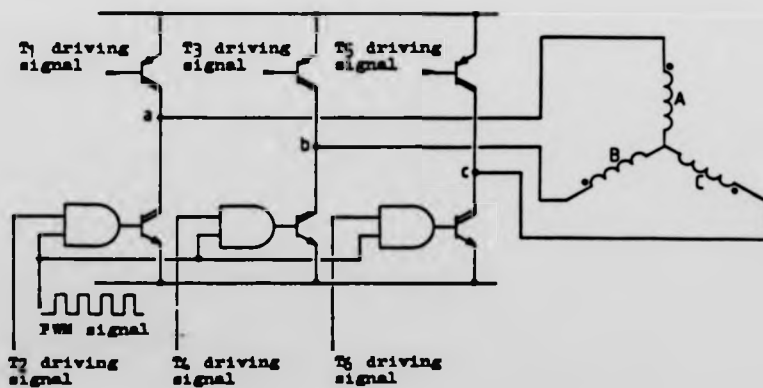


Figure 7.7 The PWM scheme used by the EPR

quite easily, by changing the modulation wave from a sinewave to a squarewave, as shown in Figure 7.6. It can be seen that the PWM wave pattern is equivalent to that of the switching of the power switch at a constant mark/space ratio. Thus a simpler PWM scheme can be sought.

If the carrier frequency has a minimum value of 20kHz and the maximum commutation frequency of the motor is 200Hz (at 3000rpm), the minimum f_c/f_m ratio is 100. With such a high f_c/f_m the amplitude of the sub-harmonics will be very small even if asynchronous modulation is used. For simplicity reasons the method of asynchronous modulation is adopted.

The final PWM scheme is illustrated in Figure 7.7. The conduction signals of the three bottom transistors are ANDed with a pulse-train whose mark/space ratio is adjustable. Current control is achieved by varying this ratio. The advantages of switching only the bottom transistors are that slower and cheaper devices can be used in the top-half of the inverter bridge as the three top transistors are only switched at the commutation frequency, and that switching losses are almost halved. Figure 7.8 shows the timing of the drive signals and the approximated effects of the pulsed voltage on the waveform of the armature current of Motor 3 in the motoring mode.

7.2.2 PWM pulse-train generation

There are two methods for generating the PWM pulse-train, they are the analogue and the digital methods. For this project the latter method was used. The reason being that digital circuits are almost free from temperature drifts, and thus a high degree of repeatability is guaranteed. But the draw back is that only a stepped change in pulse-width is permitted. The functional block diagram of the PWM generator is illustrated in Figure 7.9.

The period of the pulse train is set at 50us, and the duty-time is programmed by the 9-bit input data, which is usually generated by the Microprocessor Controller Unit (MCU). (Details about the MCU will be given in the next chapter.)

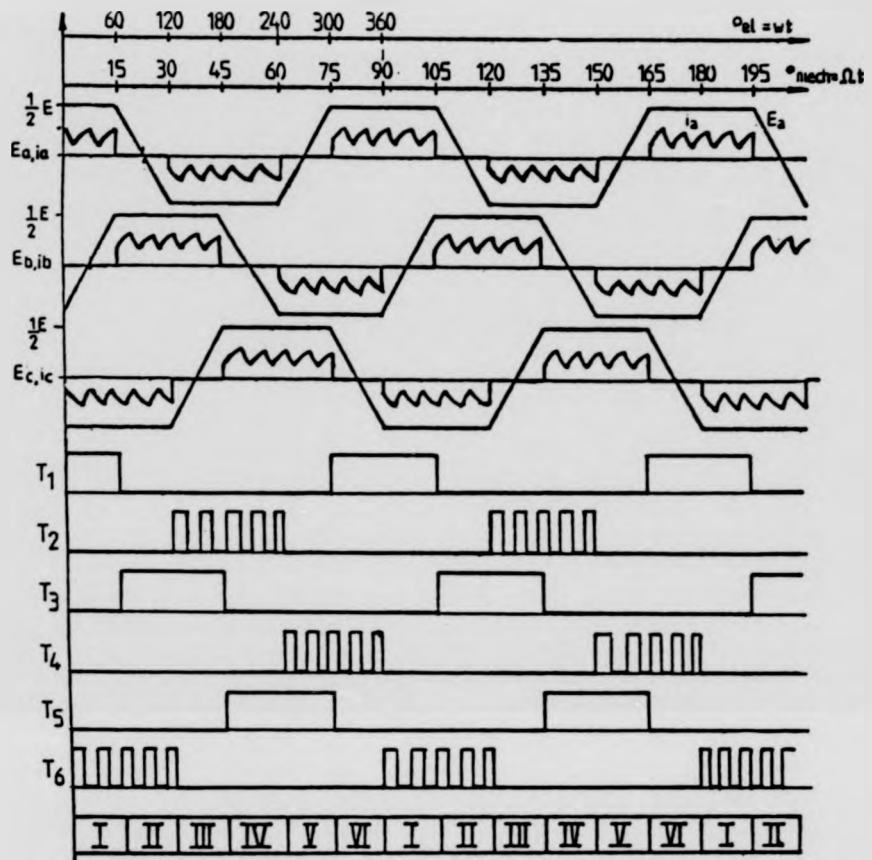


Figure 7.8 Relationship in time between the induced emfs, the driving signals and the PWMed armature current

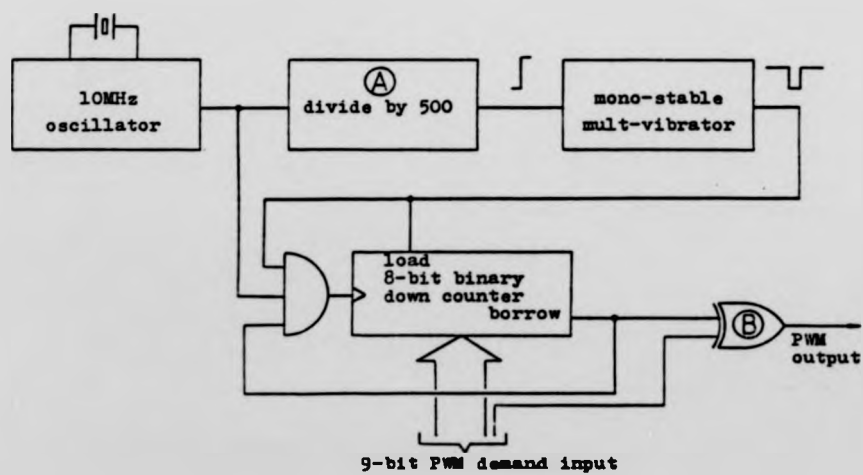


Figure 7.9 Functional block diagram of the PWM generator

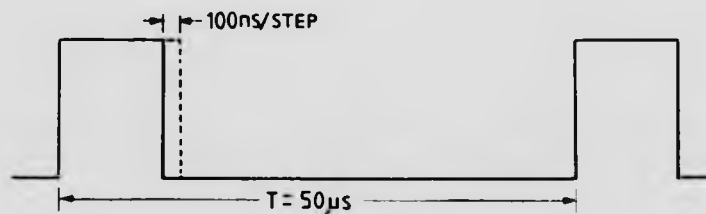


Figure 7.10 The timing of the PWM carrier signal

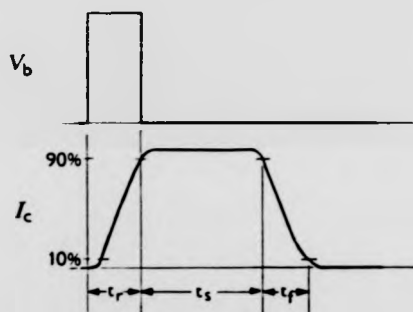


Figure 7.11(a) A minimum pulse-width base drive signal, and its effects on the collector current

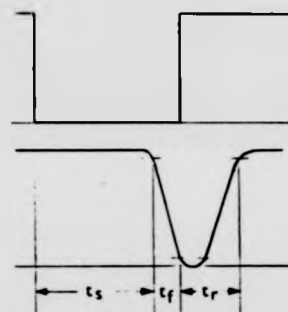


Figure 7.11(b) A maximum pulse-width base-drive signal, and its effects on the collector current

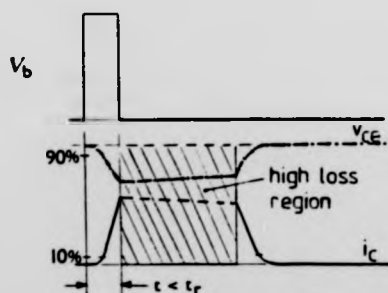


Figure 7.11(c) Effects of a driving pulse which is shorter than the minimum pulse-width

Referring to Figure 7.9, the 20kHz carrier signal is generated by dividing the 10MHz clock by 500 by the divider (A). The duty-time is determined by the pre-loaded data of the 8-bit binary down counter and the Exclusive-OR gate (B). The 10MHz clock also determines the minimum pulse-width of the carrier signal. The minimum pulse-width, which is equal to 100ns, is also equal to the step size of the duty-time. The carrier thus has a period of 50us and its pulse-width varies in 100ns steps as shown in Figure 7.10. With this timing arrangement the resolution of the PWM generator is 1 in 500, i.e. 0.2%, which gives a minimum average inverter output voltage variation of 72mV (0.2% of the 36V battery voltage).

7.3 The Power Circuit

7.3.1 Power transistor switching characteristics

Although the PWM carrier frequency of 20kHz of the EPR is not particularly high, the duty-time can be very short -- as short as 100ns. To ensure that the power devices can respond to the PWM signal with the minimum error, and at the same time produce the minimum switching losses, their switching characteristics must be studied.

Referring to the power Darlington's MJ11015 and MJ11016, which were used in the prototypes brushless dc disc-motors, these have typical turn-on (t_r), storage (t_s) and turn-off (t_f) times of 0.5, 3.5 and 1.0 us respectively. When these devices are being switched, the base must be supplied with driving signal of minimum pulse-width equal to the turn-on time, as shown in Figure 7.11(a). Otherwise, they may be driven into the linear region, where the device dissipation is very high, for a short but undetermined period as shown in Figure 7.11(c). Also, due to the storage time of bipolar devices, a minimum-width driving signal will produce an output pulse much longer than the driving pulse. The width of the output pulse t_{on} is equal to the sum of the switching times, i.e. $t_{on} = t_r + t_s + t_f$, and has a value of 5.0us. This is also illustrated in

Figure 7.11(a). The switching delays not only limit the minimum controllable average output voltage to 10% of the supply, but also induces a significant percentage error in the demanded output. In the case of a minimum-width driving pulse, the ratio of the output pulse-width to the base drive pulse-width is 10, which represents a 900% error in the demanded output. Such switching delay induced output error will of course reduce as the width of the driving pulse increases. Another switching delay induced limitation of the power Darlington is the minimum off-time, when the driving signal must be removed for a minimum period equal to the sum of the storage time and the turn-off time, as illustrated in Figure 7.11(b). This minimum off-time limits the maximum controllable average output voltage to 97% of the supply for similar reasons to those giving rise to the minimum controllable output.

In addition to the switching time problems there are also switching losses associated with the turn-on and turn-off periods of the transistor. These losses are directly proportional to the switching frequency, and the rise and fall times of the transistor. To increase the range of controllable output voltage and to reduce the switching losses, faster switching devices must be used.

7.3.2 Selecting the PWM power devices

The power Darlington's used in the prototype brushless machines have slow switching speeds and are unsuitable for PWM switching as explained in the last section. Fortunately, a host of new power devices capable of fast switching are now generally available. They include power MOSFET (59), gate turn-off thyristor (GTO) (60,61) and high-speed bipolar transistor. Their relative performance are given in Figure 7.12 where other conventional power devices are also included for comparison purposes.

power MOSFET

The power MOSFET is clearly the fastest device. It has extremely short turn-on and turn-off times, which result in very low switching losses. Like other metal-oxide semiconductor (MOS) devices, it is a voltage-controlled

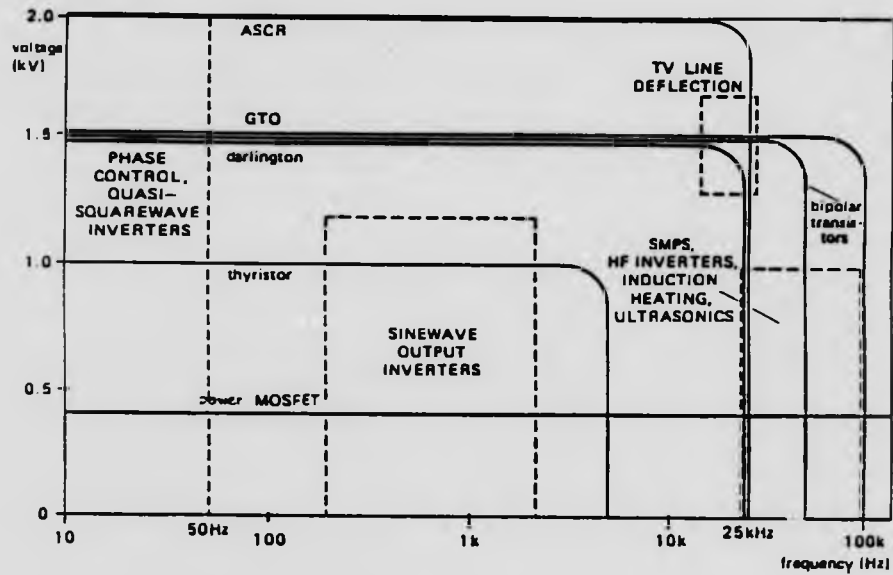


Figure 7.12 Relative performance of switching power devices

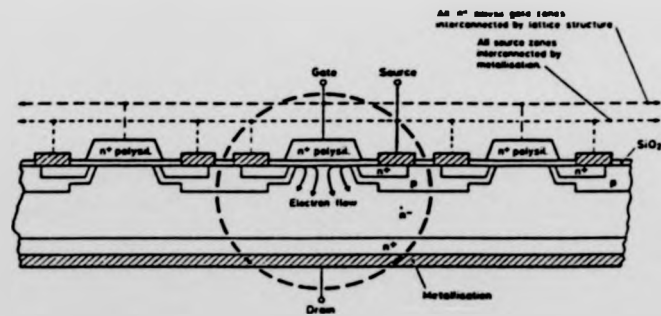


Figure 7.13 Double-diffused structure of a MOSFET cell

device, and is very easy to control. However, its on-state resistance is higher than the collector-emitter saturation slope resistance of a similarly rated bipolar transistor, and therefore it has a higher on-state loss. Furthermore, a power MOSFET is rather more expensive than a bipolar transistor.

GTO

The new generation of gate turn-off thyristors, such as the Mullard BTV60 (62), have shorter turn-off time than the Darlington's. The GTO is a fast three-terminal four-layer pnpn device similar in construction to the conventional thyristor. Like a thyristor, the GTO can block a high-level forward voltage when turned off, and pass high forward currents when turned on. It is also like a transistor in that it can be switched on and off at high speed by a low-level gate drive.

To turn on the GTO, a forward gate current, which must be greater than the minimum triggering current I_{GT} , is required. But to minimise the turn-on delay it may be necessary to increase the forward gate current to 5 times of I_{GT} . To turn off the GTO, a low-impedance negative voltage is applied between the gate and the cathode. The turn-off time is inversely proportional to the amount of current that is being extracted from the gate, and a low series impedance is therefore essential for the turn-off circuit.

The GTO exhibits the same dv/dt problem which is associated with thyristors in that the rate of rise of the cathode-anode voltage must be limited during the forward recovery time by a snubber circuit to prevent miscommutation.

High-speed bipolar transistor

The bipolar transistor has a lower on state dissipation than other types of power devices; and is relatively inexpensive. It has a very short switching time, and some recently introduced bipolar transistors, such as the

Motorola's Switchmode III series, have switching times even approaching to those of power MOSFETs.

However, the bipolar transistor has the infamous thermally induced secondary breakdown problem (63), which makes it susceptible to current overload. It also has the property of reduced gain at increased collector current. This requires a higher base current to prevent it from pulling out of saturation. The increased minority charges in the emitter region due to the higher base current will however increase the turn-off time.

Because of the superior switching characteristics, the ease of driving and the forecast price-drop of the power MOSFET (64), it was chosen for the PWM power regulator. As the power MOSFET is a relatively new device, some understanding of its characteristics is necessary before its potential can be explored. The following section will describe the characteristics of the power MOSFET in more detail.

7.3.3 The power MOSFET

7.3.3.1 Construction and properties

The chip in a power MOSFET carries an array of several thousand identical enhancement mode MOSFET transistor elements (over 500,000 per sq. in.), all of which have their sources, gates and drains connected in parallel. In cross-section, each element is based on a double-diffused (DMOS) structure as shown in Figure 7.13. This construction enables current to flow vertically, thus high current operation is achieved within a small area. Like other MOS devices, the power MOSFET is a majority-carrier semiconductor, and is an extremely fast switching device. Another feature of the power MOSFET is that it has a built-in integral reverse 'body-drain' diode, which has the same current handling capability as the transistor itself. This eliminates the need for additional discrete rectifiers connected in anti-parallel with the MOSFETs in the inverter circuit. Other advantages of the power MOSFET are briefly discussed below:

High gain

The power MOSFET is a voltage-controlled device; the transconductance of a

40A device, e.g. the International Rectifier's IRF150, is typically 10A/V. With such a high gain, it therefore only requires a relatively simple drive circuit. But it should be noted that the gate input characteristic of the MOSFET is purely capacitive. If a very fast switching speed is desired, the drive circuit must have a sufficiently low output impedance to supply the required charging and discharging current.

Ruggedness

The device has a positive temperature coefficient, and this makes it act in a self-protective manner to force the drain current to distribute evenly over the silicon die. It therefore does not display the secondary breakdown phenomenon of the bipolar transistor. This means that the power MOSFET is generally a much more rugged device than the bipolar transistor.

Temperature stability

MOSFETs have outstanding gain and switching time stability with temperature variations relative to those of bipolar transistors. The transconductance of power MOSFETs typically varies less than +20% from the 25°C value, over a -55 to 125°C range. The dc current gain of a bipolar transistor commonly varies by a factor of 2 to 3 over the same temperature range. The switching time of power MOSFETs is essentially independent of operating temperature. This is because the response time is primarily dependent on the input capacitance, which is essentially temperature invariant.

Ease of paralleling

Power MOSFETs are easy to parallel because their positive temperature coefficient forces current sharing among the paralleled devices.

7.3.3.2 Driving the power MOSFET

As has been mentioned before, the power MOSFET is a voltage-controlled device. A voltage must be applied between the gate and source terminals to produce a flow of current in the drain. The switching speed is proportional to how fast the

gate-source voltage can be applied or removed. The gate of a MOSFET is isolated electrically from the source by a thin layer of silicon oxide, and therefore the gate-source input impedance is capacitive. For a device to be turned on very quickly, a voltage source which is capable of supplying any amount of current in the shortest possible time must be used. For fast turn-off, a low impedance current sink is required.

The simplest way to drive a MOSFET is by means of a CMOS gate as shown in Figure 7.14. In this case the turn-on and turn-off times are limited by the source/sink resistance (about 500 ohms) of the CMOS gate. If faster switching times are needed, gates can be paralleled in any number to lower the resistance.

For even faster switching times, an emitter-follower buffer circuit can be used, as shown in Figure 7.15. With this circuit the current available to the MOSFET will be the output current of the CMOS gate multiplied by the current gain of the drive transistors. Because the transistors are operating as emitter-followers there will be no storage time to worry about, and the frequency limit will be determined by either the CMOS gate or the f_t of the transistors, whichever comes first.

A power MOSFET can also be driven directly from a TTL gate. But as the 'high' output of a TTL gate is limited to about 3.5V, the output current of the MOSFET will be limited to some value less than its maximum rated value. A higher current output can be obtained by pulling the gate output to the 5V rail by an additional pull-up resistor, as illustrated in Figure 7.16. But the turn-on time will be limited by the sourcing impedance.

For very high speed requirements a capacitive driver such as the MH0026 should be used (Figure 7.17). This drive configuration can give extremely fast rise and fall times; switching of less than 10nsec are achieved by some VMOS devices (65).

7.3.4 The power circuit

Having chosen the type of power devices for PWM switching, the power circuit of

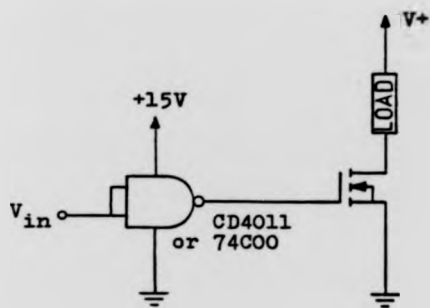


Figure 7.14 Power MOSFET driven by a CMOS gate

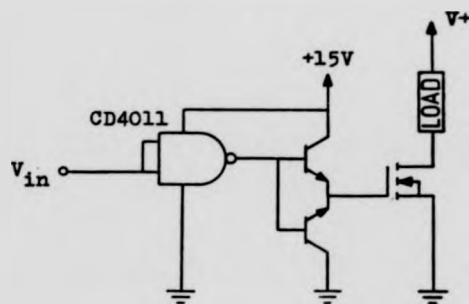


Figure 7.15 Power MOSFET driven by an emitter-follower buffer

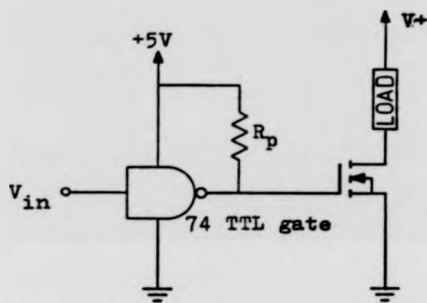


Figure 7.16 Power MOSFET driven by a 74 TTL gate

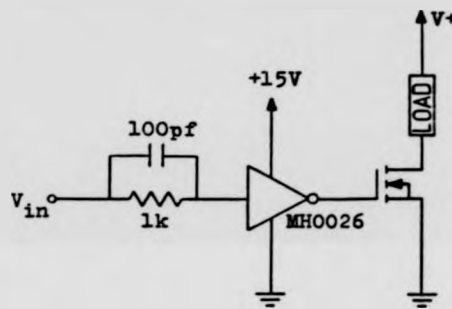


Figure 7.17 Power MOSFET driven by a high-speed capacitive driver

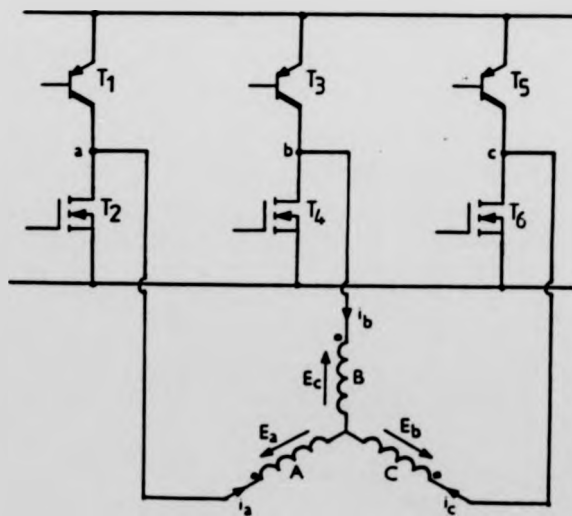


Figure 7.18 The basic power circuit of the EPB

the EPR was then designed. The basic circuit consists of three power Darlington's and three power MOSFETs, as shown in Figure 7.18. Each of the Darlington's in the top-half of the inverter bridge is made up of two discrete PNP transistors. The driver and the output devices are of types BD304B and 2N5684 respectively. The output device has a continuous collector current rating of -30A and a peak rating of -45A. The collector-emitter saturation characteristic of the resulting Darlington is given in Figure 7.19. The power MOSFETs in the bottom-half of the bridge are of type IRF150, which has a continuous drain current rating of 40A and a pulsed rating of 160A; the on state drain-source resistance is typically 0.055ohm.

Figure 7.21 gives the schematic circuit diagram of one leg of the power regulator. The MOSFET Q_6 is driven by six paralleled CMOS Schmitt-trigger buffers to provide a low sourcing/sinking impedance for fast switching. Diodes D_2 and D_3 are used to suppress the inductive voltage-transients which are produced across the drain and source of Q_6 at the time when it is switching off.

The Darlington (made up of Q_4 and Q_5) is driven by a complementary common-emitter driver stage (Q_2 and Q_3). Driving speed of this driver stage is not essential as the Darlington is being switched at the commutation frequency which is only 200Hz maximum.

The Schottky diode D_1 which is connected in anti-parallel with Q_5 provides a path for the commutation transients and the free-wheeling current. Schottky diode is necessary in order to increase the switching efficiency of the power regulator [66]; its forward characteristic is given in Figure 7.20.

The logic gates A and E provide the mutual exclusion function for the conduction of Q_5 and Q_6 . The logic truth table relating the input signals and the output is given in Table 7.1. Also, the static equivalent circuit of the power output states are given in Figure 7.22.

7.3.5 Power circuit switching efficiency

The block diagram of the test circuit for assessing the EPR's switching

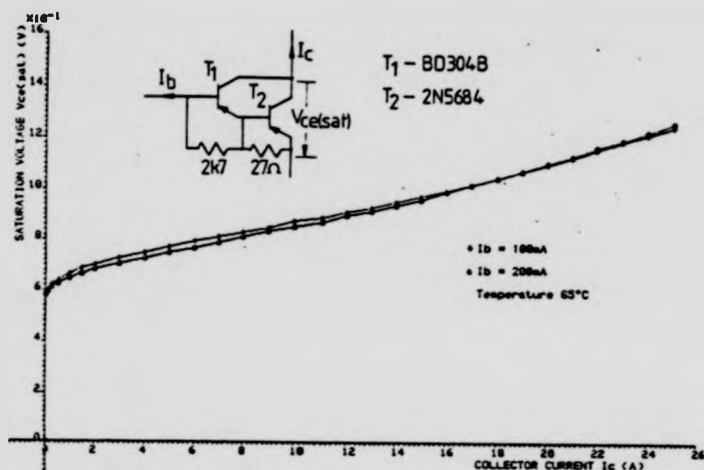


Figure 7.19 The collector-emitter saturation characteristics of the Darlington

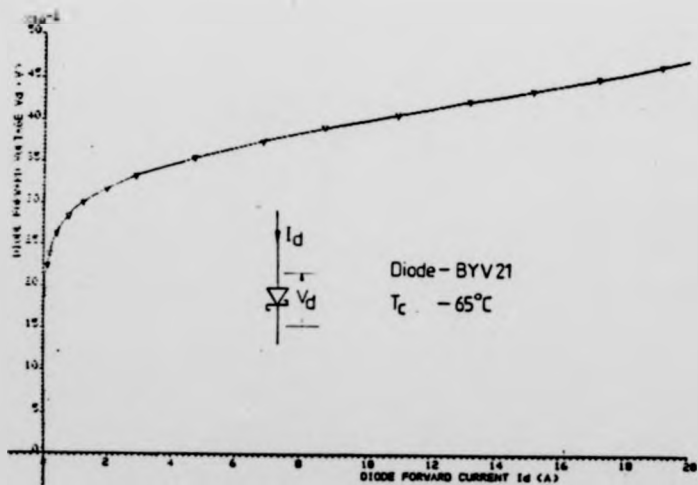


Figure 7.20 Forward characteristics of the Schottky diode

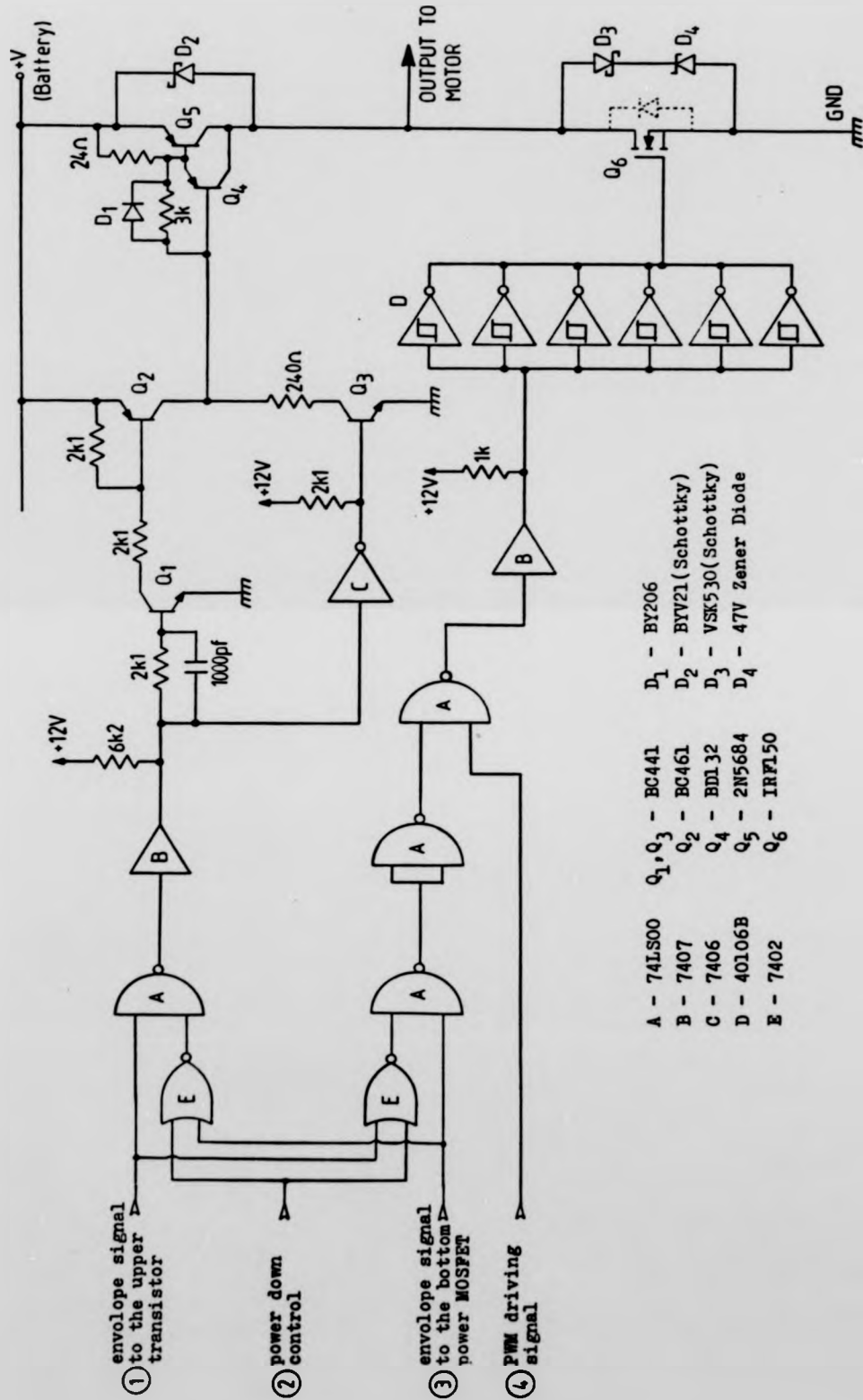


Figure 7.21 Schematic circuit diagram of the power regulator

①	②	③	④	output
X	X	1	X	high impedance
1	1	0	X	high impedance
1	0	0	X	-V
0	1	0	1	0V
0	1	0	0	high impedance

Table 7.1 Logic truth table of the power circuit

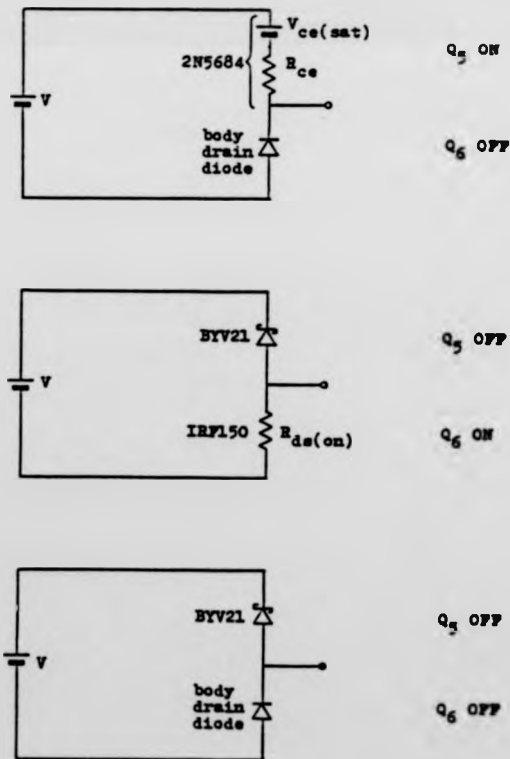


Figure 7.22 Static equivalent circuit of the power circuit output-states

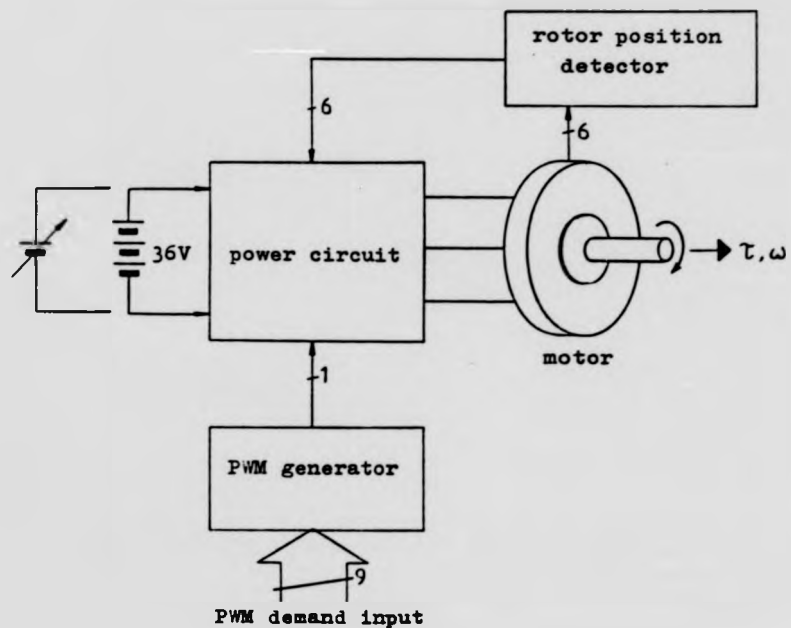


Figure 7.23 Block diagram of the test circuit for assessing the EPR's switching efficiency

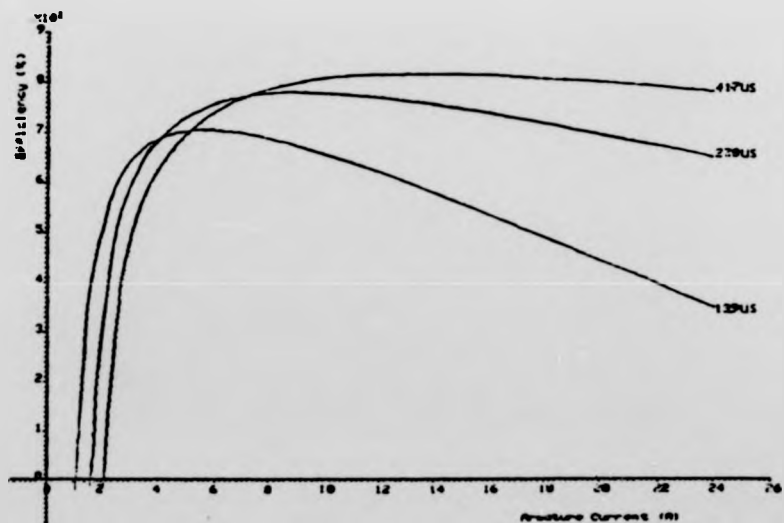


Figure 7.24 Efficiency characteristics of the drive system under PWM control

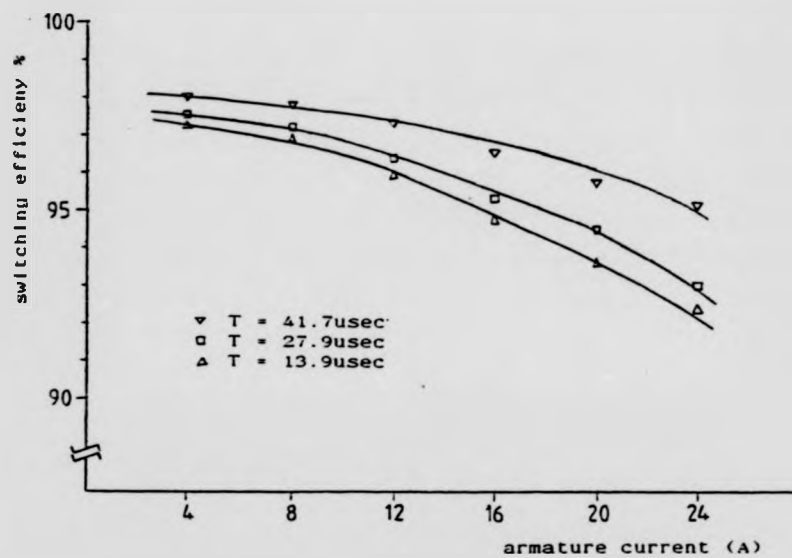


Figure 7.25 Switching efficiency of the power circuit

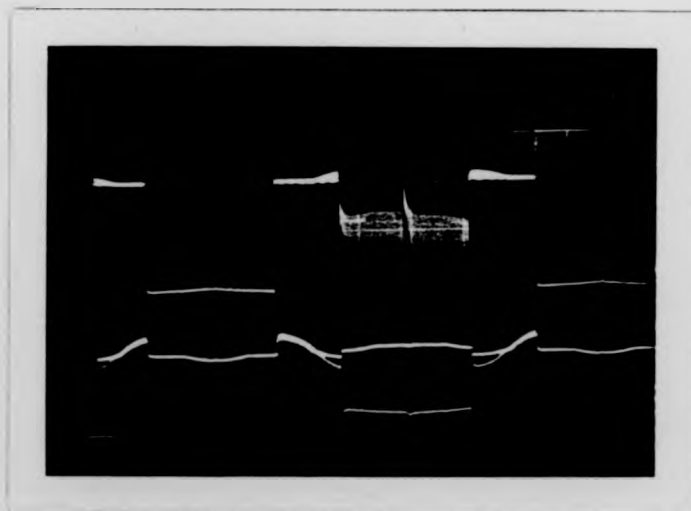


Figure 7.26 PWM terminal voltage waveform (upper trace)
and current waveform (lower trace)
Horizontal scale - 1μsec/div
Vertical scale - upper trace 10.9A/div
lower trace 22.5V/div

efficiency is shown in Figure 7.23. The efficiency characteristics of the drive system are first obtained by setting the PWM duty-times to 13.9, 27.8 and 41.7 μ sec, which corresponded to average output voltages of 10, 20 and 30V respectively. The results are given in Figure 7.24. These results are then compared with those obtained by supplying the unmodulated power circuit with dc voltage of 10, 20 and 30V. The switching efficiencies are then calculated; they are given in Figure 7.25. The oscillogram of the PWM waveforms is shown in Figure 7.26.

7.4 Current Transfer Characteristics of the EPR

The current transfer characteristic is the relationship between the PWM on-time and the output current of the EPR. This section will establish such transfer characteristics under steady state condition.

7.4.1 Assumptions

The EPR can operate the brushless motor in two modes, i.e. (1) forward and reverse motoring, and (2) forward and reverse regenerative braking. As the only difference between the forward and reverse operations in each mode is the commutation sequence, they will not be discussed separately. But before analysing the two modes of operation, it is important to recognise the following assumptions underlying the derivations:

- (1) During a conduction-state, the disc-motor induces a constant emf in its armature, and the switching transistor sees only a dc emf. It is assumed that the average armature current will rise rapidly to a steady-state value, and only this value will be considered.
- (2) As all the conduction-states are electrically identical, only one of the conduction-state is needed to be studied.
- (3) It is assumed that the air-gap flux density remains constant.
- (4) It is assumed that there is no magnetic saturation, and circuit inductances

remain constant irrespective of the armature current.

- (5) It is assumed that the angular speed ω of the motor remains constant and the induced emf is also constant.
- (6) It is assumed that the switching time of the power MOSFET is negligible.
- (7) All active devices are represented by their first order approximations.
- (8) Skin effects are neglected.

7.4.2 Motoring mode

The relationship in time between the voltages, currents and driving signals for the motoring mode is already shown in Figure 7.8. During a conduction-state there are only two transistors conducting, and one of them (the MOSFET) is switching at the PWM frequency. The current flow paths of a switching period are shown in Figure 7.27.

Let the period during which the transistor and the MOSFET both conduct be T_{on} , and the free-wheeling period be T_{off} . During T_{on} the supply voltage is driving current into the load against its emf so that the current is increasing. At the end of this period the MOSFET is turned off, and the load current circulates through the transistor and the free-wheeling diode for the period T_{off} . Energy to maintain the current flow is drawn from the circuit inductance, and the current consequently diminishes.

Based on the assumptions stated earlier, equivalent circuits can be drawn to represent the switching period. The circuits are shown in Figure 7.28.

7.4.2.1 The on-period equations (Figures 7.27(a) & 7.28(a))

The current equation for the on-period is

$$V - V_{tr} - E_a - E_b = i_1(R_{tr} + R_a + R_b + R_{ds}) + (L_a + L_b)\frac{di_1}{dt} - 2M\frac{di_1}{dt} \quad \dots(7.7)$$

For a three-phase balanced-armature, the following apply

$$E_a = E_b, R_a = R_b \text{ and } L_a = L_b$$

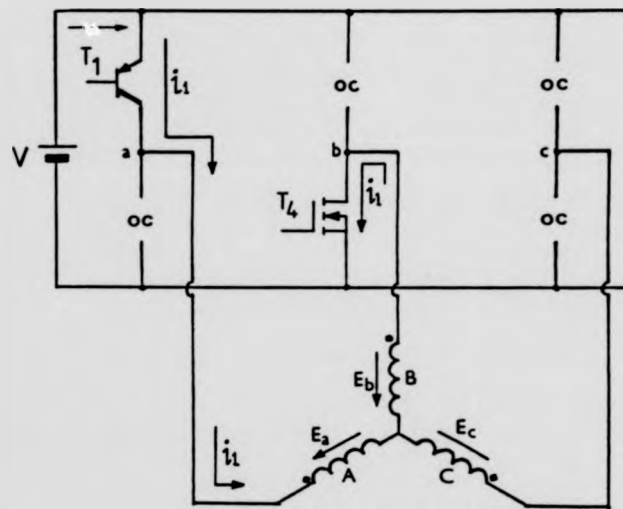


Figure 7.27(a) Motoring mode on-period current flow path (conduction-state VI)

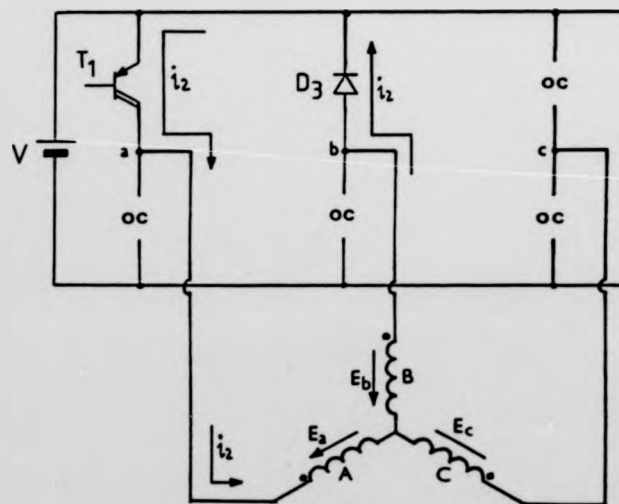
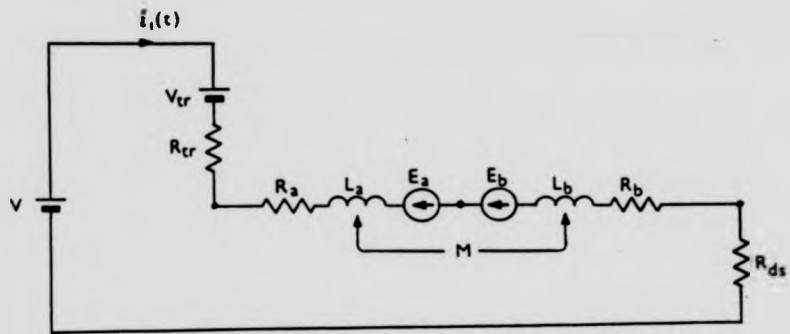
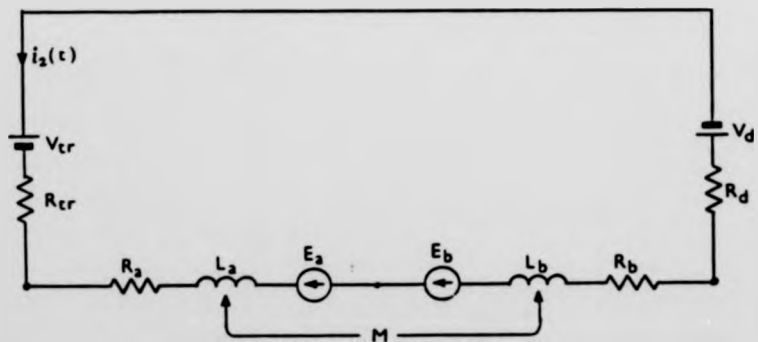


Figure 7.27(b) Motoring mode off-period (free-wheeling period) current flow path (conduction-state VI)

Figure 7.23(a) Motoring mode on-period equivalent circuitFigure 7.23(b) Motoring mode off-period equivalent circuit

- V_{tr} = Darlington equivalent voltage source
- R_{tr} = Darlington forward slope resistance
- R_{ds} = power MOSFET drain-source resistance
- V_d = Schottky diode equivalent voltage source
- R_d = Schottky diode forward slope resistance

The solution of the differential equation is

$$i_1(t) = \frac{E_1}{R_1}(1 - \exp(-t/Z_1)) + I_1 \exp(-t/Z_1) \\ = I_n + (I_1 - I_n) \exp(-t/Z_1) \quad \dots(7.8)$$

where

$$L_1 = 2(L_a - M)$$

$$R_1 = R_{tr} + 2R_a + R_{ds}$$

$$E_1 = V - V_{tr} - 2E_a$$

$$Z_1 = L_1/R_1$$

I_1 = initial current at the start of the duty cycle

$$I_n = E_1/R_1$$

7.4.2.2 The off-period (free-wheeling) equations (Figures 27(b) & 28(b))

The current equation for the off-period is

$$-V_{tr} - 2E_a + V_d = i_2(R_{tr} + 2R_a + R_d) + 2(L_a - M) \frac{di_2}{dt} \quad \dots(7.9)$$

The solution of the differential equation is

$$i_2(t) = \frac{E_2}{R_2}(1 - \exp(-t/Z_2)) + I_2 \exp(-t/Z_2) \\ = I_m + (I_2 - I_m) \exp(-t/Z_2) \quad \dots(7.10)$$

where

$$L_2 = 2(L_a - M)$$

$$R_2 = R_{tr} + 2R_a + R_d$$

$$E_2 = -(V_{tr} + 2E_a + V_d)$$

$$Z_2 = L_2/R_2$$

I_2 = initial current at the start of the off cycle

$$I_m = E_2/R_2$$

(Note: the time 't' is measured from the beginning of each on or off period.)

7.4.2.3 Continuous and discontinuous conductions

If the on-period T_{on} is sufficiently long, the armature current never becomes zero, and the conduction is continuous. Under such circumstances $T_{off} = T_{on} - T$, and the situation is depicted in Figure 7.29(a). If the on-period is shorter,

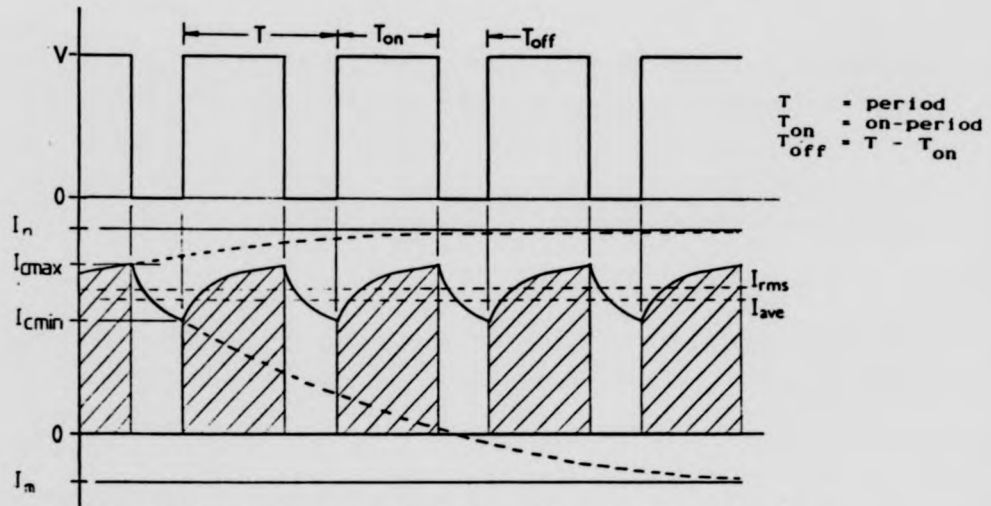



Figure 7.29(a) Motoring mode steady-state armature current (continuous conduction)

 active power transfer

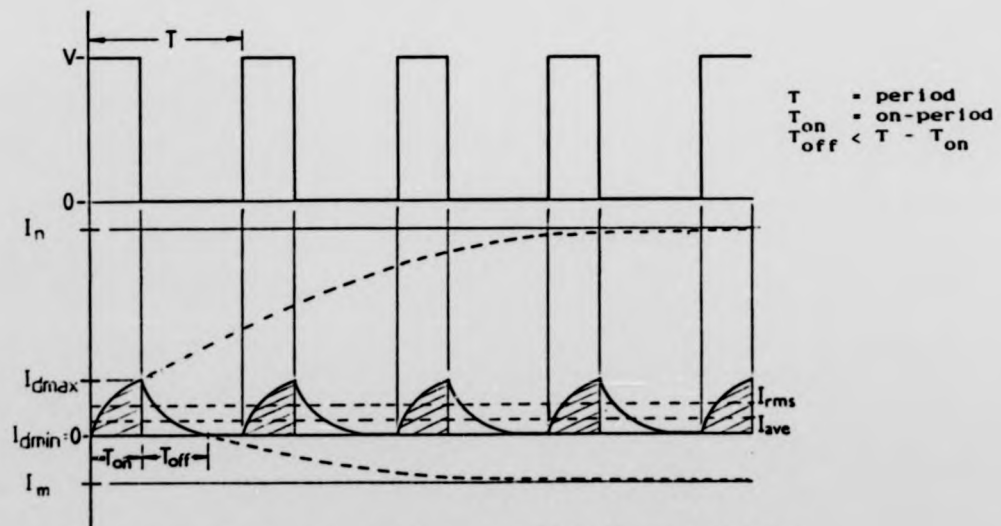


Figure 7.29(b) Motoring mode steady-state armature current (discontinuous conduction)

the energy stored in the circuit inductance may not be sufficient to maintain current until the end of the cycle. Conduction is then discontinuous, and $T_{\text{off}} < T - T_{\text{on}}$ (Figure 7.29(b)). When the armature current is continuous the average armature current is proportional to T_{on}/T . But when the armature current is discontinuous the armature current and T_{on}/T transfer relationship becomes non-linear.

To determine the steady-state current transfer function, the maximum and minimum values of the armature current at given speeds and T_{on} s must first be calculated.

Continuous conduction

(i) During on-period

Let I_{cmin} = initial current ... ①

I_{cmax} = current after T_{on} sec ... ②

By substituting ① and ② to (7.7), the following is obtained

$$i_1(T_{\text{on}}) = I_{\text{cmax}} = I_n + (I_{\text{cmin}} - I_n) \exp(-T_{\text{on}}/Z_1) \dots (7.11)$$

(ii) During off-period

Let I_{cmax} = initial current ... ③

I_{cmin} = current after T_{off} sec ... ④

By substituting ③ and ④ to (7.10), the following is obtained

$$i_2(T_{\text{off}}) = I_{\text{cmin}} = I_m + (I_{\text{cmax}} - I_m) \exp(-T_{\text{off}}/Z_2) \dots (7.12)$$

Substituting (7.12) to (7.11), we have

$$I_{\text{cmax}} = I_n + \{I_m + (I_{\text{cmax}} - I_m) \exp(-T_{\text{off}}/Z_2) - I_n\} \exp(-T_{\text{on}}/Z_1)$$

$$\therefore I_{\text{cmax}} = \frac{I_n \{1 - \exp(-T_{\text{on}}/Z_1)\} + I_m \{1 - \exp(-T_{\text{off}}/Z_2)\} \exp(-T_{\text{on}}/Z_1)}{1 - \exp(-T_{\text{off}}/Z_2) \exp(-T_{\text{on}}/Z_1)} \dots (7.13)$$

Similarly, substituting (7.11) into (7.12), we have

$$I_{cmin} = I_m + (I_n + (I_{min} - I_n)\exp(-T_{on}/Z_1) - I_m)\exp(-T_{off}/Z_2)$$

$$I_{cmin} = \frac{I_m(1 - \exp(-T_{off}/Z_2)) + I_n(1 - \exp(-T_{on}/Z_1))\exp(-T_{off}/Z_2)}{1 - \exp(-T_{off}/Z_2)\exp(-T_{on}/Z_1)} \dots (7.14)$$

Discontinuous conduction

(i) During on-period

Let I_{dmin} = initial current = 0 ... ⑤

I_{dmax} = current after T_{on} sec ... ⑥

By substituting ⑤ and ⑥ to (7.7), the following is obtained

$$I_1(T_{on}) = I_{dmax} = I_n(1 - \exp(-T_{on}/Z_1)) \dots (7.15)$$

(ii) During off-period

Let I_{dmax} = initial current ... ⑦

I_{dmin} = current after T_{off} sec = 0 ... ⑧

By substituting ⑦ and ⑧ to (7.10), the following is obtained

$$I_2(T_{off}) = 0 = I_m + (I_{dmax} - I_m)\exp(-T_{off}/Z_2) \dots (7.16)$$

By substituting (7.15) to the above, T_{off} is obtained:

$$T_{off} = Z_2 \ln(1 - \frac{I_n}{I_m}(1 - \exp(-T_{on}/Z_1))) \dots (7.17)$$

7.4.2.4 Average armature current

The average armature current I_{av} can be calculated by integrating and averaging the coil current over a period, i.e.

$$I_{av} = \frac{1}{T} \left(\int_0^{T_{on}} I_1(t) dt + \int_0^{T_{off}} I_2(t) dt \right) \dots (7.18)$$

And, the solutions are:

For continuous conduction ($T_{off} = T - T_{on}$)

$$\begin{aligned}
 I_{av} &= \frac{1}{T} \left(\int_0^{T_{on}} (I_n + (I_{cmin} - I_n) \exp(-t/Z_1)) dt \right. \\
 &\quad \left. + \int_0^{T_{off}} (I_m + (I_{cmax} - I_m) \exp(-t/Z_2)) dt \right) \\
 &= \frac{1}{T} (I_n T_{on} + I_m T_{off} + Z_1 (I_{cmin} - I_n) (1 - \exp(-T_{on}/Z_1)) \\
 &\quad + Z_2 (I_{cmax} - I_m) (1 - \exp(-T_{off}/Z_2))) \quad \dots (7.19)
 \end{aligned}$$

For discontinuous conduction ($T_{off} < T - T_{on}$)

$$\begin{aligned}
 I_{av} &= \frac{1}{T} \left(\int_0^{T_{on}} I_n (1 - \exp(-t/Z_1)) dt \right. \\
 &\quad \left. + \int_0^{T_{off}} (I_m + (I_{dmax} - I_m) \exp(-t/Z_2)) dt \right) \\
 &= \frac{1}{T} (I_n T_{on} + I_m T_{off} - Z_1 I_n (1 - \exp(-T_{on}/Z_1)) \\
 &\quad + Z_2 (I_{dmax} - I_m) (1 - \exp(-T_{off}/Z_2))) \quad \dots (7.20)
 \end{aligned}$$

7.4.2.5 Average dc link current

The average dc link current $I_{av(link)}$ is obtained by integrating the coil current over the on-period and averaging over a switching period, i.e.

$$I_{av(link)} = \frac{1}{T} \left(\int_0^{T_{on}} i_1(t) dt \right) \quad \dots (7.21)$$

And the solutions are:

For continuous conduction ($T_{off} = T - T_{on}$)

$$I_{av(link)} = \frac{1}{T} \int_0^{T_{on}} (I_n + (I_{cmin} - I_n) \exp(-t/Z_1)) dt$$

$$= \frac{1}{T} (I_n T_{on} + Z_1 (I_{cmin} - I_n) (1 - \exp(-T_{on}/Z_1))) \quad \dots (7.22)$$

For discontinuous conduction ($T_{off} < T - T_{on}$)

$$I_{av(link)} = \frac{1}{T} \int_0^{T_{on}} I_n (1 - \exp(-t/Z_1)) dt$$

$$= \frac{1}{T} (I_n T_{on} - I_n Z_1 (1 - \exp(-T_{on}/Z_1))) \quad \dots (7.23)$$

7.4.2.7 Computed results

Based on Equations (7.19) and (7.20), the steady-state armature current transfer characteristics of the PWM power regulator are calculated. Figure 7.30 gives the computed results where the switching period T is 50us (freq. = 20kHz). For comparison purposes the computed results for a switching period of 100us (freq. = 10kHz) is also given (Figure 7.31). It can be seen that the boundary between continuous and discontinuous conduction increases as the switching frequency decreases. To minimise the non-linearity caused by the discontinuous conduction, the switching frequency shall be kept as high as possible. The computed dc link current transfer characteristics are shown in Figure 7.32.

7.4.3 Regenerative braking mode

One of the major advantages of a PWM controlled brushless motor is its ability to brake regeneratively with a partial return of power to the source. The conduction sequence of the regenerative braking mode is given in Figure 7.33. For example in conduction-state VI, the power MOSFET T_2 is first of all turned on so as to build up an armature current. T_2 is then switched off, and the current is driven, through one of the free-wheeling diodes, back into the supply by the combined emfs of the armature and the circuit inductance. The regeneration process is depicted in the current flow diagrams in Figure 7.34. Using the current flow diagrams as a basis, equivalent circuits can be drawn to represent the regeneration period (Figure 7.35), and the equation describing such a period can be formulated.

7.4.3.1 The on-period equations (Figures 7.34(a) & 7.35(a))

The current equation for the on-period is

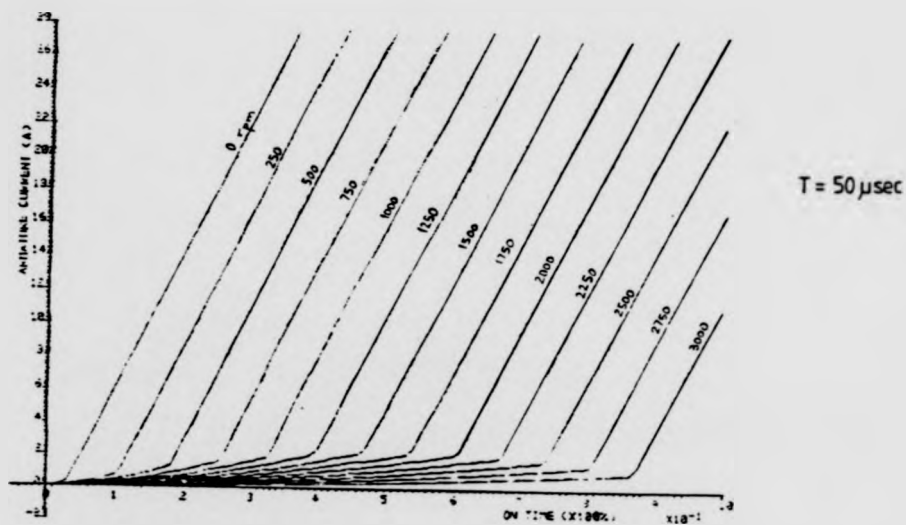


Figure 7.30 Motorino mode steady-state armature current transfer characteristics (carrier frequency = 20KHz)

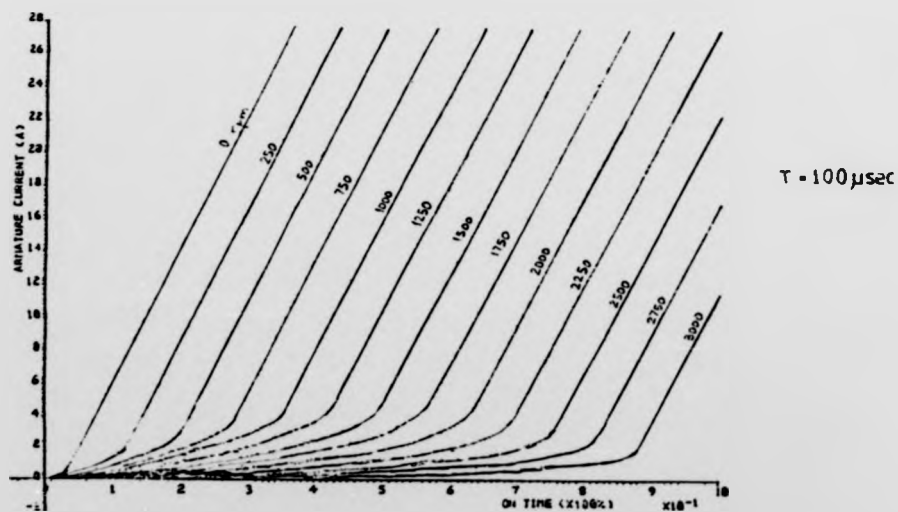


Figure 7.31 Motorino mode steady-state armature current transfer characteristics (carrier frequency = 10KHz)

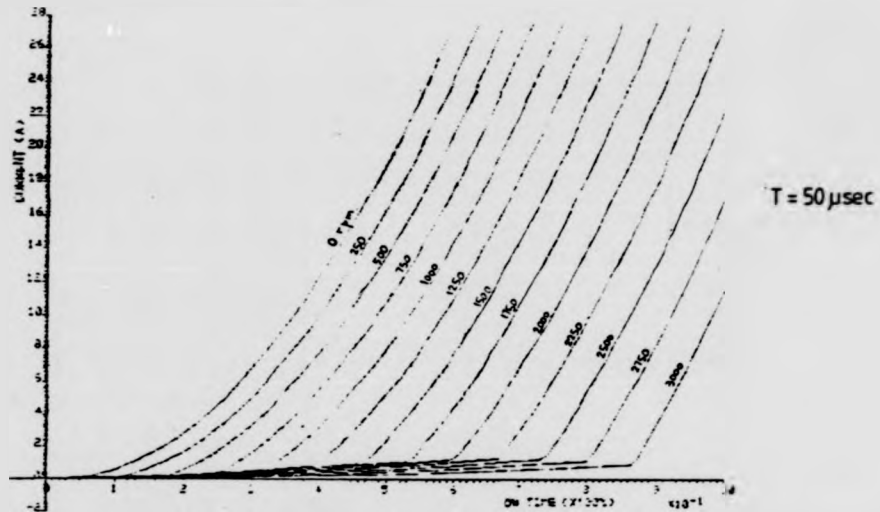


Figure 7.32 Motor mode steady-state dc-link current transfer characteristics (carrier frequency = 20KHz)

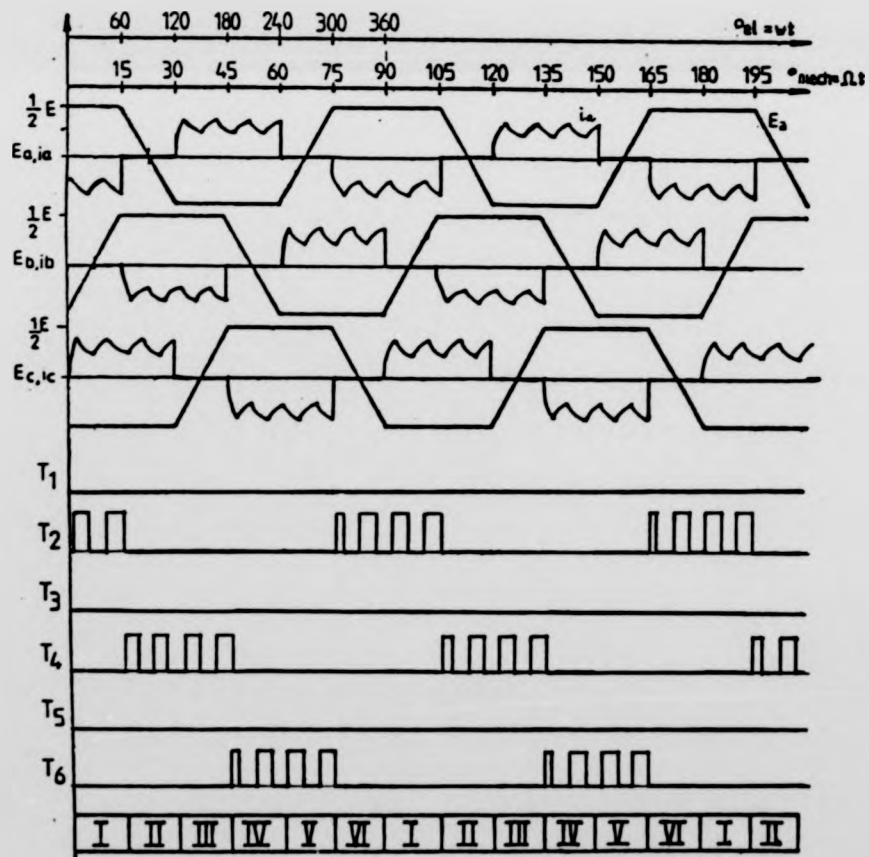


Figure 7.33 Relationship in time between the induced emfs, the driving signals, and the PWMed armature current for regenerating mode

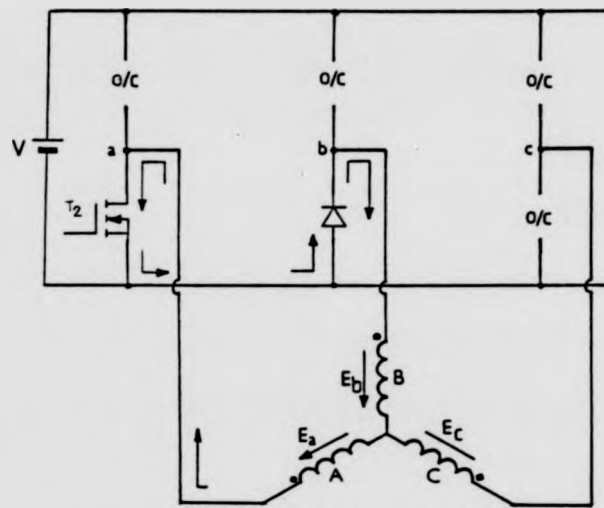


Figure 7.34(a) Regen. mode on-period current flow path (conduction-state VI)

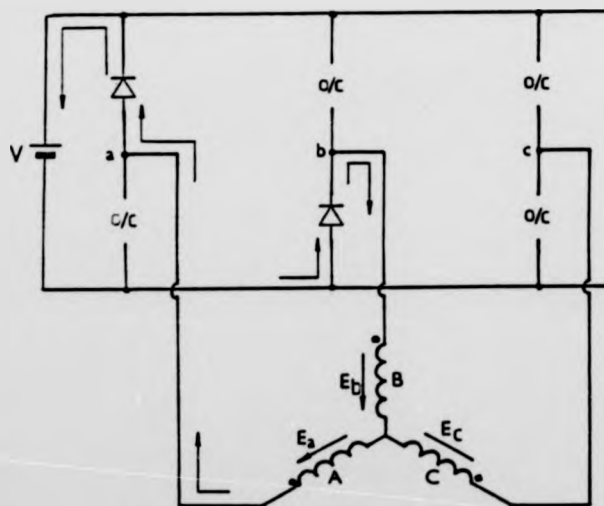


Figure 7.34(b) Regen. mode off-period current flow path (conduction-state VI)

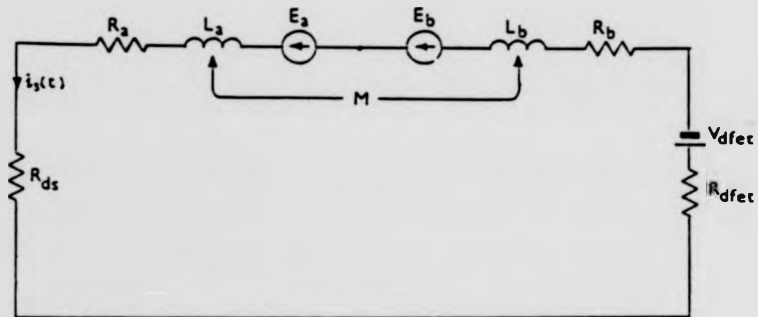


Figure 7.35(a) Regen. mode on-period equivalent circuit

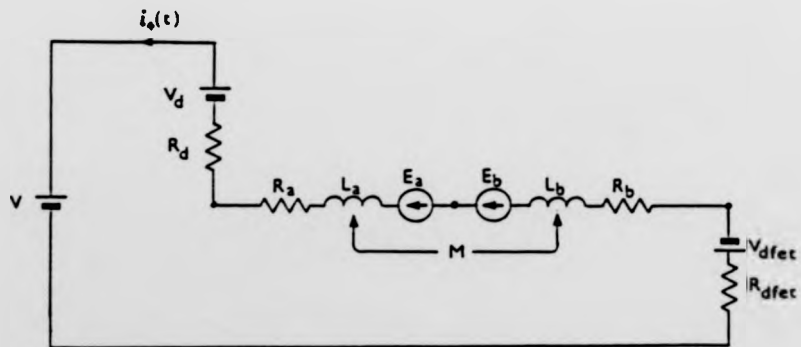


Figure 7.35(b) Regen. mode off-period equivalent circuit

- V_d = Schottky diode equivalent voltage source
- R_d = Schottky diode forward slope resistance
- R_{ds} = power MOSFET drain-source on-resistance
- V_{dfet} = body-drain diode equivalent voltage source
- R_{dfet} = body-drain diode forward slope resistance

$$E_a + E_b - V_{dfet} = i_3(R_{ds} + R_a + R_b + R_{dfet}) + (L_a + L_b)\frac{di_3}{dt} - 2M\frac{di_3}{dt} \quad \dots(7.24)$$

For a balanced winding, we have $E_a = E_b$, $R_a = R_b$ and $L_a = L_b$. The solution of the above differential equation is

$$i_3(t) = I_x + (I_3 - I_x)\exp(-t/Z_3) \quad \dots(7.25)$$

where

$$L_3 = 2(L_a - M)$$

$$R_3 = R_{ds} + 2R_a + R_{dfet}$$

$$E_3 = 2E_a - V_{dfet}$$

$$Z_3 = L_3/R_3$$

I_3 = initial current at the start of the on-period

$$I_x = E_3/R_3$$

7.4.3.2 The regen-period equation (Figure 7.34(b) & 7.35(b))

The current equation for the regen-period is

$$E_a + E_b - V - V_d - V_{dfet} = i_4(R_d + R_a + R_b + R_{dfet}) + (L_a + L_b)\frac{di_4}{dt} - 2M\frac{di_4}{dt} \quad \dots(7.26)$$

The solution of the above equation is

$$i_4(t) = I_y + (I_4 - I_y)\exp(-t/Z_4) \quad \dots(7.27)$$

where

$$L_4 = 2(L_a - M)$$

$$R_4 = R_d + 2R_a + R_{dfet}$$

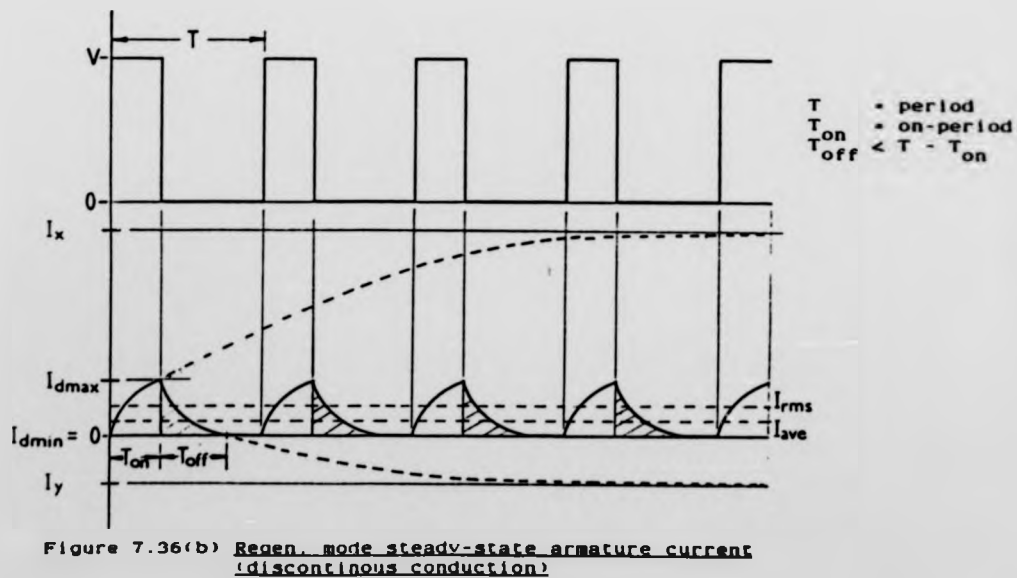
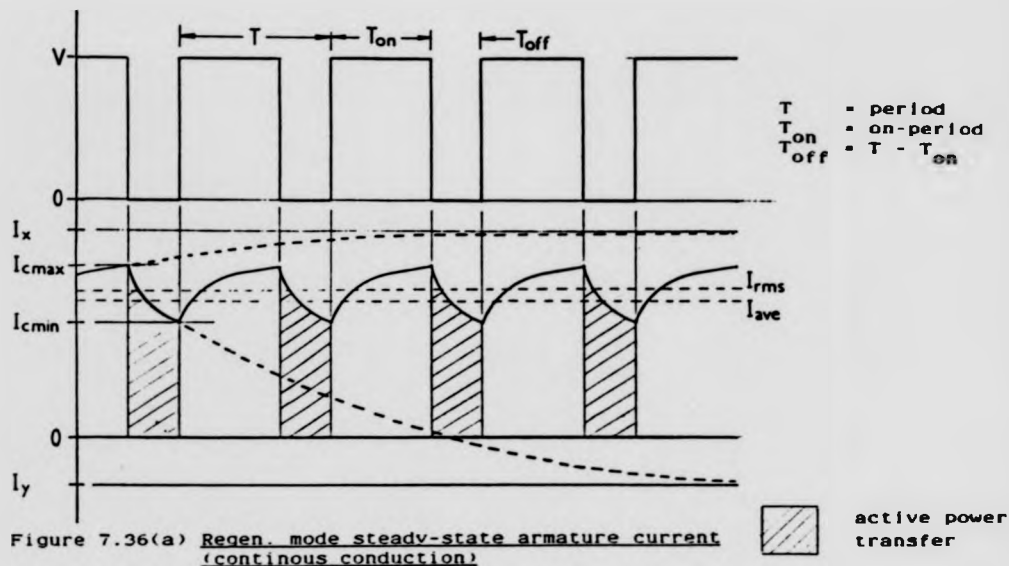
$$E_4 = 2E_a - V - V_d - V_{dfet}$$

$$Z_4 = L_4/R_4$$

I_4 = initial current at the start of the regen-period

$$I_y = E_4/R_4$$

Typical current waveforms governed by Equations (7.25) and (7.27) are illustrated in Figure 7.36. Using the two equations the steady-state maximum and minimum values of the braking current at a given speed can be calculated.



Continuous conduction

(i) During on-period

Let I_{cmin} = initial current ... ⑨

I_{cmax} = current after T_{on} ... ⑩

By substituting ⑨ and ⑩ to (7.25), the following is obtained

$$I_3(T_{on}) = I_{cmax} = I_x + (I_{cmin} - I_x) \exp(-T_{on}/Z_3) \quad \dots (7.28)$$

(ii) During regen-period

Let I_{cmax} = initial current ... ⑪

I_{cmin} = current after T_{off} sec ... ⑫

By substituting ⑪ and ⑫ to (7.27), the following is obtained

$$I_4(T_{off}) = I_{cmin} = I_y + (I_{cmax} - I_y) \exp(-T_{off}/Z_4) \quad \dots (7.29)$$

By solving (7.28) and (7.29), we get

$$I_{cmax} = \frac{I_x (1 - \exp(-T_{on}/Z_3)) + I_y (1 - \exp(-T_{off}/Z_4)) \exp(-T_{on}/Z_3)}{1 - \exp(-T_{off}/Z_4) \exp(-T_{on}/Z_3)} \quad \dots (7.30)$$

$$I_{cmin} = \frac{I_y (1 - \exp(-T_{off}/Z_4)) + I_x (1 - \exp(-T_{on}/Z_3)) \exp(-T_{off}/Z_4)}{1 - \exp(-T_{off}/Z_4) \exp(-T_{on}/Z_3)} \quad \dots (7.31)$$

Discontinuous conduction

(i) During on-period

Let I_{dmin} = initial current = 0 ... ⑬

I_{dmax} = current after T_{on} sec ... ⑭

By substituting ⑬ and ⑭ to (7.25), we have

$$I_3(T_{on}) = I_{dmax} = I_x (1 - \exp(-T_{on}/Z_3)) \quad \dots (7.32)$$

(ii) During regen-period

Let I_{dmax} = initial current ... (15)

I_{dmin} = current after T_{off} sec = 0 ... (16)

By substituting (15) and (16) to (7.27), we have

$$i_4(T_{off}) = 0 = I_y + (I_{dmax} - I_m) \exp(-T_{off}/Z_4) \quad \dots (7.33)$$

Substituting (7.32) to the above, T_{off} is obtained:

$$T_{off} = Z_4 \ln \left(1 - \frac{I_x}{I_y} (1 - \exp(-T_{on}/Z_3)) \right) \quad \dots (7.34)$$

7.4.3.3 Average braking current

The average braking current $I_{av}(\text{brake})$ is

$$I_{av}(\text{brake}) = \frac{1}{T} \left(\int_0^{T_{on}} i_3(t) dt + \int_0^{T_{off}} i_4(t) dt \right) \quad \dots (7.35)$$

And, the solutions are:

For continuous conduction ($T_{off} = T - T_{on}$)

$$\begin{aligned} I_{av}(\text{brake}) &= \frac{1}{T} \left(\int_0^{T_{on}} (I_x + (I_{cmin} - I_x) \exp(-t/Z_3)) dt \right. \\ &\quad \left. + \int_0^{T_{off}} (I_y + (I_{cmax} - I_y) \exp(-t/Z_4)) dt \right) \\ &= \frac{1}{T} (I_x T_{on} + I_y T_{off} + Z_3 (I_{cmin} - I_x) (1 - \exp(-T_{on}/Z_3)) \\ &\quad + Z_4 (I_{cmax} - I_y) (1 - \exp(-T_{off}/Z_4))) \quad \dots (7.36) \end{aligned}$$

For discontinuous conduction ($T_{off} < T - T_{on}$)

$$\begin{aligned} I_{av}(\text{brake}) &= \frac{1}{T} \left(\int_0^{T_{on}} I_x (1 - \exp(-t/Z_3)) dt \right. \\ &\quad \left. + \int_0^{T_{off}} (I_y + (I_{dmax} - I_y) \exp(-t/Z_4)) dt \right) \end{aligned}$$

$$\begin{aligned}
 &= \frac{1}{T} (I_x T_{on} + I_y T_{off} - Z_3 I_x (1 - \exp(-T_{on}/Z_3)) \\
 &\quad + Z_4 (I_{dmax} - I_m) (1 - \exp(-T_{off}/Z_4))) \quad \dots (7.37)
 \end{aligned}$$

7.4.3.4 Average regenerative current

The regenerative current returning power to the source flows only during the regen-period (the off-period). The average regenerative current $I_{av}(\text{regen})$ is thus:

$$I_{av}(\text{regen}) = \frac{1}{T} \int_0^{T_{off}} i_4(t) dt \quad \dots (7.38)$$

And, the solutions are:

For continuous conduction ($T_{off} = T - T_{on}$)

$$\begin{aligned}
 I_{av}(\text{regen}) &= \frac{1}{T} \int_0^{T_{off}} (I_y + (I_{cmax} - I_y) \exp(-t/Z_4)) dt \\
 &= \frac{1}{T} (I_y T_{off} + Z_4 (I_{cmax} - I_y) (1 - \exp(-T_{off}/Z_4))) \quad \dots (7.39)
 \end{aligned}$$

For discontinuous conduction ($T_{off} < T - T_{on}$)

$$\begin{aligned}
 I_{av}(\text{regen}) &= \frac{1}{T} \int_0^{T_{off}} (I_y + (I_{dmax} - I_y) \exp(-t/Z_4)) dt \\
 &= \frac{1}{T} (I_y T_{off} + Z_4 (I_{dmax} - I_y) (1 - \exp(-T_{off}/Z_4))) \quad \dots (7.40)
 \end{aligned}$$

7.4.3.5 Computed results

From Equations (7.36) and (7.37) the steady-state braking current transfer characteristics are calculated, and are given in Figure 7.37. And, Figure 7.38 gives the regenerative current transfer characteristics.

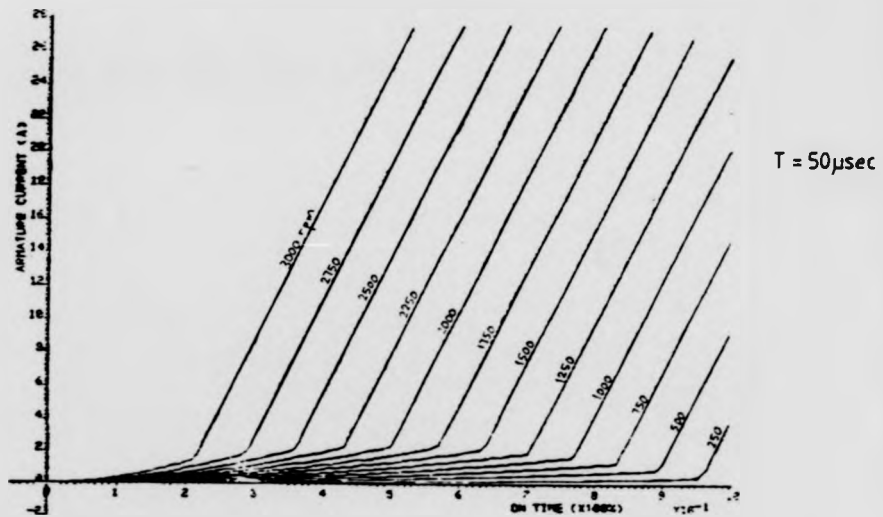


Figure 7.37 Regen. mode steady-state armature current transfer characteristics
(carrier frequency = 20KHz)

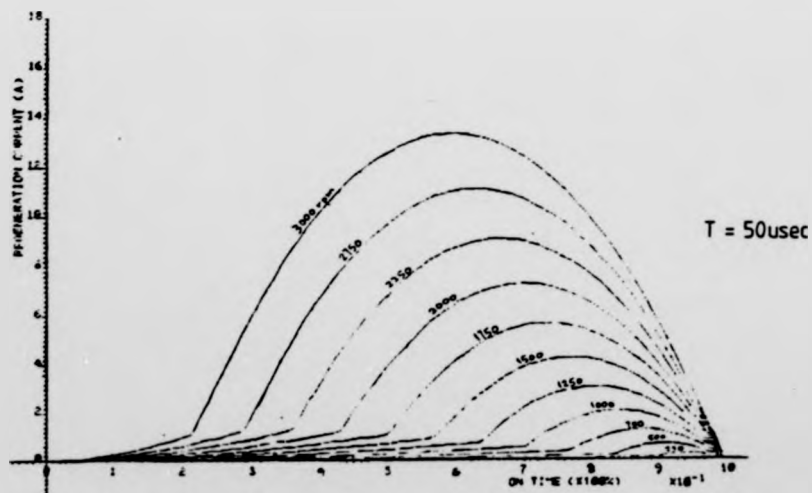


Figure 7.38 Regen. mode steady-state regen. current transfer characteristics
(carrier frequency = 20KHz)

CHAPTER 8 MOTOR DRIVE CONTROL SUB-SYSTEM

8.0 Introduction

Microprocessors as general purpose building blocks have become increasingly popular in electronic and control systems. They were first introduced by Intel Corporation in 1972 as programmable logic devices with 'restricted computing power' to replace a multiplicity of logic gates (67).

As the potential of microprocessors came to be recognised, the race for greater computing power and increased speed was on. And during the next three years, half a dozen or so manufacturers managed to develop single-chip microprocessors with performances approaching those of the CPUs of some minicomputers.

In recent years, advances in VLSI (Very Large Scale Integrated-circuits) technology and manufacturing processes have not only crammed enormous computing power into tiny silicon wafers, but they have also made it possible for these microprocessor components to be manufactured at a realistic price level. And as the cost of these components continue to fall, their use is rapidly penetrating new application frontiers. To name but a few of the marvels, microprocessors have already replaced TTL logics in such applications as intelligent terminals, peripheral device controllers, NC machines, industrial robots and information systems. Recently, a great deal of interest has also been generated in the applications of microprocessors in industrial drives (67,68,69). A microprocessor-based motor drive control system promises several distinct advantages, the greatest one being that of flexibility. The control scheme is implemented in software, which means that only the software needs to be modified in order to change the control scheme for obtaining a different drive characteristic, and minimal, or no, change in the hardware is necessary. Also, the operation of a microprocessor-based controller can be completely digital.

CHAPTER 8 MOTOR DRIVE CONTROL SUB-SYSTEM

8.0 Introduction

Microprocessors as general purpose building blocks have become increasingly popular in electronic and control systems. They were first introduced by Intel Corporation in 1972 as programmable logic devices with 'restricted computing power' to replace a multiplicity of logic gates (67).

As the potential of microprocessors came to be recognised, the race for greater computing power and increased speed was on. And during the next three years, half a dozen or so manufacturers managed to develop single-chip microprocessors with performances approaching those of the CPUs of some minicomputers.

In recent years, advances in VLSI (Very Large Scale Integrated-circuits) technology and manufacturing processes have not only crammed enormous computing power into tiny silicon wafers, but they have also made it possible for these microprocessor components to be manufactured at a realistic price level. And as the cost of these components continue to fall, their use is rapidly penetrating new application frontiers. To name but a few of the marvels, microprocessors have already replaced TTL logics in such applications as intelligent terminals, peripheral device controllers, NC machines, industrial robots and information systems. Recently, a great deal of interest has also been generated in the applications of microprocessors in industrial drives (67,68,69). A microprocessor-based motor drive control system promises several distinct advantages, the greatest one being that of flexibility. The control scheme is implemented in software, which means that only the software needs to be modified in order to change the control scheme for obtaining a different drive characteristic, and minimal, or no, change in the hardware is necessary. Also, the operation of a microprocessor-based controller can be completely digital.

which makes the system less susceptible to thermal drifts and environmental changes. A microprocessor-based controller, if rationally designed, can allow considerable simplification, and hence improved reliability in the hardware.

This chapter describes the microprocessor-based controller sub-system of a prototype brushless drive system. This drive system consists of three main system elements. These are: the brushless dc disc-motor, the electronic power regulator (EPR), and the controller.

The first two system elements have already been covered in Chapter 6 and Chapter 7 respectively.

Section 8.1 of this chapter gives the functional requirements of the controller, and presents the design solution to the requirements by partitioning the controller into the hardware sub-system and software sub-system. Section 8.2 will describe the hardware sub-system design in detail, and Section 8.3 gives the software sub-system design. The test results are given in Section 8.4, and Section 8.5 will discuss the results.

8.1 Functional Requirements and Design Solution

The controller sub-system was intended to be a general purpose controller for studying the output characteristics of various brushless drive configurations. It had to be flexible enough to adapt to different drive methods with minimum modifications to the hardware. Another requirement was that extra control functions can be easily added if necessary.

8.1.1 Commutation control

The relationship in time between the motor's emfs and the power regulator's commutation control signals were depicted in Figure 4.7. These signals are obtained by decoding the data outputs of the rotor position detector. The

decoding is carried out by the microprocessor's interrupt logic and the associated interrupt handler. The block diagram of the commutation control logic is given in Figure 8.1.

The implementation of the position decoding in software means that the controller can be adapted to operate different drive configurations with changes in the software only. Also, automatic commutation advance can be easily incorporated.

8.1.2 PWM torque-control

The drive system is required to operate in the torque-control mode. As torque is directly proportional to the armature current (due to the fact that the disc-motor is completely free of magnetic saturation and has negligible armature reaction), it is therefore possible to achieve torque control by controlling the armature current. To achieve current control three methods are available, these are: (1) feed-back control, (2) real-time calculation of the required PWM duty-time (by solving the current equations (7.19), (7.20), (7.36) and (7.37)), and (3) look-up table technique.

The first is an active (closed-loop) control method, and when judiciously designed this method provides the most accurate control over the armature current. However, to implement a closed-loop scheme, analogue to digital conversion circuits are required, and the system cost will be increased.

The second and the last methods both fall into the passive (open-loop) control scheme, which is less accurate than the active scheme. But although the passive scheme may be less accurate, it does not require transducers or sensors to measure the controlled parameter for feed-back purposes, and are inherently cheaper.

For cost reasons, the last method was chosen to perform the control function, as such method can be conveniently implemented using a low cost 8-bit microprocessor. The reason for not using the real-time computational method was

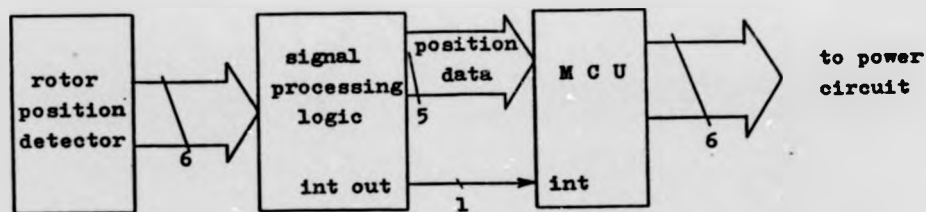


Figure 8.1 Block diagram of the commutation control logic

	SPEED (rpm)				
	0	50	100	...	3000
0	0	0	0	...	0
0.5	14	21	24	...	240
1.0	16	23	29	...	341
⋮	⋮	⋮	⋮		⋮
⋮	⋮	⋮	⋮		⋮
20.0	63	70	77	...	483

Figure 8.2 Two-dimensional array of PWM on-times

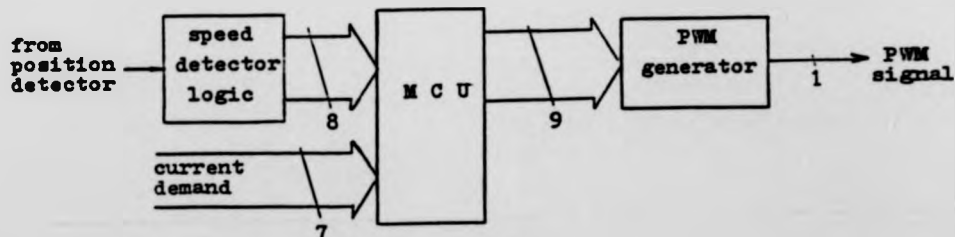


Figure 8.3 Block diagram of the PWM torque-control logic

that it is computationally intensive, which would involve the solving of several non-linear equations. It is unlikely that today's low cost 8-bit microprocessors could accomplish such a task in real-time.

In implementing the look-up table technique, the current transfer characteristics of the EPR are firstly calculated and, secondly quantised into a two-dimensional array of PWM on-times, as shown in Figure 8.2. The row- and column- variable represent current demand and the rotor angular speed respectively. The array is then stored in the Read Only Memory (ROM) of the controller. At run time, the required PWM data is retrieved by the microprocessor from the ROM according to the demanded current and the angular speed.

In this implementation, the PWM data are quantised into 51 speed-steps and 41 current-steps. The speed range is between 0rpm to 3000rpm, each speed-step represents a 50rpm change in speed. The maximum armature current is set to 20A, which gives a 0.5A change per step from zero to full current. As the PWM data are 9-bit wide, it is not possible to store them in single bytes. To save memory space, the data are split into two parts, and each part is held in a separate table. The first part is 8-bit wide and is held in the main look-up table. The other part is only 1-bit long, and is held in a smaller auxiliary table.

The block diagram of the PWM torque-control logic is shown in Figure 8.3. The function of the microprocessor is to provide a linearised transfer characteristic for the EPR, such that the output current is directly proportional to the input demand and is independent of the rotor speed. The equivalent system diagram is illustrated in Figure 8.4.

8.2 Hardware Sub-system Design and Implementation

8.2.1 Overview

An outline of the controller's hardware sub-system is shown in Figure 8.5. From a functional point of view, the controller can be sub-divided into five modules. They are:

1. Microprocessor Controller Unit (MCU)
2. Position Detector
3. Speed Detector
4. PWM Generation Logic

and

5. Over-current Protection Logic.

Input signals from the position detector are conditioned by the Position Detector and then processed by the MCU to provide rotor position information. This information will be decoded further to generate the envelope conduction signals to the power regulator. One of the optical scanners is also responsible for driving the Speed Detector to provide the speed information. This speed information, together with the demand input, form the basis for generating the PWM signal. The Over-current Logic provides a concerted system shut-down in case of current overloading of the EPR.

Each module is built individually on a 114mm Strip Board. The whole of the sub-system is housed in a 19in. sub-rack as illustrated in Figure 8.6. Most of the electrical signals are passed between modules via the edge connectors situated at the back of the sub-rack.

8.2.2 The MCU Module

The microprocessor chosen for the controller is a 1MHz Motorola M6809 8-bit microprocessing unit (70,71). This third-generation microprocessor has major architectural improvements over the popular M6800. They included additional registers, instructions and addressing modes. Such enhancements have made this processor very suitable for control applications. Apart from the microprocessing unit, the MCU Module also has other supporting chips to provide the module with interfacing and other hardware functions. The functional block diagram of this module is given in Figure 8.7.

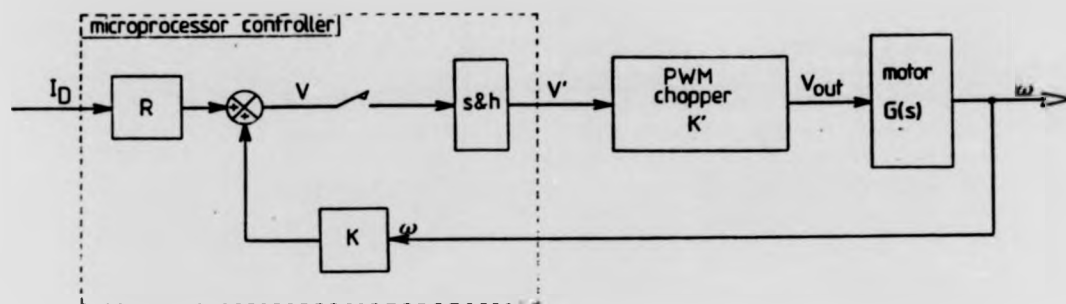


Figure 8.4 Equivalent system diagram of the controller

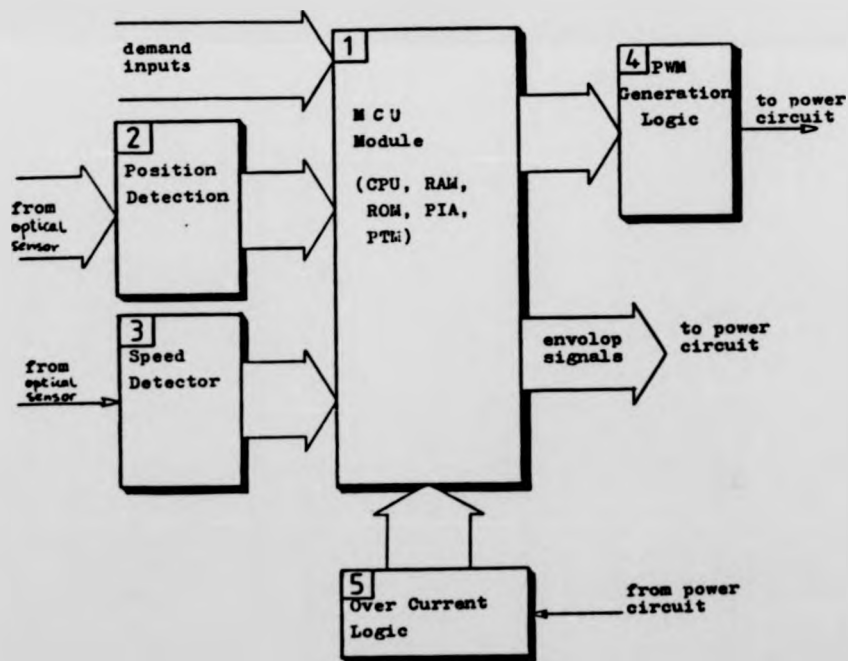


Figure 8.5 Outline of the controller's hardware sub-system

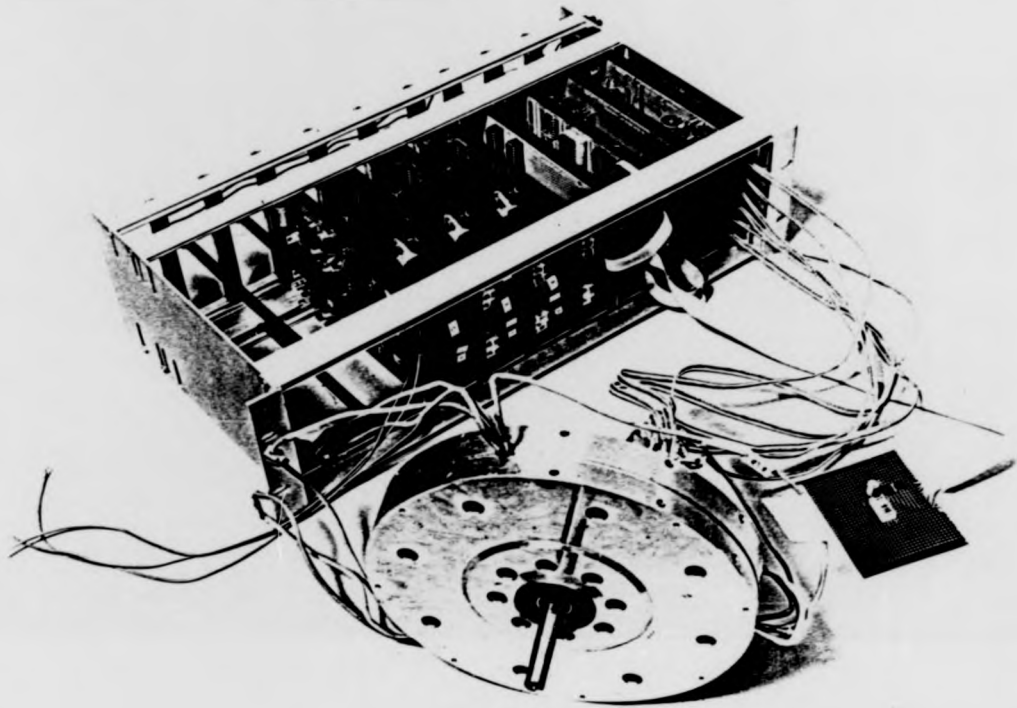


Figure 8.6 Picture of the hardware sub-system

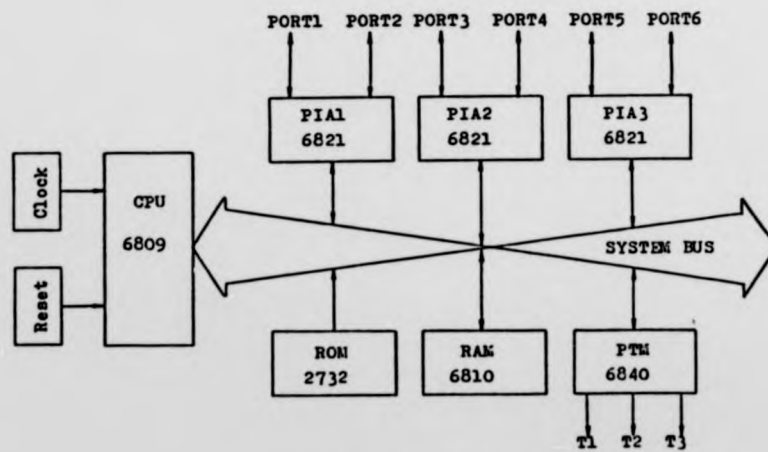


Figure 8.7 Function block diagram of the MCU Module

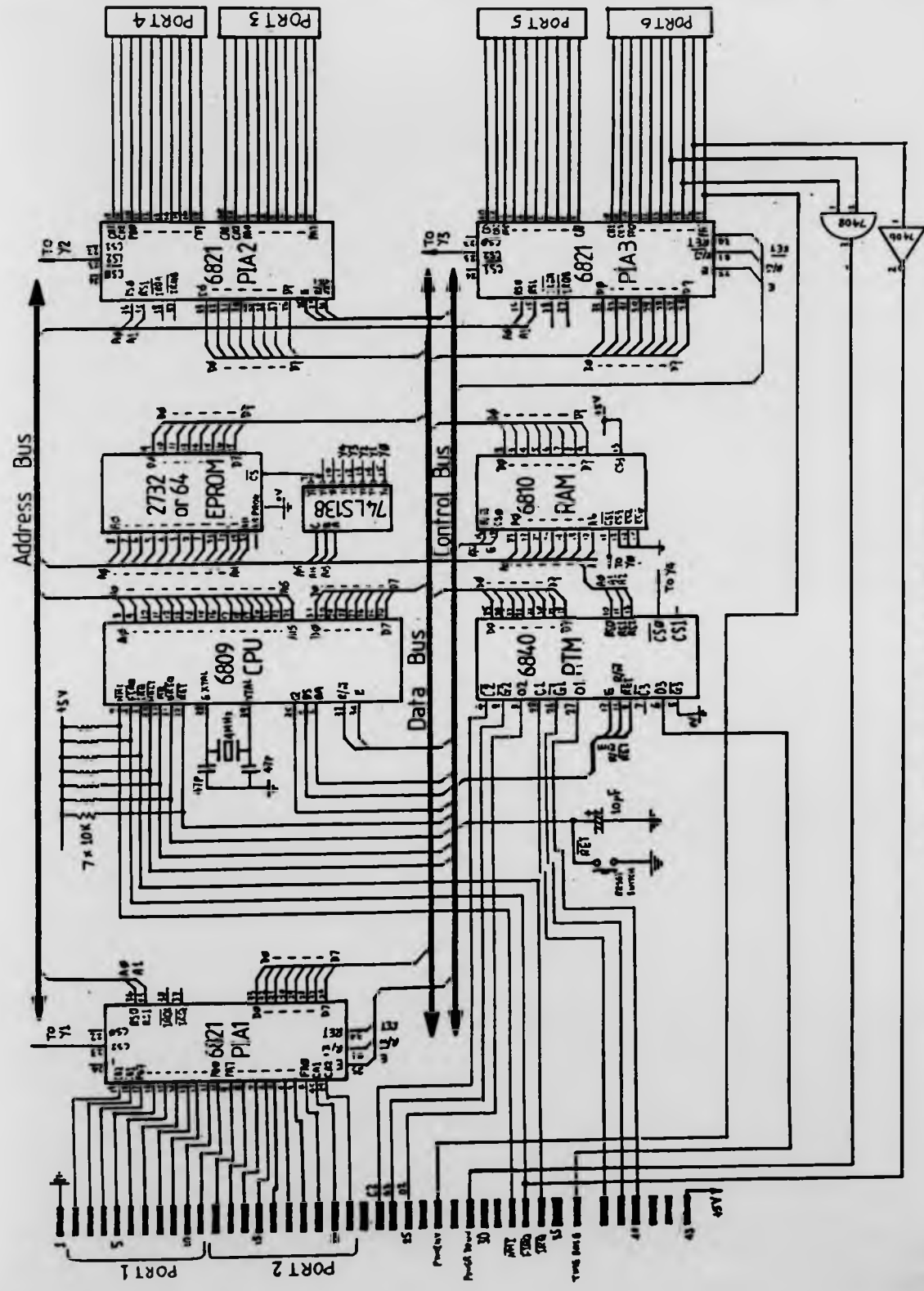


Figure 8.8 Schematic of the MCII logic

The control program is stored in the ROM. The read/write memory (RAM) is used by the system stack and the data pool. Three peripheral interface adapters (PIAs) are used to interface the microprocessor with the external circuits. A programmable timer module (PTM) is also provided. One of the counters is used to generate hardware interrupts for the main control routine. The two remaining counters were initially used to generate the PWM signals, but they have since been substituted by a faster PWM generation logic. The schematic diagram of the MCU Module is given in Figure 8.8; its memory map and port assignments are given in Appendix E.

8.2.3 Position Detector Module

This module consists of three elements: a coded reflective disc, an optical sensor assembly and signal processing logic. The functional diagram of the Position Detector is shown in Figure 8.9. The first two elements have already been described in Section 6.6, and this section will describe the signal processing logic.

The function of the signal processing logic is to prepare the rotor position data for the MCU, and to inform the MCU of the availability of a new position data. Figure 8.10 gives the schematic circuit diagram. The phototransistor T_1 of an optical scanner channel is connected as part of a Schmitt Trigger, which consists of T_1 , T_2 and T_3 , such that the positive feed-back action of the Schmitt Trigger accelerates the switching of the phototransistor. This ensures that the scanners are following the data pattern closely even when the motor speed is higher than 3000rpm.

Assuming that the motor is running at 3000rpm, the maximum designed speed, and the coded pattern, which is scanned by the scanners, is just changing from white to black (or vice versa), it will take the rotor a further 100usec to move half of a rectangular-pattern (see Section 6.6), relative to the scanners. This 100usec allows enough time for the phototransistors to stabilise in their new output states. By that time the S3010-3 scanner would have detected the presence

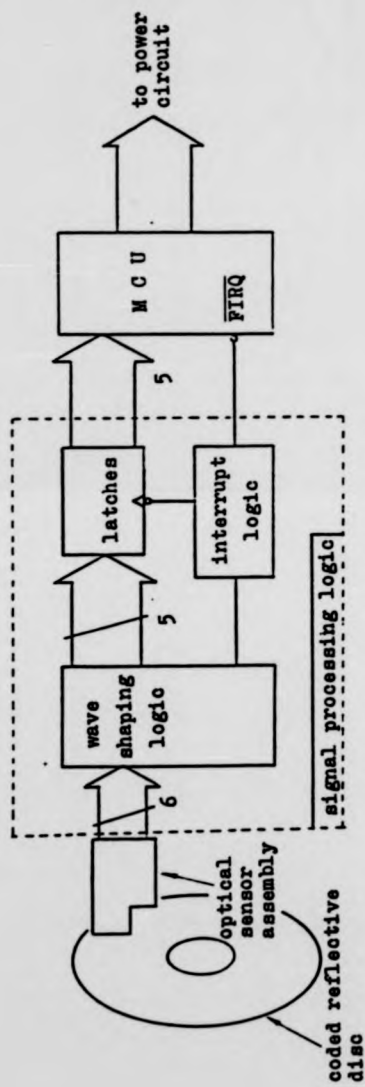


Figure 8.9 Function block diagram of the Position Detector Module

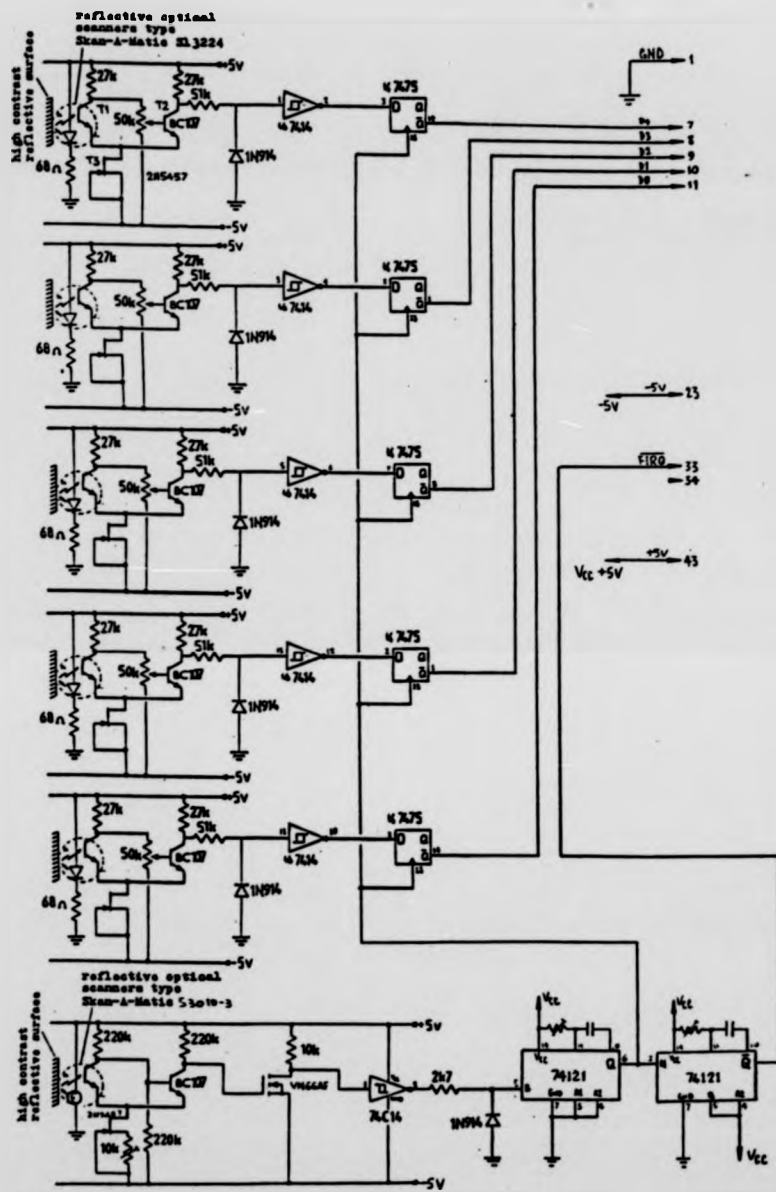


Figure 8.10 Schematic of the Position Detector Logic

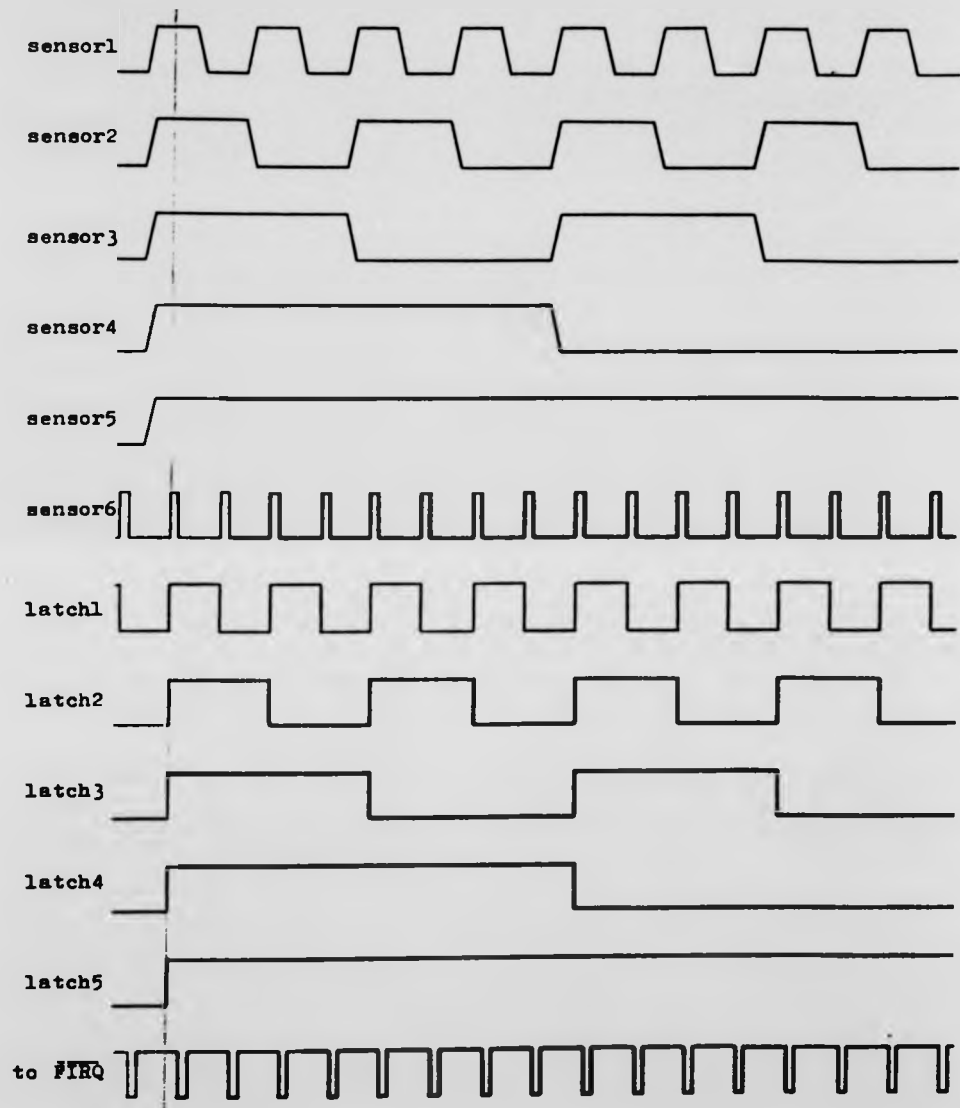


Figure 8.11 Timing relationships of the signal processing logic

of a white line. This signal will first latch the 5-bit position data, and then alert the MCU, via the FIRQ line, of a new position data. Upon reception of a FIRQ request, the microprocessor will suspend the current task and process the position data immediately. Figure 8.11 shows the timing relationships of the signal processing logic.

In this implementation of position detection, the data decoding, and the generating of the commutation signals are achieved by a software routine. The software can easily be modified to suit other types of brushless motor configurations, and is therefore very flexible. However, such a scheme uses up a large portion of the processor time, which could have been used to perform other control tasks. At the maximum motor speed, the detector logic interrupts the microprocessor 4800 times a second, i.e. about 200usec between interrupts. It is estimated that the FIRQ routine takes about 115usec to complete, such that there is a time slot of only 85usec before the occurrence of the next FIRQ interrupt. In other words, there is only 43% of the processor time left for other tasks. This severely limits the scope of any real-time control scheme. Fortunately, the constant torque control scheme used by the controller takes up less than 30% of the processor time, and the total processor loading is less than 87%. This gives a safety margin of 13% before the processor is overloaded.

8.2.4 Speed Detector Module

The function of this module is to detect the rotor speed, and to generate the IRQ timing signal required by the main control routine. The schematic and the timing relationship diagrams are both shown in Figure 8.12.

The speed-detecting function is provided by two 4-bit binary counters, the time-base frequency of which (10HZ) is generated by the Timer 2 of the PTM of the MCU Module. A count period is initiated by the rising edge of a time-base cycle. At the start of each count period, a 2usec pulse is generated to reset the counters. Immediately after this reset pulse the counting input is enabled. The count-pulses are derived from the outputs of the S3010-3 scanner. At the

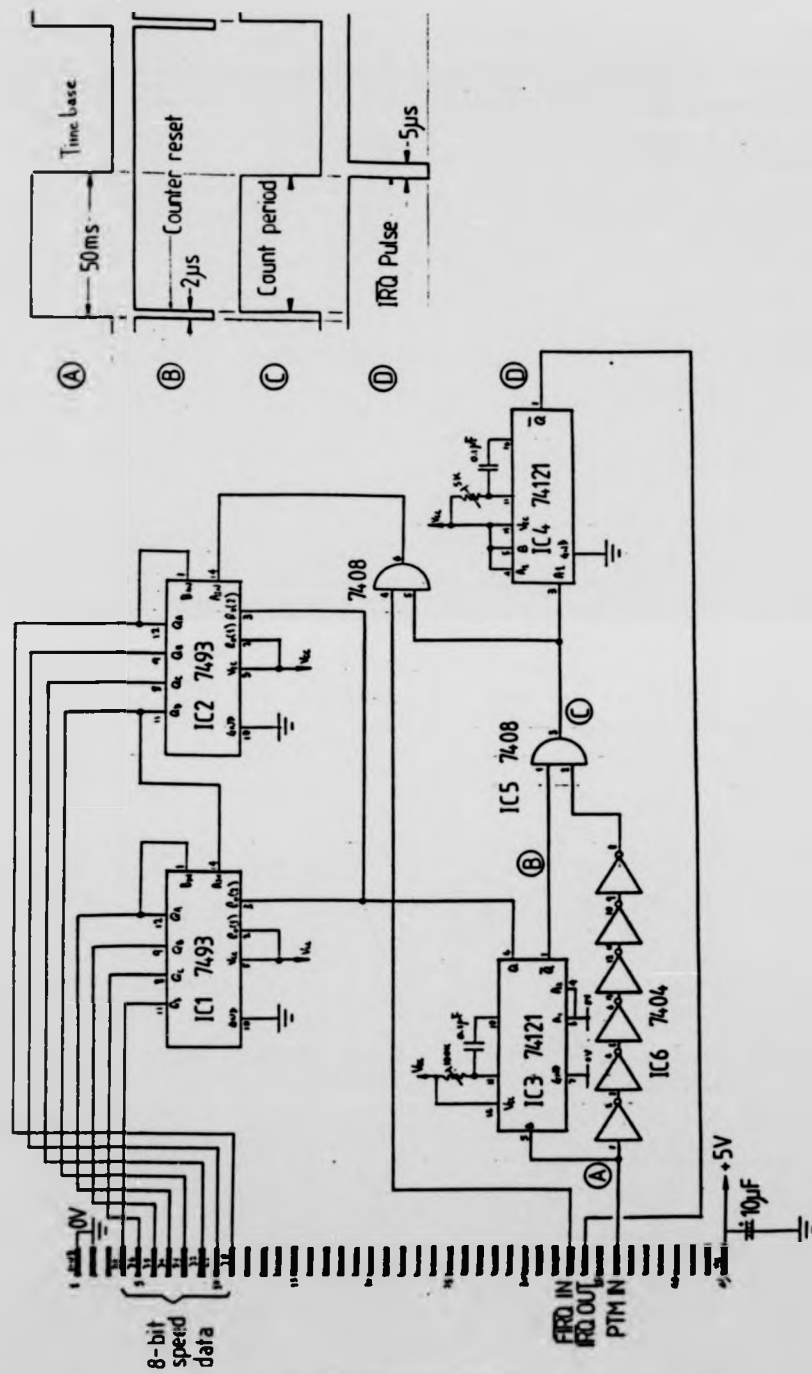


Figure 8.12 Schematic and signal timings of the Speed Detector Logic

falling edge of the time-base cycle the counting input is disabled, and an IRQ interrupt request is issued. The IRQ handler is then activated, the rotor speed is read, and the control algorithm executed. The IRQ handler must be completed before the next IRQ request, which occurs 100msec after the initiation of the last request. This 100msec interval is the sampling period of the control scheme. As the brushless motor is intended for traction applications where the time-constants of the driven systems are much longer than 100msec, a sampling period of 100msec will be adequate. But for fast response application such as servo control, the sampling period must be reduced to give a faster response.

The resolution of the speed detector can be calculated as follows:

no. of FIRQ pulses generated per mechanical revolution	= 96
no. of FIRQ pulses generated per min. at speed w rpm	= $96w$
if count-period	= 50 msec
then no. of counts in one count-period	= $96w \times 50 / 60 \times 10^{-3}$ count/rev
\therefore each count represents $w / (\text{count/rev})$ rpm	= 12.5 rpm

8.2.5 PWM Generation Logic

The operation principle of the PWM generator was described in Section 7.2.2, and its electronic circuit will now be described. Figures 8.13 and 8.14 give the schematic diagram and the timing relationships respectively.

The PWM carrier frequency is 20kHz; this frequency is generated by the 10MHz crystal and the three decade counters (IC7, IC8 and IC9). At the rising edge of a carrier cycle, an 8-bit data is loaded onto the synchronous down counters (IC2 and IC3) by the strobe signal C, which is generated by the monostable (IC10). At the same time, point E changes to logic high and the clock pulse input to IC2 is enabled. After a predefined number of clock pulses, which is determined by the pulse-width data, IC2 and IC3 will both be down-counted to zero. The output of IC4 E will change to logic low, and this will inhibit the clock pulse input to IC2 until the next data strobe. This process of loading and down counting

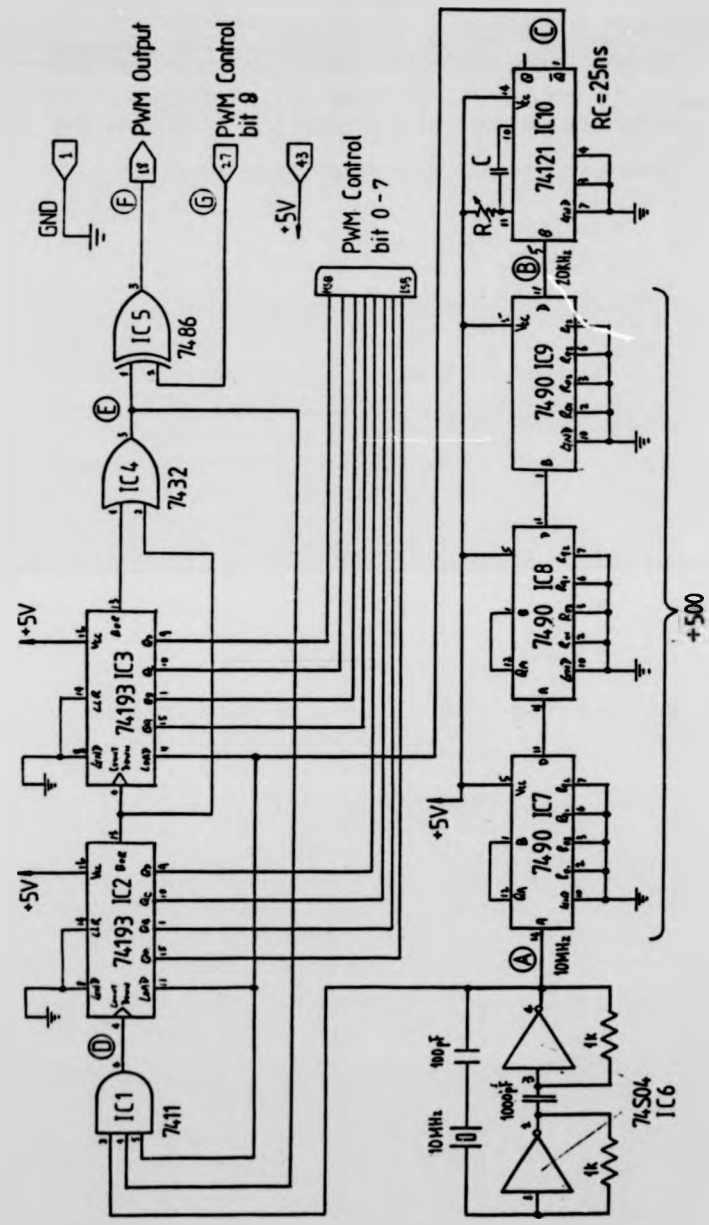


Figure 8.13 Schematic diagram of the PWM Generation Logic

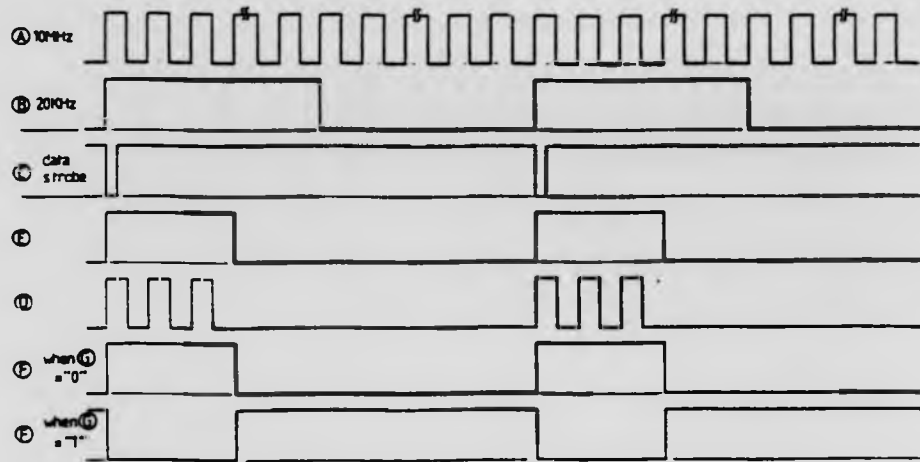


Figure 8.14 Signal timings of the PWM Generation Logic

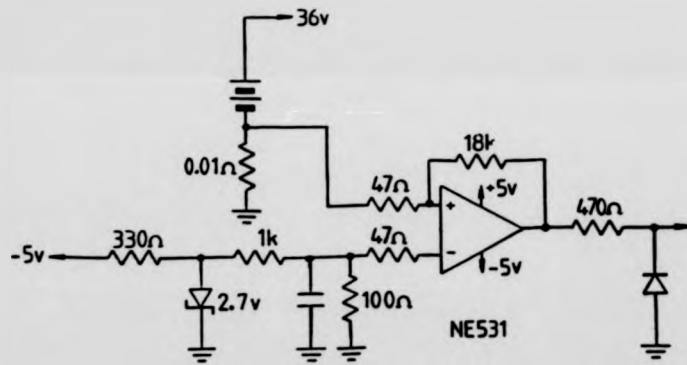


Figure 8.15 Schematic diagram of the Over-current Protection Logic

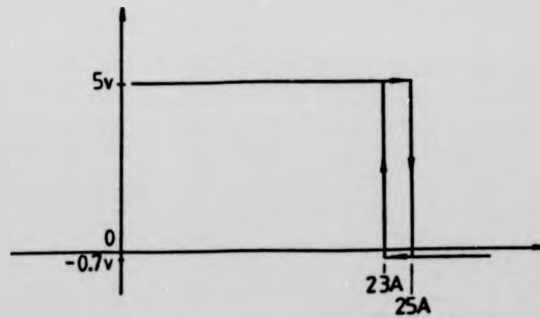


Figure 8.16 Transfer characteristic of the Over-current Protection Logic

repeats at a rate equal to the carrier frequency; and the pulse-width of the PWM pulse-train is determined by the data loaded to the down counters.

With the two 4-bit counters, the PWM logic can only generate pulses with width up to 25.5usec, while 50usec is the required maximum. In order to generate longer pulses, IC5 is added to perform an Exclusive-OR function. The IC5 will either invert or maintain the logic level of output E, depending on the logic level of the PWM control-bit 8.

When bit-8 is high, E is inverted, and when bit-8 is low, E is unchanged. Hence to produce pulses longer than 25.5usec, control-bit 8 is set high and the 8-bit counter data is changed to a smaller value, as shown in Figure 8.14.

8.2.6 Over-current Protection Logic

The function of this module is to protect the power circuit from accidental current overload. The protection circuit consists of a high-speed comparator, a voltage reference and a number of other passive components. The schematic diagram is shown in Figure 8.15. The peak armature current is monitored by the comparator IC1, whose output assumes a logic high state in normal operation. If the armature current accidentally exceeds 25A, it will immediately set the comparator output to logic low which in turn switches off all power devices and initiates a non-maskable interrupt (NMI) sequence. The drive system will then stay inactive until a system reset is issued by the operator. Figure 8.16 gives the transfer characteristic of the protection logic.

8.3 Software Sub-system Design and Implementation

8.3.1 Overview

Like most microprocessor-based control systems, the brushless dc disc-motor (the plant) and its controller interact in a real-time mode. This simply means that the controller must perform the required control tasks simultaneously as it

operates or interacts with the plant. These tasks include input signals sampling, calculations to actually implement the control algorithm and output the control signals to the plant. In real-time control, execution timing is crucial. If the control tasks are not executed at the right moment, input measurements can be missed and/or false timing signals generated. This can, at worst, lead to system failure, and, at best, to inefficient or unreliable performance. To enable the control tasks to run in synchronism with the plant's operation, an interrupt-driven control strategy must be used.

An interrupt-driven system usually has more than one interrupt request input. Each input is used to initiate the execution of a particular task. To resolve the possible conflicting requests, the inputs are assigned different priority levels whereby a request will not be serviced while a task of a higher priority is running. The interrupt-driven tasks are usually known as the foreground tasks. As for the least time critical tasks, they will not be assigned interrupt inputs, and the tasks will assume the lowest priorities. These tasks are called the background tasks, and will be executed only when the foregrounds are asleep, i.e. when the foregrounds are pending interrupt requests.

8.3.2 Software design

In order to synchronise the control tasks, an interrupt driven system is used. The functional diagram of the software sub-system is outlined in Figure 8.17. The sub-system is functionally divided into five modules, they are:

1. Power Down (A1) - this foreground module assumes the highest priority and uses the Non-Maskable Interrupt (NMI) input channel. Its task is to shut down the power regulator under over-current condition.
2. Position Decoding (A2) - the task of this foreground module is to detect the rotor position and to control the commutation sequence. It has the 2nd highest priority.
3. PWM Control (A3) - this foreground module embodies the main control algorithm of the drive system and has the 3rd highest priority.

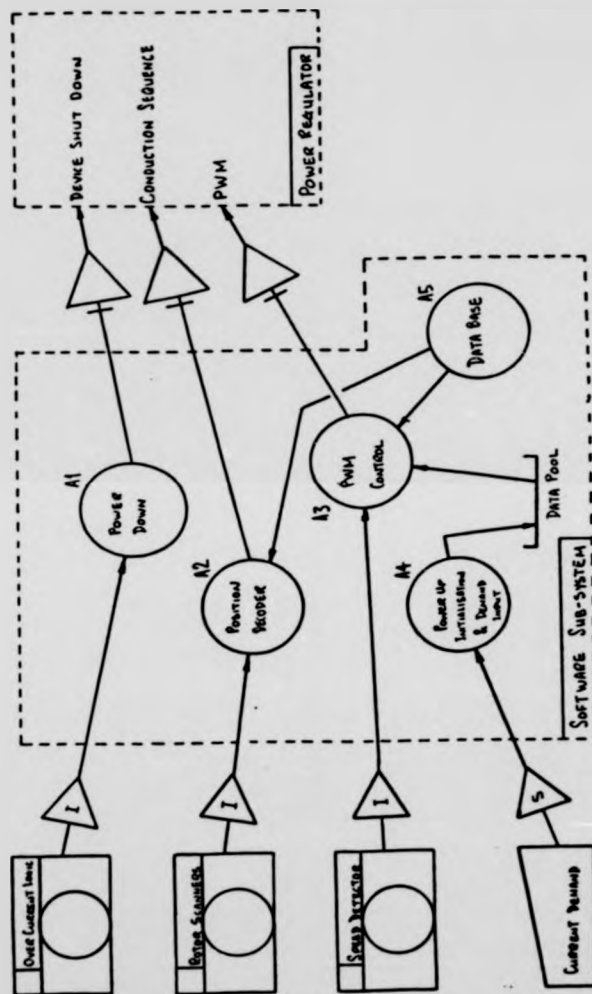


Figure 8.17 Functional diagram of the software sub-system

4. Power-up Initialisation and Demand Input (A4) - this lowest priority module performs the system power-up initialisation and other non-time-critical monitoring functions.
5. Data Base (A5) - the data base consists of various look-up tables and interrupt vectors. This module is non-executable.

8.3.3 Power Down (A1)

The operation of this module is shown in Figure 8.18. In receiving an NMI request, the processor will suspend its current task, and execute the NMI handler. The handler disables all the power devices by setting all the PORT2 outputs to logic low. It also disables the PWM generator by putting the PORT5 outputs and the PWM control bit-8 to logic low, masks off further interrupts, and enters into an endless waiting loop until a system reset is issued by the operator.

8.3.4 Position Decoding (A2)

This FIRQ handler is executed every time new position data is available from the Position Detector. Its task is to control the conduction sequence of the power devices. When this handler is invoked, the processor will firstly read in the position data via PORT1. Secondly, based on the position data, the conduction pattern of the power devices is picked up from the position-decoding look-up table (TABLE1). Finally, the conduction pattern is output to PORT2 which in turn controls the conductions of the power devices. The flow-chart is shown in Figure 8.19.

The execution frequency of this handler is proportional to the angular speed of the motor. As the speed increases the processor loading also increases. It is therefore essential to minimise the overheads incurred in servicing this interrupt. To this end the FIRQ input is assigned to this handler. On reception of a FIRQ request, the microprocessor saves only the Program Counter (PC) and the Condition Code Register (CCR) to the system stack, and jumps straight to the handler. The interrupt sequence takes only 11 machine cycles instead of the

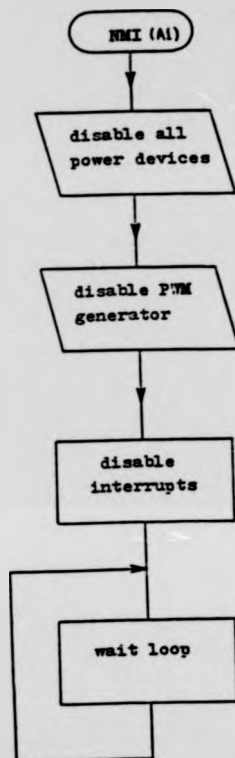


Figure 8.18 Flow-chart of the Power Down Module

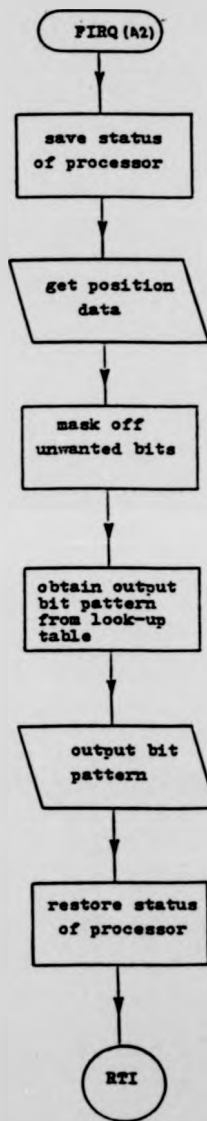


Figure 8.19 Flow-chart of the Position Detector Module

normal 21 cycles. The end of interrupt sequence also take less machine cycles for obvious reasons. To further enhance the execution speed of the FIRQ handler, the Y index-pointer of the processor is assigned permanently as the pointer of the position look-up table.

8.3.5 PWM Control (A3)

This IRQ handler embodies the main control algorithm, and its flow-chart is given in Figure 8.20. The routine is scheduled to run every time when new speed data is available. When the handler is executed, it first reads the speed data from the rotor speed detector via PORT3, and then checks if the speed is exceeding the maximum of 3000rpm. If it is, than all the driving signals to the power regulator will be inhibited. The execution of the handler will then terminate. This is to prevent the possible mis-triggering of the power devices which may occur due to the fact that the S13224 scanners may generate incorrect position data if the speed is exceeding 3000rpm.

Execution continues if the speed does not exceed 3000rpm, and the current demand is then read via PORT6. The speed and the current demand become the searching co-ordinates of the PWM on-time look-up table. Provided that this pair of co-ordinates matches up with one of the quantised pairs, subroutine SUB1 is called. Otherwise, SUB2 will be executed. SUB1 is a simple routine whose function is to pick up the PWM data directly from the look-up table and output the data to the PWM generator via PORT3. Its flow-chart is given in Figure 8.21. When the pair of co-ordinates does not match up with any of the preprogrammed ones, the PWM data will be computed by linear interpolation. This task is carried out by the subroutine SUB2. The flow-chart of which is shown in Figure 8.22.

Another function of the IRQ handler is the implementation of automatic commutation advancing. The relationship between the rotor speed, armature current, and the optimum angle of advancing has been described in Chapter 5. To implement the commutation advancing scheme, it is required that the relative

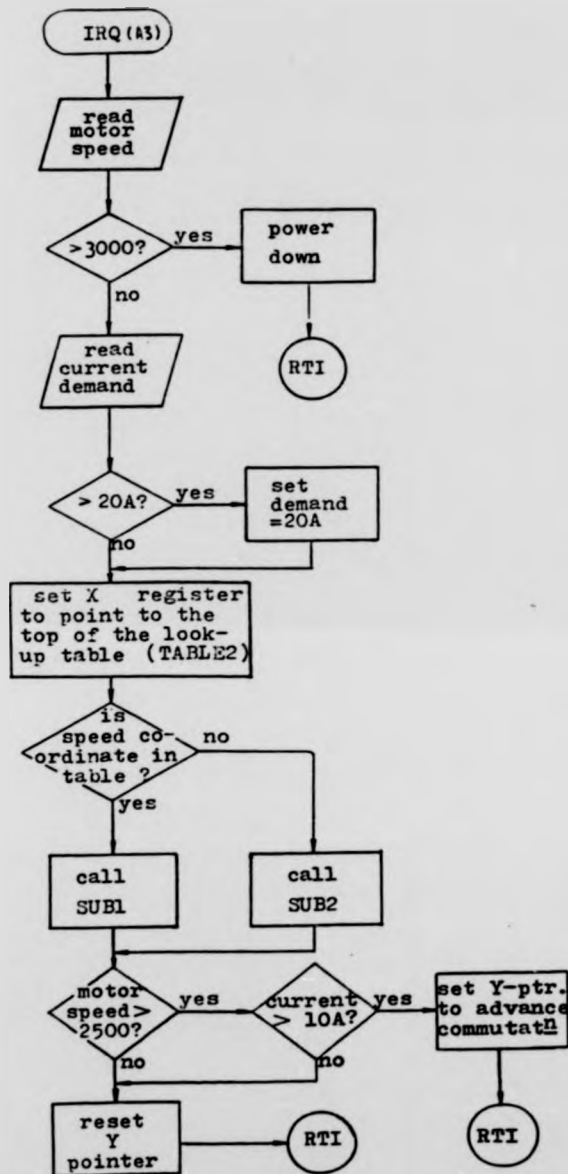


Figure 8.20 Flow-chart of the PWM Control Module

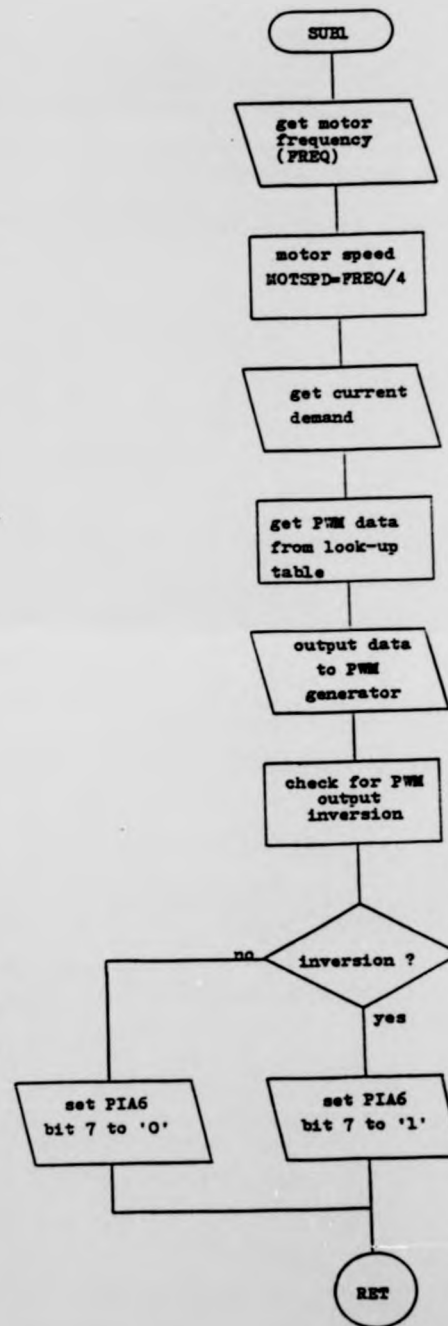


Figure 8.21 Flow-chart of subroutine SUB1

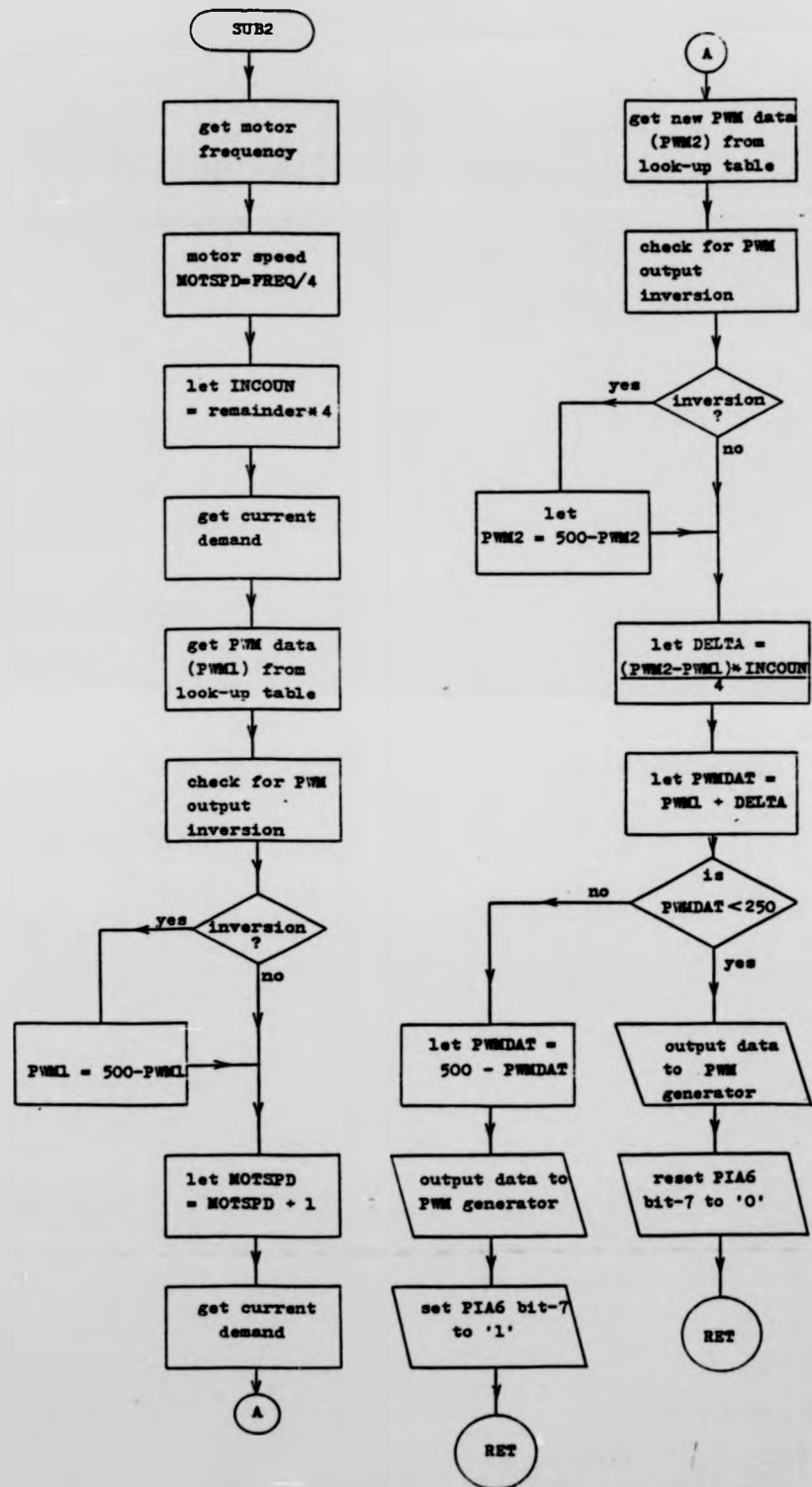


Figure 8.22 Flow-chart of subprogram SUB2

angular orientation between the position detector and the stator can be adjusted. Such adjustments are achieved in the software by changing the datum pointer of the position-decoding look-up table, i.e. by modifying the value of the Y index-pointer. However, because of the discrete nature of the position detector, it is not possible to have a full implementation of the scheme. In fact the minimum angle of advance that can be achieved is 15°elec, and this greatly exceeds of the desired values. But as there are already some commutation delays being introduced by the finite response time of the optical scanners (about 50usec), the actual angle of advance will be less than 15°elec. It was decided, therefore, that a simplified form of commutation advancing should be experimented upon.

The scheme is that if the speed and current are both greater than 2500rpm and 10A respectively, an advance of 15°elec is introduced. At the transition speed, the position detector introduces a 4°elec delay, such that the actual angle of advance is 11°elec. The calculated optimum value at 2500rpm and 10A is 5°elec (Figure 5.7), in other words an over advance of 6 elec is introduced. This leads to a slight over-shoot of the leading edge armature current -- about 20% at 2500rpm and 10A.

8.3.6 Power-up Initialisation and Demand Input (A4)

This background routine is executed automatically upon system power-up or by pressing the reset switch. Its first task is to initialise the interfacing devices, and to preset the relevent processor registers. It then enters into a continuous loop to detect operator inputs. The flow-chart is shown in Figure 8.23.

8.3.7 Data Base

The data code area consists of the system vectors and three look-up tables.

VECTOR

This area contains the power-up vector, and the interrupt vectors of the various handlers.

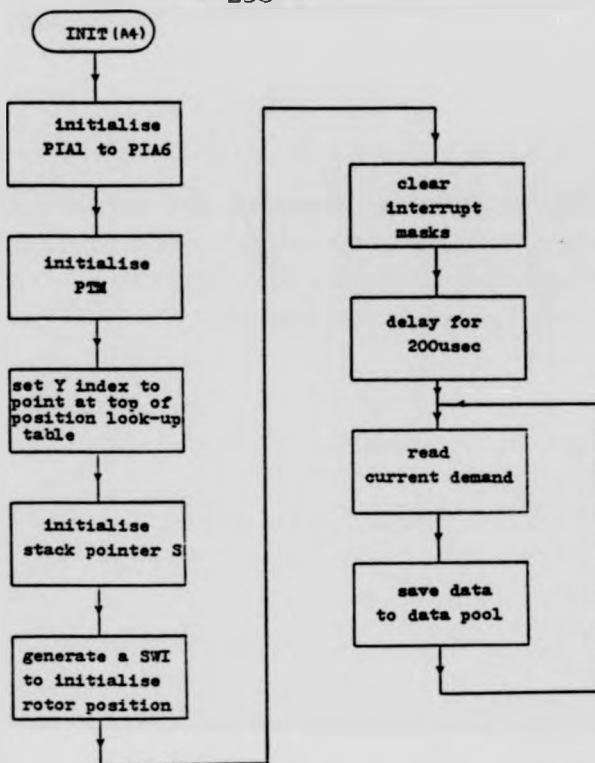


Figure 8.23 Flow-chart of Power-up Initialisation & Demand Input Module

	DATA	OFFSET ADDRESS (abs addr-TABLE)-OFFSET
ADV	00001001	-1
TABLE:	00001001	0
	00100001	1
	00100001	2
	00100001	3
	00100001	4
	00100100	5
	00100100	6
	00100100	7
	00100100	8
	00001100	9
	00001100	10
	00001100	11
	00001100	12
	00100010	13
	00100010	14
	00100010	15
	00100010	16
	00110000	17
	00110000	18
	00110000	19
	00110000	20
	00001001	21
	00001001	22
	00001001	23

Figure 8.24(a) Position decoding look-up table for forward motoring

	DATA	OFFSET ADDRESS (abs addr-TABLE)-OFFSET
ADV	00000010	-1
TABLE:	00000010	0
	00000010	1
	00000010	2
	00000010	3
	00000010	4
	00001000	5
	00001000	6
	00001000	7
	00001000	8
	00001000	9
	00001000	10
	00001000	11
	00001000	12
	00100000	13
	00100000	14
	00100000	15
	00100000	16
	00100000	17
	00100000	18
	00100000	19
	00100000	20
	00000010	21
	00000010	22
	00000010	23

Figure 8.24(b) Position decoding look-up table for forward regen. braking

TABLE1

This table contains the position decoding data. Its contents are given in Figure 8.24. Each bit of a data byte corresponds to the conduction state of a power device, with a '1' representing the on-state. In normal operation, the datum pointer is set to point at TABLE1. When commutation advance is required, the pointer is changed to point at ADV; the net effect is the shifting of the commutation sequence by 15°elec.

TABLE2

The size of this table is 1271 bytes, and the data are grouped into 41 blocks, each block containing the pulse width data for a particular rotor speed and different current demands. The data within a block are arranged in ascending order of current demands, and the blocks are arranged in ascending order of rotor speed.

TABLE3

This table contains the 8th bit of the PWM data. It is used to control the inversion of the PWM generator's output signal.

8.4 System Performance

After the hardware and software were built and debugged, tests were carried out on the experimental controller. The performance characteristics of the motor/controller system were measured on a Ward Leonard system as shown in Figure 8.25. The test motor was coupled to the loading motor HDC via a Vibrometer torque transducer for accurate torque measurement. To minimise thermal drift, the Vibrometer was switched on at least an hour before the readings were taken. Calibrations of the transducer were also carried out from time to time to ensure consistency of the readings. Figure 8.26 shows the layout of the test rig.

During an initial test it was found that the proposed commutation advancing

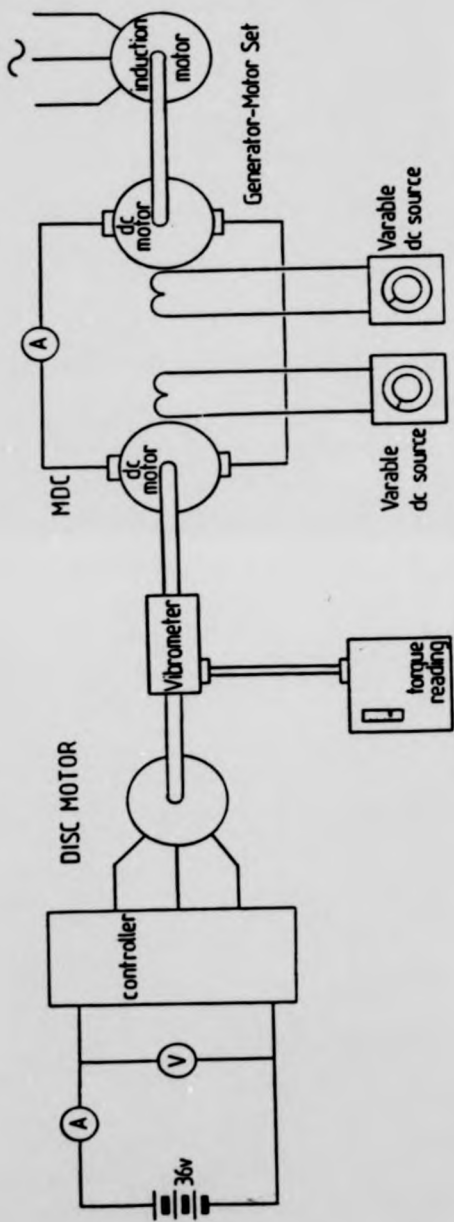


Figure 8.25 Circuit diagram of the Ward Leonard test system

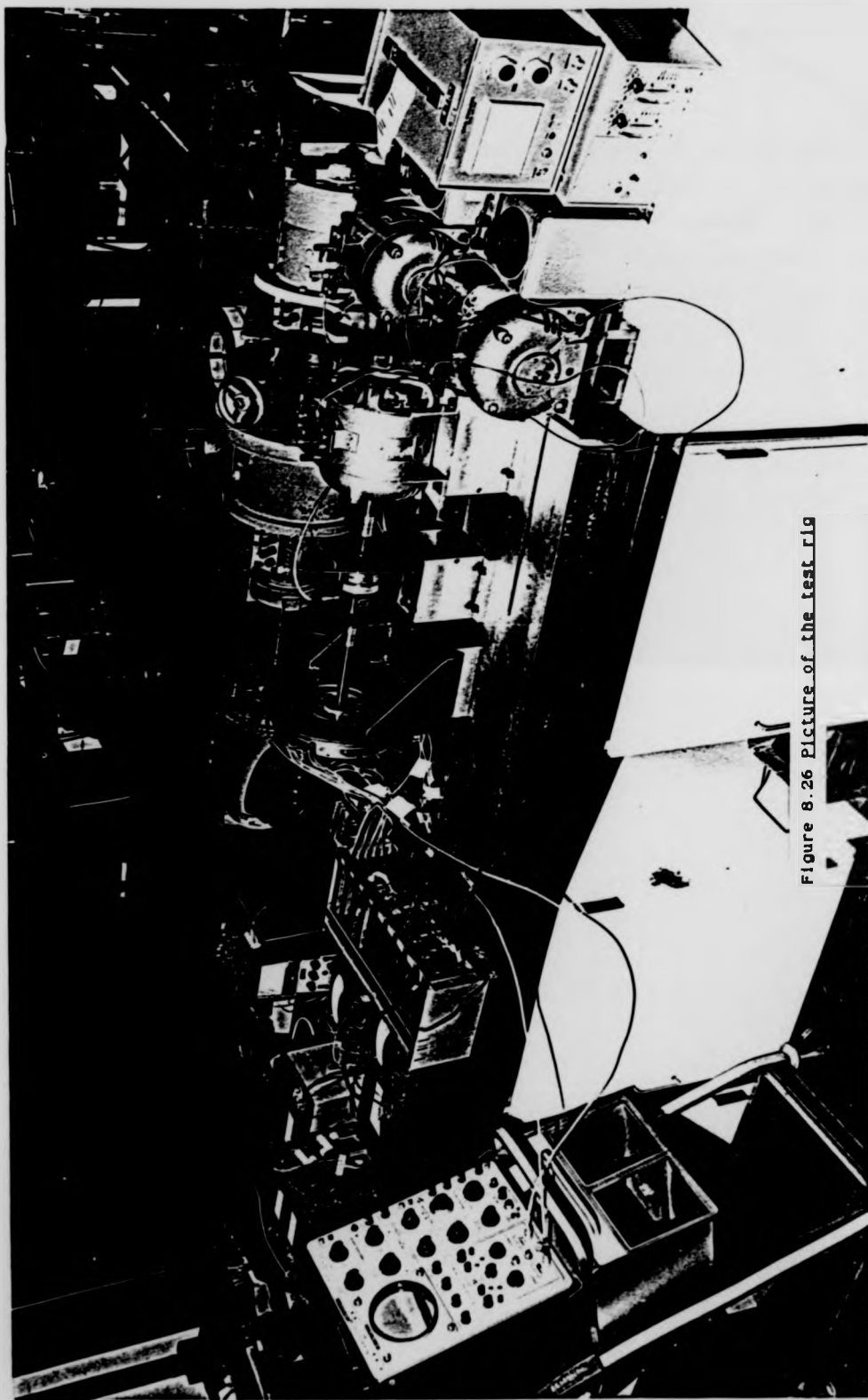


Figure 8.26 Picture of the test rig

scheme has given rise to an abrupt change in the torque output at the transition points. A 10% increase in torque was recorded. While such non-linearity in the torque characteristic has no significant effect on an open-loop system, the effect on a closed-loop system can be detrimental and could induce instability. As it was anticipated that some form of speed loop would be required in the future, the commutation advancing scheme was dropped in favour of a smoother torque characteristic.

With the torque demand being set equal to 25%, 50%, 75% and 100% full torque, the battery currents and torque values were measured at various speeds. The test results were then plotted. Figures 8.27 and 8.28 give the motoring, and the braking characteristics of the system, respectively.

8.5 Discussion of Drive Characteristics

8.5.1 Motoring Mode

As the MCU was programmed to control the armature current only, i.e. the shaft torque, the output torque was expected to drop slightly with increasing rotor speed. This is confirmed by the output torque characteristics given in Figure 8.27(a). The fall in torque is largely accounted for by the bearing friction, windage losses and eddy losses. Also contributing to the drop in torque output is the effect of undercommutation as described in Chapter 5. Although the effect of undercommutation on the output torque characteristics was not measured, the effect is not expected to be significant as the armature inductance is extremely low.

During the test, it was observed that there were some systematic fluctuations in the output torque with increasing rotor speed. This is caused by the digital quantisation effect of the controller. It is calculated that the maximum torque fluctuation is about 0.025Nm, and is independent of the average shaft torque. Figure 8.29 shows the calculated torque fluctuation at demanded shaft torque of

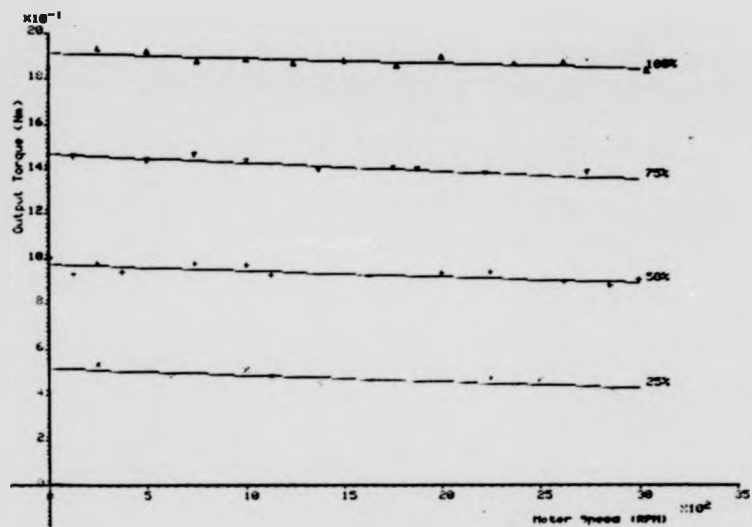


Figure 8.27(a) Motoring mode output torque characteristics

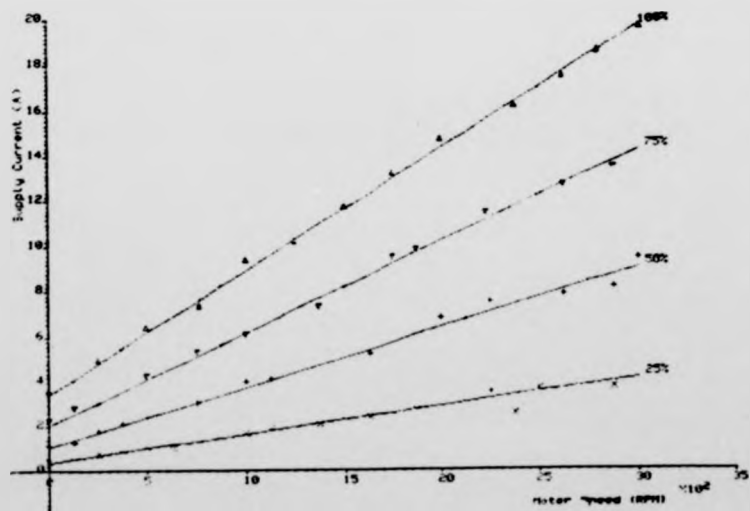


Figure 8.27(b) Motoring mode dc-link current characteristics

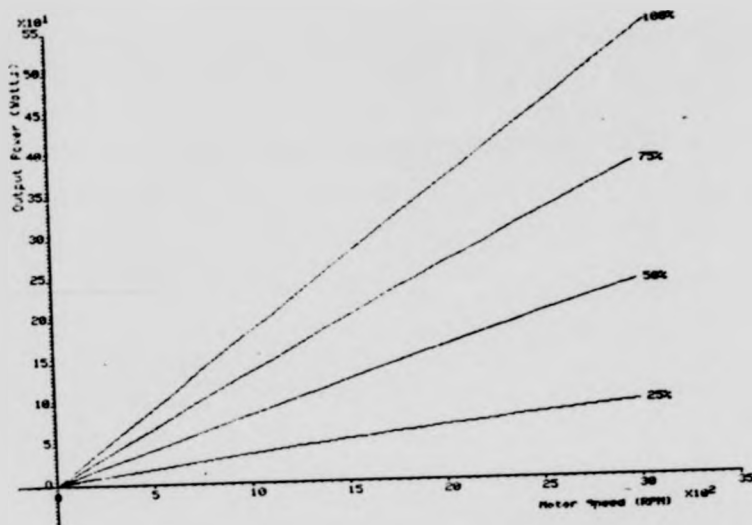


Figure 8.27(c) Motoring mode output characteristics

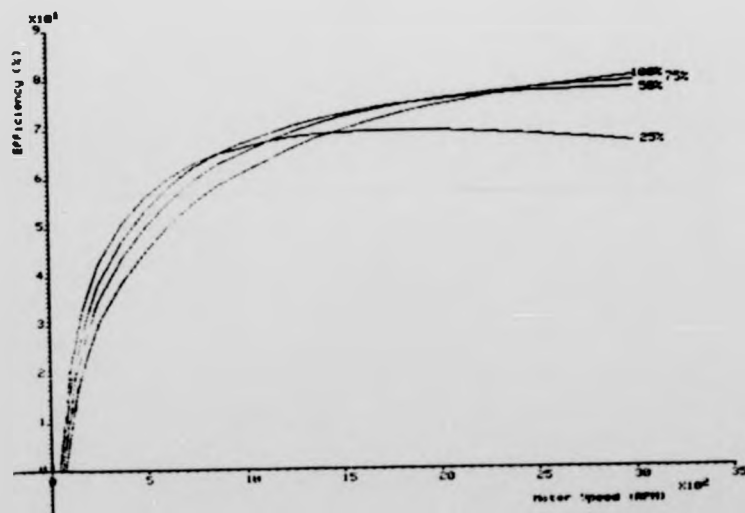


Figure 8.27(d) Motoring mode efficiency characteristics

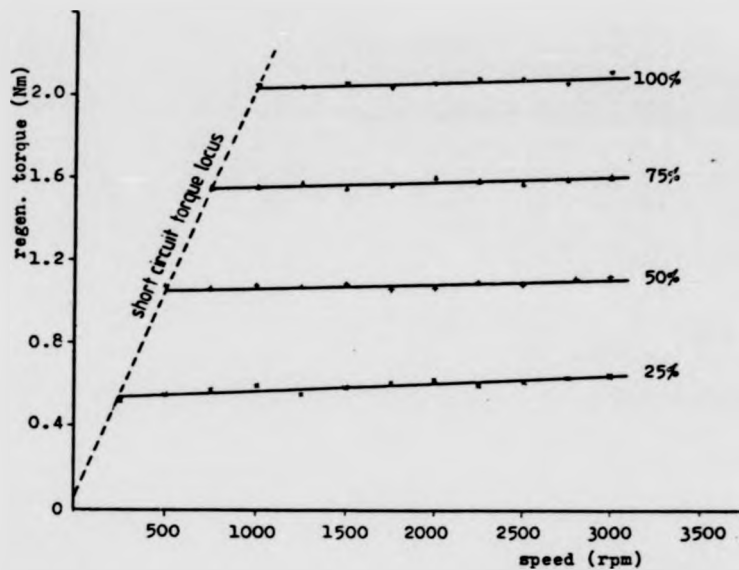


Figure 8.28(a) Regenerative mode torque characteristics

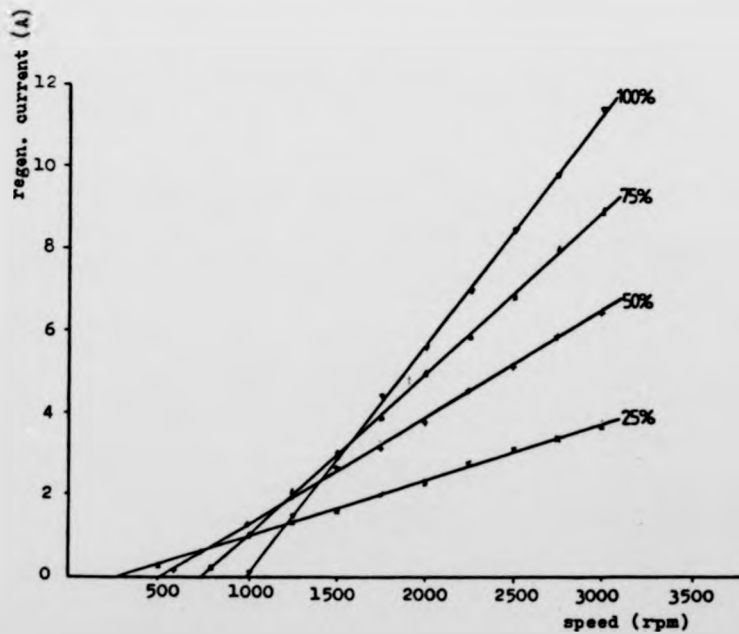


Figure 8.28(b) Regenerative mode dc-link current characteristics

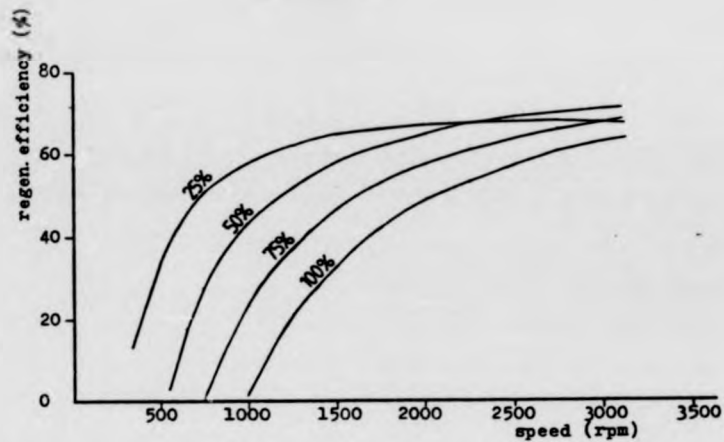


Figure 8.28(c) Regenerative mode efficiency characteristics

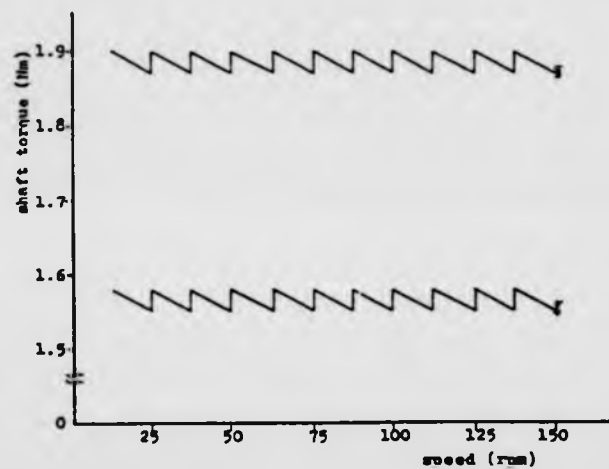


Figure 8.29 Calculated motoring mode torque variations against rotor speed

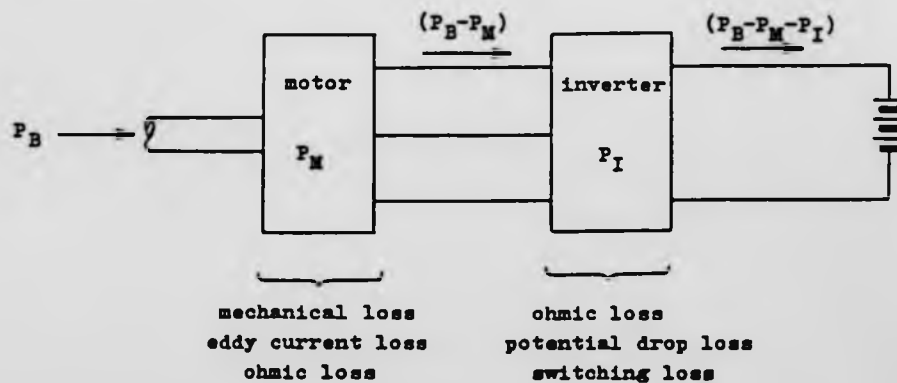


Figure 8.30 Braking energy flow diagram

1.89Nm and 1.57Nm. It can be seen that the percentage torque fluctuation is low at high torque (e.g. 1.3% at 1.89Nm), but increases as the torque decreases (e.g. 1.6% at 1.57Nm). At very low torque, the torque fluctuation becomes extremely high (e.g. 26% at 0.095Nm), and this could be unacceptable in some application. If the quantisation effect is to be minimised, the resolution of the speed detector, which is 12.5rpm at present, must be increased. For example, a 1rpm resolution can reduce the torque fluctuation by 13 times.

Figure 8.27(d) shows the efficiency characteristics; the maximum efficiency is obtained at 3000rpm and full torque demand, and is equal to 80.5%.

8.5.2 Regenerating mode

Although regeneration is not the most effective means of electrical braking, it does allow braking of the machine with return of the braking energy to the battery. But it should be understood that not all the braking power produced at the shaft is returned to the source; Figure 8.30 illustrates this point. The system losses must be provided for before the battery receives charges. For a specific braking torque, there is a critical rotor speed at which input power equals system losses, and regeneration only occurs above this speed. By plotting the locus of the critical regeneration speed, a straight line is obtained. This straight line is in fact the short circuit characteristics of the motor. The programmed constant braking torque loci will only start from points along the short circuit line and extend to the right with increasing speed. The braking characteristics are shown in Figure 8.28(a). The increase in torque with increasing speed is due to the speed related mechanical losses, and eddy current losses.

The regeneration current characteristics are shown in Figure 8.28(b), where the effects of critical speeds are clearly shown, i.e. that regenerations only occur above the critical speeds. The efficiency characteristics are shown in Figure 8.28(c).

CHAPTER 9 CONCLUSIONS AND SUGGESTIONS FOR FURTHER WORK

9.1 General

This thesis has presented an in depth study of the principle and operation of axial-field brushless dc motors. In this project three prototype motors were built in order to investigate the characteristics of the different drive configurations, and their performances have been presented. A PWM power regulator using power MOSFETs and a microprocessor-based motor controller sub-system were also developed. The conclusions concerning the brushless dc disc-motors are now presented; these are followed by conclusions concerning the power regulator and the motor controller.

9.1 The Brushless DC Disc-motors

The aim of designing a new type of disc-motor which is suitable for brushless dc operation has been achieved. This was done by using a rotating magnet arrangement, and by choosing a suitable value of the pole-arc/pole-pitch ratio α for the field system. It was found that an α value of 0.9 gave the best compromise between the interpolar flux leakage and the squareness of the circumferential air-gap flux distribution, for disc-motors with 8-poles.

Because of the highly non-sinusoidal nature of the air-gap flux distribution, and thus the induced emf, a Fourier series representation of the emf equation was used. Although the emf equation (Equ.(2.37)) developed in Chapter 2 is quite complex, it can predict very accurately the induced emf waveform. Based on this waveform the output characteristics of a brushless dc disc-motor can be calculated using a discrete-time method. Such a method was used to calculate the output characteristics of the 600W star-connected bi-polar motor (Motor 3), and the calculated results were very close to the experimental results, despite the

fact that switching transients were not taken into account.

Motors 2 and 3, both having an α of 0.9, induced a near trapezoidal phase emf that has a constant voltage region of 120° elec per half-cycle. It has been demonstrated that such a trapezoidal emf is most suited for both uni-polar and bi-polar brushless operations. But to achieve the highest power-to-weight ratio and the simplest inverter configuration, the star-connected bi-polar mode should always be used.

A scheme for optimum commutation advancing has been proposed in Chapter 5. However, due to the low resolution of the rotor position detector, it was not possible to carry out enough tests to verify the scheme. But from the test results which were taken with a 5° elec overcommutation, it was found that increases of up to 4% in the output power and 4% in the output efficiency were achieved. It is expected that an even better result can be obtained when the conditions of optimum commutation advancing are brought about.

9.2 The Electronic Power Regulator (EPR)

A new power inverter which capitalised on the special characteristics of the disc-motor has been developed. The unusual feature of the inverter is that only the bottom-half of the inverter bridge is pulse-width modulated, while the top-half inverter bridge is switched at the commutation frequency of only 200Hz maximum. This arrangement allowed the use of slower, and thus cheaper, power devices in the top-half inverter bridge.

However, where pulse-width modulation (PWM) was concerned, the disc-motors were found to have a major disadvantage, i.e. they have extremely low armature inductances. In order to limit the current ripples caused by PWM, to obtain a better linearity of the armature current transfer characteristics, and to maximise the range of controllable output voltage, a relatively high carrier

frequency and the more expensive power MOSFETs were used. It was found that despite a 20kHz carrier frequency, the armature current transfer characteristics were still very non-linear. This was caused by the discontinuous conduction of the armature current during the off-time of a PWM period. To improve the linearity, the carrier frequency must be increased. While the existing EPR can easily be put to operate at 40kHz, or even higher frequencies, but as the power rating of the brushless dc disc-motor system increases, the switching losses will become very large. The main cause of switching losses is the reverse recovery time of the free-wheeling diodes. This is because the extremely fast Schottky diodes, which have a maximum breakdown voltage of only 45V, can no longer be used if the power rating, and thus the voltage, of the motor system increases.

It is suggested that for higher power systems, a separate dc chopper (Figure 9.1), which uses power MOSFETs, epitaxial diodes, a small series inductance and a switching frequency of about 20kHz, is used. At first glance, such an arrangement may seem to be rather more expensive than a PWM inverter bridge. But it should be noted that slower power devices can now be used instead in the bottom-half of the inverter circuit, and only two power MOSFETs are needed. At the time of the project, the price ratio of similarly rated MOSFETs and Darlington's being about 3 to 1, the saving of one power MOSFET is enough to cover the three additional transistors. But the power device driving circuitries are necessarily more complicated, and costly.

9.3 The Motor Controller Sub-system

Despite the open-loop nature of the motor controller, it performed satisfactorily thanks to the processing power of the microprocessor. However, the processor was heavily loaded by the interrupt driven rotor position detector which limits the recursion time of the main control program to 100msec. While the long recursion time is satisfactory for loads whose speeds do not change

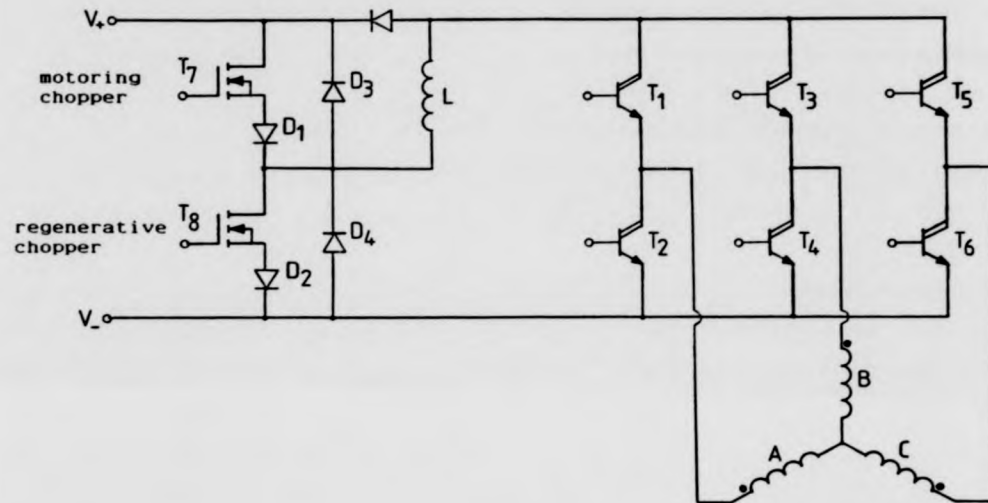


Figure 9.1 Suggested configuration for higher power regulator

appreciably within a recursion period, but it may not be adequate for fast acting applications, such as servo drives. The rotor position decoding function should be removed from the microprocessor, and a separate decoding circuit used. As it is unlikely to obtain high resolution position encoders at low cost, it is not advisable to implement the commutation advancing electronically. The new position encoder should consist of three low speed reflective optical detectors scanning three Grey-coded tracks, and the position data should be decoded by a separate ROM. If extremely high performance is required, commutation advancing can be incorporated by using a stepper motor to control the relative angular position between the optical detector assembly and the armature.

The various components used in the controller are standard integrated circuits. By today's standards these are low integration components and are not cost effective for use in mass production. To be cost effective, the motor controller should be implemented on a single chip microcontroller such as the Intel 8051 (72), and all the interfacing electronics can be implemented on a custom ULA (uncommitted logic array) (73).

9.4 Suggestions for Further Work

Although the brushless dc disc-motors were developed with special reference to traction applications and two 600W prototype motors were delivered to the sponsor to be installed in a research vehicle, circumstances did not allow the motors to be field-tested. It is important to obtain field-test data to enable much valuable information to be gained and to highlight areas where improvements or modifications to the motor system are necessary. In pursuing this goal, the following actions are suggested for further work:

1. To build a higher power prototype of around 10kW using SmCo_5 magnets.
2. To develop a more accurate computer model of the motor which takes into account the switching transients.

3. To build a 10kW power regulator using the configuration suggested in Figure 9.1 and to analyse its operations.

Appendix A Delta Function

The delta, or impulse, function $\delta(t)$ is a singularity function which is of great importance in system analysis. The intuitive interpretation of an impulse is that it is an idealisation of a very narrow pulse having a finite total area. For convenience, the area is usually taken to be unity. The graphical representation of $\delta(t)$ is illustrated in Figure A1(a). It should be emphasised that the factor multiplying an impulse is really designating the area of the impulse and is not just scaling its magnitude. Thus, $A\delta(t - a)$ is an impulse with an area of A located at $t = a$.

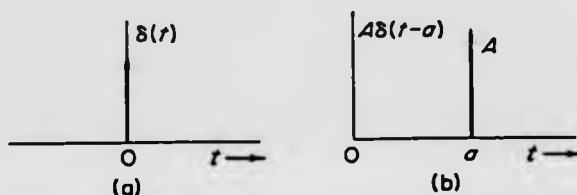


Figure A1 Graphical representation of the impulse function.
(a) The unit impulse. (b) Time-shifted impulse with area A.

The delta function have the folling properties:

- (1) $\delta(t - t_0) = 0$ $t \neq t_0$
- (2) $\int_{t_1}^{t_2} \delta(t - t_0) dt = 1$ $t_1 < t_0 < t_2$
- (3) $\int_{-\infty}^{\infty} f(t)\delta(t - t_0)dt = f(t_0)$ $f(t)$ continuous at t_0
- (4) $f(t)\delta(t - t_0) = f(t_0)\delta(t - t_0)$ $f(t)$ continuous at t_0
- (5) $\int_{t_1}^{t_2} \delta(\lambda - t)\delta(\lambda - t_0)d\lambda = \delta(t - t_0)$ $t_1 < t_0 < t_2$

Appendix B Discrete Fourier Transform

The discrete Fourier transform (DFT) is a sequence of (complex) samples $\{F_D(k\Omega)\}$ in the frequency domain defined by

$$F_D(k\Omega) = \sum_{n=0}^{N-1} f(nT) \exp(-j\Omega Tnk), \quad k=0,1,\dots,N-1 \quad \dots(b1)$$

where N is the number of samples, and $\Omega = 2\pi/NT$ is the separation of the components in the frequency domain. With this definition there are only N distinct values of $F_D(k\Omega)$ that can be computed, since $F_D(k\Omega)$ is periodic in with a period of $N\Omega$.

Consider a continuous-time function $f(t)$ that exist over the time interval $0 < t < t_0$. Such a function can be represented exactly by a continuum of impulses. A less exact but more computationally tractable representation can be obtained by representing the function as a sequence of equally spaced impulses, where the strength of the impulse at $t=nT$ is the area under the function $f(t)$ in the interval $T(n-1/2) < t < T(n+1/2)$. such a representation is shown in Figure B1. If the sampling interval T is small enough so that the function does not change appreciably over one interval, then the strength of the δ function can be taken as $Tf(t)$. Thus, the representation can be written as:

$$\begin{aligned} f(t) &= \hat{f}(t) = Tf(t) \sum_{n=0}^{N-1} \delta(t - nT) \\ &= T \sum_{n=0}^{N-1} f(nT) \delta(t - nT) \quad \dots(b2) \end{aligned}$$

This type of representation is very useful (and quite accurate) when the computations to be made involve integrations of $f(t)$ with other functions that do not change very much over the interval T . Such applications include computing the spectrum up to a frequency on the order of $f_c = (T/2)$. By making the interval T smaller, the fidelity of the representation can be extended to higher frequencies. As an example, let it be assumed that it is desired to compute the Fourier transform of the function represented by (b2). This lead to

$$\begin{aligned}
 F(\omega) &= T \int_{-\infty}^{\infty} \exp(-j\omega t) \sum_{n=0}^{N-1} f(nT) \delta(t - nT) dt \\
 &= T \sum_{n=0}^{N-1} f(nT) \exp(-j\omega nT) \quad \dots (b3)
 \end{aligned}$$

Where $\omega = 2\pi k/NT = k\Omega$, it is seen that (b3) given the DFT of $f(nT)$; that is

$$\left. \tilde{F}(\omega) \right|_{\omega=k\Omega} = T \sum_{n=0}^{N-1} f(nT) \exp(-j\omega nT), \quad 0 \leq k \leq N-1 \quad \dots (b4)$$

From (b4) it is seen that the DFT is equal to $1/T$ times the sequence of samples taken at intervals of $\Omega = 2\pi/NT$ from the Fourier transform of the δ -function approximation to the continuous-time function.

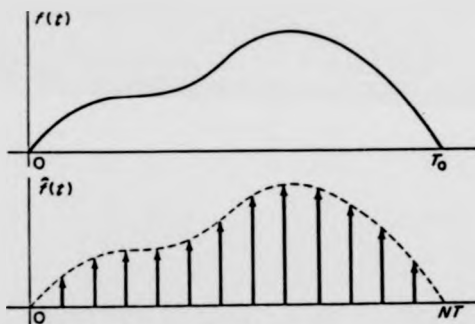


Figure B1 Impulse approximation of function

Appendix C Design Data and Performance of the Wheelchair Motor (11)

The design data of the wheelchair motor is given below:

DISC-ARMATURE MOTOR DESIGN

DESIGN NO: 64930

DESIGN SPECIFICATION

OUTPUT: 130. WATTS
VOLTS: 24. V
SPEED: 1960. RPM

DESIGN DATA

D2: 190. MM
D1: 105. MM
POLES: 8.

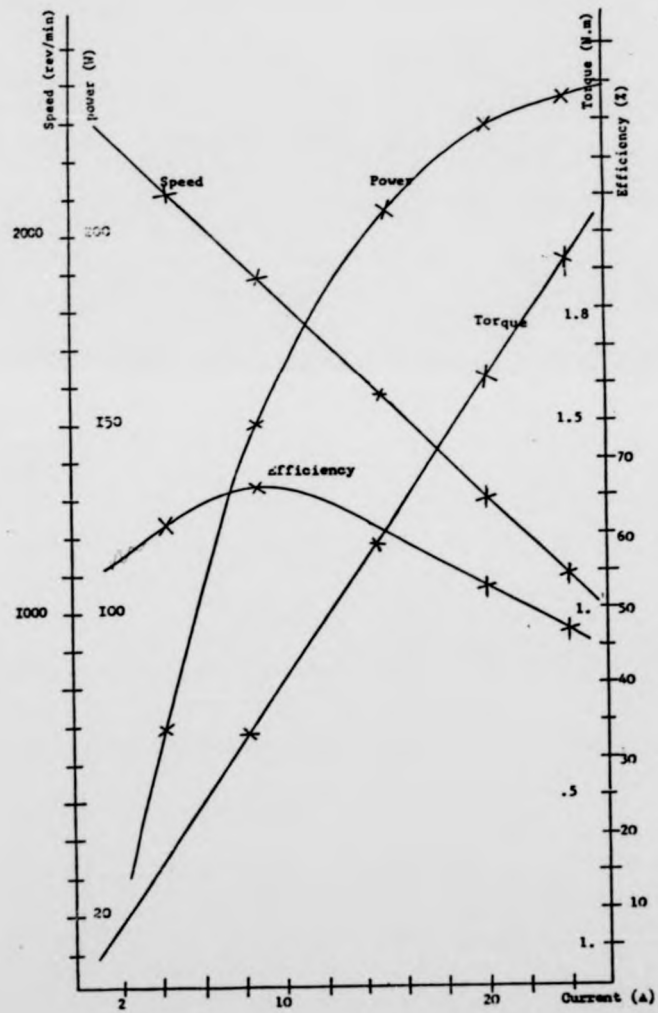
MAGNETIC CIRCUIT DATA

BM 0.236 TESLA
HM 94586. A/M
LCDEFF 1.30
LFACT 1.25
PHI .000293 WEBERS
ALPHA .75
LMAG 9.3 MM
MGTMAG 0.65 KG
THICK 2.49 MM
MGTFRR 0.76 KG
GAP 5.60 MM
MAGDSY 4700. KG/M²
BMS 1.80 TESLA

ELECTRIC CIRCUIT DATA

PATHS 2.
COILS 41.
TURNS 6.
Z 492.
GAUGE 1.00 MM
MGTWIR 0.41 KG
CRTDSY 5.0 A/MM²
APMCRT 7.85 AMPS
LOSS 34.61 WATTS
LAY 2
TEMP 59. DEGREES
SF .45
RARM 0.370 OHMS
ER 19.59 VOLTS

And the performance characteristics, at supply voltage = 24 V, are:



Appendix D Measurement of Armature Self-Inductance

The self-inductance of the armature windings were measured using the circuit given in Figure D1. The current equation of the circuit when T_1 is switched on is

$$V = (R_a + R_{ds})i + L \frac{di}{dt} \quad \dots(d1)$$

and the solution is

$$i(t) = \frac{V}{R} (1 - \exp(-t/T)) + I_0 \exp(-t/T) \quad \dots(d2)$$

where $R = R_a + R_{ds}$, $T = L/R$, and $I_0 =$ initial current

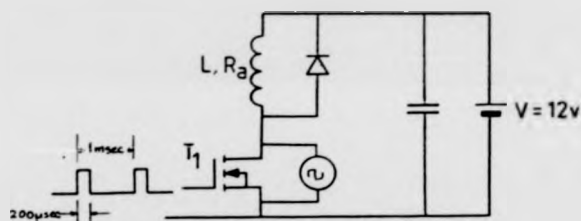


Figure D1 Circuit to measure armature self-inductance

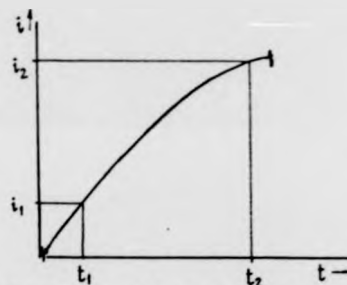


Figure D2 Coil current oscillogram

Figure D2 shows an example of the coil current oscillogram measured across the drain and source of T_1 , when T_1 is switched on. If (t_1, i_1) and (t_2, i_2) are two arbitrary points on the current locus they must satisfy Equation (d2), i.e.

$$i(t_1) = i_1 = \frac{V}{R}(1 - \exp(-t_1/T)) + I_0 \exp(-t_1/T) \quad \dots(d3)$$

$$i(t_2) = i_2 = \frac{V}{R}(1 - \exp(-t_2/T)) + I_0 \exp(-t_2/T) \quad \dots(d4)$$

(Note: the two points must be taken away from the switching instants to avoid errors caused by the transients.) By solving (d3) and (d4) the coil inductance is obtained, i.e.

$$L = (t_2 - t_1)R / \ln \left| \frac{i_1 - V/R}{i_2 - V/R} \right| \quad \dots(d5)$$

Appendix E MPU Memory Map and Port Assignments

The memory map is given below:

-----	\$0000
:	:
:	RAM
:	:
-----	\$007F
*	*
-----	\$2000
:	:
:	PIA1
:	:
-----	\$2003
*	*
-----	\$4000
:	:
:	PIA2
:	:
-----	\$4003
*	*
-----	\$6000
:	:
:	PIA3
:	:
-----	\$6003
*	*
-----	\$8000
:	:
:	PTM
:	:
-----	\$8003
:	:
:	:
:	:
-----	\$E000
:	:
:	E 2764
:	P
:	R ----- \$F000
:	O
:	M 2732
:	:
-----	\$FFFF

The six digital I/O ports are denoted as PORT1 to PORT6, the port assignments are given as follows:

PORT1 (PIA1 pA) - inputs, connected to the position detector, 5-bit

PORT2 (PIA1 pB) - outputs, commutation envelop drive signals to the power devices, 6-bit

PORT3 (PIA2 pA) - inputs, connected to the speed detector, 8-bit

PORT4 (PIA2 pB) - inputs, connected to the demand input, 8-bit
PORT5 (PIA3 pA) - outputs, connected to the PWM generator, 8-bit
PORT6 (PIA3 pB) - inputs/outputs, miscellaneous control lines
PTM: channel 1 - not assigned
channel 2 - 10HZ time base generation
channel 3 - not assigned

REFERENCES

- (1) Carter, A.H. and Corbett, A.E.: "Electric motor", British Patent 1231782, 1971.
- (2) Corbett, A.E.: "Disc-armature motors - a review of work done", Technical Note, University of Warwick, Sept 1970.
- (3) Corbett, A.E. and Campbell, P.: "The pancake motor", Automotive Design Engineering, July/Aug 1974, pp34-35.
- (4) Roerig, C.S.: "The dc disc-armature traction motor", PhD Thesis, University of Warwick, 1981.
- (5) Editorial: "Hybrid buses get ahead faster than car", Electrical Review, Jan 1972, p20.
- (6) Knights, D.E.: "Prospects for the printed motor", Engineering, March 1975, pp199-202.
- (7) Stanton, D.P., Rosenberg, D.J. and Campbell, P.: "The computer design and optimization of axial-field permagnet motors", IEEE Trans. on Power Apparatus and Systems, Vol. PAS-100, No. 4, April 1981, pp1490-1497.
- (8) Corbett, A.E.: "A disc-armature dc motor", EM70 Conference, University of Dundee, July 1970.
- (9) Campbell, P.: "Pancake shaped dc motor for efficient fan drives", Electrical Review, March 1974, pp211-212.
- (10) Campbell, P.: "A new wheel motor for electric commuter cars", Electrical Reviews, Vol. 190, 1972, pp332-333.
- (11) Ozpolat, A.M.M.: "Design and development of dc disc-armature motor", MSc Thesis, University of Warwick, 1981.
- (12) Corbett, A.E. and Ali, M.R.N.: "Design and performance of a 10kw dc disc-motor with ferrite magnets", International Conference on Electrical Machines, Budapest, Sept 1982.
- (13) Leung, W.S. and Chan, C.C.: "A new design approach for axial-field electrical machines", IEEE Trans. on Power Apparatus and Systems, Vol. PAS-99, No. 4, July/Aug 1980, pp1679-1685.
- (14) Soylemez, S.: "Disc geometry synchronous machines with permanent magnets", MSc Thesis, University of Warwick, December 1981.

- (15) Sommerfield, A.: "Electrodynamics", Academic Press, 1952.
- (16) Campbell, P.: "The magnetic circuit of an axial-field dc electrical machine", IEEE Trans. on Magnetics, Vol. MAG-11, No. 5, Sept 1975, pp1541-1543.
- (17) Campbell, P.: "Principle of a permanent magnet axial-field dc machine", Proceedings IEE, Vol. 121, No. 12, Dec 1974, pp1489-1494.
- (18) Campbell, P.: "The dc disc-armature electric motor", PhD Thesis, University of Warwick, 1974.
- (19) Krezsig, E.: "Advanced Engineering Mathematics", J. Wiley and Sons.
- (20) Alexanderson, E.F.W. and Mittag, A.H.: "The thyatron motor", AIEE Trans., Vol. 53, 1938, pp1517-1523.
- (21) Brown, M. and Moore, E.: "Brushless dc or inverter motor drive - a comparison of attributes", Motorcon Proceedings, Sept 1982, pp111-123.
- (22) Bradley, D.A., Clarke, D.L.C., Davies, R.M. and Jones, D.A.: "Adjustable frequency invertors and their application to variable-speed drives", Proc. IEE, Vol. 111, No. 11, Nov 1964, pp1833-1846.
- (23) Agarwal, P.D.: "The GM high-performance induction motor drive system", IEEE Trans. on Power Apparatus and Systems, Vol. PAS-88, No. 2, Feb 1969, pp86-93.
- (24) Lipo, T.A. and Turnbull, F.G.: "Analysis and comparison of two types of squarewave inverter drives", IEEE Trans. on Industry Applications, Vol. IA-11, No. 2, Mar/Apr 1975, pp137-147.
- (25) Murphy, J.M.D.: "Inverter-fed induction motor drives", Electrical Reviews, Vol. 206, No. 3, Jan 1980, pp41-44.
- (26) Dewan, S.B. and Mirbod, S.A.: "Slip-frequency control in a induction motor drive with a phase-locked loop", Canadian Elec. Eng. Journal, Vol. 5, No. 2, Apr 1980, pp5-8.
- (27) Joshi, A. and Dewan, S.B.: "Modified steady-state analysis of current source inverter - squirrel cage motor drive", IEEE Conference Record, IAS 1980 Annual Meeting, pp598-604.
- (28) Sen, P.C. and Mok, W.S.: "Induction motor drives with microcomputer control system", IEEE Conference Record, IAS 1980 Annual Meeting, pp653-662.
- (29) Sen, P.C., Trezise, J.C. and Sack, M.: "Microprocessor control of an

induction motor with flux regulation", IEEE Trans. on Industrial Electronics and Control Instrumentation, Vol. IECI-28, No. 1, Feb 1981, pp17-21.

- (30) Engineering Staffs: "SCR Manual", General Electric Company.
- (31) Chalmers, B.J., Pacey, K. and Gibson, J.P.: "Brushless traction drives", Proc-IEE, Vol. 122, No. 7, July 1975.
- (32) Maeno, T. and Kobata, M.: "AC commutatorless and brushless motor", Paper 71c 1-ZGA, Sixth Annual Meeting of the IEEE Industrial and General Applications Group, 1971.
- (33) The editorial: "Electronically commutated motor development", Electrical Vehicle Developments, June 1981, pp10-25.
- (34) Weh, H., Wahlen, H.J., Grumbrecht, R. and Branckmann, W.: "Vehicle traction motor fed by transistor inverter", Proceedings of 3rd Motorcon Conference, Geneva, Sept 1982, pp50-60.
- (35) Morgan, R.A.: "Update of ac drive technology", Power Conversion International, Jan 1981, pp25-30.
- (36) Demerdash, N.A. and Nehl, T.W.: "Dynamic modelling of brushless dc motor power conditioner unit for electromechanical actuator application", IEEE Power Electronic Specialist Conference Record, 1979, pp333-343.
- (37) Studer, P.: "A sealed brushless dc motor", NASA Report TND-2819, May 65.
- (38) Firk, R.A.: "The brushless motor types and sources", Control Engineering, June 1970, pp42-45.
- (39) Firk, R.A.: "The brushless dc motor - link to system versatility", Control Engineering, June 1970, pp75-78.
- (40) Radziwill, W.: "A highly efficient small brushless dc motor", Philips Technical Review, Vol. 30, No. 1, 1969, pp7-12.
- (41) Huggins, E.: "Fractional and sub-fractional horse power motors", Pitman.
- (42) PCN Micropaedia: "Disk drives", Personal Computer News, Vol. 1, No. 12, Dec 1983.
- (43) Moran, T.: "New developments in Floppy disks", Byte, Vol. 8, NO. 3, March 1983, pp68-82.
- (44) Kanda, Y., Migitaka, M., Yamamoto, H., Morozumi, H., Okabi, T. and Okazaki,

- S.: "Silicon Hall-effect power ICs for brushless dc motors", IEEE Trans of Electronic Devices, Vol ED-29, No. 1, Jan 1982, pp151-154.
- (45) Fitzgerald, A.E., Kinsley, C. and Kusko, A.: "Electric Machinery", McGraw-Hill Ltd.
- (46) Draper, A.: "Electrical Machines", Longman Group Ltd.
- (47) Blumenthal, M.K.: "Why PWM inverters beat other drive actuators when it comes to flexibility and distribution system compatibility", Proceedings, 17th IEEE IAS Annual Meeting, 1982, pp536-543.
- (48) Hoft, R.G. and Nayak, P.H.: "Optimizing the PWM waveform of a thyristor inverter", IEEE Trans. on Industry Applications, Sept/Oct 1975, pp526-530.
- (49) Slicker, J.M.: "A PWM transistor inverter for an ac electric vehicle drive", Proceedings, IEEE IAS Conference, 1981, pp292-299.
- (50) Patel, H.S. and Hoft, R.G.: "Generalised techniques of harmonic elimination and voltage control in thyristor inverters", Part I, IEEE Trans. on Industry Applications, Vol. IA-9, No. 3, May/June 1973, pp310-317, and Part II, Vol. IA-10, No.5, Sept/Oct 1974, pp666-673.
- (51) The Brown Boveri Review: "Static frequency changers with sub-harmonic control in conjunction with reversible variable-speed speed ac drives", Aug/Sept 1964, pp555-577.
- (52) Kliman, G.B. and Plunlett, A.B.: "Development of a modulation strategy for a PWM inverter", IEEE Trans. on Industry Applications, Vol. IA-15, No. 1, Jan/Feb 1979, pp72-79.
- (53) Bowes, S.R. and Mount, M.J.: "Microprocessor control of PWM inverters", IEE Proc. B, Vol. 128, No. 6, Nov 1981, pp293-305.
- (54) Grant, D.A.: "The use of ratio changing in pulse-width modulated inverters", Proceedings of Eurocon 1980, pp420-422.
- (55) Bose, D.K. and Sutherland, H.A.: "A high-performance pulse-width modulator for an inverter-fed drive system using a microcomputer", Proceedings, 17th IEEE IAS Annual Meeting, 1982, pp847-853.
- (56) Casteel, J.B. and Hoft, R.G.: "Optimum PWM waveforms of a microprocessor controlled inverter", IEEE Trans. of Industrial Applications, Vol. IA-14, No. 5, 1978, pp243-250.
- (57) Rhanit, N., Jacob, A., Le-Huy, P., Sevigny, A. and Rajagopalan, V.:

- "Microprocessor controlled power MOSFET transistor current source inverter", Proceedings, IEEE IAS Annual Meeting, 1981, pp835-838.
- (58) Clemente, S., Pelly, B.R. and Ruttonsha, R.: "Current ratings, safe operating area, and high frequency switching performance of power HEXFETs", International Rectifier Application Note 949.
- (59) Oxner, E.S.: "MOSPOWER Semiconductor", Siliconix Technical Article TA82-2.
- (60) Yasuhiko, I.: "Gate turn-off thyristors", Hitachi Review, Vol. 31, No. 4, 1982, pp169-172.
- (61) Mullard: "Understanding GTO gata as an aid to circuit design", Mullard Technical Publication M81-0046.
- (62) Mullard data sheet, No. M83-1436/Y: "Fast gate turn-off thyristors, BTW59 series".
- (63) Noble, p.G.: "The safe operation of power transistors", Mullard Technical Publication, No. TP1668/1 1978.
- (64) The editorial: "Product focus - power switching devices", Electronic Engineering, March 1981, pp86-93.
- (65) Siliconix: "Driving MOSPOWER FETs", Application Note AN79-4.
- (66) Woodworth, F.A.: "Choosing a fast rectifier", Electronic Engineering, Dec 1981, pp75-81.
- (67) Noyce, R.N. and Hoff, M.E.: "A history of microprocessor development at Intel", IEEE MICRO, Feb 1981, pp8-21.
- (68) Bellini, A., Del-Mastro, C., Figalli, G. and Ulivi, G.: "An approach for the implementation on a microcomputer of the control circuit of variable frequency three-phase inverters", IEEE Proceedings, 17th IAS Annual Meeting, 1981, pp650-655.
- (69) Faldella, E., Fillicori, F. and Monaco, V.A.: "A microprocessor controller of variable-frequency PWM inverters for ac motor drives", Conference Proceedings, 3rd Motorcon, Geneva, Sept 1982, pp260-276.
- (70) Ritter, T. and Boney, J.: "A microprocessor for the revolution: the 6809", 'Part I: Design philosophy', Byte, Vol. 4, No. 1, Jan 1979, pp14-42; 'Part II: Instruction set dead ends, old trails and apologies', Byte, Vol. 4, No. 2, Feb 1979, pp33-42; 'Part III: Final thoughts', Byte, Vol. 4, No. 3, Mar 1979, pp47-52.

(71) Thomson EFCIS Technical Brochure No. ADI-804A 1/26: "SFF9-6809 8-bit microprocessing unit".

(72) Intel Corporation: "Microcontroller Handbook"

(72) Ferranti Electronic Limited: "ULA Technical Handbook".